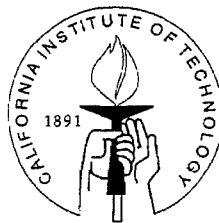


# Investigations of Novel Effects in Semi-inclusive Deep Inelastic Scattering

Thesis by

Andrea Paulina Dvoredsky

In Partial Fulfillment of the Requirements  
for the Degree of  
Doctor of Philosophy



California Institute of Technology  
Pasadena, California

2000

(Submitted September 29, 1999)

© 2000

Andrea Paulina Dvoredsky

All Rights Reserved

# Acknowledgements

*I was taught that the way of progress is neither swift nor easy....*

- Marie Curie

Insofar as the receipt of a doctorate can be called “progress,” my years of graduate school have proved the truth of this statement. Fortunately, I worked with extremely talented and inspirational people; because of these special persons, the path, though difficult at times, was ultimately richly rewarding.

The Kellogg Laboratory is a wonderful home for a graduate student and I am grateful for the opportunity to work there. I would like to begin by thanking Bob McKeown for his strong support of all my efforts. Bob’s immense love of science, his deep understanding of physics, and his gift for explaining complex ideas have inspired and humbled me. My appreciation also goes to Brad Filippone, who always had time to answer any question, large or small, and who offered a helpful jet-lag hint: You can’t wake up at 3 a.m. if you stay out until 3 a.m. Mark Pitt and Wolfgang Korsch taught me by direction and by example. In the painful final days of the completion of this work, Bira van Kolck provided theoretical guidance and encouragement. Paul Carter, my studymate and friend, was always available for important discussions at the Baskin Robbins conference center. The entire Kellogg staff gave me valuable help; in particular, Kim Stapp’s aid was appreciated, as was the technical skill of Bob Carr, Jim Pendlay, and Jack Richards.

Of the many helpful HERMES collaborators, there are a few without whom this work would have been truly impossible; in particular, Erik Volk guided me through the intricacies of the Monte Carlo studies. Naomi Makins also helped by listening willingly to my simulation woes in order to ultimately improve the entire process. Antje Brüll gave me extremely useful direction and welcome friendship. Andy Miller, originator of the word “TOMfoolery” to describe my laboratory exploits, egged me

on cheerfully in the additional experiments of 1996.

While I am particularly grateful to the many friends I made at Caltech and at DESY who enriched my experience, there are a few people who deserve special recognition. Infinite thanks go to my mother, who carried me through the most difficult chapter in my life. Mom and my beloved sister, Alexandra, lovingly supported me throughout this entire endeavor, while making sure that I never took myself too seriously.

Finally, I would like to thank my fiancé, Eric Belz, for being my sounding board, travel partner, and closest friend. Eric made my HERMES experience, and so many other journeys, much more interesting than I could have possibly imagined.

## Abstract

Azimuthal distributions in hadron production were measured in unpolarized deep inelastic scattering with unpolarized light gas targets. For pions, measurements of  $\langle \cos \phi \rangle$  are consistent with previous measurements at moderate  $Q^2$  values, although at low  $Q^2$ , there are indications that simple kinematic models are insufficient to describe these data. This effect appears to be charge-independent. The  $\langle \cos 2\phi \rangle$  moment is extracted as well and at an average  $Q^2$  of  $1.2 \text{ GeV}^2$ , a significant value for  $\langle \cos 2\phi \rangle / f_2(y)$  of  $0.302 \pm 0.029 \pm 0.064$  is seen and decreases with  $Q^2$ . In addition, first measurements are shown for the same azimuthal distributions in electroproduction of  $\Lambda$  and  $K_S$  and indicate that, unlike in pion production, the azimuthal moments for strange particles are much smaller. The  $\Lambda$  events are also used in a new search for spin transfer in deep inelastic scattering. Terms that depend on beam polarization are consistent with zero and show no clear kinematic variation, indicating that the polarized fragmentation function is small at these kinematics. On the other hand, the transverse polarization of  $P_y = -0.429 \pm 0.149 \pm 0.120$  seen at  $\langle x_F \rangle = 0.44$  suggests that unpolarized transverse fragmentation functions grow with  $x_F$  and  $z$ ; these measurements may be compared with hadroproduction data.

# Contents

<b>Acknowledgements</b>	<b>iii</b>
<b>Abstract</b>	<b>v</b>
<b>1 Physics Motivation.</b>	<b>1</b>
1.1 Formalism for Deep Inelastic Scattering. . . . .	1
1.1.1 Inclusive Deep Inelastic Scattering. . . . .	1
1.1.2 Semi-inclusive Reactions. . . . .	3
1.1.3 The Parton Model. . . . .	4
1.1.4 Hadronization. . . . .	6
1.2 Azimuthal Distributions. . . . .	9
1.2.1 Theory. . . . .	9
1.2.2 Previous Measurements. . . . .	13
1.3 $\Lambda$ Polarization. . . . .	14
1.3.1 Theory. . . . .	14
1.3.2 Measurements. . . . .	17
1.4 Deviations from the Parton Model. . . . .	18
<b>2 Experimental Apparatus.</b>	<b>22</b>
2.1 The HERA Beam. . . . .	22
2.2 The Internal Target. . . . .	24
2.3 The HERMES Detector. . . . .	25
2.3.1 Tracking Detectors. . . . .	26
2.3.2 The Calorimeter. . . . .	27
2.3.3 Particle Identification (PID) Detectors. . . . .	28
2.3.4 The Luminosity Monitor. . . . .	29

2.3.5	The Trigger. . . . .	30
2.3.6	The Gain Monitoring System. . . . .	30
2.3.7	Reconstruction Software. . . . .	31
<b>3</b>	<b>Signal Extraction.</b>	<b>33</b>
3.1	Monte Carlo Simulations. . . . .	33
3.2	Particle Identification. . . . .	34
3.2.1	Detector Parameterizations. . . . .	35
3.2.2	Likelihood PID. . . . .	36
3.3	Selection of Candidate Events. . . . .	37
3.3.1	Run and Burst Selection. . . . .	37
3.3.2	Particle Identification. . . . .	40
3.3.3	The Scattered Positron. . . . .	43
3.4	Identification of $(e, e'\pi)$ Events. . . . .	44
3.4.1	Fiducial Cuts. . . . .	44
3.4.2	Quadrant Analysis. . . . .	50
3.4.3	Kinematic Bins. . . . .	51
3.5	Identification of $(e, e'\Lambda)$ and $(e, e'K_S)$ Events. . . . .	52
3.5.1	Fiducial Cuts. . . . .	52
3.5.2	Background Reduction. . . . .	53
3.5.3	Lifetime. . . . .	53
3.5.4	Monte Carlo Models of Detector Resolution. . . . .	55
3.5.5	Vertex Distributions. . . . .	60
3.5.6	Additional Kinematic Cuts. . . . .	64
3.5.7	Final Cut Selection. . . . .	65
3.5.8	Mass Distributions. . . . .	65
3.5.9	Background Subtraction to Strange Particles. . . . .	66
3.5.10	Kinematic Distributions. . . . .	67
3.5.11	Quadrant Analysis. . . . .	73
3.5.12	Kinematic Bins. . . . .	74

<b>4 Results.</b>	<b>76</b>
4.1 Overview of Acceptance Corrections. . . . .	76
4.2 Azimuthal Distributions of Pions. . . . .	77
4.2.1 The Monte Carlo Generator. . . . .	77
4.2.2 Simulations of the Acceptance. . . . .	78
4.2.3 Analysis. . . . .	85
4.2.4 Systematic Studies and Uncertainties. . . . .	89
4.2.5 Results for Pion Azimuthal Distributions. . . . .	97
4.2.6 Charge-separated Results. . . . .	102
4.3 Azimuthal Distributions of Strange Particles. . . . .	105
4.3.1 Acceptance Corrected Results. . . . .	105
4.3.2 Systematic Uncertainties. . . . .	107
4.3.3 Results for Azimuthal Moments of Strange Particles. . . . .	112
4.4 $\Lambda$ Polarization. . . . .	115
4.4.1 Analysis. . . . .	115
4.4.2 Acceptance Corrected Results. . . . .	117
4.4.3 Systematic Uncertainties. . . . .	120
4.4.4 Polarization Results. . . . .	125
<b>5 Summary and Conclusions.</b>	<b>130</b>
<b>A Formalism.</b>	<b>132</b>
A.1 The Coincidence Cross Section. . . . .	132
A.1.1 The Lepton Tensor. . . . .	132
A.1.2 The Hadron Tensor. . . . .	135
A.1.3 Kinematic Factors. . . . .	137
A.2 Twist. . . . .	139
A.3 Notation. . . . .	141
A.4 Interpretation of Observable Asymmetries. . . . .	142



<b>B The Target Optical Monitor (TOM).</b>	<b>144</b>
B.1 $^3\text{He}$ Optical Pumping and Polarimetry. . . . .	144
B.2 The Principle of the TOM. . . . .	146
B.3 The Helium Target. . . . .	150
B.3.1 Spectroscopy. . . . .	150
B.3.2 Results. . . . .	151
B.3.3 Search for Depolarization. . . . .	154
B.4 The Hydrogen Target. . . . .	155
B.4.1 Rate Dependence on the Magnetic Field. . . . .	159
B.4.2 The "Amplifier" Effect. . . . .	160
B.4.3 Dependence on the Density. . . . .	162
B.5 Interpretation of the Hydrogen Results. . . . .	163
B.5.1 Beam Properties. . . . .	163
B.5.2 Ionization. . . . .	163
B.5.3 The Magnetic Mirror Effect. . . . .	165
B.5.4 The Density Dependence of the Chain Reaction. . . . .	167
B.6 Summary and Conclusions. . . . .	168
 <b>Bibliography</b>	 <b>169</b>

# List of Figures

1.1	Feynman diagram of single photon exchange. . . . .	1
1.2	Semi-inclusive scattering at the parton level. . . . .	7
1.3	Definition of the angle $\phi$ . . . . .	10
1.4	Lepton-parton scattering in the $\gamma - N$ CMS. . . . .	20
1.5	The role of transverse momentum in generating $\Lambda$ polarization. . . . .	21
2.1	Risetime of the beam polarization. . . . .	23
2.2	The HERA ring and the rotation of the beam polarization. . . . .	24
2.3	The target cell assembly . . . . .	25
2.4	A schematic of the detector. . . . .	26
3.1	Responses of the PID detectors. . . . .	36
3.2	Efficiencies of the FC's. . . . .	39
3.3	PID distribution. . . . .	41
3.4	Momentum dependence of Čerenkov $p - \pi$ separation. . . . .	42
3.5	$Q^2$ dependence of the acceptance. . . . .	44
3.6	Kinematics of $(e, e'\pi)$ events. . . . .	47
3.7	The correlation between $x_F$ and $z$ for $(e, e'\pi)$ events. . . . .	48
3.8	The correlation between $p_T$ and $z$ for $(e, e'\pi)$ events. . . . .	48
3.9	Evidence of factorization in $(e, e'\pi)$ interactions. . . . .	49
3.10	The division of the detector into quadrants for systematic studies. . . . .	50
3.11	Search for geometric effect on pion kinematics. . . . .	51
3.12	The collinearity in decays of strange particles. . . . .	55
3.13	Collinearity in Monte Carlo. . . . .	56
3.14	Definition of the two distances $d_{\text{hadron}}$ and $d_{e-X}$ . . . . .	57
3.15	$d_{e-\Lambda}$ and $d_{p-\pi}$ in Monte Carlo. . . . .	58
3.16	$d_{e-K_S}$ and $d_{\pi^+-\pi^-}$ in Monte Carlo. . . . .	58

3.17 $\Lambda$ mass distribution in Monte Carlo. . . . .	59
3.18 $K_S$ mass distribution in Monte Carlo. . . . .	59
3.19 $z'$ vertex distributions for $\Lambda$ and $K_S$ events. . . . .	61
3.20 Transverse vertex distributions in Monte Carlo. . . . .	63
3.21 Reconstructed mass peaks with all cuts applied. . . . .	66
3.22 $S/B$ as a function of $\Lambda$ energy. . . . .	67
3.23 $\Lambda$ energy distribution. . . . .	68
3.24 The momentum correlation between the $p$ and the $\pi$ from $\Lambda$ decays. . . . .	69
3.25 $\Lambda$ kinematic distributions. . . . .	70
3.26 $S/B$ as a function of $K_S$ energy. . . . .	71
3.27 $K_S$ energy distribution. . . . .	71
3.28 $K_S$ kinematic distributions. . . . .	72
3.29 Search for geometric effect on $\Lambda$ kinematics. . . . .	73
3.30 Search for geometric effect on $K_S$ kinematics. . . . .	74
4.1 Effect of the acceptance on azimuthal distributions. . . . .	79
4.2 Acceptance in $\phi$ as a function of $Q^2$ . . . . .	81
4.3 Example of the $\phi$ distribution for $(e, e'\pi)$ . . . . .	82
4.4 Acceptance in $\phi$ as a function of $p_T$ . . . . .	83
4.5 Acceptance in $\phi$ as a function of $z$ . . . . .	84
4.6 Acceptance in $\phi$ as a function of $x_F$ . . . . .	84
4.7 Effect of the reconstruction on $\phi$ in $(e, e'\pi)$ events. . . . .	89
4.8 Data/Monte Carlo comparison for $(e, e'\pi)$ events if $1 < \phi < (2\pi) - 1$ . . . . .	90
4.9 Systematic effects of discarding bins. . . . .	91
4.10 Radiative corrections to $\langle \cos \phi \rangle$ . . . . .	93
4.11 Effect of the reconstruction on kinematics in $(e, e'\pi)$ events. . . . .	94
4.12 The $Q^2$ variation of the $\langle \cos \phi \rangle$ moment. . . . .	98
4.13 $p_T$ dependence of $\langle \cos \phi \rangle$ moments. . . . .	98
4.14 $z$ dependence of $\langle \cos \phi \rangle$ moments. . . . .	99
4.15 $Q^2$ and $z$ dependence of $\langle \cos 2\phi \rangle$ moments. . . . .	100

4.16	Variation of $\langle \cos \phi \rangle$ and $\langle \cos 2\phi \rangle$ with parton kinematic factors. . . . .	101
4.17	$Q^2$ dependence of moments for $\pi^+$ and $\pi^-$ . . . . .	103
4.18	Moments in $\phi$ for the $(e, e'\Lambda)$ events. . . . .	114
4.19	Moments in $\phi$ for the $(e, e'K_S)$ events. . . . .	115
4.20	Raw angular distributions for lambdas. . . . .	117
4.21	A histogram to determine polarization in one direction. . . . .	118
4.22	Effect of reconstruction on $\Lambda$ angular distributions. . . . .	123
4.23	Extracted spin transfer coefficients. . . . .	126
4.24	$P_y$ for $(e, e'\Lambda)$ and hadroproduced lambdas. . . . .	128
4.25	$P_y$ of both $\Lambda$ and $K_S$ events. . . . .	129
4.26	Dependence of $P_y$ with $Q^2$ . . . . .	129
B.1	Level diagram for optical pumping of $^3\text{He}$ . . . . .	144
B.2	Level diagram for optical polarimetry of $^3\text{He}$ . . . . .	145
B.3	Polarimeter optics. . . . .	146
B.4	Polarimetry with an internal target. . . . .	147
B.5	The principle of the TOM. . . . .	148
B.6	TOM signal variation. . . . .	149
B.7	The level diagram for TOM polarimetry. . . . .	151
B.8	Comparison of the two TOM signals. . . . .	152
B.9	Comparison of the TOM and PCP polarization measurements. . . . .	153
B.10	Temperature dependence of TOM signal. . . . .	154
B.11	Beam current dependence of TOM signal. . . . .	155
B.12	TOM signal fluctuations with the ABS. . . . .	157
B.13	TOM rate studies with a shutter. . . . .	158
B.14	Magnetic field dependence of TOM: ABS. . . . .	159
B.15	Magnetic field dependence of TOM: $\text{H}_2$ . . . . .	160
B.16	The "amplifier" effect. . . . .	161
B.17	Density dependence of TOM rates: Unpolarized gases. . . . .	162
B.18	Ionization cross section of atomic hydrogen. . . . .	164

B.19 Ionization cross section of molecular hydrogen. . . . . 164

# List of Tables

1.1	Variables used in semi-inclusive deep inelastic scattering. . . . .	2
3.1	Discarded runs. . . . .	40
3.2	Čerenkov $p - \pi$ separation parameters for 1996 and 1997. . . . .	43
3.3	Final cut selection for pions. . . . .	46
3.4	Evidence of factorization in $(e, e'\pi)$ interactions. . . . .	49
3.5	Average kinematic values and bins for $(e, e'\pi)$ events. . . . .	52
3.6	$S/B$ and $\delta S/S$ for $(e, e'\Lambda)$ and $(e, e'K_S)$ as a function of lifetime. . . . .	54
3.7	Vertex distributions for $\Lambda$ and $K_S$ . . . . .	64
3.8	Final cut selection for $(e, e'\Lambda)$ and $(e, e'K_S)$ events. . . . .	65
3.9	Evidence of factorization in strange particle production. . . . .	70
3.10	Average kinematic values and bins for semi-inclusive $\Lambda$ and $K_S$ . . . . .	75
4.1	Generated $\phi$ moments. . . . .	78
4.2	Extracted moments in $\phi$ for $(e, e'\pi)$ events for each year. . . . .	86
4.3	Photon polarization factors in $(e, e'\pi)$ events. . . . .	87
4.4	Corrected moments in $\phi$ in $(e, e'\pi)$ for each year. . . . .	88
4.5	Systematic effects of restricting the range in $\phi$ . . . . .	92
4.6	Systematic uncertainties in azimuthal moments in $(e, e'\pi)$ . . . . .	96
4.7	$\langle \cos \phi \rangle$ and $\langle \cos 2\phi \rangle$ moments for the $(e, e'\pi)$ events. . . . .	97
4.8	Results for $\langle \sin \phi \rangle$ for the $(e, e'\pi)$ events. . . . .	102
4.9	$\langle \cos \phi \rangle$ and $\langle \cos 2\phi \rangle$ separated for $\pi^+$ and $\pi^-$ . . . . .	104
4.10	Photon polarization factors in $(e, e'\Lambda)$ and $(e, e'K_S)$ events. . . . .	105
4.11	Extracted moments in $\phi$ for $(e, e'\Lambda)$ and $(e, e'K_S)$ events for each year. . . . .	106
4.12	Corrected moments in $\phi$ for $(e, e'\Lambda)$ and $(e, e'K_S)$ for each year. . . . .	107
4.13	The $S/B$ as a function of kinematic bin for the $\Lambda$ events. . . . .	108
4.14	Background corrections for azimuthal distributions. . . . .	109

4.15	Misidentification of $\Lambda$ or $K_S$ as other particles. . . . .	110
4.16	Systematic uncertainties in $\phi$ moments of $(e, e'\Lambda)$ and $(e, e'K_S)$ events. . . . .	111
4.17	$\langle \cos \phi \rangle$ and $\langle \cos 2\phi \rangle$ in $(e, e'\Lambda)$ and $(e, e'K_S)$ events. . . . .	112
4.18	$\langle \sin \phi \rangle$ in $(e, e'\Lambda)$ and $(e, e'K_S)$ events. . . . .	113
4.19	Extracted $P_x$ for each year. . . . .	119
4.20	Extracted $P_y$ for each year. . . . .	119
4.21	Extracted $P_z$ for each year. . . . .	120
4.22	Background corrections to polarization values. . . . .	121
4.23	Polarization of the $K_S$ . . . . .	122
4.24	Systematic uncertainties for polarization extractions. . . . .	125
4.25	Extracted spin transfer coefficients $\Delta P_x$ and $\Delta P_z$ . . . . .	125
4.26	The transverse polarization $P_y$ . . . . .	127
A.1	Single-spin leading-twist observables. . . . .	142

# Chapter 1 Physics Motivation.

## 1.1 Formalism for Deep Inelastic Scattering.

### 1.1.1 Inclusive Deep Inelastic Scattering.

The term *deep inelastic scattering* (DIS) describes the process in which a lepton beam is scattered off a hadronic target such that the energy and momentum transfer are sufficient to break up the hadron. Although at higher energies  $Z^0$  exchange is relevant, at the energies of the experiments discussed here (27.5 GeV), the single photon exchange approximation is sufficient. The relevant Feynman diagram is shown in Figure 1.1, with the four-vectors shown as they are defined in Table 1.1. *Inclusive*

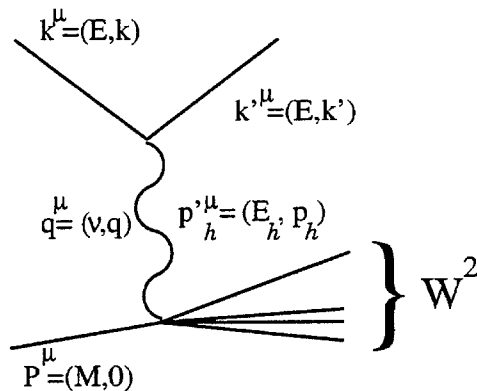


Figure 1.1: Feynman diagram of single photon exchange. All four-vectors are evaluated in the laboratory frame and represented as  $(E, \vec{p})$ .

measurements characterize those in which only the scattered lepton is detected. In the following discussion, the formalism and conventions of References [1] and [2] will be used in terms of the variables defined in Table 1.1. A differential cross section in the laboratory frame for particles of energy  $E$  that are scattered with energy  $E'$  into



solid angle  $d\Omega$  may be written in the following way:

$$\frac{d\sigma}{d\Omega dE'} = \frac{\alpha^2}{Q^4} \frac{E'}{E} L_{\mu\nu} W^{\mu\nu}, \quad (1.1)$$

where  $\alpha$  is the fine structure constant and  $Q^2$  represents the invariant momentum transfer. The indices  $\mu$  and  $\nu$  typically refer to the Cartesian coordinates in which the tensors may be evaluated.

The target nucleon	
$M$	Mass of target nucleon
$P^\mu$	4-momentum of target nucleon
The lepton	
$E$	Energy of incident lepton
$k^\mu$	4-momentum of incident lepton
$E'$	Energy of scattered lepton
$k'^\mu$	4-momentum of scattered lepton
$\theta$	Scattering angle of lepton
$q^\mu$	4-momentum of virtual photon = $k^\mu - k'^\mu$
$Q^2$	Squared momentum transfer = $-q^2 = 4EE'\sin^2\theta/2$
$W^2$	Invariant mass of hadronic system = $(p + q)^2 = M^2 + 2M\nu - Q^2$
$\nu$	Energy loss to hadronic system = $E - E'$
$y$	Fractional energy loss = $(E - E')/E$
$x$	Scaling variable in parton model = $(Q^2/P \cdot q) = Q^2/2M\nu$
The coincident hadron	
$M_h$	Mass of hadron
$P_h^\mu$	4-momentum of hadron
$E_h$	Energy of hadron
$z$	Fractional energy of hadron = $P \cdot P_h / P \cdot q = E_h/\nu$
$x_F$	Fractional longitudinal momentum of hadron in $\gamma$ -N CM = $2\vec{p}_h \cdot \vec{q} / \sqrt{W^2}$
$p_T$	Transverse momentum of hadron in $\gamma$ -N CM

Table 1.1: Variables used in semi-inclusive deep inelastic scattering and definitions in terms of Lorentz invariants. Unless otherwise specified, all quantities are evaluated in the target rest frame (the laboratory frame for fixed-target experiments).

Assuming a massless lepton, the lepton tensor  $L_{\mu\nu}$  can be written as:

$$L_{\mu\nu} = 2k_\mu k'_\nu + 2k_\nu k'_\mu - Q^2 g_{\mu\nu}. \quad (1.2)$$

The hadron tensor  $W_{\mu\nu}$  can be expanded in terms of currents  $J_\mu$  operating between

the proton state  $|P\rangle$  and all  $N$  particle final states  $\langle X|$ . It is appropriate to average over initial spins  $s$  and sum over final spin states  $s'$ ; doing so explicitly, the following expression may be obtained:

$$4\pi MW_{\mu\nu} = \sum_N \frac{1}{2} \sum_s \int \prod_{i=1}^N \left( \frac{d^3 p_N}{(2\pi)^3 2E'_N} \right) \sum_{s'} \langle P|J_\nu|X\rangle \langle X|J_\mu|P\rangle (2\pi)^4 \delta^4(P - q - \sum_N p_N). \quad (1.3)$$

For the inclusive case where only a lepton with final momentum  $p'$  is detected and no information is gained regarding the final hadronic state  $X$ , this reduces to

$$4\pi MW^{\mu\nu} = \sum_X \langle P|J^\nu|X\rangle \langle X|J^\mu|P\rangle (2\pi)^4 \delta(P + q - p'). \quad (1.4)$$

Furthermore, this tensor can be decomposed into its Lorentz components. Current conservation, gauge invariance, and parity conservation lead to

$$W^{\mu\nu} = W_1 \left( \frac{q^\mu q^\nu}{q^2} \right) - g^{\mu\nu} + W_2 \frac{1}{M^2} (p^\mu - \frac{p \cdot q}{q^2} q^\mu) (p^\nu - \frac{p \cdot q}{q^2} q^\nu), \quad (1.5)$$

where  $W_1$  and  $W_2$  will be further elucidated below.

### 1.1.2 Semi-inclusive Reactions.

*Semi-inclusive* reactions are those in which one, but not all, of the final state particles are detected. This work will be concerned principally with three such reactions:  $ep \rightarrow e'\pi X$ ,  $ep \rightarrow e'\Lambda X$ , and  $ep \rightarrow e'K_S X$ . The pions allow generous access to the valence quarks as their multiplicity is high. The measurements of the  $\Lambda$  and the  $K_S$  are interesting because the quark structure of the  $\Lambda$  is  $uds$  and that of the  $K_S$  is  $\bar{d}s$ . Consequently, both of these particles sample the strange nucleon sea, and in fact the  $K_S$  is composed only of sea particles.

Following Reference [3] and using Equation 1.3, the hadron tensor can be rewritten

for the case of one detected hadron  $h$  and an undetected remnant  $X$ :

$$2MW_{\mu\nu} = \frac{1}{(2\pi)^4} \sum_X \int \frac{d^3 P_X}{(2\pi)^3 2E_X} \langle P | J_\nu | P_X, p_h \rangle \langle p_h, P_X | J_\mu | P \rangle (2\pi)^4 \delta^4(P + q - p_h - P_X). \quad (1.6)$$

The differential cross section analogous to Equation 1.1 can then be rewritten as

$$\frac{2E_h d\sigma}{d^3 p_h d\Omega dE'} = \frac{\alpha^2 E'}{Q^4 E} L_{\mu\nu} W^{\mu\nu}. \quad (1.7)$$

### 1.1.3 The Parton Model.

The discussion of Section 1.1.1 provides exact expressions for the scattering cross section in both inclusive and semi-inclusive DIS interactions. In general, such processes are characterized by the theory of *quantum chromodynamics* (QCD). QCD describes both the confinement of the quarks inside the hadron and the  $x$ -scaling behavior seen in the first quark scattering experiments [4]. Thus, the QCD coupling constant,  $\alpha_S(Q^2)$ , must grow with distance; equivalently, by the Heisenberg uncertainty principle,  $\alpha_S(Q^2)$  must decrease as the momentum transfer  $Q^2$  grows.

If  $Q^2$  is large enough, the virtual photon probes a short distance inside the nucleon. Furthermore, at high energies, the time scale of the probe is shorter than the parton interaction time scale. These two assumptions together constitute an impulse approximation known as the *parton model*. In this case, the single-photon exchange diagram of Figure 1.1 indicates that the leading process is governed by the theory of *quantum electrodynamics* (QED). Assuming that the partons are non-interacting free particles, the tensor  $W_{\mu\nu}$  may be rewritten once its Lorentz structure is specified and current conservation is imposed. The structure functions  $W_1$  and  $W_2$  of Equation 1.5 can be simplified to give the following well-known result:

$$\begin{aligned} \nu W_2(\nu, Q^2) \rightarrow F_2(x) &= \sum_i e_i^2 x f_i(x), \\ MW_1(\nu, Q^2) \rightarrow F_1(x) &= \frac{1}{2x} F_2(x). \end{aligned} \quad (1.8)$$

These sums run over  $i$  quarks with charges  $e_i^2$ . The parton model is defined by the assumption that each parton carries a fraction  $x$  of the momentum of the nucleon and that the partons do not interact. The function  $f_i(x)$  is the parton *distribution function* (DF) which defines the number of partons with the momentum fraction  $x$ . An important assumption in this model is that the partons carry only longitudinal momentum; the influence of transverse components will be considered below in a more realistic model.

The unpolarized function  $F_1(x)$  and the related function  $F_2(x)$  are seen to be equivalent to Fourier transforms of matrix elements via Equations 1.5 and 1.6. They are known as “distribution” functions since they elucidate the momentum distributions of the quarks inside the nucleon. The polarized DF’s  $g_1(x)$  and  $g_2(x)$  have also been studied experimentally and access the spin distributions of the quarks (discussed in References [5] and [6] and the references therein), which may be explained straightforwardly in the parton model as well.

A more complete representation of the nucleon demands the inclusion of QCD in order to properly account for the confinement of partons, interactions between them, and transverse momenta. Such calculations exploit the behavior of the coupling constant  $\alpha_S$  under the assumption that high energy processes can be *factorized* into short and long distance physics; this is equivalently explained as a separation into *hard* and *soft* processes and is detailed in Appendix A.2. The differential cross section for  $N_h$  coincident hadrons detected with energy fraction  $z$  can be expressed in this fashion, summing over  $i$  flavors of quarks carrying momentum fraction  $x$  and with charges  $e_i^2$  gives

$$\frac{1}{N_h} \frac{dN_h}{dz} = \frac{\sum_i e_i^2 q_i(x) D_i(z)}{\sum_i e_i^2 q_i(x)}, \quad (1.9)$$

where  $q_i$  are DF’s and  $D_i$  are *fragmentation functions* (FF), which characterize the hadronization. Equation 1.9 indicates that the dependence on the lepton kinematics resides entirely in the DF’s, while the hadronization behavior is fully contained in the FF’s. Thus, semi-inclusive cross sections may be expressed as sums of products of DF’s and FF’s.

The factorization into long and short distance processes is important for the following reason: At short distances, where the coupling constant,  $\alpha_S$ , is smaller, the partons behave more as free particles and hence perturbative techniques may be used to calculate the cross sections. On the other hand, at large distances,  $\alpha_S$  grows and the coupling can no longer be expanded analytically.  $\alpha_S$  is written as a function of  $Q^2$  in order to characterize its variation with length scale. For this reason, a mechanism that may contribute to a high energy process is identified by its *twist*, which is fully defined in Appendix A.2. Dominant terms appear at *leading* twist, whereas other effects appear with *higher* twist. These terms will be used in the discussions following.

#### 1.1.4 Hadronization.

In principle, these DF's and the FF's should characterize universal properties of hadronization. In particular, soft processes provide information regarding confinement and hence should be common to all high energy processes [7]. It is precisely these interesting soft processes that cannot be calculated perturbatively.

An alternative approach to calculations with current algebra is that developed by Ellis, *et al.* [8], in which the structure functions are expanded diagrammatically. Intrinsic transverse momentum enters naturally and  $1/Q$  corrections are derived. Extensions of these techniques allow for the determination of similar diagrammatic expansions for semi-inclusive processes.

In the parton model, the physics is expressed in the Breit (or "infinite momentum") frame, in which the target parton is considered to have "bounced" off the brick wall of the photon. That is, the nucleon absorbs no energy in this frame. An alternative reference frame has been widely considered for semi-inclusive processes and is elucidated clearly in References [9] and [10]. In this new frame, the target momentum vector is collinear with that of the exiting hadron (thus it will be referred to as the  $h - N$  frame). The process is then written in terms of the four-vectors  $p^\mu$  and  $k^\mu$ , which distinguish the quark before and after the interaction, respectively.

This representation is shown diagrammatically in Figure 1.2.

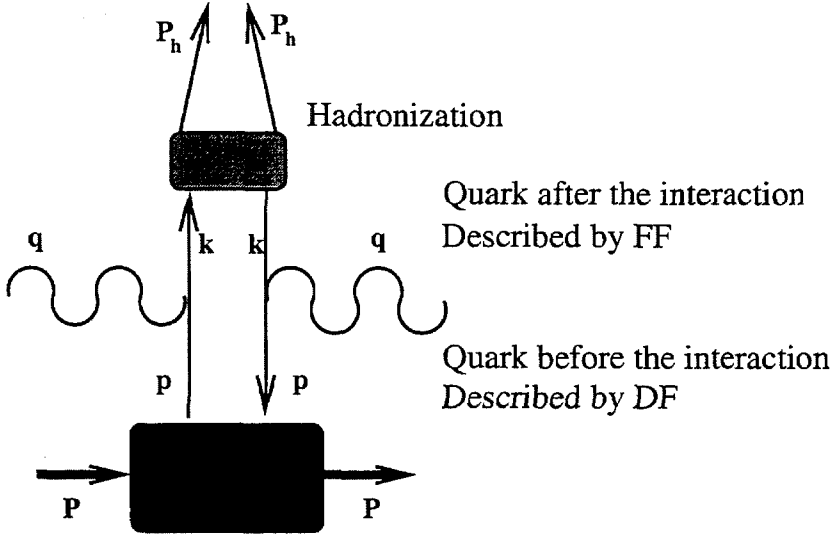


Figure 1.2: Semi-inclusive scattering at the parton level. Taken from Reference [10].

Under the assumption that the matrix elements will be nonzero only for quark momenta limited to the hadronic length scale given by  $Q$ , the quark momenta may be approximated:

$$\begin{aligned} p^2 &\approx P^2 = M^2 \ll Q^2, \\ k^2 &\approx P_h^2 = M_h^2 \ll Q^2. \end{aligned} \quad (1.10)$$

Meanwhile, the following relations still hold true:

$$\begin{aligned} q^2 &= -Q^2, \\ P^2 &= M^2, \\ P_h^2 &= M_h^2, \\ 2P \cdot q &= \frac{Q^2}{x_B}, \\ 2P_h \cdot q &= -z_h Q^2. \end{aligned} \quad (1.11)$$

A transformation is chosen from  $p^\mu$  and  $k^\mu$  to new lightlike coordinates,  $n_+$  and  $n_-$ . These basis vectors satisfy  $n_+ \cdot n_- = 1$ ;  $n_+^2 = n_-^2 = 0$ .

The observed momenta  $P$  and  $P_h$  may be resolved easily in this  $h-N$  basis (where they are, after all, collinear). The virtual photon's momentum  $q$  is decomposed here as well (its transverse momentum  $q_T$  is trivially transformed into  $-p_T/z$  in the  $\gamma-N$  frame):

$$P = \frac{1}{\sqrt{2}} \left( \frac{xM^2}{Q} n_- + \frac{Q}{x} n_+ \right), \quad (1.12)$$

$$q = \frac{1}{\sqrt{2}} (Qn_- - Qn_+) + q_T, \quad (1.13)$$

$$P_h = \frac{1}{\sqrt{2}} \left( zQn_- + \frac{M_h^2}{zQ} n_+ \right). \quad (1.14)$$

Hard parts of the interaction will go as  $Q$  and soft parts will go as  $1/Q$ . In order to investigate the soft parts, the appropriate contributions are  $P^-$  and  $P_h^+$ . Returning to the relevant quark momenta, the soft part of the interaction is thus reduced to terms in  $p^-$  and  $k^+$ .

The DF's and FF's may be expressed in terms of these new transformed momentum four-vectors. New correlation functions  $\Phi_{ij}$  and  $\Delta_{ij}$  are introduced in order to represent the action of the non-local field operators  $\psi$  in this frame. Their expressions as Fourier transforms of matrix elements are

$$\Phi_{ij}(p, P, S) = \frac{1}{(2\pi)^4} \int d^4x e^{ip \cdot x} \langle P, S | \bar{\psi}_j(0) \psi_i(x) | P, S \rangle, \quad (1.15)$$

$$\Delta_{ij}(k, P_h, S_h) = \sum_X \frac{1}{(2\pi)^4} \int d^4x e^{ik \cdot x} \langle 0 | \psi_i(x) | P_h, S_h; X \rangle \langle P_h, S_h; X | \bar{\psi}_j(0) | 0 \rangle. \quad (1.16)$$

The correlation function  $\Phi_{ij}$  acts on the proton ground state and hence represents the DF's. On the other hand, the correlation function  $\Delta_{ij}$  provides for the creation of hadrons from the vacuum (thus the sum over final states  $|X\rangle$ ); for that reason, it is related to the FF's. These functions are projected onto the space of Dirac operators  $\Gamma$ :

$$\Phi^{[\Gamma]}(x, \mathbf{p}_T) = \int dp^- \frac{Tr[\Phi\Gamma]}{2}, \quad (1.17)$$

$$\Delta^{[\Gamma]}(z, \mathbf{k}_T) = \int dk^+ \frac{Tr[\Delta\Gamma]}{4z}. \quad (1.18)$$

The tensor of Equation 1.6 may then be rewritten in terms of these correlation functions:

$$\begin{aligned}
2MW_{\mu\nu}(q, P, p_h) &= \int d^2\mathbf{p}_T d^2\mathbf{k}_T \delta^2(\mathbf{p}_T + \mathbf{q}_T - \mathbf{k}_T) \frac{1}{4} \text{Tr}[\Phi(x, p_T) \gamma_\mu \Delta(z, k_T) \gamma_\nu] \\
&+ (q \leftrightarrow -q, \mu \leftrightarrow \nu).
\end{aligned}
\tag{1.19}$$

Thus, the hadron tensor has been expressed in terms of calculable matrix elements rather than the poorly understood currents. Just as in the parton model, albeit in a different frame, the DF's and FF's may be expressed in this formalism as Fourier transforms of matrix elements via Equations 1.15 and 1.16. For instance, the unpolarized DF and FF discussed previously may be extracted if the Dirac projection is simply the vector operator  $\gamma^\mu$ :

$$\begin{aligned}
\Phi^{[\gamma^+]}(x, \mathbf{p}_T) &= f_1(x, \mathbf{p}_T^2), \\
\Delta^{[\gamma^-]}(z, \mathbf{k}_T) &= D_1(z, -z\mathbf{k}_T).
\end{aligned}
\tag{1.20}$$

The notation to identify these Dirac projections follows that of Mulders and is summarized in Appendix A.3. In general, invariance under Lorentz, parity, and time-reversal (TR) transformations can be used to constrain the form of these functions. Final state interactions, however, may produce FF's that are not even under TR invariance. The interesting behavior of DF's and FF's for various final states are the subject of this thesis.

## 1.2 Azimuthal Distributions.

### 1.2.1 Theory.

The azimuthal angle  $\phi$  is shown in Figure 1.3; it is the angle between the hadron production plane and the lepton scattering plane. For an unpolarized target and a lepton beam with longitudinal polarization  $P_e$ , the most general form for the normalized cross section for  $N$  detected hadrons is given by the following (see Appendix A.1



for details) [11]:

$$\frac{1}{N} \frac{dN}{d\phi} = 1 + Af_1(y)\cos \phi + Bf_2(y)\cos 2\phi + P_e C f_3(y)\sin \phi. \quad (1.21)$$

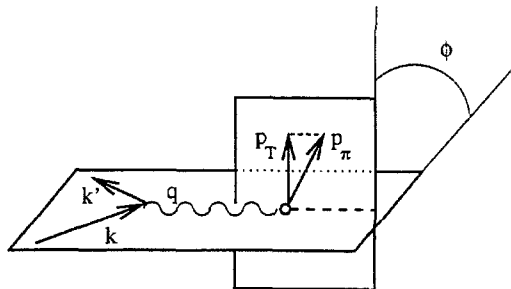


Figure 1.3: The definition of the angle  $\phi$  between the lepton scattering plane and the hadron production plane.

The functions  $f_i(y)$  in Equation 1.21 describe the components of the photon's polarization in terms of the lepton's kinematics:

$$\begin{aligned} f_1(y) &= (2-y)\sqrt{1-y}/[1+(1-y)^2], \\ f_2(y) &= (1-y)/[1+(1-y)^2], \\ f_3(y) &= y\sqrt{1-y}/[1+(1-y)^2]. \end{aligned} \quad (1.22)$$

The moments of the distribution can then be identified:

$$\langle \cos \phi \rangle = A/2f_1(y), \quad \langle \cos 2\phi \rangle = B/2f_2(y), \quad \langle \sin \phi \rangle = C/2f_3(y). \quad (1.23)$$

In the language of nuclear physics, the photon's coupling can be decomposed into the longitudinal (L) and two transverse (T) components. In Equation 1.21, the quantities  $A$  and  $C$  reflect the L-T and L-T' interference terms, respectively, and  $B$  identifies the T-T interference.<sup>1</sup>

<sup>1</sup>In intermediate energy nuclear physics, the terms analogous to  $A$ ,  $B$ , and  $C$  are, respectively,  $W_{LT}$ ,  $W_{TT}$ , and the "fifth structure function"  $W'_{LT}$ .

These expressions do not elucidate the hadronization process but rather just the terms allowed by angular momentum algebra. These distributions are actually sensitive to the parton transverse momentum distributions, as discussed by Cahn [12]. Although it was originally proposed that such distributions would also result from radiative QCD processes [13, 14], it appears that the transverse momentum effects dominate, although the two effects may be considered simultaneously [15, 16]. The physics of transverse momentum effects will be discussed further in Section 1.4.

The hadronization process may also induce such azimuthal distribution phenomena via final state interactions that result in so-called time-reversal (TR) odd fragmentation functions. (Note that these functions do not indicate a violation of fundamental TR-invariance.) In particular, such effects can produce a non-zero leading order  $\langle \cos 2\phi \rangle$  moment [17] as opposed to higher twist (order  $1/Q^2$ ) processes, considered by Berger in Reference [18]. Separation of the kinematic and higher-twist effects was considered in Reference [19], specifically for pion production.

Recent work by Mulders [20] and others have couched these observables in the language of the quark fragmentation process. In this framework, the leading moments can be evaluated and expressed in terms of weighted and integrated cross sections. For beam polarization  $P_B$  and target polarization  $P_T$ , the expectation value for the weighting function  $W$  may be expressed as

$$\langle W \rangle_{P_B P_T} = \int d\phi d^2\mathbf{q}_T W(Q_T, \phi, \phi_S, \phi_S^h) \frac{d\sigma_{P_B P_T}}{dx dy dz d\phi d^2\mathbf{q}_T}, \quad (1.24)$$

with transverse spin vectors for the target (detected hadron) defined by  $\phi_S$  ( $\phi_S^h$ ). With an unpolarized target and no determination of the spin of the detected hadron<sup>2</sup>, this reduces to

$$\langle W \rangle_{UU} = \int d\phi d^2\mathbf{q}_T W(Q_T, \phi) \frac{d\sigma_{UU}}{dx dy dz d\phi d^2\mathbf{q}_T}, \quad (1.25)$$

---

<sup>2</sup>In principle, additional asymmetries would be accessible for the  $\Lambda$ , in which the  $\phi$  dependence of the polarization would access additional structure functions; furthermore, such effects are not expected to contribute up to order  $(1/Q)$  [20]. The statistics of this experiment were limited such that a search for deviations from this model were impossible. For this reason, the polarization and  $\phi$  measurements for the  $\Lambda$  will be considered to be independent.

where the subscript  $U$  refers to the unpolarized beam or target.

For instance, for an unpolarized beam incident on an unpolarized target, the expectation value of the constant (i.e.,  $\langle 1 \rangle$ ) should simply be the unpolarized cross section,

$$\langle 1 \rangle_{UU} = (1 + (1 - y)^2) \sum_i e_i^2 f_1^i(x) x D_1^i(z). \quad (1.26)$$

That is, the  $\phi$ -independent term of Equation 1.21 is simply a product of the properly weighted DF and FF. Both the DF and FF are even under time reversal.

Another leading-twist contribution is the expectation value for the  $\langle \cos 2\phi \rangle$  weighting function, which gives rise to an asymmetry

$$\left\langle \frac{Q_T^2}{4MM_h} \cos 2\phi \right\rangle_{UU} = (1 - y) \sum_i e_i^2 x h_1^{\perp(1)i}(x) H_1^{\perp(1)i}(z). \quad (1.27)$$

In this expression, the term  $Q_T^2$  is the photon's transverse momentum in the frame where the proton and detected hadron are collinear;  $Q_T = p_T/z$  where  $p_T$  is the hadron's transverse momentum in the  $\gamma - N$  CMS<sup>3</sup>.

The observable of Equation 1.27 contains a DF and a FF that are both odd under time reversal. (If only T-even terms are included, this term contributes at order  $1/Q^2$  [18].) The DF  $h_1^\perp$  describes the momentum-weighted distribution of quarks with transverse spin in an unpolarized nucleon. The FF  $H_1^\perp$  represents fragmentation of a quark with transverse spin. It has been widely discussed in terms of experiments with transversely polarized targets [21, 22, 23]; here, it appears as a leading contribution only when weighted over the  $k_T$  distribution. This moment corresponds to the term  $B$  in Equation 1.21 expressed in terms of FF's.

Interestingly, the moment  $\langle \cos \phi \rangle$  (the labels  $UU$  will be assumed and hence suppressed hereafter) does not appear at leading order in the unpolarized cross sections. Its complicated form is discussed in Reference [20]. If the dynamics in the DF and

---

<sup>3</sup>The observed  $p_T$ , the hadron's transverse momentum in the  $\gamma - N$  CMS, should be carefully distinguished from  $p_\perp$ , the *parton's* transverse momentum in the same frame. In the simplest model, they are related simply by the factor dilution  $z$ :  $p_\perp = p_T/z$ . Thus,  $Q_T$  is simply equal to the parton's transverse momentum  $p_\perp$ . This is equivalent to the observation that the parton's transverse momentum in the  $\gamma - N$  frame is transformed into the photon's transverse momentum in the  $h - N$  frame.

FF are suppressed and the quark has only transverse momentum  $p_T$ , this expectation value reduces to the simple form

$$\langle \cos \phi \rangle = -2 \frac{(2-y)\sqrt{1-y} p_{\perp}}{1+(1-y)^2 Q}. \quad (1.28)$$

This term was first predicted by Cahn [12]. It measures the transverse momentum of the struck quark but provides no determination of the spin vector. As the quark's momentum would be diluted by a factor of  $z$  in the hadronization process, this factor should properly be included in experimental work. The fragmentation also affects this measurement because the random motion of hadronization is expected to dilute the strong  $\phi$  dependence.

Cahn also predicts a kinematic model to produce a non-vanishing  $\langle \cos 2\phi \rangle$  term. Under such kinematic considerations, this term appears at order  $(1/Q^2)$ :

$$\langle \cos 2\phi \rangle = \frac{(1-y)}{1+(1-y)^2} \left( \frac{2p_{\perp}^2}{Q^2} \right). \quad (1.29)$$

For it to contribute at leading order, more complex dynamics, such as the TR-odd functions discussed in Equation 1.27, must be included as well.

Parity considerations allow polarized leptons to provide an additional term in  $\langle \sin \phi \rangle$ ; however, it is expected to appear at order  $1/Q$  [24]. It is the product of a higher twist DF and a TR-odd, twist-two FF, as considered in Reference [25]. The spin dependence of the  $\langle \cos \phi \rangle$  moments by a polarized beam was also considered in Reference [26] as a new technique to extract polarized nucleon structure functions.

## 1.2.2 Previous Measurements.

Azimuthal distributions were studied by the European Muon Collaboration (EMC) [27, 28] in doubly polarized  $\mu-N$  scattering experiments, in which all charged hadrons in coincidence with the scattered muon were detected. Since there was not sufficient particle identification, the final states were not separated, though the sample was largely composed of pions. Using the notation of Equation 1.21, measured values for

$A$  were negative and showed variation with increasing  $p_T$ ,  $z$ , and  $x_F$ , while values for  $B$  and  $C$  were consistent with zero.  $A$  was also insensitive to variations in  $Q^2$  and  $W^2$ . These observations agreed with Cahn's kinematic model and were consistent with the idea that the hadron production mechanism is independent of the lepton kinematics. Further measurements by the E665 Collaboration in  $\mu - p$  and  $\mu - d$  interactions similarly indicated that the  $\langle \cos \phi \rangle$  moment was negative and could be explained by the quark's transverse momentum [29].

These distributions were also measured in deep inelastic neutrino scattering [30], where a  $\langle \cos \phi \rangle$  value of  $-0.0224 \pm 0.0032$  was measured. This was combined with hadronization models to extract a value for the quark's transverse momentum of  $\langle k_T \rangle \sim 0.3$  GeV/c by using Cahn's model.

A related set of measurements is published in Reference [31], in which a polarized target is used to extract a spin-dependent asymmetry in  $\phi$ . This measurement accesses different spin-dependent parton distributions.

### 1.3 $\Lambda$ Polarization.

The  $\Lambda$  baryon is particularly conducive to polarization measurements; its weak decay into a  $p^+\pi^-$  pair (BR=64%) is self-analyzing since the polarization of the  $\Lambda$  can be directly related to the momentum of the decay particles. For the case of an unpolarized beam and unpolarized target, the resulting polarization of the exiting  $\Lambda$  must result from so-called final-state interactions.

Andersson's semi-classical model for production of  $\Lambda$  polarization [32] is expounded more fully in Section 1.4. The following discussion, however, provides the mathematical expressions for polarization in terms of DF's and FF's.

#### 1.3.1 Theory.

Using the formalism of Section 1.1.4, the polarization of the detected  $\Lambda$  may be expressed in terms of these DF's and FF's. The full expressions for the polarization along each axis are listed below.  $S_{x,y,z}$  refers to the polarization axis of the target. The

summations run over  $i$  quarks and antiquarks, each with charges  $e_i$ . The coefficients that describe the photon's polarization vector can be written in different ways; a convention has been chosen here that will make the relation between the azimuthal distributions and the polarization more evident:

$$\begin{aligned}
P_z(x, z)N_\Lambda &= P_e \frac{y(2-y)}{1+(1-y)^2} \frac{\sum_i e_i^2 f_1^i(x) G_1^i(z)}{\sum_i e_i^2 f_1^i(x)} \\
&+ S_z \frac{\sum_i e_i^2 g_1^i(x) G_1^i(z)}{\sum_i e_i^2 f_1^i(x)} \\
&- S_x \frac{4(2-y)\sqrt{1-y}}{1+(1-y)^2} \left[ \frac{M}{Q} \frac{\sum_i e_i^2 x g_T^i(x) G_1^i(z)}{\sum_i e_i^2 f_1^i(x)} \right. \\
&+ \left. \frac{M_\Lambda}{Q} \frac{\sum_i e_i^2 h_1^i(x) H_L^i(z)/z}{\sum_i e_i^2 f_1^i(x)} \right] \\
&- S_y \frac{4y\sqrt{1-y}}{1+(1-y)^2} \frac{M_\Lambda}{Q} \frac{\sum_i e_i^2 h_1^i \tilde{E}_L^i(z)/z}{\sum_i e_i^2 f_1^i(x)},
\end{aligned}$$

$$\begin{aligned}
P_y(x, z)N_\Lambda &= \frac{4(2-y)\sqrt{1-y}}{1+(1-y)^2} \frac{M_\Lambda}{Q} \frac{\sum_i e_i^2 f_1^i(x) D_{1T}^{1(1)i}(z)}{\sum_i e_i^2 f_1^i(x)} \\
&+ P_e S_z \frac{4y\sqrt{1-y}}{1+(1-y)^2} \frac{M_\Lambda}{Q} \frac{\sum_i e_i^2 g_1^i(x) D_{1T}^{1(1)i}(z)}{\sum_i e_i^2 f_1^i(x)} \\
&+ S_y \frac{2(1-y)}{1+(1-y)^2} \frac{\sum_a e_a^2 h_1^i(x) H_1^i(z)}{\sum_i e_i^2 f_1^i(x)},
\end{aligned}$$

$$\begin{aligned}
P_x(x, z)N_\Lambda &= -P_e \frac{4y\sqrt{1-y}}{1+(1-y)^2} \left[ \frac{M}{Q} \frac{\sum_i e_i^2 x e^i(x) H_1^i(z)}{\sum_i e_i^2 f_1^i(x)} \right. \\
&+ \left. \frac{M_\Lambda}{Q} \frac{\sum_i e_i^2 f_1^i(x) \tilde{G}_T^i(z)/z}{\sum_i e_i^2 f_1^i(x)} \right] \\
&- S_x \frac{2(1-y)}{1+(1-y)^2} \frac{\sum_i e_i^2 h_1^i(x) H_1^i(z)}{\sum_i e_i^2 f_1^i(x)} \\
&- S_z \frac{4(2-y)\sqrt{1-y}}{1+(1-y)^2} \left[ \frac{M}{Q} \frac{\sum_i e_i^2 x h_L^i(x) H_1^i(z)}{\sum_i e_i^2 f_1^i(x)} \right. \\
&+ \left. \frac{M_\Lambda}{Q} \frac{\sum_i e_i^2 g_1^i(x) \tilde{G}_T^i(z)/z}{\sum_i e_i^2 f_1^i(x)} \right].
\end{aligned}$$

By setting  $S_i = 0$ , these equations can be reduced to the expressions that can be measured with an unpolarized target and polarized beam. Naturally, many new functions can be accessed with a polarized target as well, though such data were not available with sufficient precision when this analysis was performed. The measurements available with a polarized target have also been discussed [33, 34] in order to access the contribution of the strange sea to the spin of a longitudinally polarized nucleon.

### Longitudinal Polarization $P_z$ .

$$P_z(x, z)N_\Lambda = P_e \frac{y(2-y)}{1+(1-y)^2} \frac{\sum_i e_i^2 f_1^i(x) G_1^i(z)}{\sum_i e_i^2 f_1^i(x)}. \quad (1.30)$$

This term, the transfer of longitudinal polarization from the beam to the target, has been widely discussed as an interesting measurement [35]. Its importance lies in the access to the polarized fragmentation function  $G_1(z)$ . At the energies of these measurements, it is expected to probe the contribution from the valence quarks to the  $\Lambda$  polarization rather than the contribution from the  $s$  quark in the sea.

The kinematic coefficient is familiar as the depolarization factor  $D(y)$ , which is used to extract inclusive asymmetries; it relates the longitudinal polarization of the lepton to that of the photon and hence is needed here as well.

### Transverse Polarization $P_x$ .

$$P_x(x, z)N_\Lambda = -P_e \frac{4y\sqrt{1-y}}{1+(1-y)^2} \left[ \frac{M}{Q} \frac{\sum_i e_i^2 x e^i(x) H_1^i(z)}{\sum_i e_i^2 f_1^i(x)} - \frac{M_\Lambda}{Q} \frac{\sum_i e_i^2 f_1^i(x) \tilde{G}_T^i(z)/z}{\sum_i e_i^2 f_1^i(x)} \right]. \quad (1.31)$$

$P_x$  is transverse polarization in the scattering plane. Its leading term is proportional to  $1/Q$  and requires polarized beam to observe a spin transfer. This process is higher twist. This kinematic coefficient appeared previously as  $f_3(y)$ , the imaginary part of the longitudinal-transverse interference term in Section 1.2.

### Transverse Polarization $P_y$ .

$$P_y(x, z)N_\Lambda = \frac{4(2-y)\sqrt{1-y}}{1+(1-y)^2} \frac{M_\Lambda}{Q} \frac{\sum_i e_i^2 f_1^i(x) D_{1T}^{\perp(1)i}(z)}{\sum_i e_i^2 f_1^i(x)}. \quad (1.32)$$

The polarization  $P_y$ , transverse to the  $\gamma - \Lambda$  scattering plane, does not require polarized beam or target in order to conserve parity. It does, however, contain the term  $D_{1T}^{\perp(1)}(z)$ . Translation of the superscripts and subscripts leads to the understanding that this describes an unpolarized FF in which the transverse momentum dependence is explicit. The appearance of such a FF in the expression for  $P_y$  indicates that transverse momentum effects are related to the generation of polarization in a completely unpolarized (beam and target) experiment; a semi-classical model for the connection between them is described further in Section 1.4.

The kinematic factor is familiar from Section 1.2 as  $f_1(y)$ , which scales the real part of the interference between photons with longitudinal and transverse linear polarizations.  $P_y$  also varies as  $1/Q$  but it contains leading twist operators.

### 1.3.2 Measurements.

Hadron measurements of transverse polarization in  $\Lambda$  production have existed for nearly twenty-five years and have been widely discussed in terms of evolution with  $x_F$  and  $p_T$ . Recent measurements at CERN have added a new body of data produced in  $e^+e^-$  collisions. The measurements discussed in this work will complement this set of measurements by adding electroproduction data to the current body of observations.

### Hadron Physics.

Lambda polarization experiments have spanned the breadth of hadronic beams available in the past quarter-century, including neutrons on nuclear targets [36]; pions on a copper target [37]; and hyperon beams [38]. The majority of experiments were performed with protons on heavy nuclear targets [39, 40, 41, 42], although a proton target was used in the work of Reference [43]. The work from various targets has been compiled in References [44] and [45], where the polarization from Cu and Pb



targets is shown to be  $\sim 75\%$  compared with the values obtained for a Be target; whereas in H it is  $\sim 10\%$  higher than for Be, indicating that targets of higher mass dilute the polarization through nuclear effects and final state interactions. In general, the polarization grows with both  $p_T$  and  $x_F$  and reaches values of  $40\%$  for  $x_F \sim 0.7$  and  $p_T \sim 1$  GeV [46, 47].

### Collider Experiments.

Both the OPAL and ALEPH experiments have measured the longitudinal polarization of  $\Lambda$  hyperons in  $Z^0$  decays [48, 49]. The Standard Model predicts that  $Z^0$  decays will yield predominantly left-handed quarks. Straightforward SU(3) calculations show that the  $\Lambda$  spin is carried by the  $s$  quark; in this model, measurements of the  $\Lambda$  polarization access the initial  $s$  quark. Lambdas produced from  $u$  or  $d$  quarks or from secondary fragmentation processes are not expected to be longitudinally polarized. The measurements of  $\sim 35\%$  agree with these predictions of the standard model and the constituent quark model. Similarly, transverse polarization in  $Z^0$  decays is expected to be low, an assumption that is borne out by the measurements of  $\sim 1\%$ .

These experiments are interesting as they provide another avenue by which the polarized FF's may be extracted. With this information, DIS measurements may be used to obtain polarized DF's [50, 51], with QCD corrections calculated as in Reference [52].

## 1.4 Deviations from the Parton Model.

Although the discussion of Sections 1.2.1 and 1.3.1 has been highly mathematical, the underlying physics may be understood in terms of additions to the naive parton model, which, because of the uncertainty principle, cannot generate transverse momenta  $p_\perp$  larger than  $\sim 300$  MeV. As these quantities are small compared with the interaction scale  $Q^2$ , in general hadrons will be emitted in a narrow cone about the virtual photon direction.

It is precisely the transverse momentum, however, that leads to the seemingly un-

related phenomena of azimuthal distributions and  $\Lambda$  polarization. To understand the azimuthal distributions, it is best to begin by following Cahn's straightforward model, in which the massless parton's momentum four-vector is written in the following way:

$$\begin{aligned} p &= (xP, p_{\perp} \cos \phi, p_{\perp} \sin \phi, xP) \\ &= xP + p_{\perp}. \end{aligned} \quad (1.33)$$

In general, the cross section  $\sigma$  for high energy processes reduces to

$$\sigma \propto |\overline{\mathcal{M}}|^2 \propto \frac{s^2 + u^2}{t^2}, \quad (1.34)$$

where the Mandelstam invariants are written as

$$s = 2k \cdot p, \quad t = -2p \cdot p', \quad u = 2k' \cdot p, \quad (1.35)$$

for parton momentum  $p$  and the incident (scattered) lepton  $k$  ( $k'$ ). Since it is assumed that the parton's momentum direction is conserved after the collision,  $p \cdot p'$  is not  $\phi$  dependent. The invariants  $s$  and  $u$ , however, are evaluated as follows<sup>4</sup>:

$$\begin{aligned} s &\approx 2xME(1 - 2(p_{\perp}/Q)\sqrt{1-y} \cos \phi), \\ u &\approx -2xME'(1 - 2(p_{\perp}/Q)\sqrt{1-y} \cos \phi). \end{aligned} \quad (1.36)$$

Thus, the invariants in the numerator of Equation 1.34 generate the  $\phi$  dependence of the cross section directly. This may be seen in Figure 1.4.

Cahn makes the interesting point that such an azimuthal distribution requires neither the parton nor the lepton probe to have spin. Rather, it is a direct consequence of the spin-one nature of the photon and the transverse momentum demanded by confinement.

The transverse momentum of the quark induces polarization somewhat differently, as it must be transferred to spin. In a semi-classical model like that of Andersson [32],

---

<sup>4</sup>The expressions of Reference [12] were corrected as cited in Reference [30].

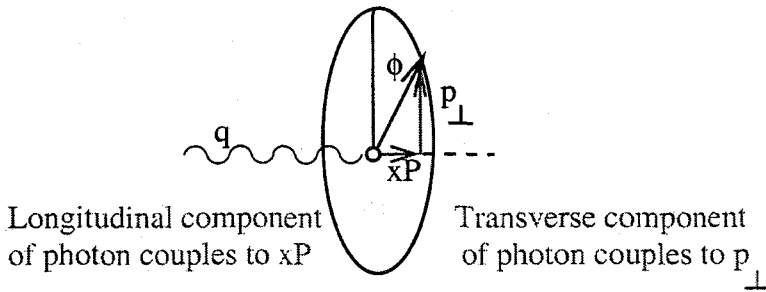


Figure 1.4: Lepton-parton scattering in the  $\gamma - N$  CMS, where the parton has a transverse momentum  $p_{\perp}$  and a longitudinal momentum  $xP$ . The strength of the photon coupling to the transverse component will then depend on the angle  $\phi$ . Taken from Reference [12].

shown in Figure 1.5, the primordial transverse momentum  $p_{\perp}$  generated in the interaction may also induce the polarization of the  $\Lambda$ . As the incident photon breaks the target proton apart, a string (or force-field) is generated between a  $q\bar{q}$  pair. In a classical model, this string must have a finite length and associated intrinsic energy in order to conserve energy and momentum. (This model is also valid for the case of partons with finite mass and no transverse momentum.) Because there is a finite length of the string, orbital angular momentum is generated<sup>5</sup>. To conserve angular momentum, the  $q\bar{q}$  system must have spin angular momentum associated with it.

Strictly speaking, however, the  $q\bar{q}$  pair is generated from the vacuum and hence inherits the vacuum's total spin  $J = 0$ ; furthermore, since a particle and antiparticle have opposite parities, the total parity is negative. Thus, the field has total spin and parity  $J^-$ . With negative parity, the string must have orbital angular momentum  $L = 1$ , and thus the spin must couple to  $S = 1$  in order to satisfy  $\mathbf{L} + \mathbf{S} = \mathbf{J}$ . Since each member of the  $q\bar{q}$  pair exists in a definite spin state, the quark fragments into a  $\Lambda$  such that the final hadron inherits this spin.

Thus, transverse momentum is seen to generate both the azimuthal distributions and  $\Lambda$  polarization. Although more complete descriptions are available, these models are sufficient to provide insight regarding the origin of these processes (see Ap-

<sup>5</sup>This is the same mechanism used to generate transverse momentum in the Feynman-Field model [53].

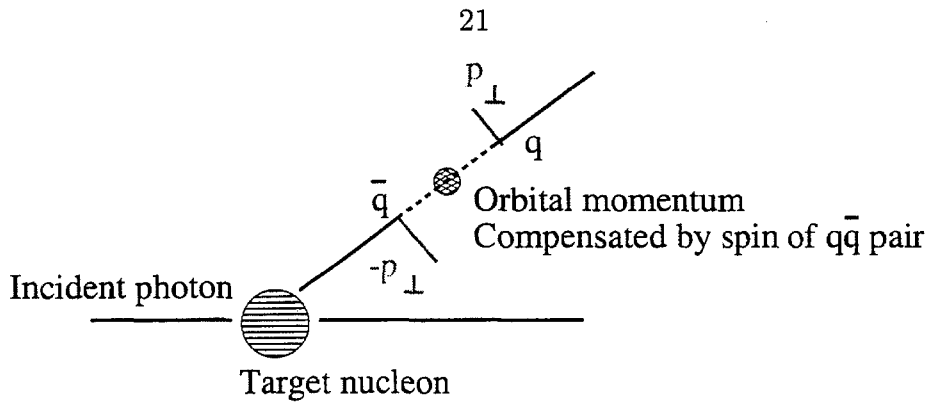


Figure 1.5: A model for the role of transverse momentum in generating  $\Lambda$  polarization. A photon scatters from quark  $q$  with transverse momentum  $p_{\perp}$ . The resulting string is created with orbital momentum, which is compensated by the  $q\bar{q}$  spin. The struck quark is not shown; the  $q\bar{q}$  pair are created from the vacuum with good quantum numbers and transfer the spin to the lambda. Taken from Reference [32].

pendix A.4). As such effects identify deviations from the parton model, these measurements are particularly interesting and could lead to a better understanding of quark confinement.

## Chapter 2 Experimental Apparatus.

The HERMES (HERa MEasurement of Spin) experiment is designed to observe a wide variety of final states in lepton-nucleon interactions. The detector was installed at the *Deutsches Elektronen-Synchrotron (DESY)* in 1994 and recorded its first data in 1995. As a result, much of the experimental apparatus has been elucidated in several publications, including References [5, 6, 54, 55]. In brief, the HERMES spectrometer was designed to have good angular and momentum resolution over a large kinematic range, with the capacity to search for spin observables by using a polarized beam and a variety of polarized targets. The implementation of these specifications will be elucidated below.

### 2.1 The HERA Beam.

The HERA ring at DESY is a collider and hence there are two beams: a 27.5 GeV positron beam and a 820 GeV proton beam circulating in opposite directions. The lepton probe is a positron beam, rather than an electron beam, because of its longer lifetime at HERA (the electrons experience more losses through interactions with residual ions). These positrons provide the lepton beam used at HERMES, while the proton beamline is separated from the center line of the experiment by 72 cm. The proton beam causes background which is reduced with the trigger, discussed below in Section 2.3.5.

The positron beam is typically injected at a current of  $\sim 35$  mA and allowed to remain in the ring for  $\sim 12$  hours. Its time structure is a 29 ps pulse every 96 ns and its shape is elliptical, with a cross section of 0.07 mm (vertical) and 0.26 mm (horizontal).

The polarization and polarimetry are fully discussed in Reference [56]. The beam is polarized by the Sokolov-Ternov mechanism, in which positrons in a storage ring

are polarized along the direction of the guide field because of a rate asymmetry in the synchrotron radiation for each spin state [57]. For the HERMES beam, the polarization builds up asymptotically over a 30 minute period to a value of  $\sim 50$ -60%, as shown in Figure 2.1.

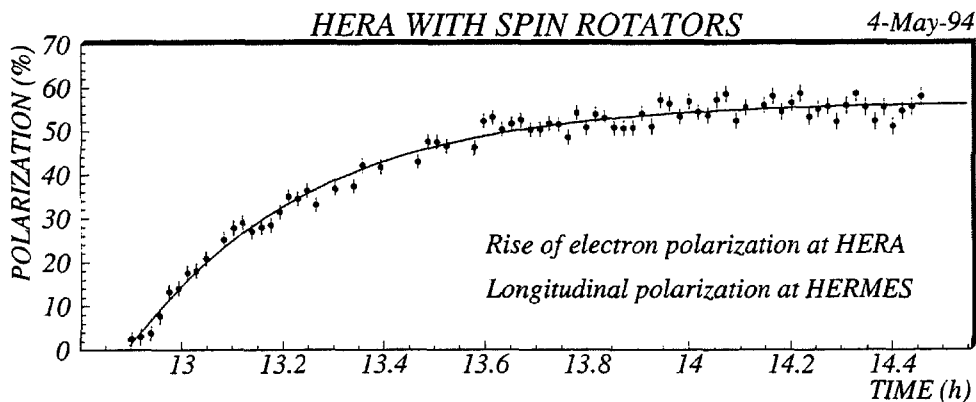


Figure 2.1: Risetime of the beam polarization.

The induced polarization is transverse to the direction of motion of the positrons. The measurements conducted at HERMES require longitudinally polarized leptons and thus the polarization vector must be translated without affecting the magnitude of the polarization or the momentum of the leptons. This is accomplished with spin rotators on either side of the HERMES experiment. The layout is shown in Figure 2.2. The spin rotators may themselves be rotated in order to flip the positron helicity, thus reducing systematic uncertainties. This was done such that the 1996 data analyzed here were all taken with positrons of positive helicity, while the 1997 data were collected with leptons of negative helicity.

The transverse polarization is measured in a Compton polarimeter, which takes advantage of the spin-dependent nature of the Compton scattering cross section. A beam of 2.4 eV polarized photons is directed onto the positron beam. The back-scattered photons are detected by a tungsten scintillator sandwich that is divided into an upper and lower portion. The polarization is then evaluated by extracting the shift in the mean vertical position when the polarization of the incident photons is flipped (the helicity is flipped at 84 Hz).

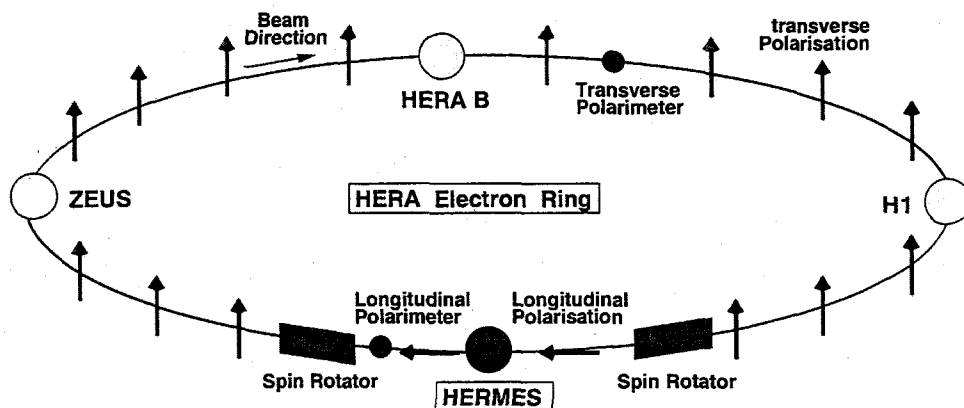


Figure 2.2: The HERA ring and the rotation of the beam polarization. Spin rotators produce longitudinal spin at the interaction point and rotate the polarization vector back to the transverse direction after the interaction. Taken from Reference [56].

## 2.2 The Internal Target.

The HERMES internal storage cell was designed to be a versatile instrument for use as both a high density polarized gas target and as an unpolarized gas target. It is discussed in detail as a polarized target in Reference [58]; the aspects relevant to filling it with unpolarized gas are summarized here. It is shown in Figure 2.3.

The target cell is made of aluminum and is 40 cm long. Because the beam at HERMES is elliptical in shape, the target cell has a cross section of 9.8 mm (vertical) by 29.0 mm (horizontal). The target gas is injected via a T-shaped tube such that it flows through the cell close to the positron beam and then is pumped away via a high speed differential pumping system. The gas density profile is longitudinally triangular (see Section 3.5.5).

For these measurements, the target cell was filled with one of several unpolarized gases:  $H_2$ ,  $D_2$ ,  $^3He$ , and  $N_2$ . Each of the gases was restricted to a density of  $10^{15}$  nucleons/cm<sup>2</sup>; at this density, the beam lifetime was kept at an acceptable level of  $\sim 8$  hours. (The contribution from the gas is limited to 45 hours in order to minimize its effect on the beam.) In contrast to the polarized gas, in which the target cell is in a 3.5 kG magnetic field, no external magnetic field exists while unpolarized gas data are collected.

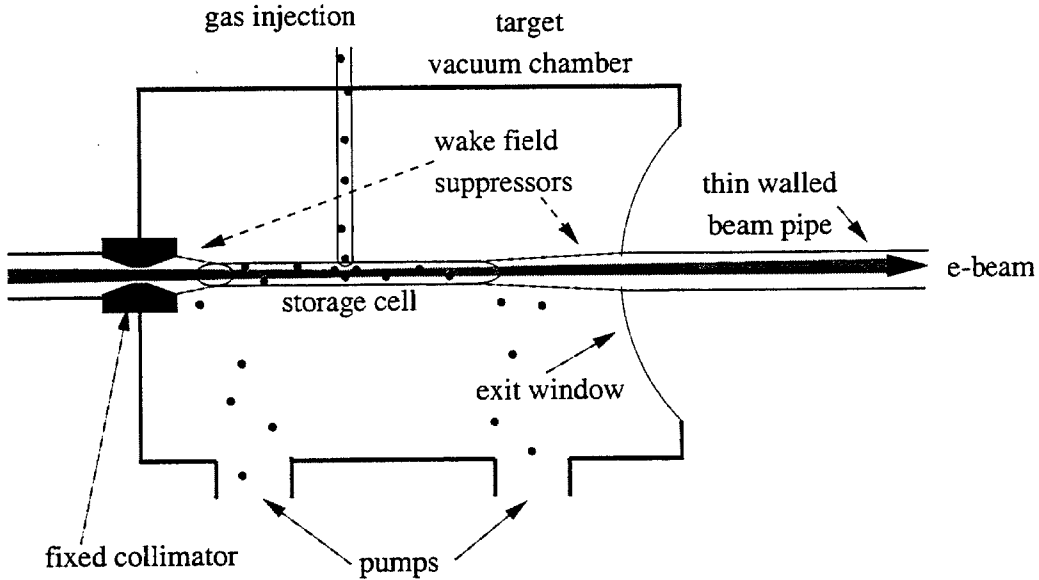


Figure 2.3: The target cell assembly. The fixed collimator C2, directly in front of the target cell, protects the cell from synchrotron radiation. The gas is injected into the storage cell via a T-shaped tube. Wake field suppressors connect the target cell to the beam pipe and reduce the consequences of the changing cavity diameter on the positron beam. Taken from Reference [59].

Since  $\sim 100$  W of synchrotron radiation exist in the target region, the cell is protected by a system of two sets of collimators, C1 and C2. C1 consists of collimators that are independently adjustable in the horizontal and vertical directions; they are placed 2 m upstream of the target. Directly in front of the storage cell is the second collimator, C2, which is fixed. It is slightly larger than C1 and protects the target from photons scattered by C1.

## 2.3 The HERMES Detector.

The HERMES detector, pictured in Figure 2.4, has been well described in Reference [59]. It is designed to look at various final states with its particle identification capabilities and its large forward acceptance. It is completely top-bottom symmetric such that the plane of the two beamlines separates the two halves. This section will elucidate those components relevant to this analysis.

The coordinate system at HERMES is defined such that when looking down the



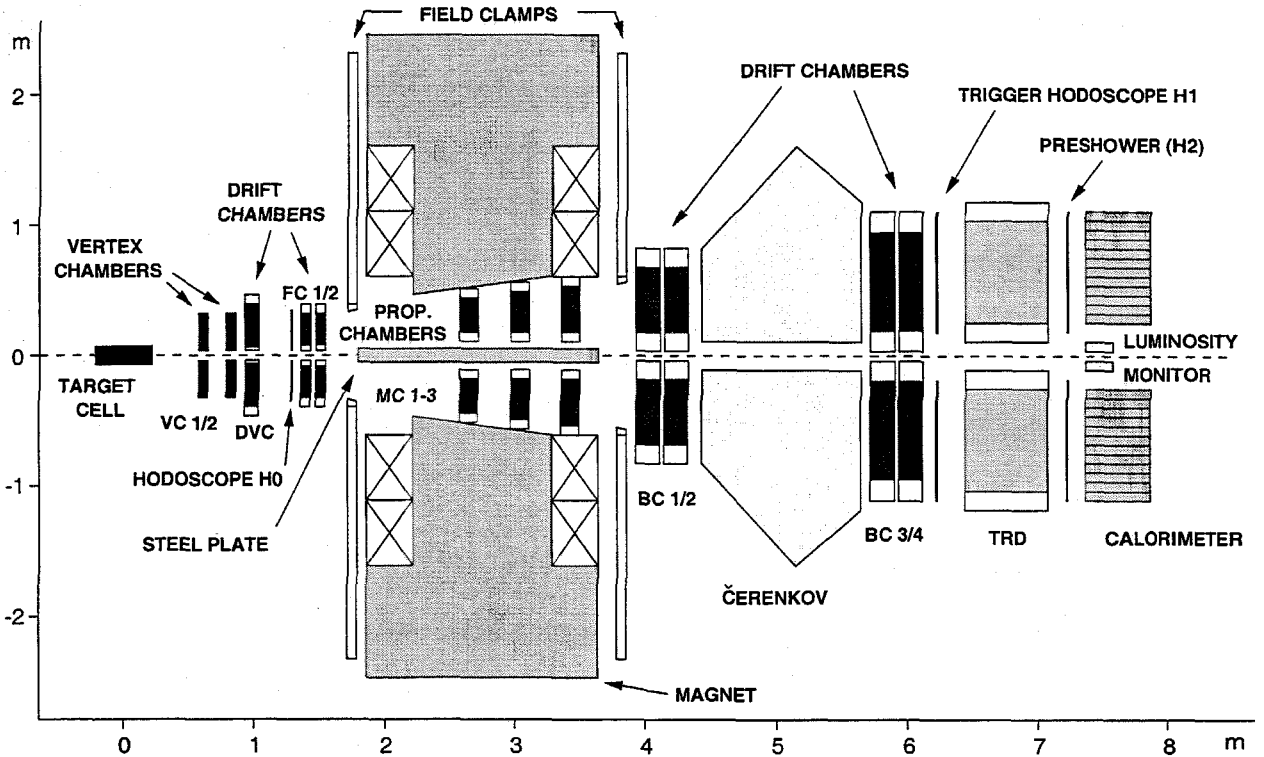


Figure 2.4: A schematic of the detector. Taken from Reference [59].

detector,  $\hat{z}$  points downstream along the beam line,  $\hat{y}$  points vertically upward, and  $\hat{x}$  points to the left.

### 2.3.1 Tracking Detectors.

The tracking system used at HERMES consists of a large dipole magnet and two sets of drift chambers. The magnet has a field integral of 1.3 T-m and contains a large steel septum plate that shields the two beamlines from the magnetic field. As a result, the lower limit of the acceptance is 40 mrad.

The front chambers (FC) are drift chambers located immediately after the target and in front of the magnet. There are two sets of 6 planes, arranged such that the wires are strung vertically for measurement in X, or tilted  $\pm 30^\circ$  right or left (for U or V planes); the actual configuration is UU'XX'VV'. Each plane has a resolution of  $220 \mu\text{m}$  and runs at an efficiency of 95%.

Since drift chambers cannot be used in the strong field inside the magnet, a set

of multi-wire proportional chambers (MWPC) known as the magnet chambers (MC) were installed there instead. The three planes are oriented, in order, in the U, X, and V planes. Rather than provide time-of-flight information like the drift chambers, the MWPC's record digital patterns where each wire is identified with a bit.

The back chambers (BC) are additional drift chambers located behind the magnet. They comprise of 4 chambers of 6 planes each for each half of the detector, oriented, like the FC, in UU'XX'VV'. The measured resolution is 275  $\mu\text{m}$  for the front and 300  $\mu\text{m}$  for the back. Their efficiencies are 99 (97)% for positrons (hadrons).

### 2.3.2 The Calorimeter.

The calorimeter is a shower counter that measures the energy of incident positrons. At high energies, the interaction of positrons in matter is dominated by showering; this is an alternating sequence of bremsstrahlung and  $e^+e^-$  pair creation. This takes place until the positron's energy decreases to  $\sim 10$  MeV, when the principal energy loss becomes ionization. The length of material required to contain the shower depends logarithmically on the incident energy  $E_0$ . The shower's transverse size is determined by the average deflection from bremsstrahlung and multiple scattering and is characterized by the Molière radius  $R_M$ , defined as  $R_M \sim 21X_0/E_0$  for a material of radiation thickness  $X_0$  [60, 61]. A material of atomic number  $Z$  may be further characterized by its critical energy  $E_c$ , defined as the energy at which ionization and bremsstrahlung losses are equal; in general,  $E_c \sim 580 \text{ MeV}/Z$ .

In a lead glass calorimeter, the energy of the incident particle is determined by collecting the radiated Čerenkov light. The HERMES calorimeter is an array of  $42 \times 10$  lead glass blocks of density  $3.86 \text{ g/cm}^3$  and radiation length  $X_0 = 10.73 \text{ g/cm}^2$  [54]; thus, the lead blocks of length 50 cm ( $\sim 18$  radiation lengths) contain most of the shower. Since  $E_c = 18 \text{ MeV}$  for this material, the  $9 \times 9 \text{ cm}^2$  face of each block is large enough such that the showers are generally contained in a  $3 \times 3$  cluster of blocks. Each block is viewed by a phototube affixed from the rear to collect the Čerenkov radiation.

### 2.3.3 Particle Identification (PID) Detectors.

The particle identification system at HERMES is designed to accurately identify positrons. In addition, a Čerenkov counter is used to separate pions from protons and kaons. The principle of operation and relevant characteristics of the four elements of the PID system are listed below. Analysis of the PID detector responses is discussed further in Section 3.2.

- The calorimeter.

The lead glass calorimeter may also be used to separate positrons and hadrons. Because hadrons and positrons experience different interactions in matter, the relevant length scales lengths differ considerably; the hadronic interaction length of  $\sim 36$  cm is large compared with the  $\sim 3$  cm radiation length for electromagnetic showers. The energy loss distributions differ in shape as well for the two processes, since secondary hadrons are generated with larger transverse momenta than electromagnetic showers. Consequently, the calorimeter may separate the two types of particles by identifying differences in the energy deposition.

- The hodoscopes.

The two scintillator hodoscopes (H1) and (H2) used for particle identification are both composed of 42 scintillators 1 cm thick, coupled to phototubes. While H1 is used primarily for the trigger (see Section 2.3.5 below), H2 is used as an additional electromagnetic calorimeter.

Directly in front of H2 is a sheet of lead 11 mm thick (2 radiation lengths). Positrons passing through this sheet create electromagnetic showers, which then deposit more energy in H2 than just the ionizing energy of a single particle. While pions deposit less than 5 MeV, positrons typically deposit  $\sim 20$  MeV. These energy losses are not sufficient to affect the final calorimetry, but the relative difference provides separation between positrons and hadrons.

- The Čerenkov counter.

The Čerenkov counter operates on the principle that in a medium where the velocity of light is given by  $\beta_t$ , a charged particle moving through it with a relativistic

velocity  $\beta > \beta_t$  will radiate visible photons. Thus, Čerenkov detectors are often characterized by the threshold  $\beta_t \gamma_t$ . The light is then collected in phototubes; Čerenkov responses are measured in terms of the number of photoelectrons collected in the phototube. The angle of emission of Čerenkov radiation is given by  $\cos \theta_c = 1/\beta n$ , where the local optical properties are given by the index of refraction  $n$ .

The HERMES Čerenkov is filled with  $C_4F_{10}$  and  $N_2$  at atmospheric pressure in a ratio of  $\sim 30:70$  by volume. This yields a threshold value  $\beta\gamma$  of  $\sim 29$ , such that the threshold momentum for positrons, pions, kaons, and protons is 0.015 GeV, 4 GeV, 14 GeV, and 27 GeV, respectively. Unfortunately, protons and kaons cannot be separated in the range of 4-14 GeV, in which most of the events occur (as shown, for instance, in Figure 3.23 for  $(e, e'\Lambda)$  events). The pion threshold, however, may be used to separate pions from the heavier hadrons at momenta greater than 4 GeV.

- The Transition Radiation Detector (TRD).

Transition radiation occurs when an ultrarelativistic particle crosses a boundary from one dielectric medium into another. As the electromagnetic field is different on each side of the boundary, the difference in these fields results in radiation. The intensity of the radiation is proportional to the relativistic  $\gamma$  factor [62]. In most dielectrics, this will yield radiation in the X-ray region. Like Čerenkov radiation, transition radiation is emitted at a characteristic angle which can be used, in principle, to identify particles. In this case the radiation is emitted inside the cone  $\theta_{TR} < 1/\gamma$ , which is too narrow to allow separation of the radiation from the incident positron.

The TRD consists of 6 modules in each half of the detector. Each module consists of a fiber matrix radiator and a Xe/CH<sub>4</sub> proportional chamber. While hadrons deposit  $\sim 5$ -20 keV in a single module, positrons deposit  $\sim 20$ -50 keV and hence the two distributions can be separated.

### 2.3.4 The Luminosity Monitor.

The luminosity monitor consists of a pair of calorimeters placed symmetrically around the beam pipe. They detect the Bhabha scattering of incident positrons from atomic

electrons in the target cell; the luminosity is simply the product of the current and the target density and is proportional to the coincidence rate between the two calorimeters.

Absolute luminosity measurements were not used for the main analyses of this thesis. Instead, it was only required that the luminosity monitor had to be functioning well in order to determine that the entire detector was not subject to poor beam conditions and significant high voltage trips. The luminosity monitor was used, however, in measurements made by the Target Optical Monitor, to be discussed further in Appendix B.

### **2.3.5 The Trigger.**

A trigger can be formed from just the two preshower hodoscopes and the calorimeter. Unfortunately, there is a large background initiated by the proton beam that satisfies the trigger requirements for DIS positrons. For this reason, an additional scintillator hodoscope (H0) was introduced in order to distinguish particles moving backward through the detector from those going forward. The total travel time through the entire set of trigger detectors is 18 ns; this provides adequate separation between forward and backward moving particles of 36 ns.

A trigger is formed by requiring hits in the three hodoscopes H0, H1, and H2. In addition, there must be 3.5 GeV deposited in the calorimeter. Finally, this is all timed in coincidence with the 10 MHz accelerator signal. This four-fold coincidence forces the entire detector to be read out; in this fashion, multi-particle events are detected.

### **2.3.6 The Gain Monitoring System.**

The scintillator-phototube systems of the preshower counter, the calorimeter and the luminosity monitor utilize the Gain Monitoring System (GMS). A 500 nm dye laser beam is directed toward these detectors via fiber optics with a frequency of 1 Hz, such that it is out of time with the positron beam. A filter wheel attenuates the pulse in

order to provide 6 different intensities. In this way the linearity of the gain could be verified as well as the absolute intensity.

### 2.3.7 Reconstruction Software.

The HERMES reconstruction software (HRC) [63] uses the information provided by the drift chambers and the proportional chambers listed in Section 2.3.1. HRC implements two innovative techniques for efficient reconstruction. First, it uses a “tree-search algorithm” for fast track finding. In its initialization, HRC calculates all allowed patterns and stores them. Then, upon running the reconstruction, the tree-search improves the resolution by a factor of two in successive steps. At each step and with that resolution, the track is compared with the complete set of all allowed track patterns. The track is then discarded if it is not allowed. This is done independently for the front and back tracks, such that there is a set of front partial tracks and one of back partial tracks. They are then matched at the magnet center (with some prespecified tolerance) to determine whether they form a full track.

The second innovation is in the determination of the momentum of a track once it has been found. Rather than propagate each track through the magnetic field, HRC generates a look-up table upon initialization. This table contains the momentum of the particle in terms of three quantities: the position of the front track; the slope of the front track; and the horizontal slope of the back track. HRC then labels each track that it finds in terms of these parameters and searches the table for the appropriate momentum.

Without the tracking provided by additional proportional and drift chambers in the front region (more chambers were installed in 1997 but were not used for this analysis), the entire track could not be determined uniquely due to the limited resolution and lever arm of the front chambers; the two front chambers are only 12 cm apart. For this reason, the “forced bridging” technique was employed, in which HRC extracted a front and back track independently. While the back track is projected back to the center of the magnet, the front chambers define only a single space point,

from which a track is constructed to the center of the magnet. The matching condition consists of well specified tolerances in  $x$  and  $y$  (5 cm in each direction); in addition, the  $dy/dz$  gradient is required to be within 0.050 for both partial tracks. This technique allows for momentum resolution of  $\sim 1.1\%$  for  $dp/p$ .

### **The Magnet Chambers.**

For those cases in which a hadron has been reconstructed using the standard techniques, additional tracks may be found using the magnet chambers (MC). It is possible for a low momentum pion from the target to traverse the FC's such that it is tracked additionally by the MC's. The MC's are bathed by low momentum pions spiraling inside the magnet. For this reason, a search is not performed for a low momentum pion unless a coincident high momentum hadron has already been tracked through the entire detector. This is known as "sparse" magnet chamber tracking and it is used for the strange particle analyses presented here, though not for the semi-inclusive pions.

Two terms used frequently in this work are *long* and *short* tracks. A long track is one that has been reconstructed through the entire detector, while one that is tracked only in the FC's and the MC's is a short track. Differences in the reconstruction using the two different algorithms were found to be negligible [64].

## Chapter 3 Signal Extraction.

### 3.1 Monte Carlo Simulations.

In the discussion of hadronization processes in Section 1.1.4, the semi-inclusive cross section was expanded into matrix elements describing parton correlations; however, these cannot be calculated explicitly without models for the correlation functions. Hence fragmentation is conventionally discussed in terms of various models that are intended for use in Monte Carlo simulations. The HERMES Monte Carlo uses the package LEPTO to calculate the well-understood lepton-quark interaction; it then uses the LUND model, realized in the JETSET software package, to perform the fragmentation of the struck quark via the creation of  $q\bar{q}$  pairs; a field is stretched between them (see Reference [65] and references therein for a detailed discussion of the implementation of the model).

The most important assumption is that of local parton-hadron duality [66], in which for any fragmentation process, quantum numbers are locally conserved until a colorless hadron is formed. In this fashion, the quantum numbers of the detected hadron can give direct information regarding the struck parton. Typically, kinematic restrictions can be applied to the data in order to enhance this correlation, namely on the variables  $x_F$  and  $z$ , as defined in Table 1.1; these variables simply measure the forward momentum in each of two reference frames (the  $\gamma$ -N and laboratory frames, respectively). The region of phase space in which the struck quark is detected is referred to as the *current fragmentation region*, whereas the recoil partons fall into the *target fragmentation region*.

Inputs to the LUND model currently use the fragmentation functions from other experiments. These parameters have been varied slightly in order to better characterize these processes at lower energies of HERMES. Events generated by this model may be passed through a simulation of the detector, which is digitized by the GEANT



package. These simulated hits may then be reconstructed again with HRC to create Monte Carlo tracks.

In these analyses, Monte Carlo events were produced on a farm of 20 personal computers (PC's), running the Linux operating system. Each computer had two 300 MHz Pentium II processors. The generator produced events at  $\sim 0.1$  s/events. The most CPU-intensive task was the GEANT digitization of the three-track events in the detector, which required 4.6 s/event. Finally, they were reconstructed in HRC at 0.15 s/event.

The events that were successfully digitized and reconstructed were written to files which were identical to the data in structure. In this fashion, they could be passed through the same analysis program as the data.

## 3.2 Particle Identification.

The PID analysis scheme at HERMES is based on a probability analysis of the responses for the four PID detectors. The general form of the analysis follows from the general case in which each detector measures either positrons or hadrons [67]. Then the probability that a particle is a positron ( $P^p$ ) is given by

$$P^p = \frac{L^p}{\Phi L^h + L^p}. \quad (3.1)$$

$\Phi = \phi^h / \phi^p$  defines the ratio of the fluxes of the two particles and is determined by the physics. Consequently, it must be parameterized in terms of variables such as momentum and scattering angle:  $\phi^i = \phi^i(p, \theta)$ .

$L^{p(h)}$  represents the conditional probability that the response was caused by a positron (hadron). For each detector, this function is generated from data measured with a clean particle sample, either with a test beam or by applying severe PID restrictions to the other detectors and then extracting a clean sample.

### 3.2.1 Detector Parameterizations.

For each detector the function  $L^{p(h)}$  is determined independently. The models follow below for particles of energy  $E$  and momentum  $p$ .

- Calorimeter.

In the calorimeter, positrons deposit most of their energy in electromagnetic showers, whereas hadrons principally lose energy only by ionization. As a result, the distribution of the ratio  $R = E/p$  will look different for each particle type. Not only does the shape differ, it is peaked at a value lower than  $R = 1$  for hadrons rather than at  $R = 1$  for positrons. The positron spectrum is well characterized by a Gaussian centered at 1 with a high energy exponential tail, while the hadron distribution is a constant with an exponential tail.

- Preshower hodoscope.

Hadrons deposit only the minimum ionizing energy and hence their spectrum results in a narrow peak, whereas positrons deposit energy roughly proportional to  $\ln E$  and yield a much broader spectrum. Asymmetric Gaussians are used to model this response while the hadrons are given an additional exponential tail.

- Čerenkov counter.

The response for the Čerenkov counter is modeled as a Poisson distribution describing the probability of recording a number of photoelectrons, convolved with a Gaussian distribution centered about that number of photoelectrons. In this analysis, each hadron type is considered separately. Since the deep inelastic trigger is set at 3.5 GeV and the pion threshold is at 4.8 GeV, the Čerenkov does not contribute much information for the positron-hadron separation. Its use in separating pions and protons will be discussed further in Section 3.3.2.

- TRD.

The responses are fit to Gaussians with tails.

The distributions for the responses of each detector are shown in Figure 3.1.

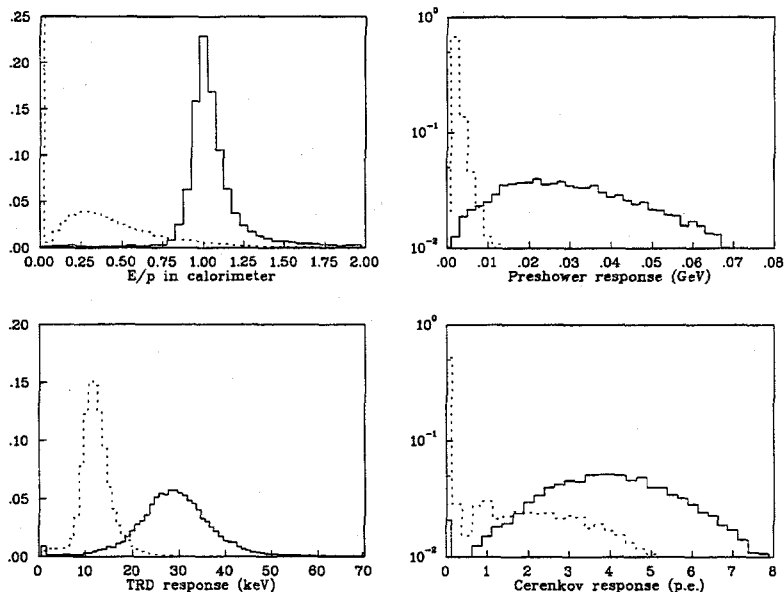


Figure 3.1: Responses of the PID detectors. Positrons (hadrons) are solid (dotted) lines.

### 3.2.2 Likelihood PID.

For one detector the likelihood PID is defined as

$$PID = \log_{10} \left( \frac{L^e}{L^h} \right) - \log_{10} \Phi. \quad (3.2)$$

The calorimeter, preshower, and Čerenkov counters all originally showed responses in the HERMES experiment which matched their responses from test beams. Consequently, their parent distributions were understood easily and a triple likelihood was constructed as

$$PID3 = \log_{10} \frac{L_{cal}^e L_{pre}^e L_{cer}^e}{L_{cal}^h L_{pre}^h L_{cer}^h}. \quad (3.3)$$

The TRD required additional study until the parent distributions were understood. Hence its likelihood function, known as PID5, was added later to the available PID data [68], though it still follows the formalism of Equation 3.2.

### 3.3 Selection of Candidate Events.

#### 3.3.1 Run and Burst Selection.

A *run* is a set of data taken over a time period of  $\sim 10$  minutes, although the exact time scale is determined by the luminosity, since the run length is set by the amount of data collected. This time scale is useful in order to monitor the detector, since variations in efficiency or beam quality typically occur over this time.

The smallest time scale used is that of a *burst*, an interval of  $\sim 10$  seconds that represents the frequency at which the scalers are read. Although the detector is read out with every event, monitors such as the luminosity monitor and the GMS are integrated over the 10 second burst. In this period, the high voltage to all the detectors can be monitored as well.

Recorded data in a run are processed through HRC, after which the surviving full tracks are written to files, known as *data summary tapes* (DST's). Two sets of these were used for this analysis.  $\mu$ -DST's comprised all multi-track events recorded by the detector and were used for the  $(e, e'\pi)$  analysis. The strange particles, however, were identified from a compressed data set known as *nano-DST's*; these files comprised all events with three or more tracks and were thus much smaller than the  $\mu$ -DST's. Aside from a small irregularity in the PID histograms (see Section 3.3.2), the  $\mu$ -DST's and nano-DST's are equivalent in quality; the nano-DST's were used only to analyze the strange particles more efficiently.

#### Target Type.

For this analysis, the runs taken with the  $H_2$ ,  $D_2$  and  $^3He$  targets were used. Specifically, in 1996, selected runs between numbers 11321-14133 were used. In 1997, data were taken with  $N_2$ ; however, it was decided to limit the analysis to light targets in order to minimize nuclear corrections. This had the added benefit of yielding approximately equal samples of events in each year and thus in each helicity state. Candidate runs from the 1997 running cycle were chosen from the dedicated unpolarized running

of runs 17185-19650.

### High Voltage Operation.

A list of candidate bursts was available that used common requirements for all the physics analyses at HERMES [69]. Additional information was available to clarify the status of the high voltage (HV) for the magnet chambers (MC) and trigger detectors independently. In this analysis, all the bursts that had any HV problems in either of these detector sets were discarded. This led to only 2.3% loss in the 1996 burst list and 1.4% in the 1997 bursts; these losses were considered acceptable in terms of obtaining the cleanest detector conditions possible<sup>1</sup>.

### Detector Configuration.

These runs comprise all the data taken with unpolarized targets in 1996 and 1997. Unfortunately, in the two years of data taking, there were three distinct configurations in which changes were made to the drift vertex chambers (DVC) and the vertex chambers (VC):

1. Early 1996: No DVC, the lower VC present.
2. Late 1996: No DVC, the lower VC removed.
3. 1997: DVC and VC both present.

Because these detectors present extra radiation and nuclear interaction lengths to be traversed, it was important to accurately describe the detector in order to perform an acceptance correction. Since there were only a few runs taken in the early part of 1996 with the first configuration, these were discarded in order to have only one acceptance correction for each year of data.

---

<sup>1</sup>The quality of the detector is summarized in a bit pattern for each half of the detector; the hexadecimal value 21E03DE from standard HERMES lists was used to select the bursts in which the entire detector was at the correct voltage.

## Tracking Efficiencies.

The tracking efficiency may be calculated in many different ways; for instance, it can be averaged over only the positrons, or over all tracks. (For polarized target use, the efficiency may be calculated for each spin state.) This analysis used the entire set of tracks in one run as the basis for the efficiency calculation. The efficiency was then calculated for each half of the front and back drift chambers. If any of these efficiencies was less than 94%, the run was discarded from the analysis. The largest spread in the efficiencies was seen in the front chambers in 1996, as is shown in Figure 3.2. These quantities may be correlated, as bad beam conditions are likely to cause low efficiencies in both halves of the same chamber. Totals for the consequences of imposing this requirement on the list of candidate runs are shown in Table 3.1.

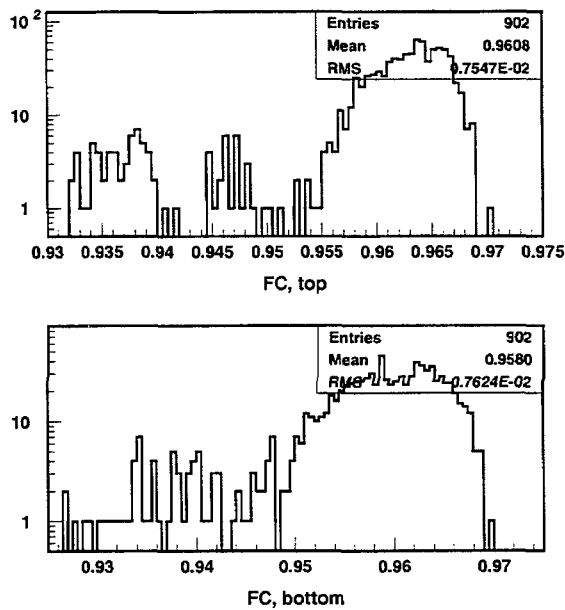


Figure 3.2: Efficiencies in the front chambers from the 1996 data. These efficiencies were calculated by averaging over all the tracks in an entire run.

Detector	1996	1997
Candidate runs	998	1257
FC, top	47	0
FC, bottom	56	0
BC, top	0	15
BC, bottom	0	15
Total discarded	58	15
Total remaining	940	1242

Table 3.1: Runs discarded due to low chamber efficiency. The total number discarded is less than the sum of discarded runs because of correlations.

### 3.3.2 Particle Identification.

#### Likelihood Analysis.

The relevant quantity in PID analysis is the expression  $PID3 + PID5$ , which refers to the summed likelihood analyses from the various detectors as discussed in Section 3.2.2.  $PID3$  describes the combined likelihood function in the preshower counter, the calorimeter, and Čerenkov detector, while  $PID5$  characterizes the response of the TRD. These functions are discussed fully in Reference [68].

A histogram of this quantity for a subsample of all events in the nano-DST's is shown in Figure 3.3. It reveals a distribution that looks almost as expected: it consists of two well-separated Gaussian distributions. The small feature at -2 is an artifact from the data compression used in the nano-DST's: Three-track events are recorded only if they contain a positively charged particle that satisfies the kinematics of a DIS positron, *and* the positron must have a summed PID value of at least -2, resulting in an artificial cutoff at -2.

Although the detectors were initially calibrated such that hadrons would appear at negative values of  $PID3 + PID5$  and positrons at positive values, subsequent calibrations changed the shape of this distribution somewhat [70]. As a result, the particles are identified as follows:

- Positrons:  $PID3 + PID5 > 2$ ;
- Hadrons:  $PID3 + PID5 < 0$ .

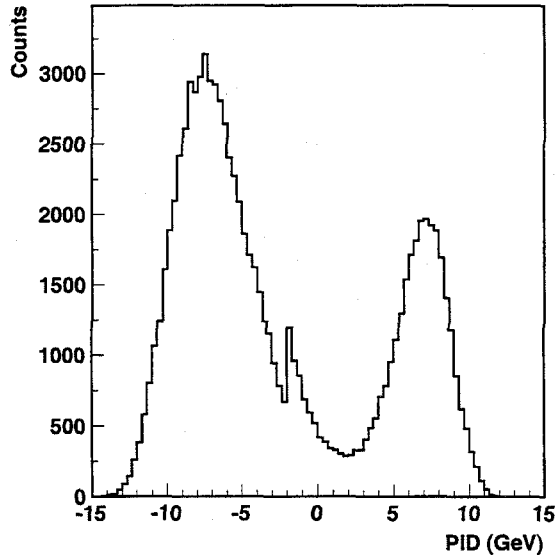


Figure 3.3: A histogram of the quantity  $PID3+PID5$ . Taken from a random sample of runs from the 1996 data set.

### The Čerenkov Counter.

The largest source of background is hadron misidentification below the Čerenkov threshold of 4.8 GeV since there is no hadron separation at those momenta; a smaller contribution results from the lack of  $p-K$  separation in the 4.8-12 GeV region. Rather than estimate the misidentification, these will be treated as sources of background and subtracted appropriately, as discussed in Section 3.5.9.

The Čerenkov pion fraction was examined to extract the lower momentum limit of 4.8 GeV. This study consisted of defining a sample of hadrons by stringent cuts on the other three PID detectors:

$$E_{calo}/p < 0.75 ,$$

$$E_{preshower} < 5 \text{ MeV},$$

$$E_{TRD} < 20 \text{ keV}.$$

A  $p - \pi$  separation fraction  $f_{\check{C}erenkov}$  for the Čerenkov counter was then constructed



in the following way:

$$f_{\check{C}erenkov} = \frac{\text{Number of good hadrons with } N(\text{p.e.})_{\check{C}erenkov} > 0.25}{\text{Number of good hadrons}}. \quad (3.4)$$

where  $N(\text{p.e.})_{\check{C}erenkov}$  indicates the number of photo-electrons detected in the Čerenkov counter. This fraction was plotted as a function of the particle momentum to determine the threshold and is seen in Figure 3.4, where it was fit with an exponential function.

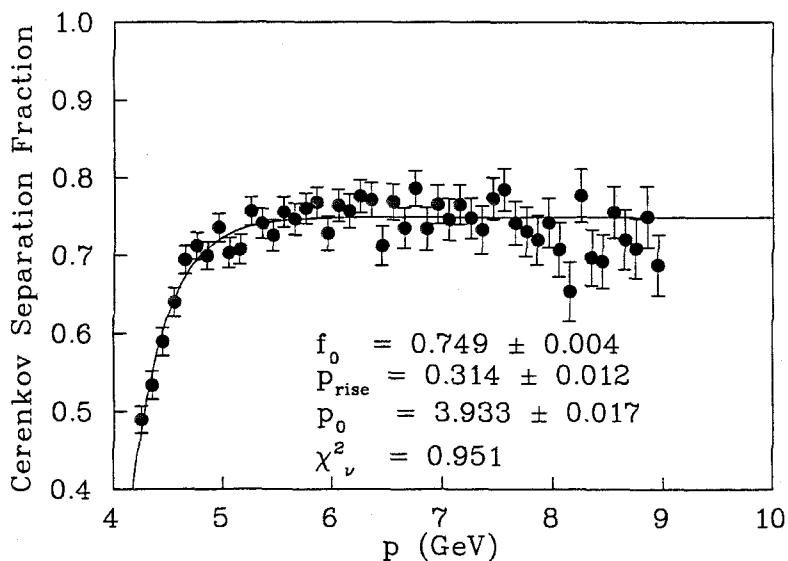


Figure 3.4: The Čerenkov separation fraction, fit to the form  $f = f_0(1 - e^{-(p-p_0)/p_{rise}})$ .

By 4.8 GeV, the fraction  $f$  has reached its asymptotic value of  $\sim 75\%$ . The fit parameters can be compared for the two years of operation to look for systematic differences; the results are shown in Table 3.2. The  $\chi^2_\nu$  values indicate that this function characterizes the data quite well and that there are not significant differences in the turn-on properties, as characterized by  $p_0$  and  $p_{rise}$ . Although the average fraction of pions was slightly higher in 1997, the difference is not large compared with other systematic effects, discussed further in Chapter 4.

Year	$f_0$	$p_{rise}$ (GeV)	$p_0$ (GeV)	$\chi^2_\nu$
1996	$0.749 \pm 0.004$	$0.314 \pm 0.012$	$3.933 \pm 0.017$	0.951
1997	$0.761 \pm 0.004$	$0.300 \pm 0.019$	$3.864 \pm 0.019$	1.273

Table 3.2: Čerenkov  $p - \pi$  separation parameters for 1996 and 1997.

### 3.3.3 The Scattered Positron.

The kinematic cuts used to identify DIS positrons were:

$$\begin{aligned}
 W^2 &> 4.0 \text{ GeV}^2, \\
 y &< 0.85, \\
 Q^2 &> 1 \text{ GeV}^2.
 \end{aligned}
 \tag{3.5}$$

The  $W^2$  cut guarantees exclusion of resonance data and inclusion of deep inelastic data. The restriction on  $y$  avoids excessive radiative corrections. The cut on  $Q^2$  restricts the data sample to deep inelastic events. Originally, it was hoped to include lower  $Q^2$  data in order to take maximum advantage of the detector acceptance. The Monte Carlo generator is valid down to  $Q^2$  of  $0.5 \text{ GeV}^2$ . The acceptance is limited at lower  $Q^2$ , as can be seen from Monte Carlo simulations; Figure 3.5 indicates that the acceptance at low  $Q^2$  is very narrow and thus more susceptible to alignment uncertainty. Since this analysis combines data from two years with possibly different alignments, the lower  $Q^2$  data are excluded. This also safeguards against the possibility that the detector is not perfectly represented at its edges by the Monte Carlo.

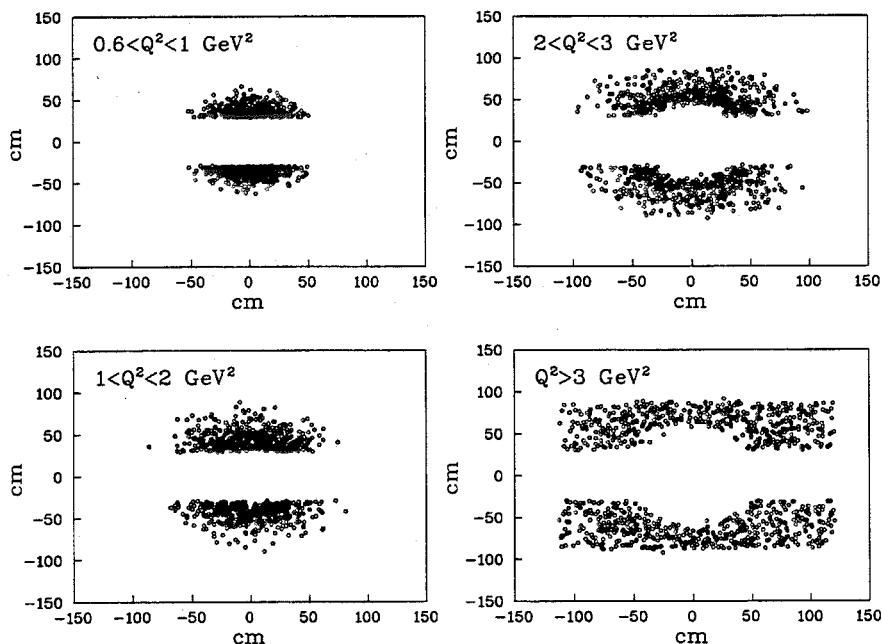


Figure 3.5: The variation in the acceptance with  $Q^2$ . The scattered positron in generated  $(e, e'\Lambda)$  events was tracked to find the position at which it hits the calorimeter face.

## 3.4 Identification of $(e, e'\pi)$ Events.

### 3.4.1 Fiducial Cuts.

The  $(e, e'\pi)$  events were extracted from the  $\mu$ -DST's. Using the candidate runs of Section 3.3, two-track  $(e, e'\pi)$  events were easily identified. The kinematics of the positron were still required to satisfy Equation 3.5.

Pions and positrons were identified as in Section 3.3.2. In addition, they were required to fall well within the fiducial region, as given by restrictions on the scattering angle  $\theta_y$  and the  $x$  and  $y$  positions at the calorimeter face ( $x_{cal}$  and  $y_{cal}$ ):

$$\begin{aligned}
 40 &< \theta_y < 110 \text{ (140) mrad for positrons (pions),} \\
 |x_{cal}| &< 170 \text{ cm,} \\
 30 &< |y_{cal}| < 90 \text{ cm.}
 \end{aligned}$$

Each track had to independently satisfy the detector's acceptance cut on  $\theta_y$  in

order to clear the septum plate. The average  $\theta_y$  is  $0.07 \pm 0.02$  rad for positrons, and  $0.08 \pm 0.03$  rad for pions. Thus, the ranges specified above allowed for  $2\sigma$  variation in  $\theta_y$ . The additional cuts guaranteed that all tracks fell well inside the calorimeter's face. The reconstructed slopes were used to calculate the  $x$  and  $y$  positions at the calorimeter face.

Given only two tracks, the scattering vertex is not as well defined as in the three-track case, although it is still possible to construct a production vertex by evaluating the distance of closest approach for both tracks. The location of this vertex can be evaluated, giving results for  $x_{prod}$ ,  $y_{prod}$ , and  $z_{prod}$  of 2.0, 2.3, and 0.07 cm, respectively. Furthermore, the mean distance between the two tracks may be calculated; for these events, the distance  $d_{prod}$  was 2 cm. Therefore, the following cuts were used to improve the  $\chi^2_\nu$  of the physics results:

$$\begin{aligned} x_{prod}, y_{prod} &< 4 \text{ cm}, \\ z_{prod} &< 0.5 \text{ cm}, \\ d_{prod} &< 4 \text{ cm}. \end{aligned}$$

It was decided not to use short tracks at all. In the case of the strange particles, one hadron is allowed to be a short track only if there is another hadron that produces a long track. By requiring the triple coincidence of the positron and hadron that reach the calorimeter as well as a short track that does not, the background can be reduced.

On the other hand, two-track events obviously lack the third coincidence that reduces background. For this reason, only long tracks were allowed in this analysis. Thus, the Čerenkov was used to separate pions and protons:

$$4.8 < p_\pi < 14 \text{ GeV}.$$

The  $\chi^2_\nu$  of the azimuthal distributions were also influenced by the kinematics of

the  $\gamma$ -N system. Consequently, kinematic cuts were imposed:

$$0.3 < p_T < 1.2 \text{ GeV},$$

$$0.2 < z < 0.95 ,$$

$$0.25 < x_F < 0.95 .$$

The final cut selection is summarized in Table 3.3.

Requirement	Minimum	Maximum
$\theta_y$ of each track (mrad)	40	
$y$ -slope of positron		0.11
$y$ -slope of pion		0.14
$x$ at prod. vertex (cm)		4
$y$ at prod. vertex (cm)		4
$z$ at prod. vertex (cm)		0.5
$x$ at calorimeter face (cm)		170
$y$ at calorimeter face (cm)	30	90
$d_{e\pi}$ (cm)		4
$p_\pi$ (GeV)	4.8	14
$Q^2$ (GeV <sup>2</sup> )	1	5
$W^2$ (GeV <sup>2</sup> )	4	
$y$		0.85
$x_F$	0.1	0.95
$z$	0.2	0.95
$p_T$ (GeV)	0.3	1.20

Table 3.3: Final cut selection for pions.

The effectiveness of these cuts is shown by comparing the resulting events with Monte Carlo simulations. The kinematic distributions are shown in Figure 3.6 to agree very well with Monte Carlo events. Limitations on the available computing power made it necessary to generate only enough  $(e, e'\pi)$  events such that the accepted number was only slightly larger than that of the data. The data analyzed comprise 170(210)k events in 1996(1997); and the number generated was 190(252)k events for 1996(1997).

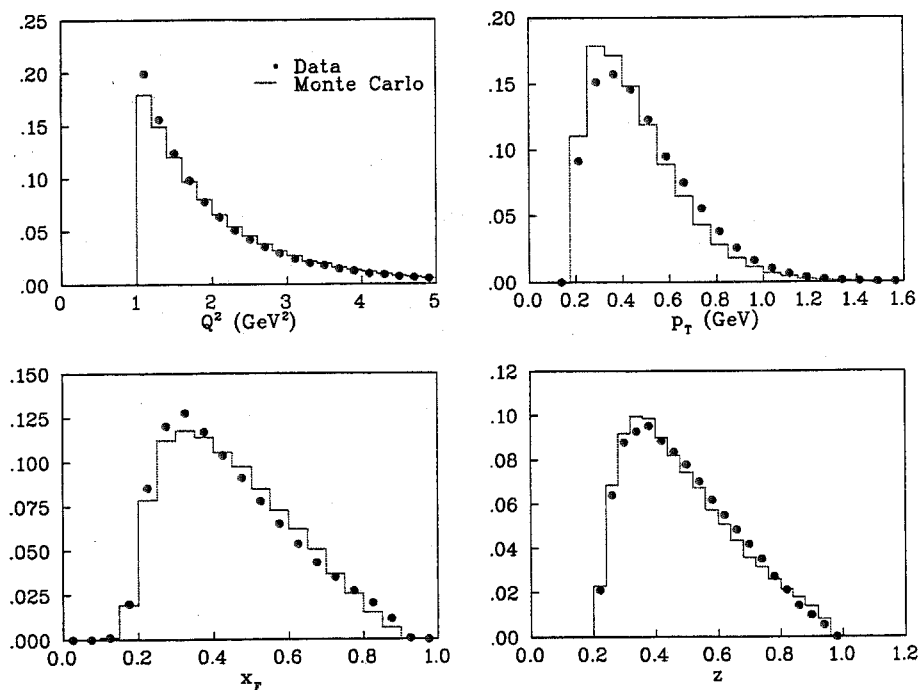


Figure 3.6: Kinematics of  $(e, e'\pi)$  events with data (filled circles) and Monte Carlo (histogram). Top left (right):  $Q^2$  ( $p_T$ ). Bottom left (right):  $x_F$  ( $z$ ).

These graphs are not all independent. For instance, Figure 3.7 indicates the strong correlation in the acceptance in  $x_F$  and  $z$ . On the other hand, the lack of a clear correlation between  $p_T$  and  $z$  is seen in Figure 3.8.

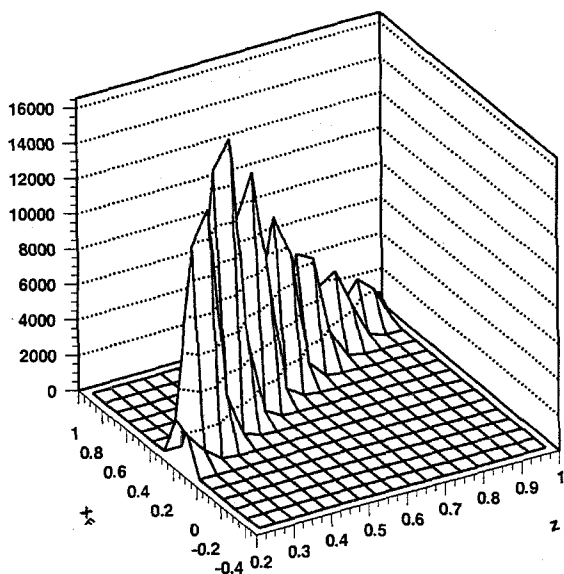


Figure 3.7: The correlation between  $x_F$  and  $z$  for  $(e, e'\pi)$  events.

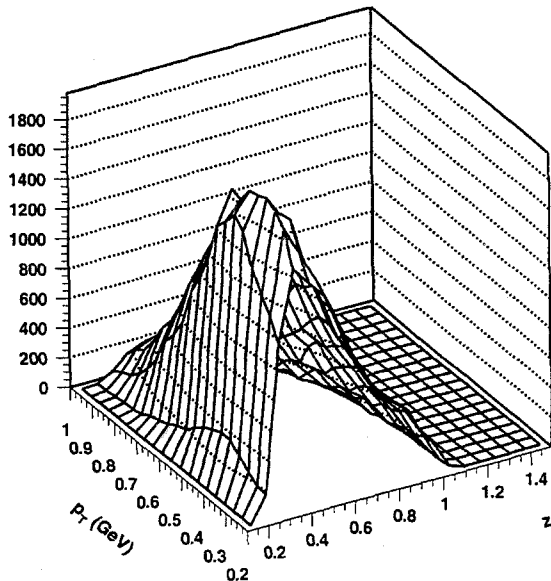


Figure 3.8: The correlation between  $p_T$  and  $z$  for  $(e, e'\pi)$  events.

The most important correlation is that between  $z$  and  $Q^2$ . If factorization holds, the process may be separated into short and long distance contributions and  $z$  and

$Q^2$  will be mutually independent, as shown in Table 3.4 and plotted in Figure 3.9.

$Q^2$ range	$\langle z \rangle$
$1.00 < Q^2 < 1.40 \text{ GeV}^2$	$1.997 \pm 0.006$
$1.40 < Q^2 < 1.70 \text{ GeV}^2$	$2.131 \pm 0.006$
$1.70 < Q^2 < 2.60 \text{ GeV}^2$	$2.114 \pm 0.007$
$2.60 < Q^2 < 5.00 \text{ GeV}^2$	$2.034 \pm 0.005$
$z$ range	$\langle Q^2 \rangle$
$0.20 < z < 0.35$	$0.497 \pm 0.001$
$0.35 < z < 0.45$	$0.501 \pm 0.001$
$0.45 < z < 0.55$	$0.502 \pm 0.001$
$0.55 < z < 0.95$	$0.497 \pm 0.001$

Table 3.4: Evidence of factorization in  $(e, e'\pi)$  interactions.

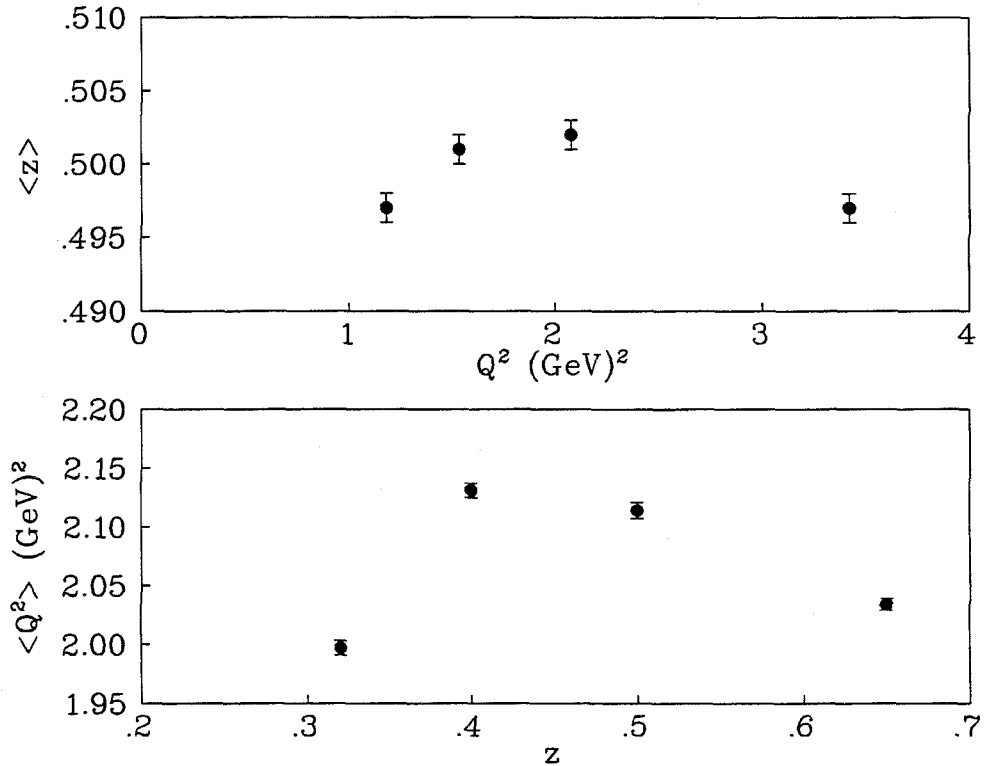


Figure 3.9: Evidence of factorization in  $(e, e'\pi)$  interactions.



### 3.4.2 Quadrant Analysis.

An additional check was performed to look for geometric effects in the kinematic distributions of the coincident hadron. This was done in the following way: The detector was divided into four quadrants, as shown in Figure 3.10.  $(e, e'\pi)$  events were sorted into the appropriate quadrant, according to the polar angle  $\phi'$  (not to be confused with the physics azimuthal angle  $\phi$ ) of the scattered positron.

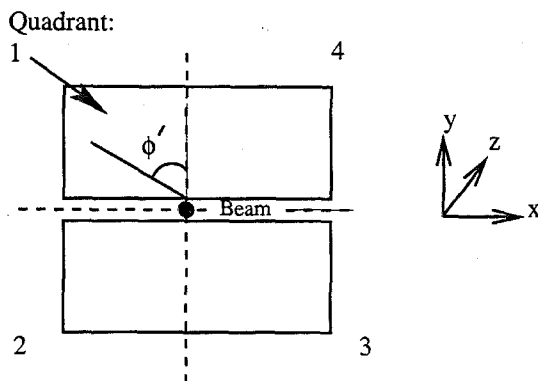


Figure 3.10: The division of the detector into quadrants for systematic studies. The events were sorted according to the region of the detector into which the associated positrons were scattered.

The kinematic distributions of each quadrant's sample were then analyzed; the mean and standard deviation were calculated. The results are shown in Figure 3.11. It is evident that no bias is seen across the four quadrants; there is no spurious geometric bias from the detector. Furthermore, the distributions agree for both years, indicating that the two data samples can be combined with confidence.

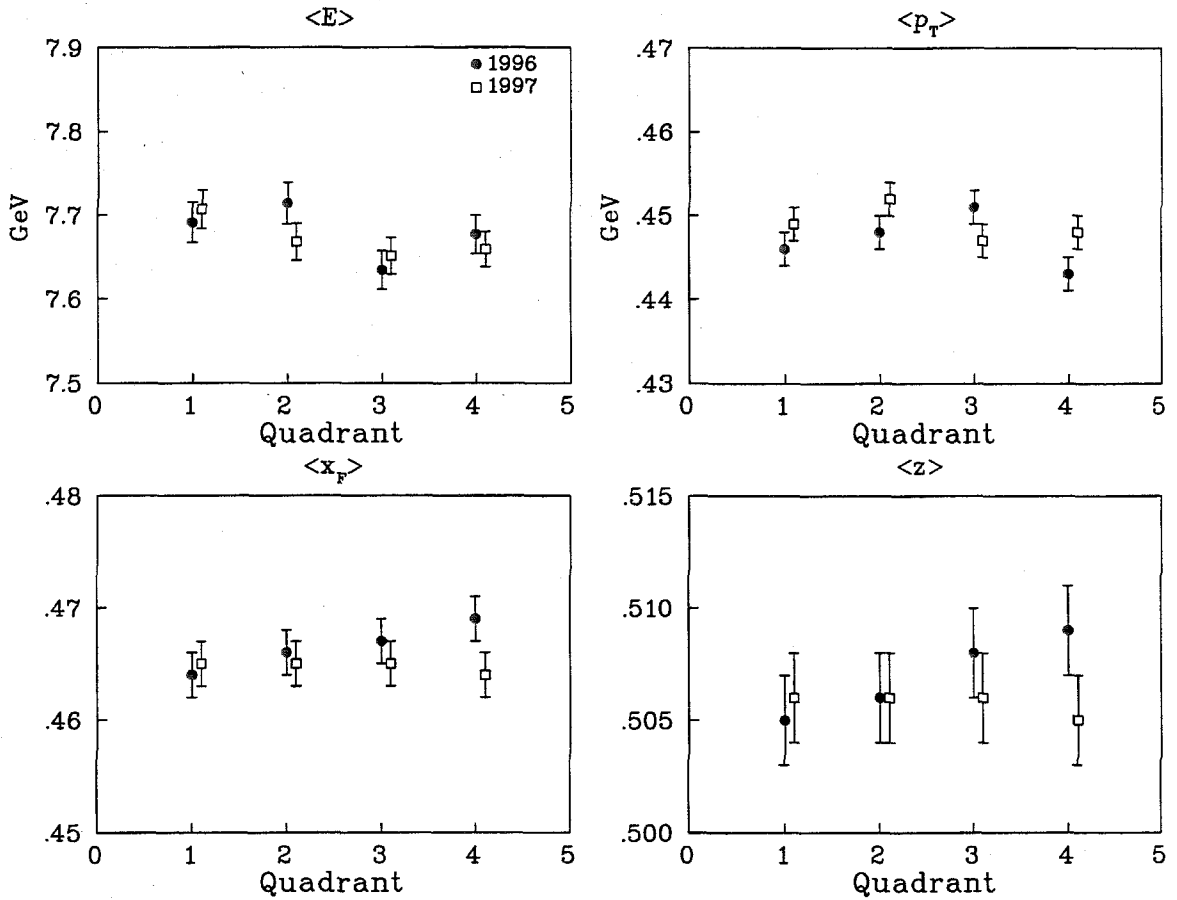


Figure 3.11: The dependence of the kinematics of the pion on the quadrant of the scattered positron.

### 3.4.3 Kinematic Bins.

In these analyses, the data are binned in various kinematic quantities. The mean values of these distributions were compared from one year to the next to look for systematic differences that could lead to an inability to combine the data sets.

The average value in each bin was evaluated for each year's ( $e, e'\pi$ ) events and are tabulated in Table 3.5, indicating that the acceptance does not differ significantly from year to year so the data may be combined.

Variable	Binning	Mean value	
		1996	1997
$p_T$	0.30 – 0.40	0.3498	0.3493
$p_T$	0.40 – 0.50	0.4479	0.4480
$p_T$	0.50 – 0.70	0.5883	0.5881
$p_T$	0.70 – 1.20	0.8472	0.8480
$Q^2$	1.00 – 1.40	1.1830	1.1841
$Q^2$	1.40 – 1.70	1.5408	1.5419
$Q^2$	1.70 – 2.60	2.0822	2.0794
$Q^2$	2.60 – 5.00	3.4155	3.4152
$z$	0.20 – 0.35	0.3176	0.3175
$z$	0.35 – 0.45	0.3983	0.3983
$z$	0.45 – 0.55	0.4978	0.4974
$z$	0.55 – 0.95	0.6913	0.6898
$x_F$	0.25 – 0.32	0.2856	0.2855
$x_F$	0.32 – 0.40	0.3585	0.3588
$x_F$	0.40 – 0.52	0.4567	0.4562
$x_F$	0.52 – 0.95	0.6516	0.6501

Table 3.5: Average kinematic values and bins for  $(e, e'\pi)$  events.

### 3.5 Identification of $(e, e'\Lambda)$ and $(e, e'K_S)$ Events.

Hereafter, any discussion of lambdas or K-shorts refers to semi-inclusive events, in which a coincident positron is also detected.

#### 3.5.1 Fiducial Cuts.

The strange particles were extracted from the nano-DST's. Again, the runs of Section 3.3 were used to extract three-track events, in which the kinematics of the positron satisfied Equation 3.5. As in the  $(e, e'\pi)$  analysis, when long tracks were used, they had to fall well within the detector's fiducial volume:

$$\begin{aligned} \theta_y &> 40 \text{ mrad,} \\ |x_{cal}| &< 170 \text{ cm,} \\ 30 &< |y_{cal}| < 90 \text{ cm.} \end{aligned}$$

### 3.5.2 Background Reduction.

Given a mass distribution with a signal  $S$  and a background  $B$ , the background may be reduced with an appropriate set of cuts. In general, such cuts should be chosen to optimize the following:

- Maximize  $S/B$  for the smallest correction.
- Minimize  $\delta S/S$  for a precision measurement.

These terms are defined as:

$$\begin{aligned} S/B &= \frac{N_{SB} - B}{B}, \\ \delta S/S &= \frac{\sqrt{N_{SB} + B}}{N_{SB} - B}, \end{aligned} \quad (3.6)$$

where  $N_{SB}$  is the number of events passing all cuts that are  $\pm 3\sigma$  from the peak; while  $B$  events satisfy all the same cuts except that they appear at  $\pm(4-7)\sigma$  from the mean mass.  $B$  can also be extracted by fitting the background, but this is a poor estimator when the actual shape of the background events is needed for physics distributions.

### 3.5.3 Lifetime.

The lifetime  $ct$  is the distance traveled by the  $\Lambda$  or  $K_S$  in the laboratory frame, where  $c\tau$  is the proper lifetime. Since the  $\Lambda$  and the  $K_S$  have proper lifetimes of 7.89 cm and 2.68 cm, respectively, this quantity can be used to better improve the signal, though it is complicated because the particles are not produced from a point source, but rather from a triangular vertex distribution. Although other quantities, such as the vertex distributions, are best understood with the Monte Carlo (see Section 3.5.5), this quantity is best optimized with the data.

No restriction was made regarding long and short tracks, as defined in Section 2.3.7. For the  $\Lambda$  events, the pion may be a short track, but the proton must traverse the detector. Either charged pion, but not both, may be a short track in the  $K_S$  selection. Furthermore, protons below the Čerenkov threshold were accepted as well.

$ct$ (cm) (minimum)	$\Lambda$		$K_S$	
	$S/B$	$\delta S/S$ (%)	$S/B$	$\delta S/S$ (%)
1996				
5	0.7	5.30	1.1	4.37
10	1.0	5.10	2.2	3.89
15	1.3	4.98	3.1	3.81
20	1.4	5.18	3.8	3.89
25	1.6	5.34	4.6	4.01
30	1.7	5.66	4.9	4.27
1997				
5	0.7	4.76	1.0	4.01
10	0.9	4.62	1.8	3.72
15	1.3	4.47	2.3	3.69
20	1.5	4.56	2.7	3.78
25	1.7	4.60	3.3	3.82
30	1.9	4.81	3.8	3.88

Table 3.6:  $S/B$  and  $\delta S/S$  as a function of travel distance in the laboratory for the semi-inclusive  $\Lambda$  and  $K_S$ . No cuts are applied beyond those to identify a DIS positron.

Table 3.6 shows the variation of  $\delta S/S$  for each data sample. These studies are independent of Monte Carlo simulation and come strictly from analysis of the data. According to this method, the optimal value is 15 cm for both the  $\Lambda$  and the  $K_S$ .  $S/B$  is not maximized here as it increases monotonically with the length used; it is simply used for later comparison to indicate the appropriateness of other cuts. Both  $S/B$  and  $\delta S/S$  vary between the years, indicating a difference in average background conditions. This is one of the many reasons why the data from each year are treated separately. Although the statistical precision naturally varies with the run list used, the average  $S/B$  does not, indicating no pathological problems with including various runs (or excluding them).

The Monte Carlo can also be used to extract the optimal range for these values such that the data can be fit with an exponential appropriately. On the other hand, it was very useful to use  $\delta S/S$  as a guide because the final physics results were insensitive to the actual cut used and only the precision was affected.

Additionally,  $\Lambda$  identification requires that  $p_p > p_\pi$  in the lab frame.

### 3.5.4 Monte Carlo Models of Detector Resolution.

The Monte Carlo was again used to understand the impact of the finite detector resolution and acceptance on the data sample. Lambda and K-short events were generated with  $\sim 10$  times the statistics of the data sample for both the 1996 and 1997 detector configurations, as discussed above in Section 3.3.1<sup>2</sup>. The decay products were passed through a digitized version of the detector. The resulting multi-track events were then subjected to the same analysis program as the data, after which distributions were generated in order to establish appropriate cuts for the actual data sample.

#### Collinearity.

The *collinearity* describes the following: Let  $\hat{\Lambda}$  be the unit vector pointing from the reconstructed decay vertex back to the production vertex, and let  $\hat{v}_{p\pi}$  be the unit vector describing the sum of the momentum vectors of the proton and the pion. The collinearity is the cosine of the angle between these two, defined as  $\text{collinearity} = \cos(\hat{\Lambda}, \hat{v}_{p\pi})$  (as shown in Figure 3.12). Variations from unity for this number result from reconstruction errors. The same quantity can be evaluated for the  $K_S$  events.

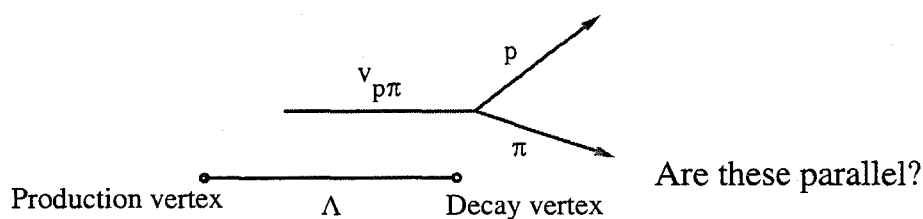


Figure 3.12: The collinearity in decays of strange particles.

To determine how well this can be measured with the spectrometer,  $(e, e'\Lambda)$  and  $(e, e'K_S)$  events were generated by the Monte Carlo and the collinearity distribution was constructed. As seen in Figure 3.13, the resolution of the detector is such that a

<sup>2</sup>The only modified files: *hmc.dg.ie*, which lists the materials in the detector, and *hmc.digi*, which parameterizes the response of the detectors.

cut of  $\cos(\vec{\Lambda}, \vec{v}_{p\pi}) > 0.99$  is sufficient (only  $< 1\%$  of the Monte Carlo events are lost).

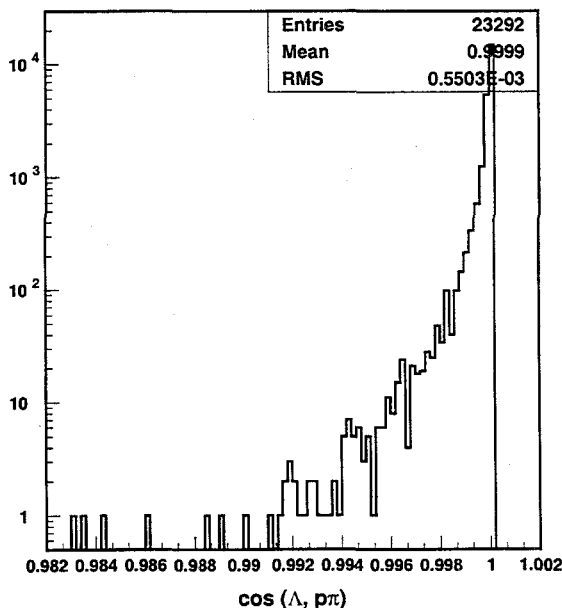


Figure 3.13: The collinearity, as defined in the text. It has been evaluated for generated semi-inclusive  $\Lambda$  and  $K_S$  that were then reconstructed.

### Track Separation at the Vertices.

The two relevant vertices are shown in Figure 3.14 and the two relevant distances,  $d_{\text{hadron}}$  and  $d_{e-X}$ , are defined. The decay vertex is reconstructed first with the two decay hadrons and then the production point is found by using that track and matching it to the positron's track.

In the decay vertex, the background can be reduced by restricting  $d_{\text{hadron}}$ , the distance of closest approach between the two decay hadrons. The reconstructed Monte Carlo events were used to determine how well the vertices can be identified. The results for the semi-inclusive  $\Lambda$  and the  $K_S$  are seen in Figures 3.15 and 3.16; these distributions were poorly described by exponential distributions. A calculation of the  $\sigma$  of the distribution (assuming a mean of zero) gives values of  $\sim 1$  cm for both the  $\Lambda$  and  $K_S$ . The value varies by  $\sim 0.2$  cm as the detector description is refined and

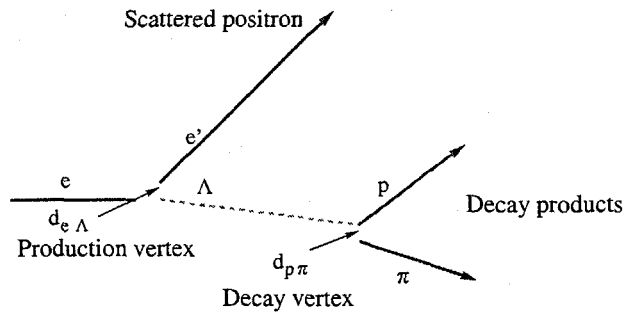


Figure 3.14: The geometry of the decay and the definition of the two distances  $d_{\text{hadron}}$  and  $d_{e-X}$ , shown for  $\Lambda$  decay.

other cuts are varied slightly. For this reason, the average value is deemed sufficiently accurate and a  $3\sigma$  cut of 3.0 cm was used.

Similarly, background can be reduced by restricting  $d_{e-X}$ , the distance of closest approach between the positron and the reconstructed particle. Figures 3.15 and 3.16 show these distributions as well and indicate how, because of the third track needed to create this figure, the distribution does not look exponential. The widths were again calculated and they were 1.0(0.7) cm for the  $\Lambda(K_S)$ , though these values varied as a function of the other cuts. Since the physics results were extremely insensitive to these values, an average of 1.0 cm was used to impose a  $3\sigma$  cut of 3.0 cm for both particles.



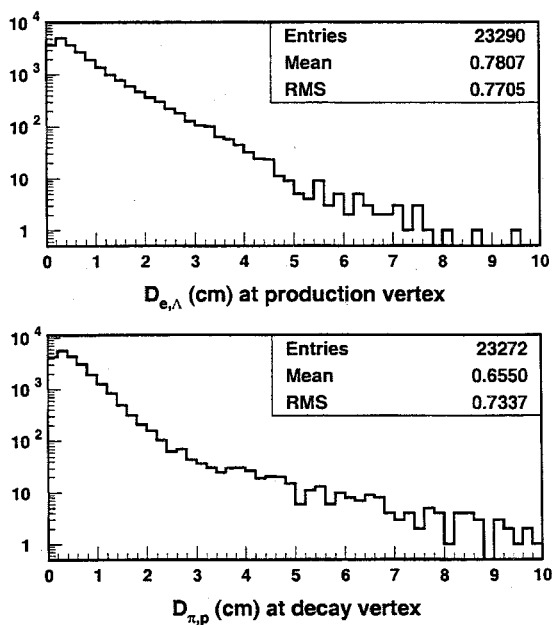


Figure 3.15: Distance between the positron and the  $\Lambda$  at the production vertex (top) and the  $\pi$  and  $p$  at the decay vertex (bottom) in Monte Carlo events.

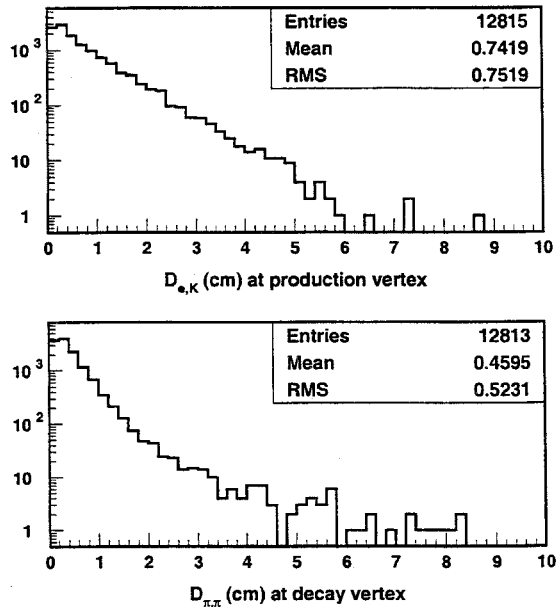


Figure 3.16: Distance between the positron and the  $K_S$  at the production vertex (top) and the two pions at the decay vertex (bottom) in Monte Carlo events.

### Mass Distributions in the Monte Carlo.

The mass distributions were constructed for both the  $\Lambda$  and the  $K_S$  generated in the Monte Carlo, as can be seen in Figures 3.17 and 3.18.

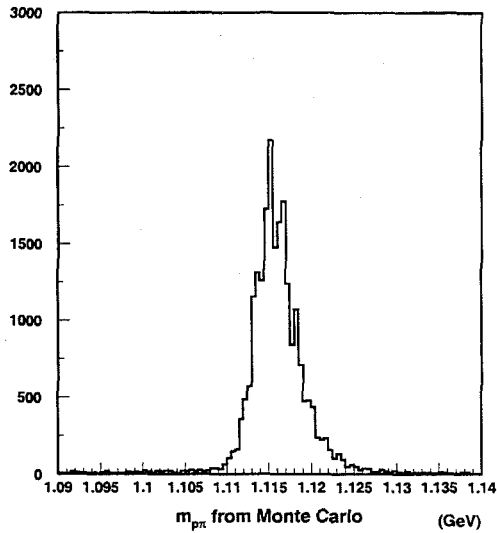


Figure 3.17: The  $\Lambda$  mass distribution in Monte Carlo events.

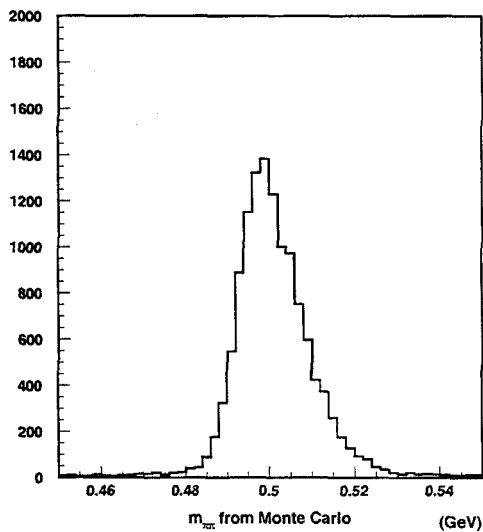


Figure 3.18: The  $K_S$  mass distribution from the Monte Carlo. The mass resolution of  $\sim 1.3\%$  may be seen from the width of the distribution.

The distribution in the  $K_S$ , which decays symmetrically to  $\pi^+\pi^-$ , can be used to examine the detector mass resolution, giving a value of  $\sim 1.5\%$ . This will be compared to data in Section 3.5.8.

### 3.5.5 Vertex Distributions.

The production vertex distributions will be discussed in terms of the coordinates  $x'$ ,  $y'$ , and  $z'$ , in order to avoid confusing them with other variables defined in this work. The origin for this system of coordinates is at the center of the target cell and following the HERMES convention ( $x'$  horizontal,  $y'$  vertical, and  $z'$  pointing downstream).

#### Longitudinal Distributions.

The  $z'$  distribution of Figure 3.19 indicates that  $\sim 5\%$  of the events are reconstructed outside of the target cell. The mean of the  $z'$  distribution is sensitive to the cuts placed on the track separation at the two vertices. If these numbers are too generous, the mean will be inconsistent with zero. Fortunately, tight cuts mitigate this problem.

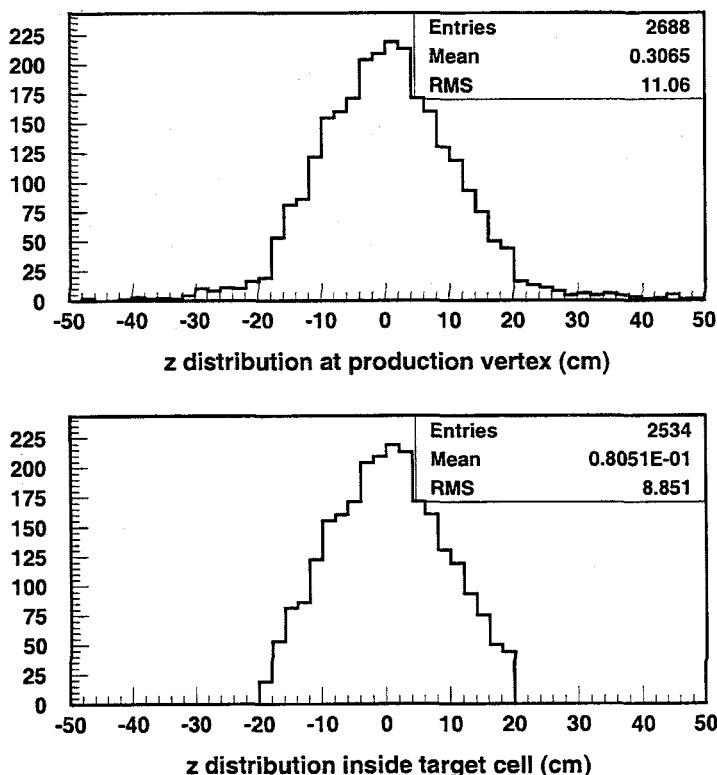


Figure 3.19: The  $z'$  distribution for  $\Lambda$  and  $K_S$  events in the data of 1996; the 1997 data look identical. Top:  $\sim 5\%$  of the events are reconstructed outside the target cell. The collimator “bump” seen at negative  $z'$  values in the inclusive distributions is not seen here. Bottom: The distribution in the target cell with the cut  $|z'| < 20$  cm.

### Transverse Distributions.

In inclusive analyses, events are restricted to the target cell region by utilizing the fact that a single track can be traced back to its point of closest approach to the beam line; this is then considered the vertex position. In coincidence measurements, more information is available to accurately reconstruct a vertex position.

The relevant distribution of vertex coordinates is that associated with the production of the strange particle. In order to understand the detector's limitation on these quantities, these histograms can be plotted for Monte Carlo events, where all events are produced at  $x' = 0$ ,  $y' = 0$ , and with a triangular distribution in  $z'$ . The finite beam size in the experiment is so small that it is unlikely to be uncovered by

the resolution of this detector. Hence comparing Monte Carlo distributions to data tests the representation of the detector.

Figure 3.20 shows that the transverse distributions are not easy to understand. One Gaussian curve does not fit the data well, while the  $\chi^2_\nu$  is significantly reduced by fitting with two Gaussian curves. The widths differ in  $x'$  and  $y'$  due to the configuration of the front chambers, which are the only tracking detectors used for the region in front of the magnet in this work. The  $x'$  position is better determined, thus producing distributions with smaller widths.

## Reconstructed MC: Vertex distributions

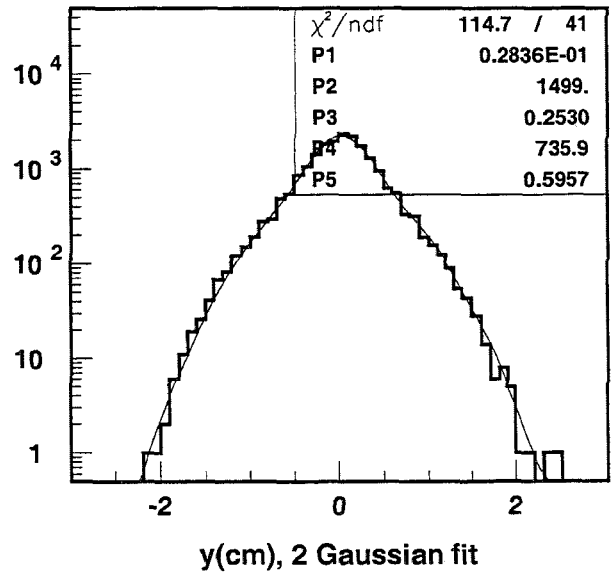
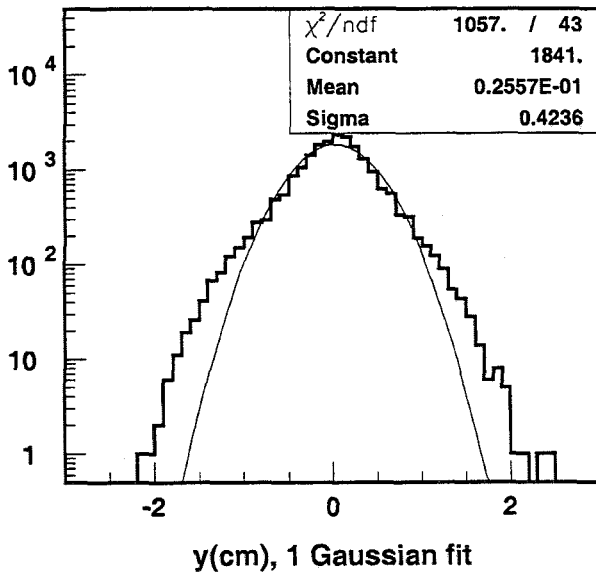
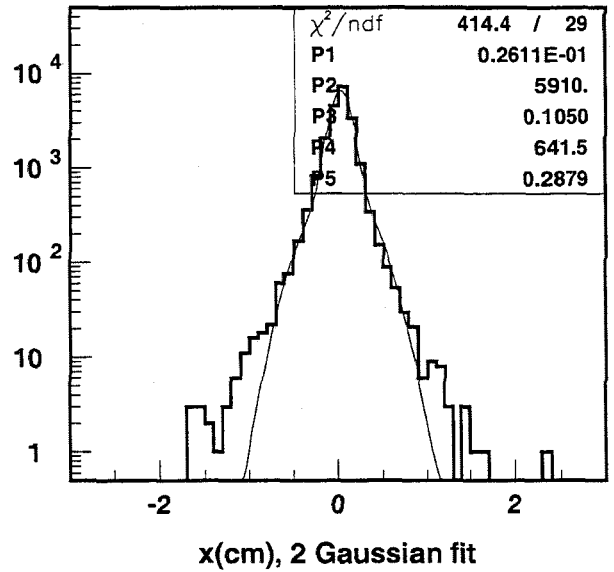
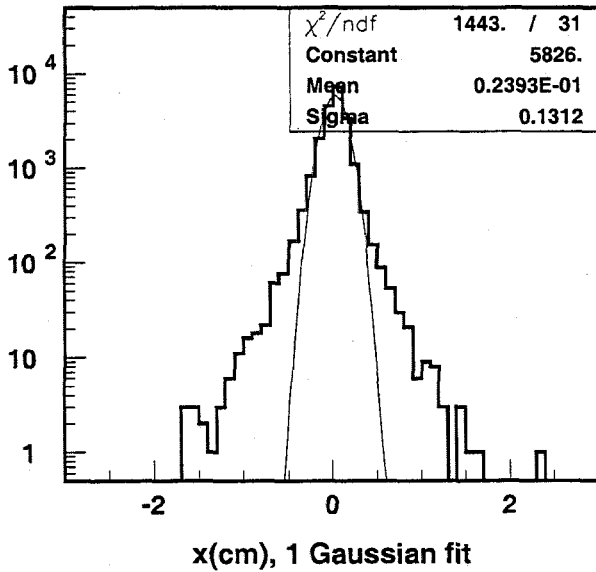


Figure 3.20: Vertex distributions resulting from reconstructed Monte Carlo events, where the events produced are  $\Lambda$  or  $K_S$ , as discussed in the text.

The transverse vertex distributions from the data look much as they do in the Monte Carlo, such that Gaussian curves do not characterize the data very well. Rather, it is preferable to calculate the widths of the  $x'$  and  $y'$  distributions. It is also possible to exclude events where the reconstructed  $z'$  origin appears to be outside the target cell. Table 3.7 describes the changes in the mean and widths when data and Monte Carlo events are compared; and when the  $z'$  origin is restricted.

	Monte Carlo		Data		Data with $ z'  < 20$ cm	
	$\mu$	$\sigma$	$\mu$	$\sigma$	$\mu$	$\sigma$
$\Lambda$						
$x'$	$0.0145 \pm 0.0013$	0.1947	$-0.1018 \pm 0.0095$	0.3587	$-0.1103 \pm 0.0074$	0.2813
$y'$	$0.0193 \pm 0.0035$	0.5032	$-0.0364 \pm 0.0160$	0.5812	$-0.0220 \pm 0.0120$	0.4218
$z'$	$1.0297 \pm 0.0643$	9.3447	$0.3160 \pm 0.3129$	11.3411	$0.0811 \pm 0.2533$	8.8994
$K_S$						
$x'$	$0.0216 \pm 0.0011$	0.1454	$-0.1054 \pm 0.0084$	0.3208	$-0.0985 \pm 0.0074$	0.2774
$y'$	$0.0258 \pm 0.0038$	0.4819	$-0.0360 \pm 0.0145$	0.5237	$-0.0450 \pm 0.0124$	0.4340
$z'$	$0.8937 \pm 0.0713$	9.0596	$0.2667 \pm 0.3006$	10.8008	$0.0793 \pm 0.2521$	8.8019

Table 3.7: Statistical measures for vertex distributions of  $\Lambda$  and  $K_S$  for Monte Carlo events, data, and data with  $z' < 20$  cm. All measurements given in centimeters.

The widths are particularly sensitive to the cuts on  $d_{e-X}$  and  $d_{hadron}$ ; though generous values for these quantities do not affect  $S/B$  or  $\delta S/S$  significantly, they do change the values for  $\sigma$ . Hence vertex information gives additional guidance regarding the validity of other cuts. Furthermore, the means are closer to zero and the transverse widths are narrowed when the  $|z'| < 20$  cm restriction is imposed.

### 3.5.6 Additional Kinematic Cuts.

The following additional cuts were imposed on kinematic variables:

$$\begin{aligned}
 0 &< x_F < 1, \\
 0.2 &< z < 1, \\
 0.1 &< p_T < 1.2 \text{ GeV}.
 \end{aligned}$$

$x_F > 0$  was required in order to guarantee that the events took place in the current fragmentation region. Singularities in the polarization histograms were seen for very low  $z$  and for low  $p_T$ . It was discovered that these additional cuts improve the  $\chi^2_\nu$  of the final results and they do not bias the results at all. These cuts were more generous than those for  $(e, e'\pi)$  events because there are far fewer events; hence, the results are less sensitive to these cuts.

### 3.5.7 Final Cut Selection.

For convenience, the cuts are summarized in Table 3.8.

Requirement	Minimum value for $\Lambda (K_S)$	Maximum value for $\Lambda (K_S)$
$Q^2$ (GeV <sup>2</sup> )	1	7
$W^2$ (GeV <sup>2</sup> )	4	
$y$		0.85
$x_F$	0	1
$z$	0.2	1
$p_T$ (GeV)	0.1	1.2
$\theta_y$ of each track (mrad)	40	
$x$ at calorimeter face (cm)		150
$y$ at calorimeter face (cm)	30	90
$ct$ (cm)	15	
$\cos(\vec{\Lambda}(K_S), \vec{v}_{p\pi(\pi\pi)})$	0.99	
$d_{e\Lambda(K_S)}$ (cm)		3(3)
$d_{\pi p(\pi)}$ (cm)		3(3)
$z'$ at prod. vertex (cm)	-20	20
width of peak (GeV)		0.002(0.008)

Table 3.8: Final cut selection for  $(e, e'\Lambda)$  and  $(e, e'K_S)$  events.

### 3.5.8 Mass Distributions.

Figure 3.21 shows the mass peaks after all cuts are applied. The  $K_S$  peak shows a mass resolution of 1.2%, which agrees impressively with Monte Carlo, and the  $\chi^2_\nu$  values are rather reasonable.



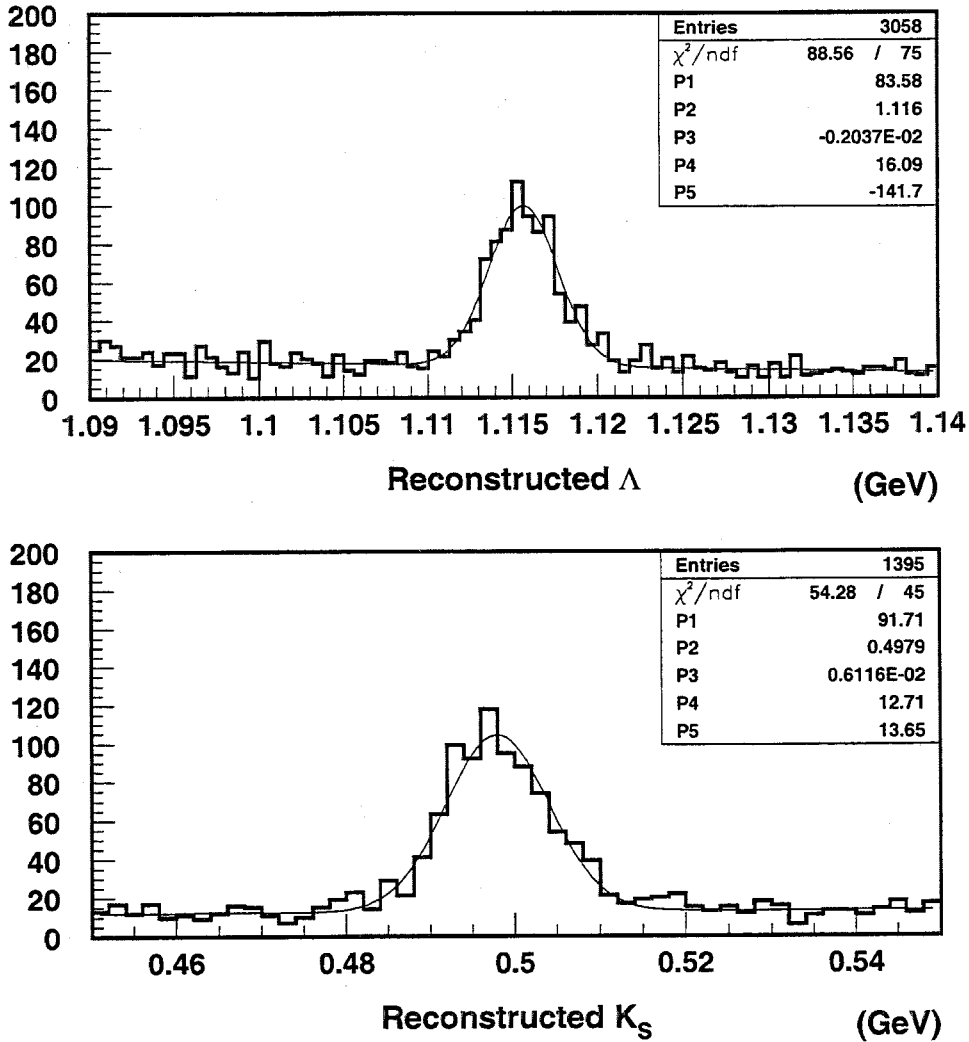


Figure 3.21: Reconstructed mass peaks with all cuts applied. Top:  $\Lambda$ ; bottom:  $K_S$ . The constants are extracted from fitting  $N$  events with  $N = P1 \exp(-0.5(m - P2)/P3)^2 + (P4 + P5(m - P2))$  for mass  $m$ .

### 3.5.9 Background Subtraction to Strange Particles.

The background is identified by looking at the region in the mass spectrum that is  $\pm(4 - 7)\sigma$  from the mean, while the signal region is defined to be  $\pm 3\sigma$ . In every distribution plotted hereafter, the signal and background regions are binned independently and then the background is subtracted. The corresponding error bar for this

yield is increased appropriately. The size of the correction is shown in the ratio of  $S/B$  as a function of  $\Lambda$  energy in Figure 3.22.

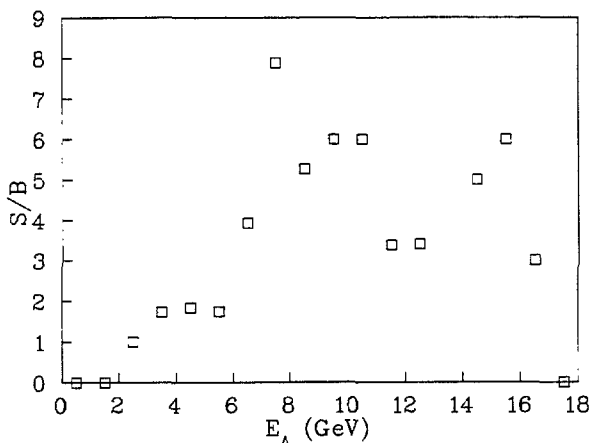


Figure 3.22: The signal-to-background ratio  $S/B$  as a function of the  $\Lambda$  energy. At low momentum, the background is high; and at high momentum, the signal is low.

Although the Monte Carlo can be used to simulate background as well, it was decided to study the background in the data sample. This is due to the proliferation of low energy pions which can cause accidental coincidences and which affect misidentification in the Čerenkov as well. The Monte Carlo does not model these extra background processes well; analyzing the background in the data is more reliable.

### 3.5.10 Kinematic Distributions.

For all the distributions shown in this thesis, the Monte Carlo and data have each been independently normalized. This is done because the Monte Carlo does not reproduce the observed rates of production for  $\Lambda$  and  $K_S$ . Thus, the distributions are used to compare the shapes and not the absolute yields of particles.

The energy distribution for the  $\Lambda$  is shown in Figure 3.23.

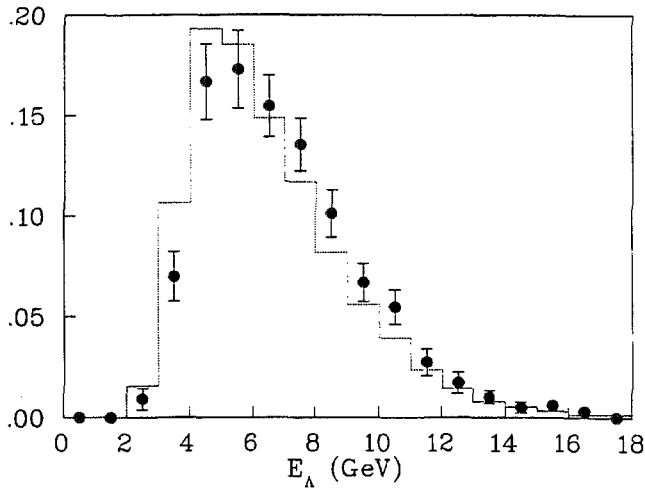


Figure 3.23: The  $\Lambda$  energy distribution. Filled circles: Data. Histogram: Monte Carlo.

Other kinematic distributions are more revealing. For instance, the momentum distributions of the decay products show a high degree of correlation, shown for the accepted  $\Lambda$  in Figure 3.24. Ideally, if a proton of a given momentum is detected, one would still find pions of all allowed momenta. Because this forward spectrometer sees such a narrow range of phase space, high (low) momentum protons correspond to high (low) momentum pions. This also explains the features of the energy dependence of the  $S/B$ . The low momentum protons are subject to background because of the failure of the Čerenkov to separate pions and protons below 4.8 GeV, while low momentum pions are immersed in coincident low energy particles at the magnet chambers. Hence, each decay particle of low momentum  $\Lambda$  events is reconstructed in a high background environment.

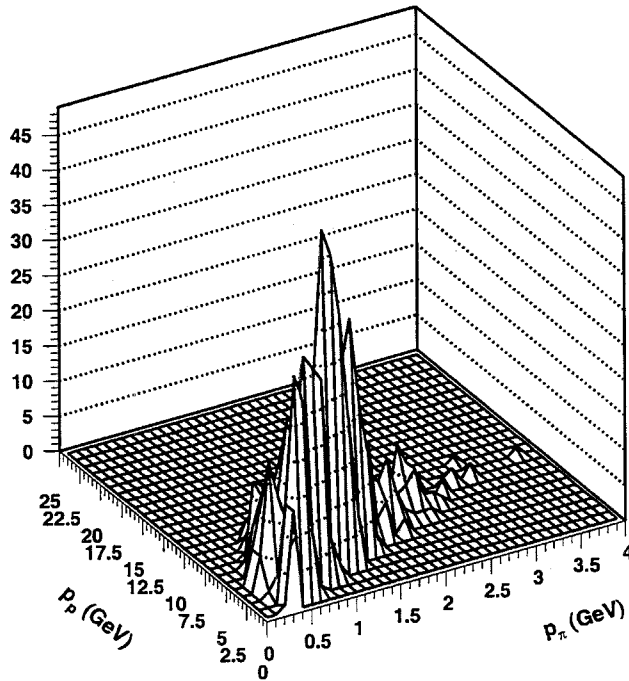


Figure 3.24: The momentum correlation between the proton and the pion of  $\Lambda$  decays in the data.

Figure 3.25 shows other kinematic distributions compared to Monte Carlo results. Data with  $Q^2 < 1 \text{ GeV}^2$  were discarded since, as discussed in Section 3.3.3, the acceptance is very sensitive to alignment at low  $Q^2$ .

Differences are seen in the variables describing the hadron. This is most likely due to inappropriate modeling of the fragmentation functions, which would also explain the discrepancy seen between the Monte Carlo and the data in the energy distribution. As in pion production, the distributions in  $x_F$  and  $z$  are not independent; however, this is an artifact of the detector.

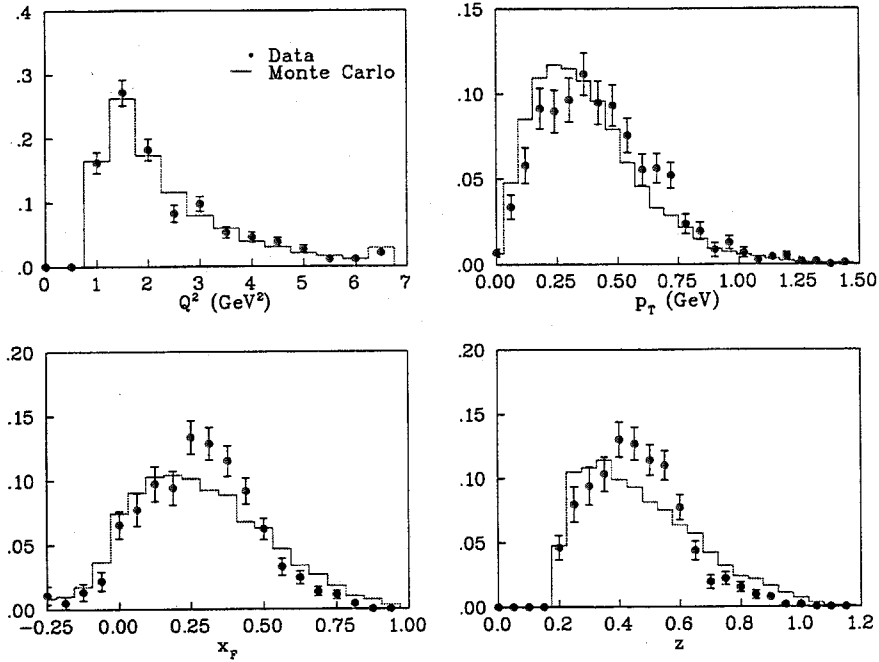


Figure 3.25: Background corrected kinematic distributions in  $(e, e'\Lambda)$  events. Top left (right):  $Q^2$  ( $p_T$ ). Bottom left (right):  $x_F$  ( $z$ ).

As before, factorization can be shown to hold for these events. Table 3.9 indicates that the mean  $z$  and  $Q^2$  are independent of one another; this is apparent in the coarser binning necessary for measurements with limited statistics.

Kinematic bin	Average value	
	1996	1997
$z < 0.5$	$\langle Q^2 \rangle = 1.910 \pm 0.034$	$\langle Q^2 \rangle = 1.833 \pm 0.029$
$z > 0.5$	$\langle Q^2 \rangle = 2.076 \pm 0.045$	$\langle Q^2 \rangle = 2.062 \pm 0.039$
$Q^2 < 2 \text{ GeV}^2$	$\langle z \rangle = 0.473 \pm 0.005$	$\langle z \rangle = 0.469 \pm 0.005$
$Q^2 > 2 \text{ GeV}^2$	$\langle z \rangle = 0.479 \pm 0.005$	$\langle z \rangle = 0.480 \pm 0.005$

Table 3.9: Evidence that factorization holds in the set of all  $(e, e'\Lambda)$  and  $(e, e'K_S)$  events, as discussed in the text. Furthermore, the average values for  $Q^2$  and  $z$  agree for the two years of data.

The associated plots for the  $K_S$  sample are shown below in Figures 3.26, 3.27, and 3.28. Compared with the  $\Lambda$  events, the kinematics are slightly different for the  $K_S$  events since at least one of the decay particles is required to be positively identified as a pion. Because the threshold of the Čerenkov counter is 4.8 GeV, this imposes a

minimum momentum on the detected  $K_S$  events.

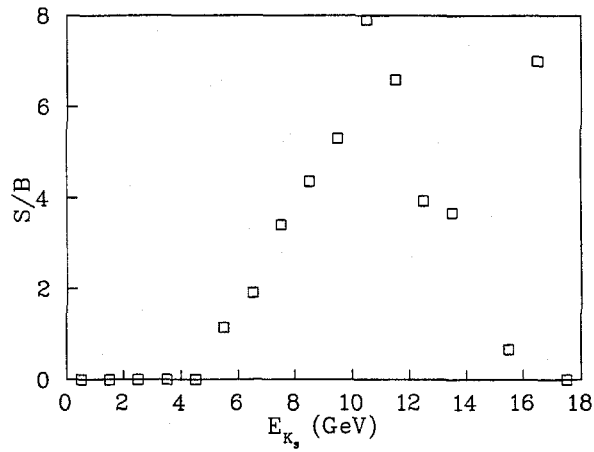


Figure 3.26: The  $S/B$  for the  $K_S$  sample, as a function of particle energy.

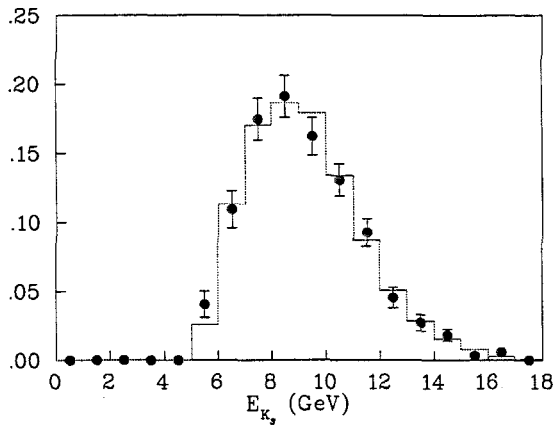


Figure 3.27: The energy distribution for the  $K_S$ , compared to Monte Carlo. The minimum momentum cutoff of 4.8 GeV is due to the requirement that at least one particle be positively identified as a pion by using the threshold Čerenkov counter.

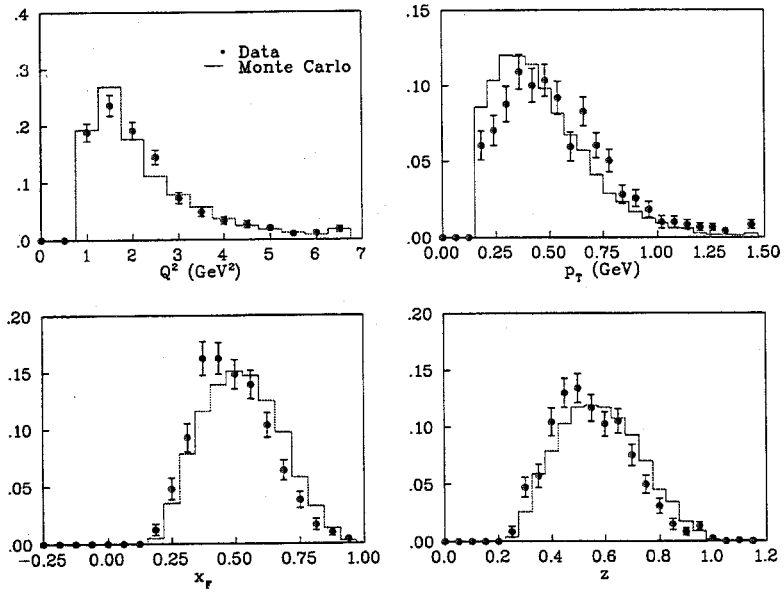


Figure 3.28: Comparison of relevant kinematic distributions for the  $K_S$ . Top left (right):  $Q^2$  ( $p_T$ ). Bottom left (right):  $x_F$  ( $z$ ).

### 3.5.11 Quadrant Analysis.

As in Section 3.4.2, the data were sorted according to the physical region of the detector into which the positron was scattered, as determined by the positron's polar angle  $\phi'$ . Each quadrant thus had a sample of  $\Lambda$  or  $K_S$  events. The mean and variance of the kinematic distributions for each quadrant's sample were calculated. The results are shown in Figures 3.29 and 3.30. It is evident that no bias exists across the four quadrants (there is no spurious geometric bias from the detector). Furthermore, the distributions agree for both years, indicating that the two data samples can be combined with confidence. It is noteworthy that the 1996 trend of the energy distribution of the  $\Lambda$  is reproduced in the 1997 data; this may hint at a small bias that is not significant in these limited statistics.

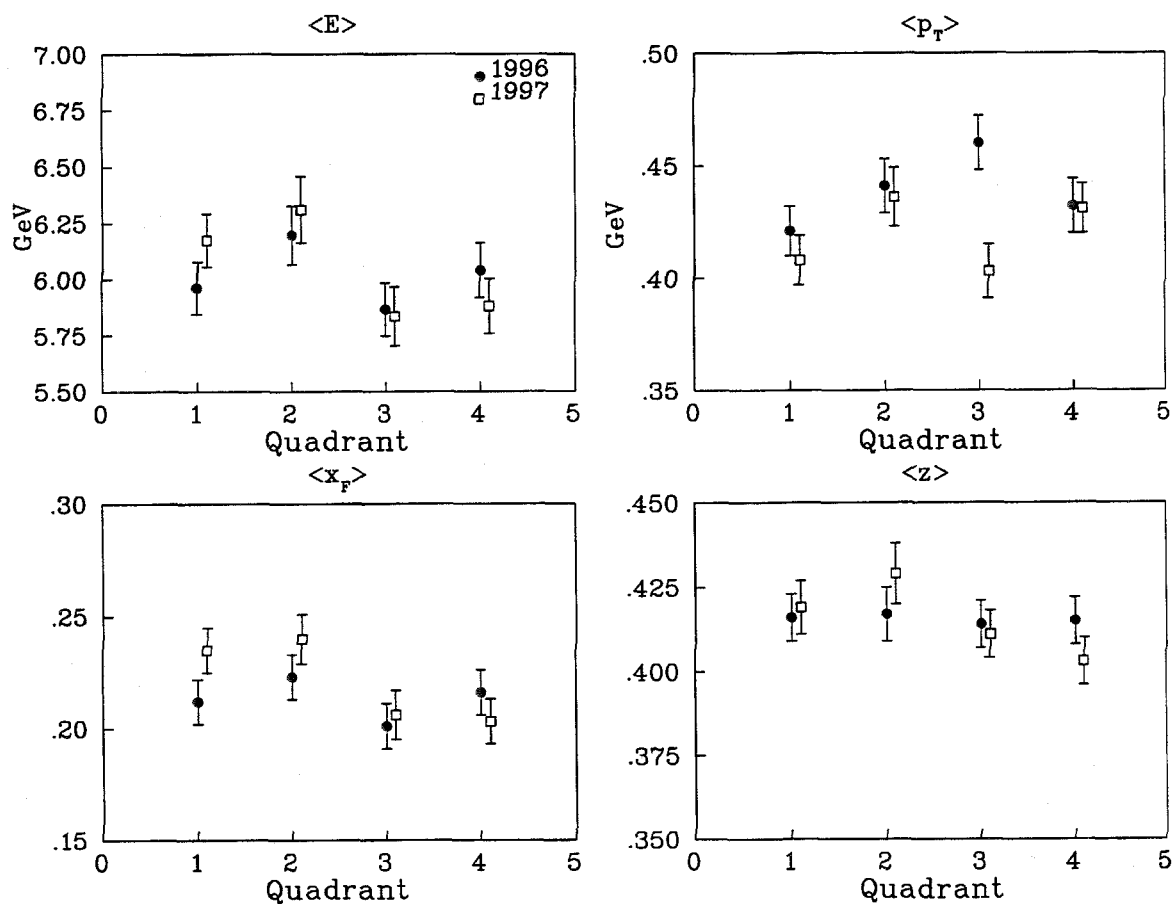


Figure 3.29: The dependence of the kinematics of the  $\Lambda$  on the quadrant of the scattered positron.



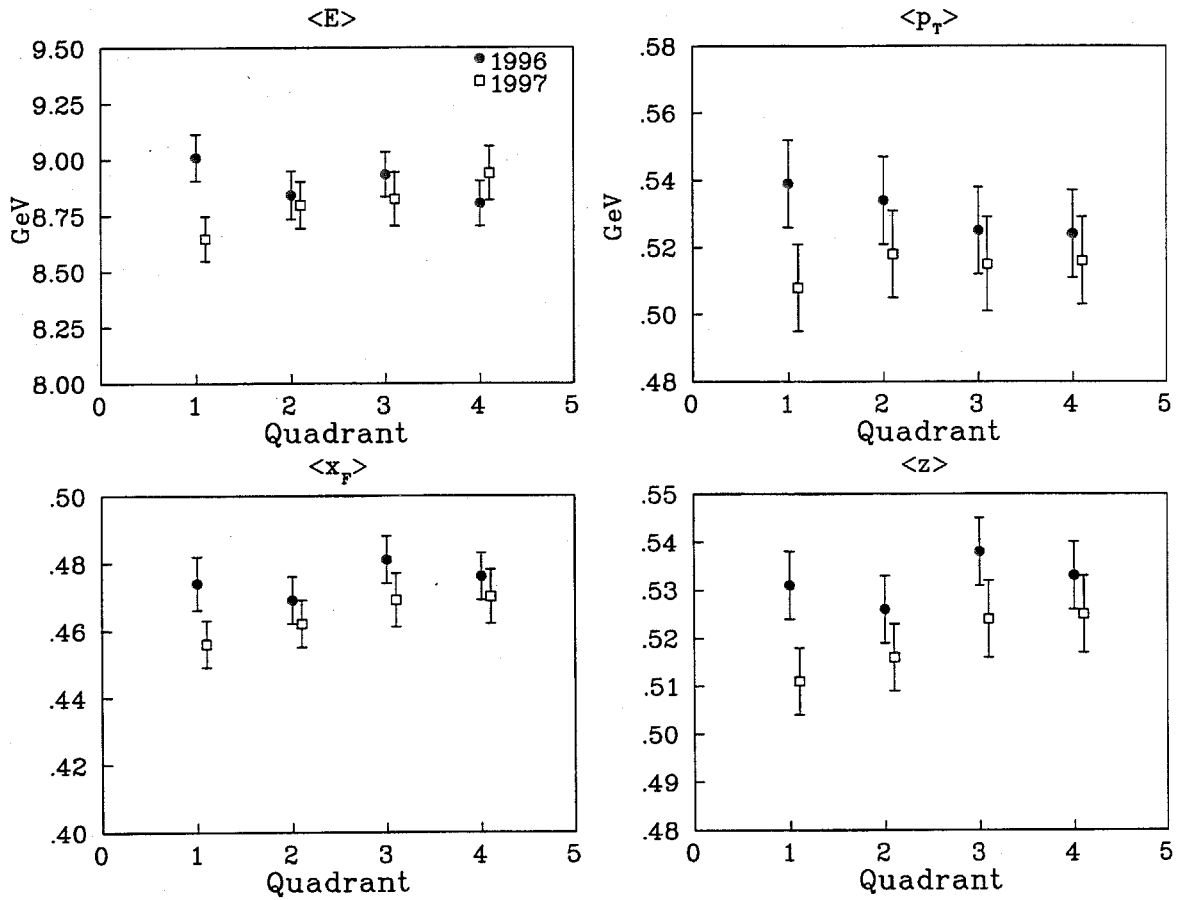


Figure 3.30: The dependence of the kinematics of the  $K_S$  on the quadrant of the scattered positron.

### 3.5.12 Kinematic Bins.

As in Section 3.4.3, the average values of the kinematic distributions were evaluated for each strange particle and are tabulated in 3.10. The acceptance differs between the  $\Lambda$  and  $K_S$  and hence different endpoints were used for the binning in  $x_F$  and  $z$  for the two samples. The results indicate that the mean value in each kinematic bin is stable from year to year and hence the results can be combined; the average value was used to characterize the results.

Variable	Binning	$\Lambda$		$K_S$	
		1996	1997	1996	1997
$p_T$	0.1-0.5	0.684	0.667	0.723	0.703
$p_T$	0.5-1.2	0.312	0.311	0.319	0.330
$Q^2$	1-2	3.193	3.276	3.248	3.171
$Q^2$	2-7	1.443	1.419	1.430	1.425
$z$	0.2-0.5(0.55)	0.606	0.621	0.682	0.676
$z$	0.5(0.55)-1	0.365	0.365	0.430	0.429
$x_F$	0-0.3(0.5)	0.439	0.444	0.624	0.624
$x_F$	0.3(0.5)-1	0.161	0.157	0.375	0.378

Table 3.10: The average values in each kinematic bin for semi-inclusive  $\Lambda$  and  $K_S$ . The  $K_S$  parameters appear in parentheses unless they are identical for both particles. The binning was chosen to give equal statistical precision in each bin.

## Chapter 4 Results.

### 4.1 Overview of Acceptance Corrections.

In general, once good events are selected, the distributions must be corrected for the acceptance of the apparatus, although the strange particles require a background correction first. The background correction can be understood by examining the events outside the central region in the mass spectrum containing good events; these “sideband” events are assumed to model the background well since they have similar kinematics.

The acceptance of the apparatus is very difficult to model, as it should take all the relevant measured quantities into account. For instance, for the  $\Lambda$  events, the acceptance function  $A_{\text{apparatus}}$  depends on many variables:

$$A_{\text{apparatus}} = A_{\text{apparatus}}(\vec{p}_{e^+}, \vec{p}_{\pi}, \vec{p}_p). \quad (4.1)$$

With few events for the strange particles, it is not possible to bin events in all variables with sufficient statistics. Hence, distributions formed from reconstructed Monte Carlo events are used to correct the data.

The pion sample has sufficient statistics so that it would be possible to follow such a model. Attempts to use the Monte Carlo simulation to simply write an acceptance correction of the form  $N_{\text{accepted}}/N_{\text{generated}}$  still demanded binning the data in the six-dimensional space of both the positron and pion momenta, although this did not produce statistically robust results. While this could work in order to extract an absolute cross section, the correlations that produce the azimuthal moments are too complex to be easily treated in this way. Consequently, a heuristic approach was followed instead and the systematic uncertainty was evaluated accordingly.

The statistical quality of each fit is measured not just by its  $\chi^2$ , but rather by the

probability  $P_\chi(\chi^2, \nu) = \int_{\chi^2}^{\infty} P_\chi(\chi^2) d\chi^2$ . In principle,  $P_\chi(\chi^2, \nu)$  defines a flat distribution between 0 and 1; thus, the fits should give uniform randomly distributed values for this quantity.

## 4.2 Azimuthal Distributions of Pions.

### 4.2.1 The Monte Carlo Generator.

Before the Monte Carlo could be used reliably to perform an acceptance correction, it was necessary to verify that the generator did not itself create false moments. Initially, the Monte Carlo simulation did produce a non-trivial azimuthal distribution, which was derived from analytic expressions for gluon radiation [14]. Using this generator would have made it very difficult to separate the relative importance of simple radiation from the physics of fragmentation, particularly when these effects both vary kinematically.

For this reason, the standard HERMES generator was modified to produce a completely flat distribution in  $\phi$ . A sample of 300,000 events was used to determine the binning of the data; for instance, at very low  $p_T$ , there was a significant moment seen. This is consistent with observations that it is difficult to construct a reliable definition of  $\phi$  at low  $p_T$  [27].

The moments extracted from generated events are separated kinematically and shown in Table 4.1. The bins differ only slightly from those used in the data analysis since they are chosen to equalize the precision in each measurement and the detector naturally samples the phase space differently. The differences are shown to be zero in Table 4.1 to within  $1\sigma$ , in general, and certainly within  $2\sigma$ . Variations are assumed to be due to the analysis that evaluates  $\phi$ , as it cannot be extracted directly from the generated events but must be reconstructed via the vector analysis of Section 4.2.3.

Kinematics	$\langle \cos \phi \rangle$	$\langle \cos 2\phi \rangle$	$\langle \sin \phi \rangle$	$\chi^2_\nu$
$0.30 < p_T < 0.35$	$-0.018 \pm 0.049$	$0.099 \pm 0.048$	$0.069 \pm 0.046$	1.317
$0.35 < p_T < 0.45$	$-0.030 \pm 0.037$	$0.009 \pm 0.037$	$0.061 \pm 0.036$	0.806
$0.45 < p_T < 0.65$	$-0.012 \pm 0.030$	$-0.063 \pm 0.032$	$-0.014 \pm 0.031$	1.474
$0.65 < p_T < 1.00$	$0.035 \pm 0.043$	$-0.053 \pm 0.043$	$0.063 \pm 0.043$	0.507
$1.00 < Q^2 < 1.35$	$-0.040 \pm 0.041$	$0.023 \pm 0.041$	$0.048 \pm 0.039$	1.320
$1.35 < Q^2 < 1.65$	$0.016 \pm 0.048$	$-0.046 \pm 0.050$	$-0.026 \pm 0.050$	0.406
$1.65 < Q^2 < 2.50$	$-0.001 \pm 0.034$	$-0.044 \pm 0.035$	$0.066 \pm 0.035$	0.571
$2.50 < Q^2 < 5.00$	$-0.008 \pm 0.026$	$-0.036 \pm 0.027$	$0.015 \pm 0.027$	0.676
$0.20 < z < 0.35$	$-0.055 \pm 0.028$	$-0.003 \pm 0.028$	$-0.011 \pm 0.028$	1.465
$0.35 < z < 0.45$	$-0.014 \pm 0.036$	$-0.044 \pm 0.036$	$-0.014 \pm 0.036$	0.500
$0.45 < z < 0.55$	$-0.037 \pm 0.043$	$0.037 \pm 0.043$	$0.133 \pm 0.042$	0.987
$0.55 < z < 0.90$	$0.016 \pm 0.035$	$-0.031 \pm 0.035$	$0.037 \pm 0.034$	1.403
$0.10 < x_F < 0.25$	$-0.040 \pm 0.028$	$-0.004 \pm 0.028$	$-0.015 \pm 0.028$	0.789
$0.25 < x_F < 0.35$	$0.013 \pm 0.031$	$-0.021 \pm 0.031$	$0.062 \pm 0.030$	1.436
$0.35 < x_F < 0.50$	$-0.030 \pm 0.040$	$-0.044 \pm 0.040$	$0.036 \pm 0.040$	0.811
$0.50 < x_F < 0.70$	$0.027 \pm 0.080$	$-0.094 \pm 0.087$	$-0.089 \pm 0.084$	1.554

Table 4.1: The generated  $\phi$  moments in  $(e, e'\pi)$  reactions. The detector geometry is not included; thus, these are the raw moments extracted from the generator when binned kinematically, although the amplitudes are set to zero.

## 4.2.2 Simulations of the Acceptance.

The Monte Carlo simulation can be used to determine the influence of the geometry of the detector, without the need to actually simulate and digitize detector responses. The full digitization can then be used later to understand the instrumental, or “smearing,” effects of the detector.

An example of this study is shown in Figure 4.1, where the distributions represent averages over all kinematic bins. Each distribution of  $N$  events in  $\phi$  has been fit with a function of the form

$$\frac{1}{N} \frac{dN}{d\phi} = 1 + A \cos \phi + B \cos 2\phi + C \sin \phi. \quad (4.2)$$

Initially, generated DIS events are selected if they have a coincident pion with momentum greater than 4.8 GeV (the Čerenkov threshold). Next, the tracks are propagated through the magnetic field look-up table used by HRC. The  $x'$  and  $y'$

positions of these tracks are then analyzed to determine if they would be detected by the calorimeter. This is effectively a geometric cut on the generated events. It is much less time-consuming than performing a full reconstruction and shows how the detector itself create false non-zero moments. This is clearly the largest effect as it produces the largest change in  $A$ . In the third and final step, a set of generated tracks is completely propagated through a digitized version of the detector. The detector's influence on the distributions thus extracted can then be separated into a contribution from the geometric acceptance and a small component from smearing.

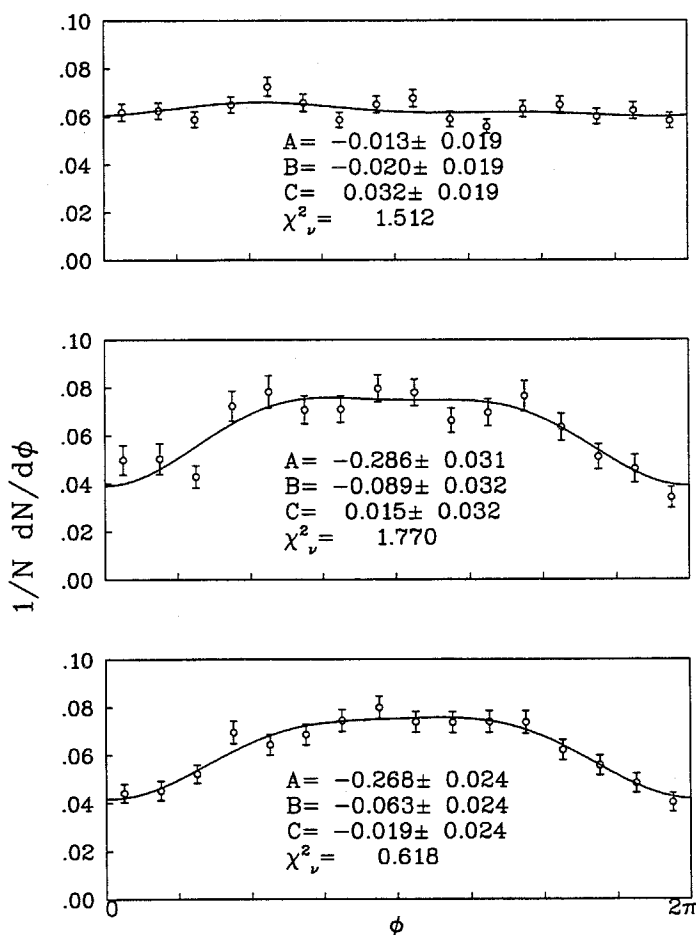


Figure 4.1: The effect of the acceptance on azimuthal distributions in generated ( $e, e'\pi$ ) events, averaged over all kinematics, where the  $\phi$  dependence is fit to the form  $\frac{1}{N} \frac{dN}{d\phi} = 1 + A \cos \phi + B \cos 2\phi + C \sin \phi$ . Top: All events; middle: events falling in the geometric acceptance of the detector; bottom: fully digitized and reconstructed events. The largest change occurs in the step wherein good events must fall in the detector, indicating that the detector's geometry produces a large false asymmetry.

It is clear that this correction will be the source of a large systematic uncertainty, as the acceptance can be parameterized with the same functional form as the signature of the physics. The acceptance does not only introduce a false moment, but the moment changes as a function of kinematics. Correcting for this is the most critical step and hence it has to be considered carefully.

For instance, Figure 4.2 indicates the variation in the acceptance as a function of  $Q^2$  by examination of Monte Carlo events for which the generated distribution is flat in  $\phi$ . Thus, it is an accurate measure of the effect of the detector. Comparison of the lower  $Q^2$  plot with Figure 3.5 suggests that  $\phi = 0$  and  $2\pi$ , the septum plate limits the acceptance; thus, there is additional sensitivity to misalignment at that edge.

Thus, it was important to restrict the data to those regions in which the description of the edge nearest to the septum plate would not be so critical. In principle, a region with low statistics should not drive a fit or the  $\chi^2$ ; however, the low yields are an indication that there is some systematic uncertainty that could be much larger there. In order to minimize such systematic effects, a correction factor  $f$  was constructed such that

$$f = \frac{N_{data} - N_{MC}}{N_{data}}. \quad (4.3)$$

At  $\phi$  values near  $\phi = 0$  and  $2\pi$ , the data were neglected if  $f > 0.25$ . In practice, with the binning chosen for this analysis, this was equivalent to discarding bins in which the yield was less than 4% of the total. Figures 4.2-4.6 indicate how the acceptance varies as a function of each kinematic quantity. This criterion was applied symmetrically, such that if  $\phi = \phi_c$  was the critical  $\phi$  value at which the yield was too low, the events at  $(2\pi - \phi_c)$  were also excluded, thus forcing the events to fall into a region symmetric in  $\phi$ . The vertical lines in Figure 4.2 indicate at which points the data were excluded.

Similar variations were seen in the region near  $\phi = \pi$ , for instance, at high  $Q^2$ . These acceptance effects are due to different edge effects and were neglected. The criterion on  $f$  excluded no events and thus the data were restricted at bins inside

those containing the maxima of the “side lobes.”

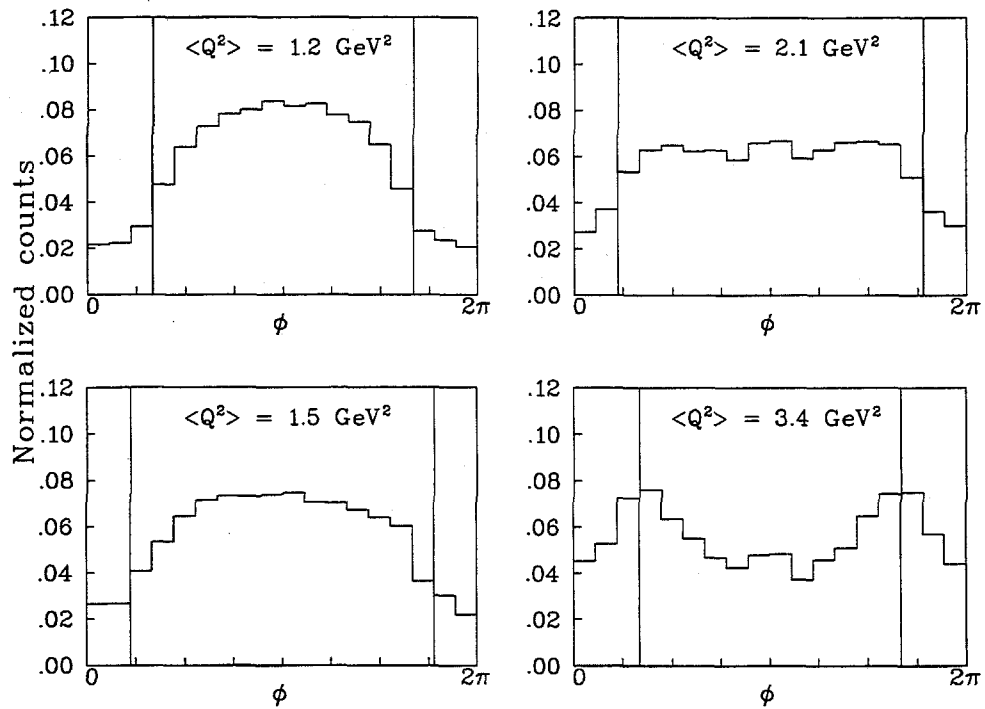


Figure 4.2: Detector acceptance in  $\phi$  as a function of  $Q^2$  for generated  $(e, e'\pi)$  events.



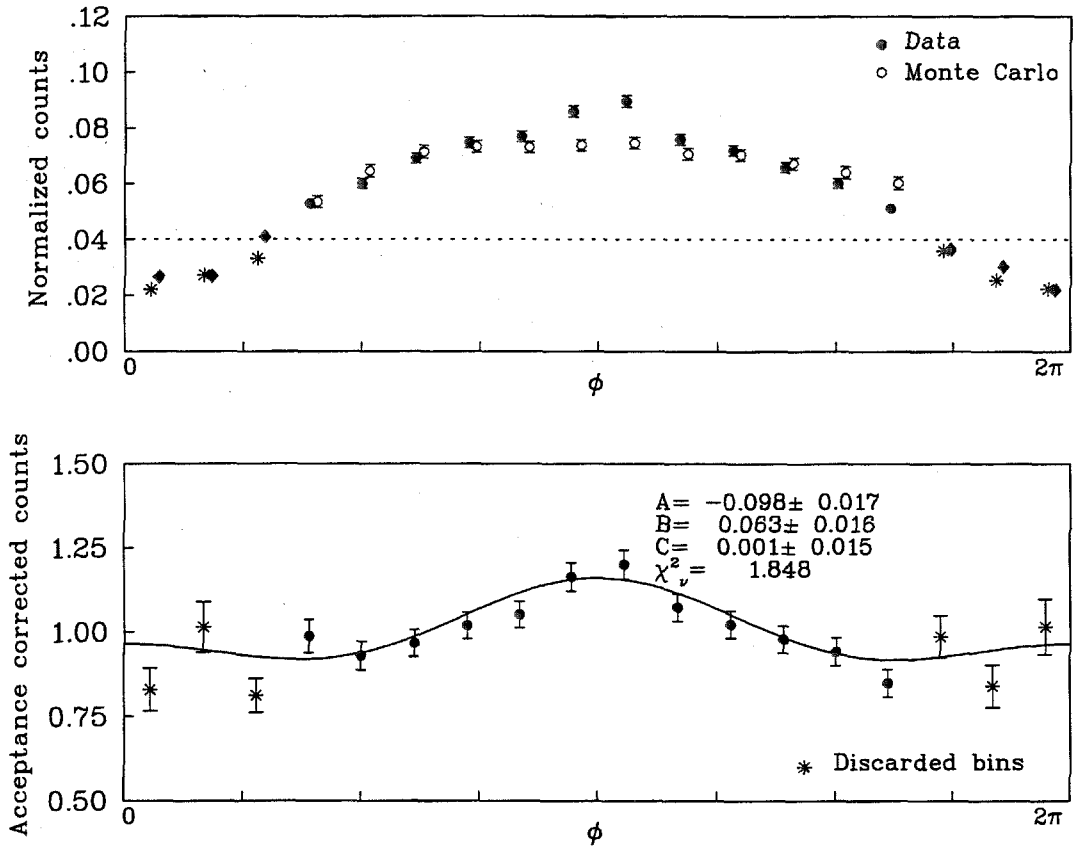


Figure 4.3:  $\phi$  distribution of pions with  $1.4 < Q^2 < 1.7 \text{ GeV}^2$ . Top: Data (filled circles) and Monte Carlo (open circles) are compared; the Monte Carlo event sample has the same statistical precision as the data. Bottom: Acceptance corrected distribution and the results of a fit to  $\frac{1}{N'} \frac{dN'}{d\phi} = 1 + A \cos \phi + B \cos 2\phi + C \sin \phi$ .

An example is shown in Figure 4.3. Bins near  $\phi = 0$  or  $\phi = 2\pi$  were not used for the fit in order to minimize systematic effects. Thus, the following guidelines were developed for determining the range of bins in which the acceptance correction is valid:

- Only those bins in which the data *and* the Monte Carlo contain more than 4% may be used.
- The kinematic regimes in which the acceptance produces a large  $\langle \cos 2\phi \rangle$  false asymmetry must be handled carefully, as it is difficult to identify the “edge” in these distributions.

Similar distributions and the associated restrictions are shown in Figures 4.4, 4.5, and 4.6.

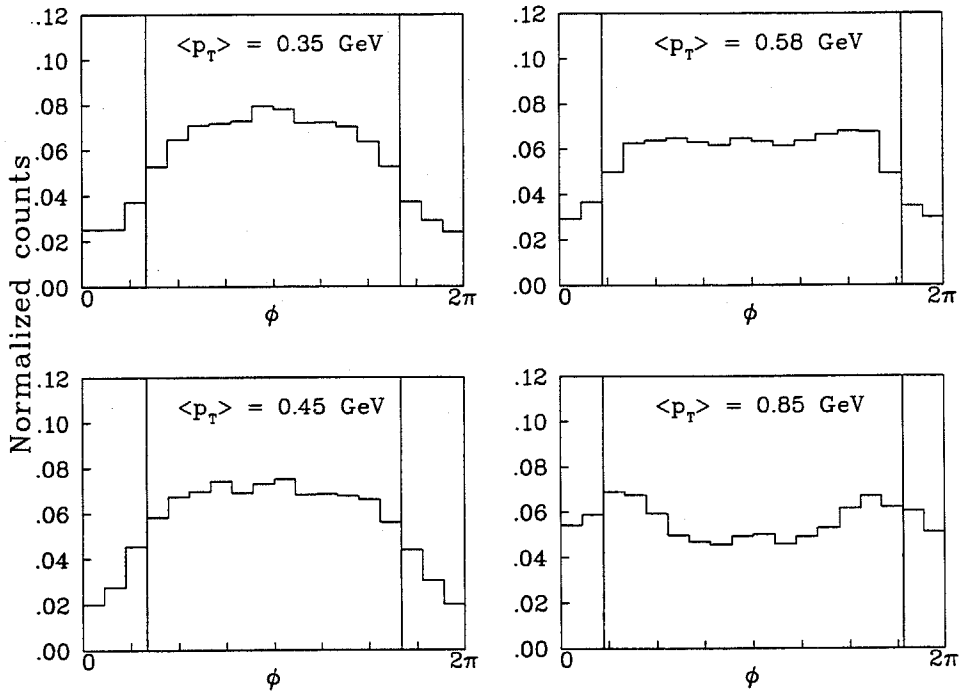


Figure 4.4: Detector acceptance in  $\phi$  as a function of  $p_T$ .

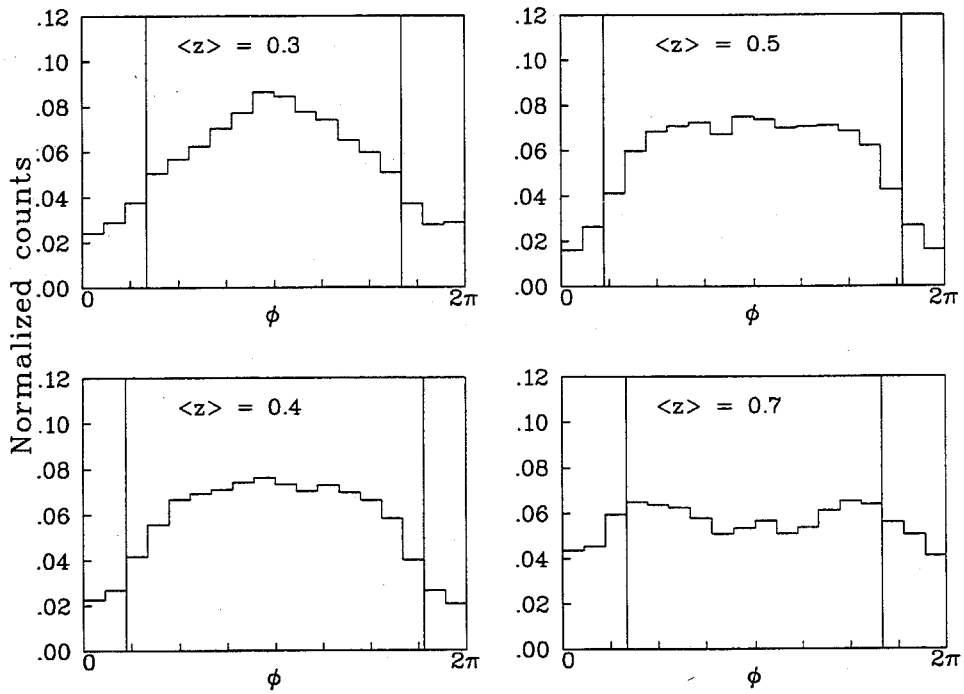


Figure 4.5: Detector acceptance in  $\phi$  as a function of  $z$ .

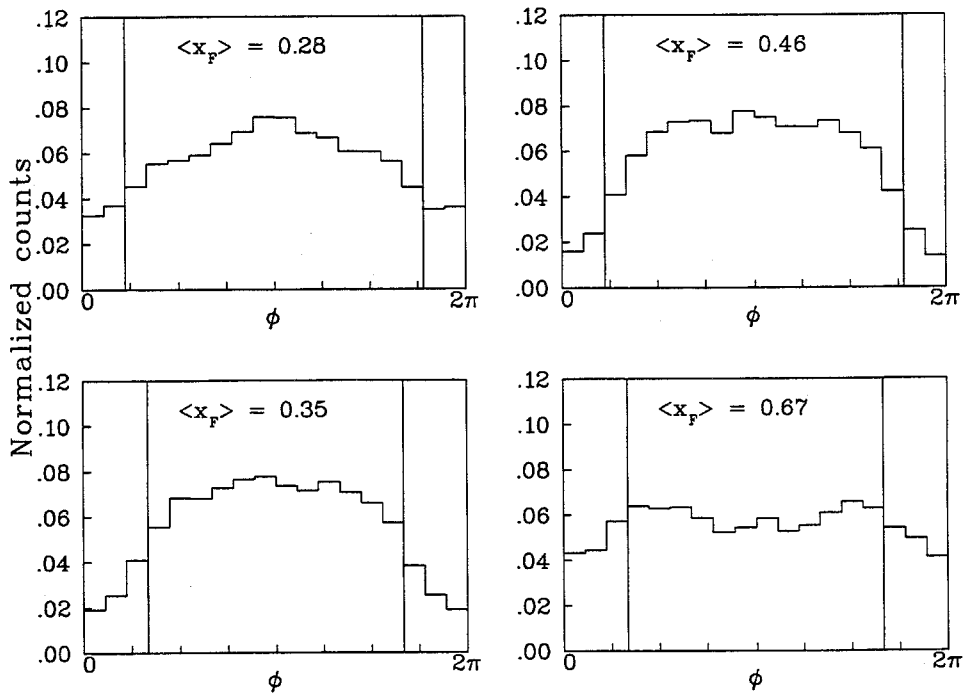


Figure 4.6: Detector acceptance in  $\phi$  as a function of  $x_F$ .

### 4.2.3 Analysis.

The angle  $\phi$  is defined as the angle between the electron scattering plane and the hadron production plane. It is defined by the following vectors in the  $\gamma$ -N CM frame:

$$\cos \phi = \frac{(\hat{q} \times \hat{\pi}) \cdot (\hat{k} \times \hat{k}')}{|\hat{q} \times \hat{\pi}| |\hat{k} \times \hat{k}'|};$$

$$\sin \phi = \frac{[(\hat{q} \times \hat{\pi}) \times (\hat{k} \times \hat{k}')] \cdot \hat{q}}{|\hat{q} \times \hat{\pi}| |\hat{k} \times \hat{k}'|}.$$

Unit vectors in the appropriate direction are all denoted by a hat.  $\hat{\pi}$  is the pion direction of motion in the  $\gamma$ -N CM frame.  $\hat{q}$ ,  $\hat{k}$  and  $\hat{k}'$  describe the direction of motion of the virtual photon, the incident lepton, and the scattered lepton, respectively. The Monte Carlo histogram is normalized and used to construct a correction factor  $C(\phi)$ :

$$C(\phi) = N_{MC}; \tag{4.4}$$

$$\int_0^{2\pi} C(\phi) d\phi = 1.$$

The data are similarly normalized to unity (such that the statistical error bars are properly transformed as well) and a corrected distribution is formed:

$$\frac{dN'(\phi)}{d\phi} = \frac{1}{C(\phi)} \frac{dN_{data}(\phi)}{d\phi}. \tag{4.5}$$

$N'(\phi)$  is then normalized to one and fit to the function

$$\frac{1}{N'} \frac{dN'}{d\phi} = 1 + A \cos \phi + B \cos 2\phi + C \sin \phi. \tag{4.6}$$

The results for the raw data are shown in Table 4.2, where they are separated for each year. The statistical quality is identified with the  $P_{\chi^2}$  from the fit. The number of bins used for the analysis is also indicated (indicating the excluded bins near  $\phi = 0, 2\pi$  where the factor  $f < 0.25$ ); this is not equivalent to the number of degrees of freedom, as this is a four-parameter fit.

Kinematics	$\langle \cos \phi \rangle$	$\langle \cos 2\phi \rangle$	$\langle \sin \phi \rangle$	$P_{\chi^2}$	$N$
$\pi : 1996$					
$\langle p_T \rangle = 0.350 \text{ GeV}$	$-0.057 \pm 0.018$	$0.114 \pm 0.015$	$-0.017 \pm 0.013$	0.044	12
$\langle p_T \rangle = 0.448 \text{ GeV}$	$-0.044 \pm 0.019$	$0.090 \pm 0.016$	$0.004 \pm 0.014$	0.115	12
$\langle p_T \rangle = 0.588 \text{ GeV}$	$-0.108 \pm 0.017$	$0.068 \pm 0.015$	$-0.018 \pm 0.012$	0.134	14
$\langle p_T \rangle = 0.848 \text{ GeV}$	$-0.099 \pm 0.025$	$-0.005 \pm 0.022$	$0.032 \pm 0.017$	0.015	14
$\langle Q^2 \rangle = 1.184 \text{ GeV}^2$	$-0.018 \pm 0.017$	$0.087 \pm 0.015$	$0.005 \pm 0.013$	0.177	12
$\langle Q^2 \rangle = 1.541 \text{ GeV}^2$	$-0.045 \pm 0.022$	$0.052 \pm 0.020$	$-0.003 \pm 0.017$	0.051	14
$\langle Q^2 \rangle = 2.081 \text{ GeV}^2$	$-0.104 \pm 0.017$	$0.057 \pm 0.015$	$-0.018 \pm 0.012$	0.021	14
$\langle Q^2 \rangle = 3.415 \text{ GeV}^2$	$-0.067 \pm 0.022$	$0.046 \pm 0.016$	$-0.010 \pm 0.014$	0.299	12
$\langle z \rangle = 0.318$	$0.000 \pm 0.021$	$0.009 \pm 0.019$	$0.004 \pm 0.016$	0.923	12
$\langle z \rangle = 0.398$	$-0.004 \pm 0.017$	$0.037 \pm 0.015$	$0.025 \pm 0.013$	0.508	14
$\langle z \rangle = 0.498$	$-0.052 \pm 0.020$	$0.094 \pm 0.017$	$-0.014 \pm 0.014$	0.096	14
$\langle z \rangle = 0.691$	$-0.098 \pm 0.019$	$0.129 \pm 0.014$	$-0.024 \pm 0.012$	0.537	12
$\langle x_F \rangle = 0.286$	$-0.013 \pm 0.019$	$0.002 \pm 0.018$	$-0.005 \pm 0.015$	0.924	14
$\langle x_F \rangle = 0.359$	$0.005 \pm 0.019$	$0.028 \pm 0.017$	$0.043 \pm 0.015$	0.061	12
$\langle x_F \rangle = 0.456$	$-0.063 \pm 0.018$	$0.088 \pm 0.016$	$-0.010 \pm 0.013$	0.131	14
$\langle x_F \rangle = 0.651$	$-0.103 \pm 0.020$	$0.135 \pm 0.015$	$-0.027 \pm 0.013$	0.764	12
$\pi : 1997$					
$\langle p_T \rangle = 0.350 \text{ GeV}$	$-0.047 \pm 0.015$	$0.121 \pm 0.013$	$0.014 \pm 0.011$	0.039	12
$\langle p_T \rangle = 0.448 \text{ GeV}$	$-0.062 \pm 0.017$	$0.112 \pm 0.014$	$-0.003 \pm 0.012$	0.283	12
$\langle p_T \rangle = 0.588 \text{ GeV}$	$-0.111 \pm 0.015$	$0.067 \pm 0.013$	$0.015 \pm 0.011$	0.250	14
$\langle p_T \rangle = 0.848 \text{ GeV}$	$-0.124 \pm 0.022$	$-0.005 \pm 0.019$	$-0.003 \pm 0.015$	0.124	14
$\langle Q^2 \rangle = 1.184 \text{ GeV}^2$	$-0.026 \pm 0.015$	$0.111 \pm 0.013$	$0.002 \pm 0.012$	0.661	12
$\langle Q^2 \rangle = 1.541 \text{ GeV}^2$	$-0.065 \pm 0.020$	$0.086 \pm 0.018$	$-0.002 \pm 0.015$	0.061	14
$\langle Q^2 \rangle = 2.081 \text{ GeV}^2$	$-0.099 \pm 0.015$	$0.038 \pm 0.013$	$0.009 \pm 0.011$	0.026	14
$\langle Q^2 \rangle = 3.415 \text{ GeV}^2$	$-0.071 \pm 0.019$	$0.051 \pm 0.014$	$0.001 \pm 0.012$	0.116	12
$\langle z \rangle = 0.318$	$0.004 \pm 0.018$	$0.013 \pm 0.017$	$0.013 \pm 0.014$	0.670	12
$\langle z \rangle = 0.398$	$-0.044 \pm 0.015$	$0.054 \pm 0.013$	$0.014 \pm 0.011$	0.172	14
$\langle z \rangle = 0.498$	$-0.063 \pm 0.018$	$0.088 \pm 0.015$	$0.017 \pm 0.013$	0.856	14
$\langle z \rangle = 0.691$	$-0.116 \pm 0.017$	$0.133 \pm 0.013$	$-0.009 \pm 0.011$	0.166	12
$\langle x_F \rangle = 0.286$	$-0.026 \pm 0.017$	$-0.005 \pm 0.016$	$0.009 \pm 0.013$	0.737	14
$\langle x_F \rangle = 0.359$	$-0.013 \pm 0.017$	$0.063 \pm 0.015$	$0.014 \pm 0.013$	0.175	12
$\langle x_F \rangle = 0.456$	$-0.057 \pm 0.016$	$0.084 \pm 0.014$	$0.012 \pm 0.011$	0.419	14
$\langle x_F \rangle = 0.651$	$-0.118 \pm 0.018$	$0.143 \pm 0.013$	$-0.003 \pm 0.011$	0.106	12

Table 4.2: Extracted moments of the  $\phi$  distributions for the  $(e, e'\pi)$  for each year, with the associated confidence level and number of analyzed bins  $N$ .

The numbers in Table 4.2 were corrected to translate the lepton polarization into photon polarization via the following equations from Section 1.3.1:

$$\begin{aligned}
 f_1(y) &= (2-y)\sqrt{1-y}/[1+(1-y)^2], \\
 f_2(y) &= (1-y)/[1+(1-y)^2], \\
 f_3(y) &= y\sqrt{1-y}/[1+(1-y)^2], \\
 D(y) &= y(2-y)/[1+(1-y)^2],
 \end{aligned}
 \tag{4.7}$$

where  $D(y)$  is included for the polarization measurements.

These functions were averaged in each kinematic bin and are tabulated in Table 4.3. In particular, the functions  $f_i(y)$  vary significantly over the accepted range of  $x_F$  and  $z$ . Photon polarization factors were applied independently for each year's data, although the differences between the factors between the years are negligible. These kinematically corrected moments are shown in Table 4.4.

Kinematics	$y$	$f_1(y)$	$f_2(y)$	$f_3(y)$	$D(y)$
$\langle p_T \rangle = 0.350$ GeV	0.556	0.780	0.357	0.293	0.660
$\langle p_T \rangle = 0.448$ GeV	0.576	0.761	0.345	0.300	0.683
$\langle p_T \rangle = 0.588$ GeV	0.596	0.742	0.333	0.306	0.707
$\langle p_T \rangle = 0.848$ GeV	0.610	0.729	0.324	0.310	0.722
$\langle Q^2 \rangle = 1.184$ GeV <sup>2</sup>	0.594	0.743	0.334	0.305	0.704
$\langle Q^2 \rangle = 1.541$ GeV <sup>2</sup>	0.584	0.751	0.339	0.301	0.692
$\langle Q^2 \rangle = 2.081$ GeV <sup>2</sup>	0.579	0.758	0.343	0.301	0.688
$\langle Q^2 \rangle = 3.415$ GeV <sup>2</sup>	0.566	0.774	0.353	0.299	0.674
$\langle z \rangle = 0.318$	0.697	0.647	0.272	0.339	0.824
$\langle z \rangle = 0.398$	0.633	0.714	0.315	0.322	0.752
$\langle z \rangle = 0.498$	0.580	0.761	0.344	0.303	0.690
$\langle z \rangle = 0.691$	0.491	0.834	0.391	0.268	0.583
$\langle x_F \rangle = 0.286$	0.683	0.662	0.282	0.336	0.808
$\langle x_F \rangle = 0.359$	0.629	0.716	0.316	0.321	0.747
$\langle x_F \rangle = 0.456$	0.579	0.760	0.344	0.302	0.688
$\langle x_F \rangle = 0.651$	0.493	0.833	0.391	0.268	0.585

Table 4.3: Photon polarization factors in  $(e, e'\pi)$  events.

Kinematics	$\langle \cos \phi \rangle / \langle f_1(y) \rangle$	$\langle \cos 2\phi \rangle / \langle f_2(y) \rangle$	$\langle \sin \phi \rangle / P_b \langle f_3(y) \rangle$
$\pi : 1996$			
$\langle p_T \rangle = 0.350 \text{ GeV}$	$-0.073 \pm 0.023$	$0.320 \pm 0.042$	$-0.105 \pm 0.081$
$\langle p_T \rangle = 0.448 \text{ GeV}$	$-0.058 \pm 0.025$	$0.261 \pm 0.046$	$0.024 \pm 0.085$
$\langle p_T \rangle = 0.588 \text{ GeV}$	$-0.146 \pm 0.023$	$0.205 \pm 0.045$	$-0.107 \pm 0.071$
$\langle p_T \rangle = 0.848 \text{ GeV}$	$-0.136 \pm 0.034$	$-0.015 \pm 0.068$	$0.188 \pm 0.100$
$\langle Q^2 \rangle = 1.184 \text{ GeV}^2$	$-0.024 \pm 0.023$	$0.261 \pm 0.045$	$0.030 \pm 0.078$
$\langle Q^2 \rangle = 1.541 \text{ GeV}^2$	$-0.060 \pm 0.029$	$0.154 \pm 0.059$	$-0.018 \pm 0.103$
$\langle Q^2 \rangle = 2.081 \text{ GeV}^2$	$-0.137 \pm 0.022$	$0.166 \pm 0.044$	$-0.109 \pm 0.072$
$\langle Q^2 \rangle = 3.415 \text{ GeV}^2$	$-0.087 \pm 0.028$	$0.130 \pm 0.045$	$-0.061 \pm 0.085$
$\langle z \rangle = 0.318$	$0.000 \pm 0.032$	$0.033 \pm 0.070$	$0.021 \pm 0.086$
$\langle z \rangle = 0.398$	$-0.006 \pm 0.024$	$0.118 \pm 0.048$	$0.141 \pm 0.073$
$\langle z \rangle = 0.498$	$-0.068 \pm 0.026$	$0.273 \pm 0.049$	$-0.084 \pm 0.084$
$\langle z \rangle = 0.691$	$-0.118 \pm 0.023$	$0.330 \pm 0.036$	$-0.163 \pm 0.081$
$\langle x_F \rangle = 0.286$	$-0.020 \pm 0.029$	$0.007 \pm 0.064$	$-0.027 \pm 0.081$
$\langle x_F \rangle = 0.359$	$0.007 \pm 0.027$	$0.089 \pm 0.054$	$0.244 \pm 0.085$
$\langle x_F \rangle = 0.456$	$-0.083 \pm 0.024$	$0.256 \pm 0.047$	$-0.060 \pm 0.078$
$\langle x_F \rangle = 0.651$	$-0.124 \pm 0.024$	$0.346 \pm 0.038$	$-0.183 \pm 0.088$
$\pi : 1997$			
$\langle p_T \rangle = 0.350 \text{ GeV}$	$-0.060 \pm 0.019$	$0.339 \pm 0.036$	$-0.087 \pm -0.068$
$\langle p_T \rangle = 0.448 \text{ GeV}$	$-0.081 \pm 0.022$	$0.325 \pm 0.041$	$0.018 \pm -0.073$
$\langle p_T \rangle = 0.588 \text{ GeV}$	$-0.150 \pm 0.020$	$0.202 \pm 0.039$	$-0.089 \pm -0.065$
$\langle p_T \rangle = 0.848 \text{ GeV}$	$-0.170 \pm 0.030$	$-0.015 \pm 0.059$	$0.018 \pm -0.088$
$\langle Q^2 \rangle = 1.184 \text{ GeV}^2$	$-0.035 \pm 0.020$	$0.333 \pm 0.039$	$-0.012 \pm -0.072$
$\langle Q^2 \rangle = 1.541 \text{ GeV}^2$	$-0.087 \pm 0.027$	$0.255 \pm 0.053$	$0.012 \pm -0.090$
$\langle Q^2 \rangle = 2.081 \text{ GeV}^2$	$-0.131 \pm 0.020$	$0.111 \pm 0.038$	$-0.054 \pm -0.066$
$\langle Q^2 \rangle = 3.415 \text{ GeV}^2$	$-0.092 \pm 0.025$	$0.145 \pm 0.040$	$-0.006 \pm -0.073$
$\langle z \rangle = 0.318$	$0.006 \pm 0.028$	$0.048 \pm 0.062$	$-0.070 \pm -0.075$
$\langle z \rangle = 0.398$	$-0.062 \pm 0.021$	$0.172 \pm 0.041$	$-0.079 \pm -0.062$
$\langle z \rangle = 0.498$	$-0.083 \pm 0.024$	$0.256 \pm 0.044$	$-0.102 \pm -0.078$
$\langle z \rangle = 0.691$	$-0.139 \pm 0.020$	$0.340 \pm 0.033$	$0.061 \pm -0.075$
$\langle x_F \rangle = 0.286$	$-0.039 \pm 0.026$	$-0.018 \pm 0.057$	$-0.049 \pm -0.070$
$\langle x_F \rangle = 0.359$	$-0.018 \pm 0.024$	$0.199 \pm 0.047$	$-0.079 \pm -0.074$
$\langle x_F \rangle = 0.456$	$-0.075 \pm 0.021$	$0.244 \pm 0.041$	$-0.072 \pm -0.066$
$\langle x_F \rangle = 0.651$	$-0.142 \pm 0.022$	$0.366 \pm 0.033$	$0.020 \pm -0.075$

Table 4.4: Corrected moments in  $\phi$  in  $(e, e'\pi)$  for each year.

## 4.2.4 Systematic Studies and Uncertainties.

### Acceptance Correction.

The algorithm used to extract the moments in  $\phi$  is complex and several questions must be answered in order to evaluate the associated systematic uncertainties:

1. What is the contribution from using a finite number of Monte Carlo events?

The number of  $(e, e'\pi)$  events generated was equal to the statistics in the data set. The weighted fits already took these statistics into account. Thus, this is a contribution to the statistical, not the systematic, error bar.

2. How does the detector affect the “real”  $\phi$  distribution?

Figure 4.7 shows the distribution in  $\delta\phi$  for  $(e, e'\pi)$  events that were generated in the Monte Carlo and then reconstructed; i.e.,  $\delta\phi = \phi^{rec} - \phi^{gen}$ . The mean  $\delta\phi$  is consistent with zero within  $1\sigma$ , indicating that the detector does not shift the  $\phi$  value. Shifting the value asymmetrically would clearly affect the evaluation of the moments. Thus, there is no systematic bias associated with the detector’s measurements of  $\phi$ .

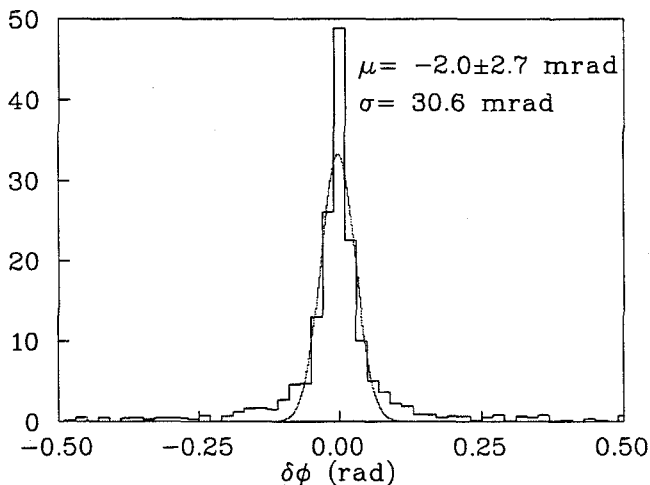


Figure 4.7: Difference in the azimuthal angle  $\phi$  for Monte Carlo  $(e, e'\pi)$  events, before and after reconstruction.



3. Does the 4% cutoff on the yields, as described in Section 4.2.2, improve the agreement between the Monte Carlo and the data?

To study this effect, the data and Monte Carlo were compared, as in Figure 3.6; however, the range in  $\phi$  was restricted to  $1 < \phi < (2\pi) - 1$ , as this represented an average range of  $\phi$  values allowed in all kinematic ranges. The results are

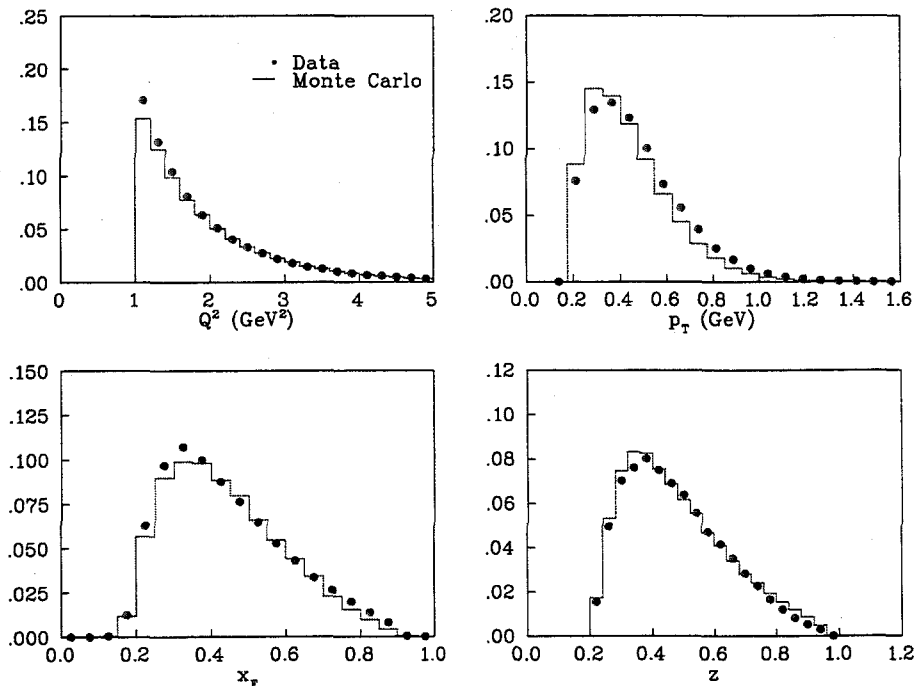


Figure 4.8: Events are restricted to the range  $1 < \phi < (2\pi) - 1$  in this comparison of data and Monte Carlo. In  $p_T$  and  $x_F$ , better agreement is seen here compared to Figure 3.6, where all values of  $\phi$  are allowed; thus, the acceptance is not well modeled at the edges in  $\phi$ .

shown in Figure 4.8. Since the data/Monte Carlo agreement has improved, particularly in the  $p_T$  and  $x_F$  distributions, the cut at the edges in  $\phi$  has removed regions where the acceptance is not well modeled. The remaining discrepancy at  $Q^2 \sim 1 \text{ GeV}^2$  indicates that the Monte Carlo generator does not produce events appropriately at low  $Q^2$ . This could most certainly be correlated with the remaining discrepancies in the hadron kinematic quantities.

This study indicates that since the restrictions in  $\phi$  do improve agreement between the Monte Carlo and the data in kinematic distributions, they improve

the reliability of the Monte Carlo in describing the detector acceptance. No systematic uncertainty is assigned for this effect.

4. Are enough bins near the septum plate removed?

This was evaluated by reducing the number of bins used in the analysis. In a kinematic range with  $n$  bins in  $\phi$ , the analysis was repeated with  $n - 4$  bins. This is illustrated in Figure 4.9 for the highest  $Q^2$  bin.

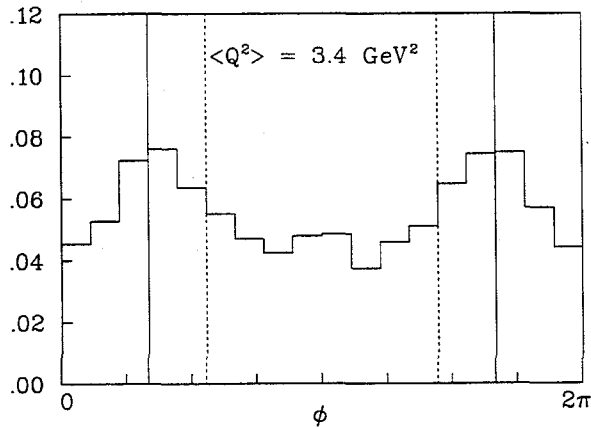


Figure 4.9:  $\phi$  distribution in accepted Monte Carlo events. Solid lines indicate the cut-off bins in  $\phi$ , as described in Section 4.2.2; dashed lines indicate the narrower range used to determine the sensitivity to the bins nearer the edge in  $\phi$ .

The quantity

$$\delta\langle W \rangle = \langle W \rangle_{all\ data} - \langle W \rangle_{narrower\ range} \quad (4.8)$$

has been tabulated independently for each year for  $\langle W \rangle = \langle \cos \phi \rangle$ ,  $\langle \cos 2\phi \rangle$ , and  $\langle \sin \phi \rangle$  in Table 4.5. The values for  $\delta\langle W \rangle$  for each year were compared and the larger one was used as the absolute systematic uncertainty associated with binning.

Kinematic bin	$\delta \langle \cos \phi \rangle$		$\delta \langle \cos 2\phi \rangle$		$\delta \langle \sin \phi \rangle$	
	1996	1997	1996	1997	1996	1997
$\langle p_T \rangle = 0.350 \text{ GeV}$	-0.001	-0.001	0.023	0.013	-0.021	0.004
$\langle p_T \rangle = 0.448 \text{ GeV}$	-0.010	0.004	-0.004	0.027	0.011	0.009
$\langle p_T \rangle = 0.588 \text{ GeV}$	-0.023	-0.020	-0.006	0.006	-0.005	0.008
$\langle p_T \rangle = 0.848 \text{ GeV}$	-0.036	-0.037	-0.003	-0.008	-0.002	-0.023
$\langle Q^2 \rangle = 1.184 \text{ GeV}^2$	-0.010	0.000	-0.017	0.001	-0.006	-0.012
$\langle Q^2 \rangle = 1.541 \text{ GeV}^2$	-0.015	-0.012	-0.003	0.002	-0.008	0.006
$\langle Q^2 \rangle = 2.081 \text{ GeV}^2$	-0.024	-0.023	-0.008	0.000	-0.004	-0.006
$\langle Q^2 \rangle = 3.415 \text{ GeV}^2$	-0.002	0.004	0.016	0.025	0.004	0.042
$\langle z \rangle = 0.318$	-0.007	-0.004	-0.013	-0.010	-0.008	-0.006
$\langle z \rangle = 0.398$	0.003	-0.011	0.004	-0.005	-0.013	0.012
$\langle z \rangle = 0.498$	-0.003	-0.009	0.008	-0.003	-0.015	0.001
$\langle z \rangle = 0.691$	0.002	-0.001	0.012	0.027	0.008	0.003
$\langle x_F \rangle = 0.286$	-0.005	-0.011	0.002	-0.002	0.001	0.003
$\langle x_F \rangle = 0.359$	-0.010	0.001	-0.027	-0.002	-0.018	-0.003
$\langle x_F \rangle = 0.456$	-0.008	-0.008	0.006	-0.002	-0.011	0.004
$\langle x_F \rangle = 0.651$	0.001	-0.002	0.017	0.027	0.004	0.006

Table 4.5: The differences in extracted moments if a narrower range in  $\phi$  is used.

### Radiative Corrections.

The radiative corrections may be evaluated for two processes: *internal* and *external* radiative processes. Internal radiative corrections refer to vertex corrections, loop diagrams, and other QED corrections to the single-photon exchange diagram, whereas external radiative corrections describe losses in the detector.

- Internal radiation.

At HERMES energies, weak corrections and multi-photon exchange may be neglected. The remaining loop and vertex corrections were recently calculated by Akushevich *et al.* in Reference [71] and are shown in Figure 4.10. These calculations suggest relative corrections to  $\langle \cos \phi \rangle$  of 10% at low  $z$  and only 1% at high  $z$ , largely independent of the Bjorken fraction  $x$  (defined in Table 1.1). These values are model-dependent and an iterative procedure would be ideal, where an input model is radiated until good agreement is reached with the data. Such a model was not available at the time of the completion of this work.

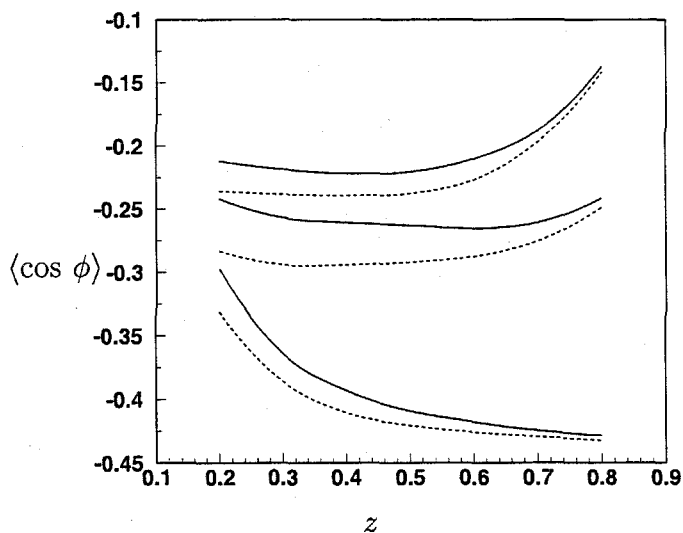


Figure 4.10: The radiative corrections to  $\langle \cos \phi \rangle$ , evaluated at HERMES kinematics as a function of  $z$ . Taken from Reference [71]. Dashed (solid) lines are Born (observed) moments. Curves from top to bottom correspond to Bjorken  $x=0.7, 0.45, 0.05$ .

Instead, the data were directly corrected in  $z$  as shown in Figure 4.10. Because  $z$  and  $x_F$  are strongly correlated, as shown previously in Figure 3.7, the same corrections were applied in  $x_F$ ; however, since  $p_T$  and  $z$  are not strongly correlated (shown in Figure 3.8), an average value of 5% was applied to each  $p_T$  bin. Similarly, as the corrections vary slowly as a function of  $x$  (relative to how fast they vary as a function of  $z$ ), it was assumed that they did not vary significantly as a function of  $Q^2$  either and an average value of 5% was applied to each  $Q^2$  bin.

Rather than correcting each event, the final results were corrected. This was done in order to facilitate studies in which a model could be corrected iteratively. In principle, each event could be corrected; however, the literature suggests that current estimates of radiative corrections to these processes are highly model-dependent and not exact at this time. Consequently, an average value was applied to the results and an associated 100% contribution was assigned to the systematic uncertainty (i.e., systematic error = size of radiative correction).

- External radiation.

In principle, external radiative corrections result from two sources. One contribution is bremsstrahlung in the target gas in addition to the DIS interaction (either before or after it). Because the target represents about  $10^{-9}$  radiation lengths at the typical density, this correction is negligible. In addition, the scattered positron may experience energy loss in the material via bremsstrahlung. It is precisely this quantity that the Monte Carlo models quite well, as shown in Figure 4.1. Because reconstructed Monte Carlo events were used to calculate the acceptance correction, no additional correction was applied to correct for external radiative effects. Each component's contribution to the detector's total number of radiation lengths is described in Chapter 2.

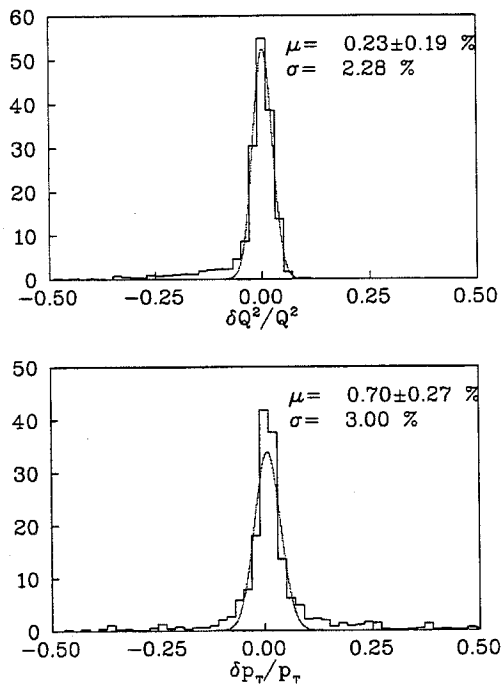


Figure 4.11: Fractional differences in kinematics for Monte Carlo  $(e, e'\pi)$  events, before and after reconstruction.

An example of the importance of external radiation may be seen in Figure 4.11, where the relative differences in  $Q^2$  and  $p_T$  in  $(e, e'\pi)$  events is shown for Monte Carlo events before and after the reconstruction;  $\delta v \equiv v^{rec} - v^{gen}$  for each variable  $v$ . The distribution in  $\delta Q^2$  shows an asymmetric radiative tail; otherwise,

these distributions are rather featureless. The means are all unaffected at the  $2\sigma$  level and the widths of these distributions indicate broadening of  $\sim 3\%$ .

These distributions are also affected by finite efficiencies in the hardware as well as in the software; however, these factors should broaden the distributions and do not contribute to the radiative tails. These distributions do not contribute independent systematic uncertainties as these effects are included in the evaluation of the uncertainty of the acceptance correction.

### Contamination.

In principle, both the leptons and the hadron samples may be contaminated. A detailed study of the particle identification scheme was performed by Menden [68] and the results will be summarized here.

- Contamination in the positron sample.

The positron sample may be contaminated in two fashions: First, hadrons may be misidentified as leptons. Secondly, positrons may originate in charge-symmetric processes (such as  $\gamma$  from  $\pi^0$  decays) that are not deep-inelastic interactions but satisfy the kinematic requirements. Detailed studies have shown that these contamination factors vary with kinematics, as expected. Assuming a particle identification efficiency of 95%, the contamination  $N_h/N_e$  is estimated to be less than 0.3% in the worst case and as low as 0.1% on average.

- Contamination in the hadron sample.

The hadrons may be contaminated by misidentified leptons. In the worst case, this factor is less than 0.4%. The hadron efficiency is 98.5% on average, and at its lowest it is 97%.

These two factors are presumed to have no azimuthal dependence; however, a conservative estimate of 0.5% was assigned for this contribution.

**Summary.**

A summary of the maximum estimates for the principal sources of systematic uncertainties is shown in Table 4.6.

Source	Uncertainty	Contribution
Binning in $\phi$	$\sim 3\%$	absolute
Radiative corrections ( $\langle \cos \phi \rangle$ only)	10%	relative
Contaminations	0.5%	absolute

Table 4.6: Systematic uncertainties in azimuthal moments in  $(e, e'\pi)$ .

### 4.2.5 Results for Pion Azimuthal Distributions.

The statistical averages are tabulated in Table 4.2.5.

Kinematics	$\langle \cos \phi \rangle / \langle f_1(y) \rangle$	$\langle \cos 2\phi \rangle / \langle f_2(y) \rangle$
$\langle p_T \rangle = 0.350$ GeV	$-0.062 \pm 0.015 \pm 0.006$	$0.331 \pm 0.028 \pm 0.024$
$\langle p_T \rangle = 0.448$ GeV	$-0.067 \pm 0.017 \pm 0.012$	$0.297 \pm 0.031 \pm 0.027$
$\langle p_T \rangle = 0.588$ GeV	$-0.141 \pm 0.015 \pm 0.025$	$0.203 \pm 0.030 \pm 0.008$
$\langle p_T \rangle = 0.848$ GeV	$-0.148 \pm 0.023 \pm 0.038$	$-0.015 \pm 0.044 \pm 0.009$
$\langle Q^2 \rangle = 1.184$ GeV <sup>2</sup>	$-0.029 \pm 0.015 \pm 0.011$	$0.302 \pm 0.029 \pm 0.018$
$\langle Q^2 \rangle = 1.541$ GeV <sup>2</sup>	$-0.071 \pm 0.020 \pm 0.016$	$0.210 \pm 0.040 \pm 0.006$
$\langle Q^2 \rangle = 2.081$ GeV <sup>2</sup>	$-0.127 \pm 0.015 \pm 0.025$	$0.135 \pm 0.029 \pm 0.009$
$\langle Q^2 \rangle = 3.415$ GeV <sup>2</sup>	$-0.085 \pm 0.019 \pm 0.008$	$0.139 \pm 0.030 \pm 0.025$
$\langle z \rangle = 0.318$	$0.003 \pm 0.021 \pm 0.009$	$0.041 \pm 0.046 \pm 0.014$
$\langle z \rangle = 0.398$	$-0.033 \pm 0.016 \pm 0.013$	$0.149 \pm 0.031 \pm 0.007$
$\langle z \rangle = 0.498$	$-0.073 \pm 0.018 \pm 0.011$	$0.263 \pm 0.033 \pm 0.009$
$\langle z \rangle = 0.691$	$-0.128 \pm 0.015 \pm 0.006$	$0.335 \pm 0.024 \pm 0.027$
$\langle x_F \rangle = 0.286$	$-0.027 \pm 0.019 \pm 0.012$	$-0.007 \pm 0.042 \pm 0.005$
$\langle x_F \rangle = 0.359$	$-0.006 \pm 0.018 \pm 0.011$	$0.151 \pm 0.036 \pm 0.027$
$\langle x_F \rangle = 0.456$	$-0.075 \pm 0.016 \pm 0.010$	$0.249 \pm 0.031 \pm 0.008$
$\langle x_F \rangle = 0.651$	$-0.132 \pm 0.016 \pm 0.006$	$0.358 \pm 0.025 \pm 0.027$

Table 4.7:  $\langle \cos \phi \rangle$  and  $\langle \cos 2\phi \rangle$  moments for the  $(e, e'\pi)$  events.



The results for the measured  $\langle \cos \phi \rangle$  moments are shown in Figure 4.12 as a function of  $Q^2$ . The HERMES data seem to smoothly connect with the higher  $Q^2$  EMC data and are also consistent with the E665 measurements of  $\langle \cos \phi \rangle = -0.004 \pm 0.020$  for  $\Pi < 1$  GeV and  $\langle \cos \phi \rangle = -0.070 \pm 0.023$  for  $\Pi > 1$  GeV, where  $\Pi$  is a generalized extension of the transverse momentum;  $\Pi \simeq \sum_{partons} |p_T|$  [29].

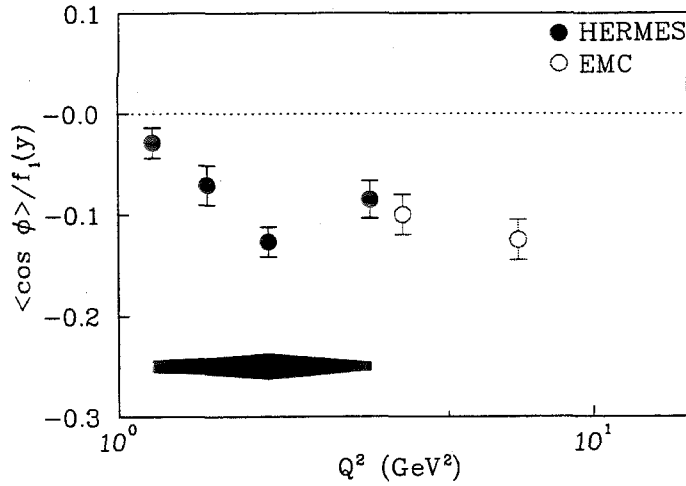


Figure 4.12: The  $Q^2$  variation of the  $\langle \cos \phi \rangle$  moment. The band represents the systematic uncertainty. These EMC data fall in the ranges  $60 \leq W^2 < 160$  GeV $^2$  and  $Q^2 > 2$  GeV $^2$ .

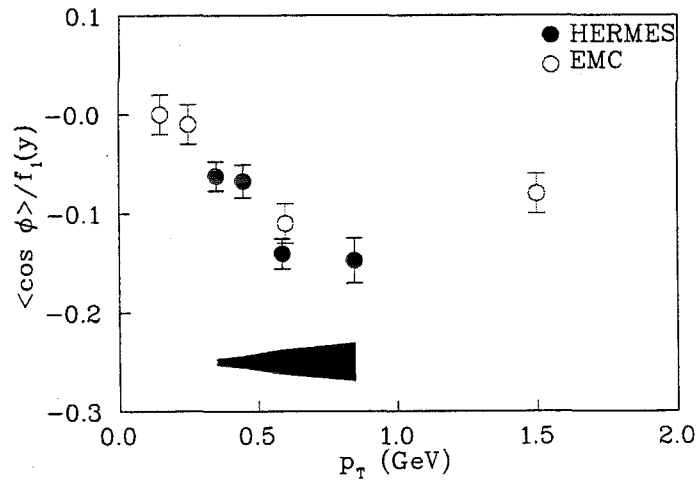


Figure 4.13:  $p_T$  dependence of  $\langle \cos \phi \rangle$  moments. The EMC data plotted here fall in the range  $160 \leq W^2 < 360$  GeV $^2$  and  $Q^2 > 10$  GeV $^2$ ; no lower  $W^2$  data were available for the  $p_T$  dependence.

Although, as Figure 4.13 indicates, the HERMES data increase with  $p_T$ , the  $Q^2$  behavior suggests that Cahn's kinematic model  $\langle \cos \phi \rangle \sim p_T/Q$  is, perhaps, incomplete. Thus, higher-twist effects may modify the asymmetries at low  $Q^2$  as parton interactions become more important.

While both measurements cover the same range in  $z$ , Figure 4.14 indicates that the enhancement at high  $z$  is very strong in the HERMES data. This effect represents a dilution of the moment by the random motion of the fragmentation process, a mechanism which is independent of  $Q^2$  and which differs from the QCD prediction [12]. In principle, different fragmentation models could be distinguished at low  $z$ ; unfortunately, the experimental restriction on low  $z$  events prevents this study.

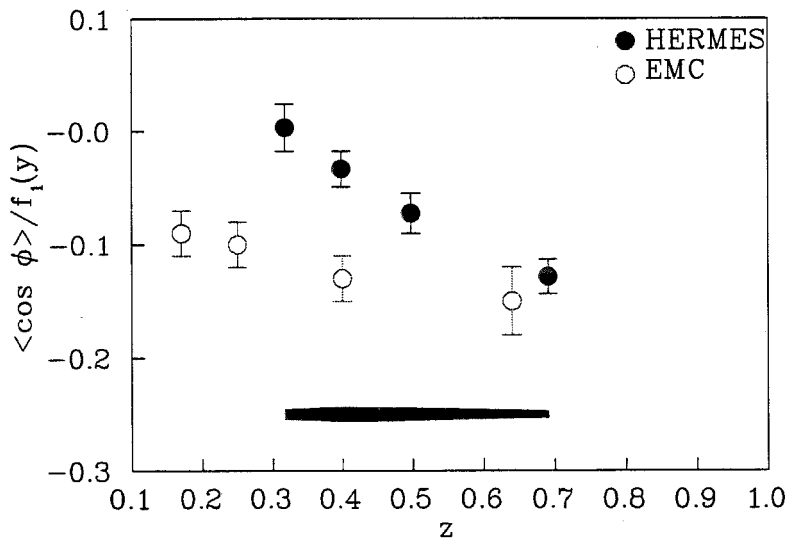


Figure 4.14:  $z$  dependence of  $\langle \cos \phi \rangle$  moments. Unlike Figure 4.13, the kinematic ranges of these EMC data are  $60 \leq W^2 < 160 \text{ GeV}^2$  and  $Q^2 > 2 \text{ GeV}^2$ .

Figure 4.15 shows the results for the extracted  $\langle \cos 2\phi \rangle$  moments. The enhancement at low  $Q^2$  is strong here, suggesting that Cahn's simple kinematic prediction of  $\langle \cos 2\phi \rangle \sim (p_T/Q)^2$  may contribute significantly; as the  $p_T$  ranges of the two experiments are roughly equivalent, the different  $Q^2$  ranges would have a greater impact. König and Kroll suggest that  $\langle \cos 2\phi \rangle \sim 0$  at low  $Q^2$ , but their calculations were performed for EMC kinematics and do not access dynamics below  $10 \text{ GeV}^2$ . Clearly it is desirable to have model calculations performed at the HERMES kinematics to facilitate a more detailed comparison with these new data. However, the variation with  $Q^2$  seems to indicate that the leading order TR-odd fragmentation functions are not important, whereas the  $1/Q^2$  higher twist processes may play a major role. Figure 4.15

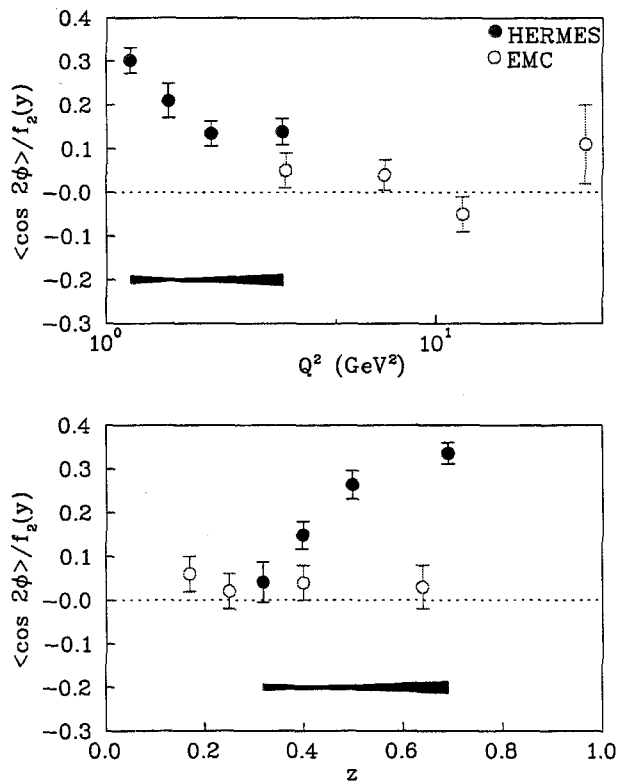


Figure 4.15: Top (bottom): Dependence of  $\langle \cos 2\phi \rangle$  moments on  $Q^2$  ( $z$ ). The band represents the systematic uncertainty.

also indicates that the variation with  $z$  is even more pronounced, suggesting again a dilution effect from the fragmentation process. This produces an average value that is higher because of the  $Q^2$  dependence, while the shape of the  $z$  dependence results

from the hadronization dilution.

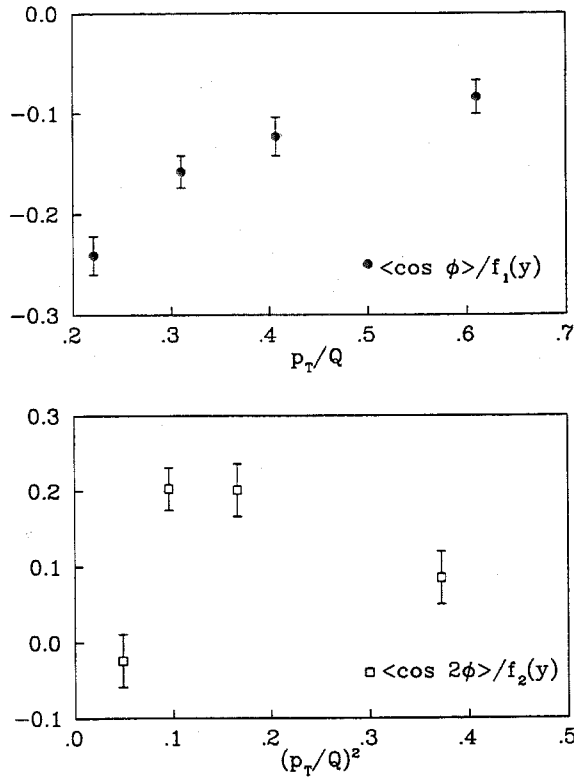


Figure 4.16: Variation of  $\langle \cos \phi \rangle$  and  $\langle \cos 2\phi \rangle$  with parton kinematic factors.

Finally, the kinematic prediction may be tested directly by considering the variation of  $\langle \cos \phi \rangle$  ( $\langle \cos 2\phi \rangle$ ) with  $p_T/Q$  ( $(p_T/Q)^2$ ), as shown in Figure 4.16. This figure indicates that these expectation values are not well described by simple parton kinematics and that such a simplistic picture may not be valid at such a low  $Q^2$  regime.

HERMES measurements of  $\langle \sin \phi \rangle$  are consistent with zero, as seen in Table 4.8.

Kinematics	$\langle \sin \phi \rangle P_b \langle f_3(y) \rangle$
$\langle p_T \rangle = 0.350 \text{ GeV}$	$-0.094 \pm 0.052 \pm 0.022$
$\langle p_T \rangle = 0.448 \text{ GeV}$	$0.021 \pm 0.055 \pm 0.012$
$\langle p_T \rangle = 0.588 \text{ GeV}$	$-0.097 \pm 0.048 \pm 0.009$
$\langle p_T \rangle = 0.848 \text{ GeV}$	$0.092 \pm 0.066 \pm 0.024$
$\langle Q^2 \rangle = 1.184 \text{ GeV}^2$	$0.007 \pm 0.053 \pm 0.013$
$\langle Q^2 \rangle = 1.541 \text{ GeV}^2$	$-0.001 \pm 0.068 \pm 0.009$
$\langle Q^2 \rangle = 2.081 \text{ GeV}^2$	$-0.079 \pm 0.049 \pm 0.008$
$\langle Q^2 \rangle = 3.415 \text{ GeV}^2$	$-0.029 \pm 0.055 \pm 0.042$
$\langle z \rangle = 0.318$	$-0.030 \pm 0.056 \pm 0.009$
$\langle z \rangle = 0.398$	$0.013 \pm 0.047 \pm 0.014$
$\langle z \rangle = 0.498$	$-0.094 \pm 0.057 \pm 0.016$
$\langle z \rangle = 0.691$	$-0.041 \pm 0.055 \pm 0.009$
$\langle x_F \rangle = 0.286$	$-0.039 \pm 0.053 \pm 0.006$
$\langle x_F \rangle = 0.359$	$0.059 \pm 0.056 \pm 0.019$
$\langle x_F \rangle = 0.456$	$-0.067 \pm 0.050 \pm 0.012$
$\langle x_F \rangle = 0.651$	$-0.064 \pm 0.057 \pm 0.008$

Table 4.8: Results for  $\langle \sin \phi \rangle$  for the  $(e, e'\pi)$  events.

### 4.2.6 Charge-separated Results.

Instead of simply combining the two charge states, it is possible to identify and separate  $\pi^+$  and  $\pi^-$ . This analysis comprises 101k  $\pi^+$  events and 74k  $\pi^-$  events. This  $\pi^+/\pi^-$  ratio of 0.73 is consistent with the value of 0.72 extracted in an independent analysis [31], although the numbers of accepted events are lower because of the exclusion of events in regions where the systematic uncertainties associated with the acceptance correction are large.

Figure 4.17 indicates that the two states give distributions and there are no large charge-dependent effects. On the other hand, the  $\pi^-$  events show a systematically larger moment in  $\langle \cos 2\phi \rangle$  compared to the  $\pi^+$ . This may indicate a charge-dependent enhancement in addition to the  $(p_T/Q)^2$  dependence expected in kinematic models that may point to different DF's or FF's for  $\pi^+/\pi^-$  production.

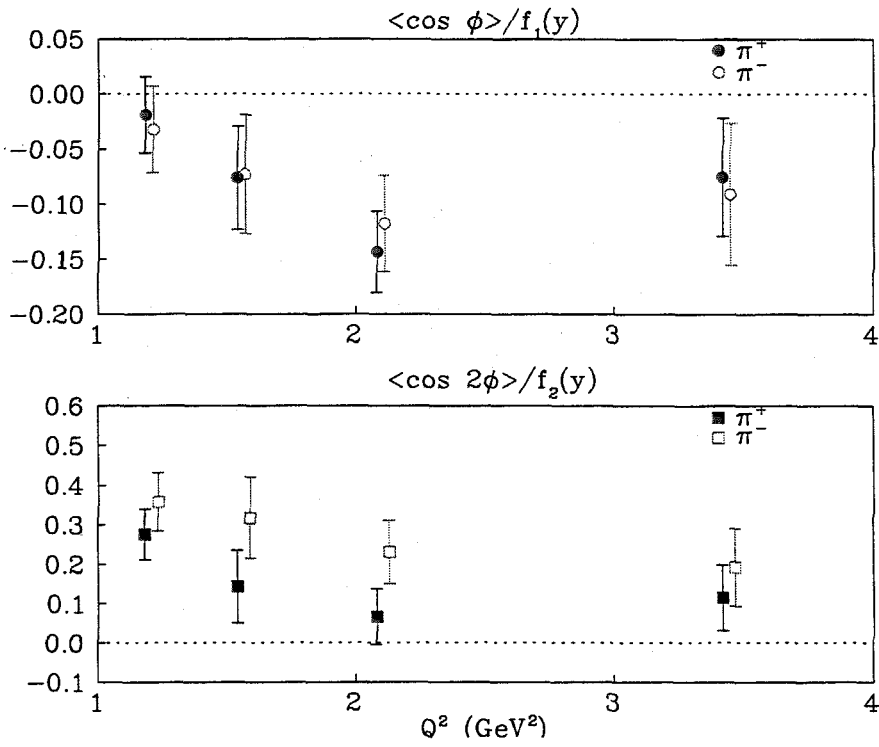


Figure 4.17:  $Q^2$  dependence of moments for  $\pi^+$  and  $\pi^-$ . Top (bottom):  $\langle \cos \phi \rangle$  ( $\langle \cos 2\phi \rangle$ ) moments.

The results are tabulated in Table 4.9.

Kinematics	$\langle \cos \phi \rangle / \langle f_1(y) \rangle$	$\langle \cos 2\phi \rangle / \langle f_2(y) \rangle$
$\pi^+$		
$\langle p_T \rangle = 0.350 \text{ GeV}$	$-0.065 \pm 0.035 \pm 0.006$	$0.312 \pm 0.061 \pm 0.024$
$\langle p_T \rangle = 0.448 \text{ GeV}$	$-0.058 \pm 0.041 \pm 0.012$	$0.255 \pm 0.071 \pm 0.027$
$\langle p_T \rangle = 0.588 \text{ GeV}$	$-0.153 \pm 0.038 \pm 0.025$	$0.127 \pm 0.073 \pm 0.008$
$\langle p_T \rangle = 0.848 \text{ GeV}$	$-0.148 \pm 0.060 \pm 0.038$	$-0.027 \pm 0.119 \pm 0.009$
$\langle Q^2 \rangle = 1.184 \text{ GeV}^2$	$-0.019 \pm 0.035 \pm 0.011$	$0.275 \pm 0.064 \pm 0.018$
$\langle Q^2 \rangle = 1.541 \text{ GeV}^2$	$-0.076 \pm 0.047 \pm 0.016$	$0.143 \pm 0.092 \pm 0.006$
$\langle Q^2 \rangle = 2.081 \text{ GeV}^2$	$-0.143 \pm 0.037 \pm 0.026$	$0.066 \pm 0.071 \pm 0.009$
$\langle Q^2 \rangle = 3.415 \text{ GeV}^2$	$-0.075 \pm 0.054 \pm 0.007$	$0.115 \pm 0.084 \pm 0.025$
$\langle z \rangle = 0.318$	$-0.051 \pm 0.049 \pm 0.010$	$-0.090 \pm 0.116 \pm 0.014$
$\langle z \rangle = 0.398$	$-0.023 \pm 0.040 \pm 0.012$	$0.090 \pm 0.082 \pm 0.007$
$\langle z \rangle = 0.498$	$-0.076 \pm 0.043 \pm 0.011$	$0.217 \pm 0.079 \pm 0.009$
$\langle z \rangle = 0.691$	$-0.120 \pm 0.035 \pm 0.006$	$0.291 \pm 0.052 \pm 0.027$
$\langle x_F \rangle = 0.286$	$-0.053 \pm 0.045 \pm 0.013$	$-0.104 \pm 0.106 \pm 0.005$
$\langle x_F \rangle = 0.359$	$0.000 \pm 0.046 \pm 0.011$	$0.091 \pm 0.090 \pm 0.027$
$\langle x_F \rangle = 0.456$	$-0.068 \pm 0.038 \pm 0.010$	$0.200 \pm 0.071 \pm 0.008$
$\langle x_F \rangle = 0.651$	$-0.128 \pm 0.036 \pm 0.006$	$0.313 \pm 0.054 \pm 0.027$
$\pi^-$		
$\langle p_T \rangle = 0.350 \text{ GeV}$	$-0.059 \pm 0.041 \pm 0.006$	$0.371 \pm 0.071 \pm 0.024$
$\langle p_T \rangle = 0.448 \text{ GeV}$	$-0.071 \pm 0.047 \pm 0.012$	$0.383 \pm 0.083 \pm 0.027$
$\langle p_T \rangle = 0.588 \text{ GeV}$	$-0.126 \pm 0.044 \pm 0.024$	$0.314 \pm 0.080 \pm 0.008$
$\langle p_T \rangle = 0.848 \text{ GeV}$	$-0.132 \pm 0.068 \pm 0.038$	$0.037 \pm 0.133 \pm 0.009$
$\langle Q^2 \rangle = 1.184 \text{ GeV}^2$	$-0.032 \pm 0.039 \pm 0.011$	$0.358 \pm 0.073 \pm 0.018$
$\langle Q^2 \rangle = 1.541 \text{ GeV}^2$	$-0.073 \pm 0.054 \pm 0.016$	$0.317 \pm 0.102 \pm 0.006$
$\langle Q^2 \rangle = 2.081 \text{ GeV}^2$	$-0.118 \pm 0.044 \pm 0.025$	$0.230 \pm 0.080 \pm 0.009$
$\langle Q^2 \rangle = 3.415 \text{ GeV}^2$	$-0.091 \pm 0.064 \pm 0.008$	$0.192 \pm 0.099 \pm 0.025$
$\langle z \rangle = 0.318$	$0.029 \pm 0.055 \pm 0.009$	$0.143 \pm 0.127 \pm 0.014$
$\langle z \rangle = 0.398$	$-0.042 \pm 0.045 \pm 0.013$	$0.241 \pm 0.088 \pm 0.007$
$\langle z \rangle = 0.498$	$-0.065 \pm 0.049 \pm 0.011$	$0.337 \pm 0.090 \pm 0.009$
$\langle z \rangle = 0.691$	$-0.141 \pm 0.043 \pm 0.006$	$0.414 \pm 0.063 \pm 0.027$
$\langle x_F \rangle = 0.286$	$0.007 \pm 0.051 \pm 0.012$	$0.120 \pm 0.115 \pm 0.005$
$\langle x_F \rangle = 0.359$	$-0.004 \pm 0.052 \pm 0.011$	$0.250 \pm 0.097 \pm 0.027$
$\langle x_F \rangle = 0.456$	$-0.080 \pm 0.044 \pm 0.010$	$0.326 \pm 0.081 \pm 0.008$
$\langle x_F \rangle = 0.651$	$-0.139 \pm 0.044 \pm 0.006$	$0.439 \pm 0.065 \pm 0.027$

Table 4.9:  $\langle \cos \phi \rangle$  and  $\langle \cos 2\phi \rangle$  separated for  $\pi^+$  and  $\pi^-$ .

## 4.3 Azimuthal Distributions of Strange Particles.

### 4.3.1 Acceptance Corrected Results.

The  $(e, e'\Lambda)$  and  $(e, e'K_S)$  data were analyzed and corrected in the same fashion as discussed in Section 4.2.3. An important difference, however, is that the Monte Carlo event sample exceeds the data by a factor of  $\sim 10$  and hence the uncertainty is dominated by the statistical precision of the data.

Function	$\Lambda$		$K_S$	
	1996	1997	1996	1997
$y$	0.549	0.554	0.622	0.630
$f_1(y)$	0.781	0.774	0.720	0.712
$f_2(y)$	0.358	0.354	0.319	0.314
$f_3(y)$	0.288	0.287	0.316	0.318
$D(y)$	0.652	0.655	0.737	0.746

Table 4.10: Photon polarization factors in  $(e, e'\Lambda)$  and  $(e, e'K_S)$  events.

Using the kinematic factors shown in Table 4.10, the raw results for each year of Table 4.11 could be corrected. Originally, it was hoped that better statistical precision could be obtained by fitting the data with only a term in  $\langle \cos \phi \rangle$  but the uncertainties increased by only 5% when all allowed terms were included; thus prompting the decision to include all terms in all the fits. The fits are separated for each year and the confidence levels are tabulated as well to show that the fits are quite robust.

The corrected values for each year are shown in Table 4.12.



Kinematics	$\langle \cos \phi \rangle$	$\langle \cos 2\phi \rangle$	$\langle \sin \phi \rangle$	$P_\chi^2$
<b><math>\Lambda : 1996</math></b>				
$\langle p_T \rangle = 0.676 \text{ GeV}$	$0.125 \pm 0.179$	$0.190 \pm 0.168$	$0.048 \pm 0.133$	0.194
$\langle p_T \rangle = 0.311 \text{ GeV}$	$-0.134 \pm 0.137$	$-0.276 \pm 0.133$	$-0.025 \pm 0.104$	0.852
$\langle Q^2 \rangle = 3.235 \text{ GeV}^2$	$-0.130 \pm 0.149$	$-0.292 \pm 0.151$	$-0.013 \pm 0.114$	0.286
$\langle Q^2 \rangle = 1.431 \text{ GeV}^2$	$0.061 \pm 0.157$	$0.008 \pm 0.144$	$-0.014 \pm 0.117$	0.459
$\langle z \rangle = 0.613$	$-0.175 \pm 0.157$	$0.040 \pm 0.154$	$0.275 \pm 0.117$	0.663
$\langle z \rangle = 0.365$	$0.081 \pm 0.143$	$-0.207 \pm 0.137$	$-0.185 \pm 0.111$	1.000
$\langle x_F \rangle = 0.441$	$-0.155 \pm 0.136$	$0.079 \pm 0.131$	$0.218 \pm 0.103$	0.401
$\langle x_F \rangle = 0.159$	$0.111 \pm 0.163$	$-0.294 \pm 0.159$	$-0.190 \pm 0.125$	0.970
<b><math>\Lambda : 1997</math></b>				
$\langle p_T \rangle = 0.676 \text{ GeV}$	$-0.131 \pm 0.174$	$0.145 \pm 0.139$	$-0.034 \pm 0.114$	0.310
$\langle p_T \rangle = 0.311 \text{ GeV}$	$-0.335 \pm 0.139$	$0.185 \pm 0.125$	$0.073 \pm 0.100$	0.598
$\langle Q^2 \rangle = 3.235 \text{ GeV}^2$	$-0.154 \pm 0.191$	$0.318 \pm 0.168$	$0.050 \pm 0.133$	0.623
$\langle Q^2 \rangle = 1.431 \text{ GeV}^2$	$-0.211 \pm 0.133$	$0.104 \pm 0.115$	$-0.037 \pm 0.094$	0.508
$\langle z \rangle = 0.613$	$-0.211 \pm 0.159$	$0.100 \pm 0.148$	$-0.124 \pm 0.116$	0.116
$\langle z \rangle = 0.365$	$-0.164 \pm 0.142$	$0.219 \pm 0.123$	$0.074 \pm 0.101$	0.516
$\langle x_F \rangle = 0.441$	$-0.389 \pm 0.138$	$0.162 \pm 0.122$	$-0.043 \pm 0.098$	0.352
$\langle x_F \rangle = 0.159$	$-0.066 \pm 0.167$	$0.175 \pm 0.149$	$0.070 \pm 0.119$	0.764
<b><math>K_S : 1996</math></b>				
$\langle p_T \rangle = 0.713 \text{ GeV}$	$0.019 \pm 0.133$	$0.016 \pm 0.128$	$0.126 \pm 0.106$	0.780
$\langle p_T \rangle = 0.324 \text{ GeV}$	$-0.252 \pm 0.130$	$0.004 \pm 0.130$	$-0.024 \pm 0.106$	0.101
$\langle Q^2 \rangle = 3.209 \text{ GeV}^2$	$-0.282 \pm 0.144$	$0.089 \pm 0.135$	$-0.081 \pm 0.108$	0.729
$\langle Q^2 \rangle = 1.427 \text{ GeV}^2$	$-0.010 \pm 0.120$	$-0.058 \pm 0.124$	$0.188 \pm 0.105$	0.271
$\langle z \rangle = 0.679$	$-0.060 \pm 0.131$	$-0.107 \pm 0.126$	$0.009 \pm 0.102$	0.085
$\langle z \rangle = 0.429$	$-0.077 \pm 0.130$	$0.175 \pm 0.131$	$0.172 \pm 0.110$	0.190
$\langle x_F \rangle = 0.624$	$-0.090 \pm 0.130$	$-0.084 \pm 0.124$	$0.001 \pm 0.100$	0.049
$\langle x_F \rangle = 0.377$	$-0.073 \pm 0.132$	$0.160 \pm 0.133$	$0.163 \pm 0.112$	0.209
<b><math>K_S : 1997</math></b>				
$\langle p_T \rangle = 0.713 \text{ GeV}$	$-0.100 \pm 0.126$	$0.071 \pm 0.118$	$-0.024 \pm 0.100$	0.789
$\langle p_T \rangle = 0.324 \text{ GeV}$	$-0.165 \pm 0.112$	$-0.192 \pm 0.117$	$-0.152 \pm 0.096$	0.381
$\langle Q^2 \rangle = 3.209 \text{ GeV}^2$	$-0.225 \pm 0.123$	$-0.038 \pm 0.117$	$-0.007 \pm 0.096$	0.342
$\langle Q^2 \rangle = 1.427 \text{ GeV}^2$	$-0.068 \pm 0.114$	$-0.062 \pm 0.117$	$-0.178 \pm 0.100$	0.838
$\langle z \rangle = 0.679$	$-0.141 \pm 0.125$	$0.127 \pm 0.125$	$-0.184 \pm 0.101$	0.470
$\langle z \rangle = 0.429$	$-0.054 \pm 0.112$	$-0.225 \pm 0.112$	$-0.021 \pm 0.097$	0.411
$\langle x_F \rangle = 0.624$	$-0.162 \pm 0.125$	$0.107 \pm 0.125$	$-0.153 \pm 0.102$	0.572
$\langle x_F \rangle = 0.377$	$-0.058 \pm 0.112$	$-0.196 \pm 0.112$	$-0.049 \pm 0.096$	0.532

Table 4.11: Extracted moments in  $\phi$  for  $(e, e'\Lambda)$  and  $(e, e'K_S)$  events for each year, with the associated confidence level.

Kinematics	$\langle \cos \phi \rangle / \langle f_1(y) \rangle$	$\langle \cos 2\phi \rangle / \langle f_2(y) \rangle$	$\langle \sin \phi \rangle / P_b \langle f_3(y) \rangle$
<b><math>\Lambda : 1996</math></b>			
$\langle p_T \rangle = 0.676 \text{ GeV}$	$0.161 \pm 0.230$	$0.534 \pm 0.472$	$0.303 \pm 0.841$
$\langle p_T \rangle = 0.311 \text{ GeV}$	$-0.172 \pm 0.176$	$-0.776 \pm 0.374$	$-0.158 \pm 0.657$
$\langle Q^2 \rangle = 3.235 \text{ GeV}^2$	$-0.167 \pm 0.192$	$-0.821 \pm 0.425$	$-0.082 \pm 0.721$
$\langle Q^2 \rangle = 1.431 \text{ GeV}^2$	$0.078 \pm 0.202$	$0.022 \pm 0.405$	$-0.088 \pm 0.740$
$\langle z \rangle = 0.613$	$-0.225 \pm 0.202$	$0.112 \pm 0.433$	$1.738 \pm 0.740$
$\langle z \rangle = 0.365$	$0.104 \pm 0.184$	$-0.582 \pm 0.385$	$-1.169 \pm 0.702$
$\langle x_F \rangle = 0.441$	$-0.199 \pm 0.175$	$0.222 \pm 0.368$	$1.378 \pm 0.651$
$\langle x_F \rangle = 0.159$	$0.143 \pm 0.210$	$-0.827 \pm 0.447$	$-1.201 \pm 0.790$
<b><math>\Lambda : 1997</math></b>			
$\langle p_T \rangle = 0.676 \text{ GeV}$	$-0.168 \pm 0.224$	$0.408 \pm 0.391$	$0.215 \pm 0.721$
$\langle p_T \rangle = 0.311 \text{ GeV}$	$-0.431 \pm 0.179$	$0.520 \pm 0.352$	$-0.461 \pm 0.632$
$\langle Q^2 \rangle = 3.235 \text{ GeV}^2$	$-0.198 \pm 0.246$	$0.894 \pm 0.472$	$-0.316 \pm 0.841$
$\langle Q^2 \rangle = 1.431 \text{ GeV}^2$	$-0.271 \pm 0.171$	$0.292 \pm 0.323$	$0.234 \pm 0.594$
$\langle z \rangle = 0.613$	$-0.271 \pm 0.204$	$0.281 \pm 0.416$	$0.784 \pm 0.733$
$\langle z \rangle = 0.365$	$-0.211 \pm 0.183$	$0.616 \pm 0.346$	$-0.468 \pm 0.638$
$\langle x_F \rangle = 0.441$	$-0.500 \pm 0.177$	$0.456 \pm 0.343$	$0.272 \pm 0.619$
$\langle x_F \rangle = 0.159$	$-0.085 \pm 0.215$	$0.492 \pm 0.419$	$-0.442 \pm 0.752$
<b><math>K_S : 1996</math></b>			
$\langle p_T \rangle = 0.713 \text{ GeV}$	$0.027 \pm 0.186$	$0.051 \pm 0.405$	$0.723 \pm 0.608$
$\langle p_T \rangle = 0.324 \text{ GeV}$	$-0.352 \pm 0.182$	$0.013 \pm 0.411$	$-0.138 \pm 0.608$
$\langle Q^2 \rangle = 3.209 \text{ GeV}^2$	$-0.394 \pm 0.201$	$0.281 \pm 0.427$	$-0.465 \pm 0.620$
$\langle Q^2 \rangle = 1.427 \text{ GeV}^2$	$-0.014 \pm 0.168$	$-0.183 \pm 0.392$	$1.079 \pm 0.603$
$\langle z \rangle = 0.679$	$-0.084 \pm 0.183$	$-0.338 \pm 0.398$	$0.052 \pm 0.585$
$\langle z \rangle = 0.429$	$-0.108 \pm 0.182$	$0.553 \pm 0.414$	$0.987 \pm 0.631$
$\langle x_F \rangle = 0.624$	$-0.126 \pm 0.182$	$-0.266 \pm 0.392$	$0.006 \pm 0.574$
$\langle x_F \rangle = 0.377$	$-0.102 \pm 0.184$	$0.506 \pm 0.421$	$0.936 \pm 0.643$
<b><math>K_S : 1997</math></b>			
$\langle p_T \rangle = 0.713 \text{ GeV}$	$-0.140 \pm 0.176$	$0.225 \pm 0.373$	$0.138 \pm 0.574$
$\langle p_T \rangle = 0.324 \text{ GeV}$	$-0.231 \pm 0.156$	$-0.607 \pm 0.370$	$0.872 \pm 0.551$
$\langle Q^2 \rangle = 3.209 \text{ GeV}^2$	$-0.314 \pm 0.172$	$-0.120 \pm 0.370$	$0.040 \pm 0.551$
$\langle Q^2 \rangle = 1.427 \text{ GeV}^2$	$-0.095 \pm 0.159$	$-0.196 \pm 0.370$	$1.022 \pm 0.574$
$\langle z \rangle = 0.679$	$-0.197 \pm 0.175$	$0.402 \pm 0.395$	$1.056 \pm 0.580$
$\langle z \rangle = 0.429$	$-0.075 \pm 0.156$	$-0.711 \pm 0.354$	$0.121 \pm 0.557$
$\langle x_F \rangle = 0.624$	$-0.226 \pm 0.175$	$0.338 \pm 0.395$	$0.878 \pm 0.585$
$\langle x_F \rangle = 0.377$	$-0.081 \pm 0.156$	$-0.620 \pm 0.354$	$0.281 \pm 0.551$

Table 4.12: Corrected moments in  $\phi$  for  $(e, e'\Lambda)$  and  $(e, e'K_S)$  for each year.

### 4.3.2 Systematic Uncertainties.

For the strange particles there are two dominant uncertainties: The background and the acceptance corrections.

### Background Correction.

One way to see the impact of the acceptance on the background is to consider Table 4.13, where the  $S/B$  numbers are tabulated for each bin, rather than integrated over all kinematics as they were in Section 3.3. Clearly, the background depends heavily on the kinematic bin, since the lower momentum events are subject to much higher backgrounds. For those measurements that are more sensitive to the acceptance, the background may be more important.

Kinematics	$\delta m = 2\sigma$	$\delta m = 3\sigma$
$\langle p_T \rangle = 0.702 \text{ GeV}$	4.3	3.7
$\langle p_T \rangle = 0.327 \text{ GeV}$	3.4	2.5
$\langle Q^2 \rangle = 3.389 \text{ GeV}^2$	3.8	2.5
$\langle Q^2 \rangle = 1.454 \text{ GeV}^2$	3.7	3.1
$\langle z \rangle = 0.615$	5.0	4.6
$\langle z \rangle = 0.365$	3.2	2.3
$\langle x_F \rangle = 0.441$	5.7	5.1
$\langle x_F \rangle = 0.160$	2.8	2.0

Table 4.13: The  $S/B$  as a function of kinematic bin for the  $\Lambda$  events. The numbers are calculated by assuming a mass window of  $2\sigma$  and then  $3\sigma$  in order to include more of the wings of the mass distribution.

It was possible to perform the entire analysis without a background correction to search for a difference:

$$\delta \left( \frac{\langle \cos \phi \rangle}{f_1(y)} \right) = \frac{\langle \cos \phi \rangle_{corrected}}{f_1(y)} - \frac{\langle \cos \phi \rangle_{uncorrected}}{f_1(y)}. \quad (4.9)$$

Results for this term are shown in Table 4.14. The other moments are neglected since  $\langle \cos \phi \rangle$  is the moment that is determined with the highest statistical precision. For both particles, these numbers are reasonably small; namely, they are  $\sim 5\%$ , with some excursions. For the  $K_S$  the numbers are consistently negative, indicating that the background produces a larger moment than the physical measurement.

$\Lambda$		$K_S$	
Kinematics	$\delta \frac{\langle \cos \phi \rangle}{f_1(y)}$	Kinematics	$\delta \frac{\langle \cos 2\phi \rangle}{f_1(y)}$
$\langle p_T \rangle = 0.676 \text{ GeV}$	0.011	$\langle p_T \rangle = 0.713 \text{ GeV}$	-0.037
$\langle p_T \rangle = 0.311 \text{ GeV}$	-0.012	$\langle p_T \rangle = 0.324 \text{ GeV}$	-0.106
$\langle Q^2 \rangle = 3.235 \text{ GeV}^2$	0.048	$\langle Q^2 \rangle = 3.209 \text{ GeV}^2$	-0.087
$\langle Q^2 \rangle = 1.431 \text{ GeV}^2$	-0.016	$\langle Q^2 \rangle = 1.427 \text{ GeV}^2$	-0.070
$\langle z \rangle = 0.613$	0.046	$\langle z \rangle = 0.679$	-0.046
$\langle z \rangle = 0.365$	0.013	$\langle z \rangle = 0.429$	-0.077
$\langle x_F \rangle = 0.441$	0.029	$\langle x_F \rangle = 0.624$	-0.058
$\langle x_F \rangle = 0.159$	0.080	$\langle x_F \rangle = 0.377$	-0.076

Table 4.14: The importance of background corrections on the extracted azimuthal distributions.

### The Acceptance Correction.

- Generator.

Like the pions, the  $\Lambda$  and  $K_S$  were generated with an isotropic distribution in  $\phi$ . Thus, no uncertainty was assigned for the generator.

- Precision.

The number of events generated was such that ten times more  $\Lambda$  and  $K_S$  events were reconstructed as were available in the data. The statistics of the Monte Carlo was accounted for in the statistical error.

- Binning.

Unlike the  $(e, e'\pi)$  analysis, this analysis did not exclude events near the edges in  $\phi$  for two reasons: First, there were not sufficient statistics to search for pathologies where the edges dominated the systematics. Secondly, because these events sample a different region of phase space, the edges of the calorimeter are not as likely to be populated by  $(e, e'\Lambda)$  or  $(e, e'K_S)$  events. Since this correction was not performed, it should not be considered a source of systematic uncertainty.

- Kinematic disagreements.

Because the  $Q^2$  distributions of the Monte Carlo and the data agreed well, discrepancies in the shapes of the  $z$  and  $x_F$  distributions reflected poor understanding of hadronization dynamics. It was assumed that this changed the relative rate of production in various kinematic bins but did not affect the  $\phi$  distributions. Hence this was neglected.

### Contamination.

Again, the contamination in each hadron sample is limited to 0.5% for the same reasons as stated in Section 4.2.4. A better indication of the contamination is to consider particles in the Monte Carlo that were reconstructed incorrectly. This is also an indication of the efficacy of the cuts. The results are shown in Table 4.15. An absolute uncertainty of 5% was assigned for misidentification of particles.

$\Lambda$ events			$K_S$ events		
$N_\Lambda$	$N_B$	$N_{K_S}$	$N_{K_S}$	$N_B$	$N_\Lambda$
0.952	0.041	0.007	0.958	0.024	0.019

Table 4.15: Misidentification of  $\Lambda$  or  $K_S$  as other particles. The background fraction depends on the width of the peak, which is estimated from the mass distribution of these events.

### Cut Selection.

Because the  $S/B$  numbers are rather insensitive to the details of the cuts, no additional systematic uncertainty was calculated for variation in the selection criteria. These differences were assumed to be included in the background correction.

### Radiative Corrections.

As shown in Section 4.2.4, internal radiation caused a 10% change in the extracted  $\langle \cos \phi \rangle$  values for pions; however, this has not been studied for any other channels. Furthermore, the other systematic and statistical uncertainties are much larger. For these reasons, this correction was neglected.

In order to understand the impact of external radiation as well as finite detector efficiencies, the Monte Carlo simulation was used to consider  $(e, e'\Lambda)$  events analyzed before and after the reconstruction. Again, although the  $\delta Q^2$  and  $\delta p_T$  distributions showed radiative effects, the mean of the  $\delta\phi$  distribution was  $(0.24 \pm 0.53)\%$ , indicating that this is not a significant bias in measuring the azimuthal angle. The  $K_S$  events showed similar distributions.

### Summary.

The dominant systematic uncertainties and their maximum sizes are summarized in Table 4.16.

Contribution	Size
Background correction	0.10
Contamination	0.05

Table 4.16: Systematic uncertainties in  $\phi$  moments of  $(e, e'\Lambda)$  and  $(e, e'K_S)$  events.

## 4.3.3 Results for Azimuthal Moments of Strange Particles.

Kinematics	$\langle \cos \phi \rangle / \langle f_1(y) \rangle$	$\langle \cos 2\phi \rangle / \langle f_2(y) \rangle$
$\Lambda$		
$\langle p_T \rangle = 0.676 \text{ GeV}$	$-0.008 \pm 0.160 \pm 0.051$	$0.459 \pm 0.301 \pm 0.051$
$\langle p_T \rangle = 0.311 \text{ GeV}$	$-0.300 \pm 0.126 \pm 0.051$	$-0.088 \pm 0.256 \pm 0.051$
$\langle Q^2 \rangle = 3.235 \text{ GeV}^2$	$-0.179 \pm 0.151 \pm 0.069$	$-0.055 \pm 0.316 \pm 0.069$
$\langle Q^2 \rangle = 1.431 \text{ GeV}^2$	$-0.125 \pm 0.130 \pm 0.052$	$0.187 \pm 0.253 \pm 0.052$
$\langle z \rangle = 0.613$	$-0.248 \pm 0.144 \pm 0.068$	$0.200 \pm 0.300 \pm 0.068$
$\langle z \rangle = 0.365$	$-0.054 \pm 0.130 \pm 0.052$	$0.081 \pm 0.257 \pm 0.052$
$\langle x_F \rangle = 0.441$	$-0.348 \pm 0.125 \pm 0.058$	$0.347 \pm 0.251 \pm 0.058$
$\langle x_F \rangle = 0.159$	$0.032 \pm 0.150 \pm 0.094$	$-0.125 \pm 0.306 \pm 0.094$
$K_S$		
$\langle p_T \rangle = 0.713 \text{ GeV}$	$-0.061 \pm 0.128 \pm 0.062$	$0.145 \pm 0.274 \pm 0.062$
$\langle p_T \rangle = 0.324 \text{ GeV}$	$-0.282 \pm 0.119 \pm 0.117$	$-0.330 \pm 0.275 \pm 0.117$
$\langle Q^2 \rangle = 3.209 \text{ GeV}^2$	$-0.348 \pm 0.131 \pm 0.100$	$0.052 \pm 0.280 \pm 0.100$
$\langle Q^2 \rangle = 1.427 \text{ GeV}^2$	$-0.057 \pm 0.115 \pm 0.086$	$-0.190 \pm 0.269 \pm 0.086$
$\langle z \rangle = 0.679$	$-0.143 \pm 0.126 \pm 0.068$	$0.034 \pm 0.281 \pm 0.068$
$\langle z \rangle = 0.429$	$-0.089 \pm 0.119 \pm 0.092$	$-0.177 \pm 0.269 \pm 0.092$
$\langle x_F \rangle = 0.624$	$-0.178 \pm 0.126 \pm 0.077$	$0.034 \pm 0.278 \pm 0.077$
$\langle x_F \rangle = 0.377$	$-0.090 \pm 0.119 \pm 0.091$	$-0.153 \pm 0.271 \pm 0.091$

Table 4.17:  $\langle \cos \phi \rangle$  and  $\langle \cos 2\phi \rangle$  in  $(e, e'\Lambda)$  and  $(e, e'K_S)$  events.

Kinematics	$\langle \sin \phi \rangle / P_b \langle f_3(y) \rangle$
$\Lambda$	
$\langle p_T \rangle = 0.676 \text{ GeV}$	$0.252 \pm 0.547 \pm 0.051$
$\langle p_T \rangle = 0.311 \text{ GeV}$	$-0.316 \pm 0.456 \pm 0.051$
$\langle Q^2 \rangle = 3.235 \text{ GeV}^2$	$-0.181 \pm 0.547 \pm 0.069$
$\langle Q^2 \rangle = 1.431 \text{ GeV}^2$	$0.107 \pm 0.463 \pm 0.052$
$\langle z \rangle = 0.613$	$1.257 \pm 0.521 \pm 0.068$
$\langle z \rangle = 0.365$	$-0.785 \pm 0.472 \pm 0.052$
$\langle x_F \rangle = 0.441$	$0.797 \pm 0.449 \pm 0.058$
$\langle x_F \rangle = 0.159$	$-0.803 \pm 0.545 \pm 0.094$
$K_S$	
$\langle p_T \rangle = 0.713 \text{ GeV}$	$0.413 \pm 0.418 \pm 0.062$
$\langle p_T \rangle = 0.324 \text{ GeV}$	$0.417 \pm 0.408 \pm 0.117$
$\langle Q^2 \rangle = 3.209 \text{ GeV}^2$	$-0.183 \pm 0.412 \pm 0.100$
$\langle Q^2 \rangle = 1.427 \text{ GeV}^2$	$1.049 \pm 0.416 \pm 0.086$
$\langle z \rangle = 0.679$	$0.559 \pm 0.412 \pm 0.068$
$\langle z \rangle = 0.429$	$0.500 \pm 0.418 \pm 0.092$
$\langle x_F \rangle = 0.624$	$0.433 \pm 0.410 \pm 0.077$
$\langle x_F \rangle = 0.377$	$0.558 \pm 0.418 \pm 0.091$

Table 4.18:  $\langle \sin \phi \rangle$  in  $(e, e'\Lambda)$  and  $(e, e'K_S)$  events.



The results are combined statistically and the appropriate kinematic functions are included in the final results, shown in Tables 4.3.3 and 4.3.3. The results for the  $\Lambda$  are shown in Figure 4.18, where all moments appear to be fully consistent with zero within  $2\sigma$ . Because of the low statistics, it is too difficult to compare these results with those of the pions to search for the validity of parton kinematic models at the  $Q^2$  range covered at HERMES. Neither TR-odd nor higher twist effects produce a significant value for the  $\langle \cos 2\phi \rangle$  moment.

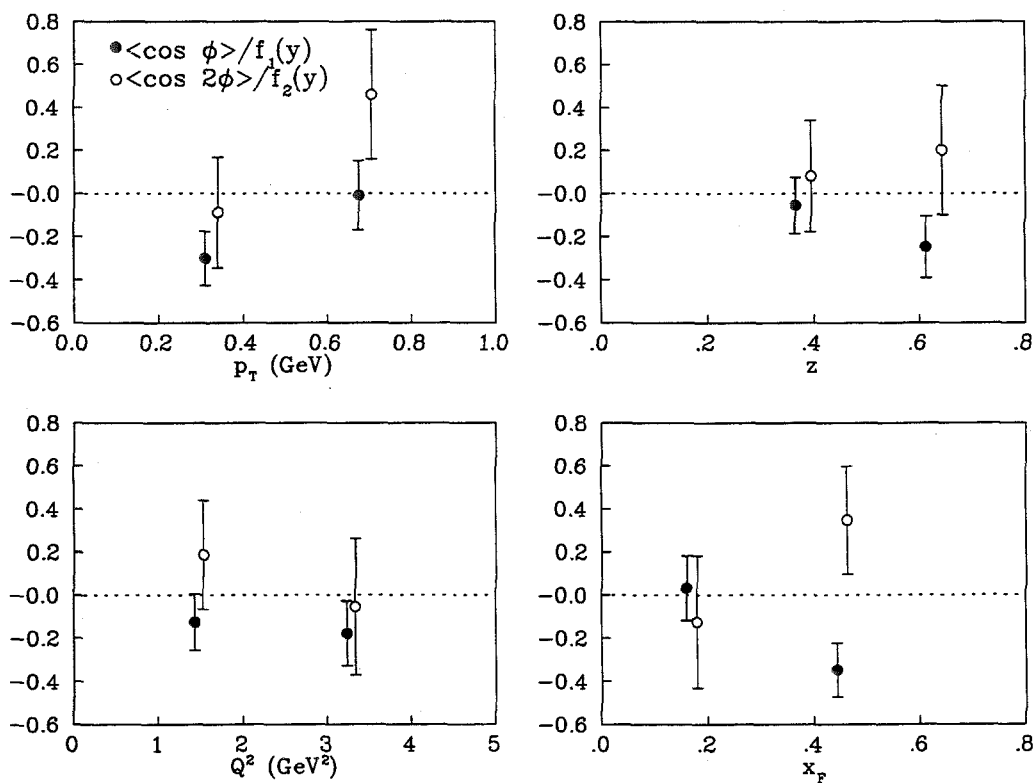


Figure 4.18: Moments in  $\phi$  for the  $(e, e'\Lambda)$  events. The measurements are taken at the same average kinematic value but have been offset in this plot.

The same measurements were carried out for the  $K_S$ ; the results are shown in Figure 4.19, where they, too, show no evidence for significant azimuthal moments. Again, more complex interactions affect the  $K_S$  production, a reasonable conclusion for a particle that is composed entirely of sea quarks.

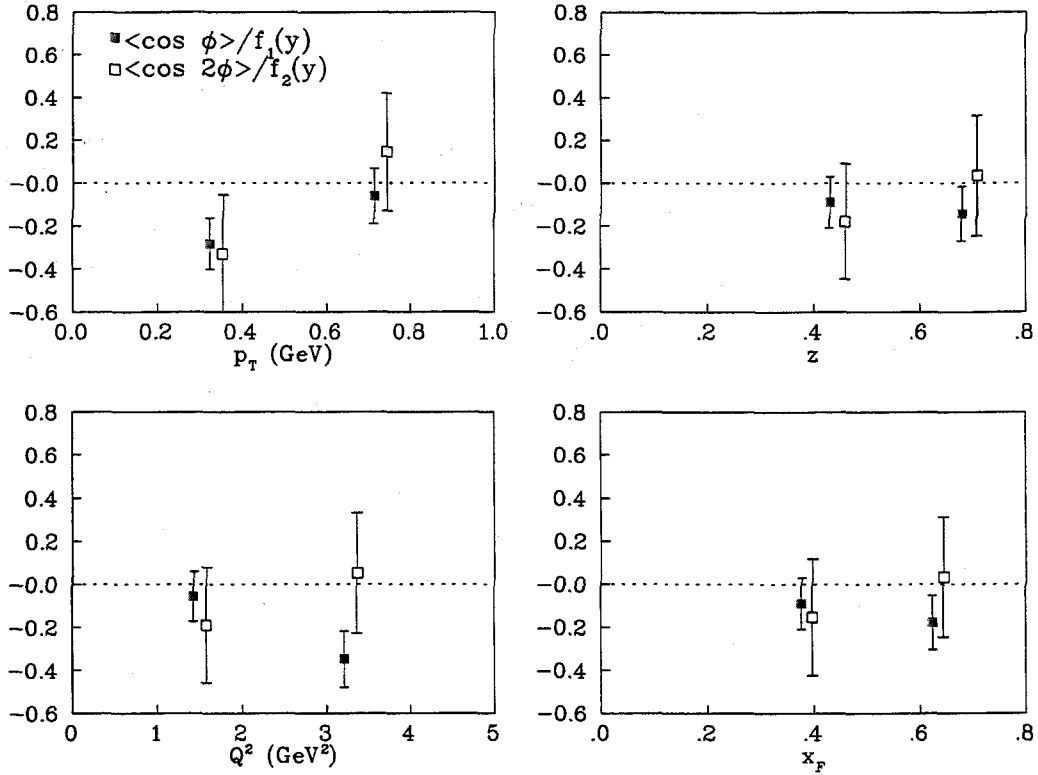


Figure 4.19: Moments in  $\phi$  for the  $(e, e'K_S)$  events. The measurements are taken at the same average kinematic value but have been offset in this plot.

## 4.4 $\Lambda$ Polarization.

### 4.4.1 Analysis.

In the  $\Lambda$  CMS, an orthonormal coordinate system can be constructed:

$$\begin{aligned}
 \hat{z} &= \hat{\Lambda}, \\
 \hat{y} &= \hat{q} \times \hat{\Lambda}, \\
 \hat{x} &= \hat{y} \times \hat{z},
 \end{aligned}
 \tag{4.10}$$

where  $\hat{\Lambda}$ , given by  $\hat{\Lambda} = (\vec{\pi} + \vec{p}) / |\vec{\pi} + \vec{p}|$  for pion(proton) momentum  $\vec{\pi}(\vec{p})$ , identifies the direction opposite the undetected recoiling target fragments. (In the laboratory, it is the  $\Lambda$  boost direction.)  $\hat{q}$  is the virtual photon direction. Nevertheless, this convention differs slightly from that used in hadron experiments, where the quantization axes are

defined with respect to the incoming and outgoing beams rather than with respect to the momentum transfer direction. This convention is, however, consistent with that used in traditional electron scattering experiments at intermediate energies [11]<sup>1</sup>.

Angular distributions are then constructed by using the decay proton as an analyzer:

$$\cos \theta_i = \hat{p} \cdot \hat{e}_i; \quad (4.11)$$

$$N = \frac{1}{2}(1 + \alpha P_i \cos \theta_i), \quad (4.12)$$

where  $\hat{p}$  is the normalized momentum vector of the decay proton in the  $\Lambda$  center of mass and  $i = x, y, z$ .  $\alpha$  is the weak decay constant for  $\Lambda$  decay, which is  $0.642 \pm 0.013$ .

These raw distributions are seen in Figure 4.20 and show the influence of the spectrometer acceptance; the Monte Carlo event sample exceeds the data by a factor of  $\sim 10$  and hence the uncertainty is dominated by the statistical precision of the data. The histogram in  $\cos \theta_z$  is particularly sensitive, as the proton must *a priori* go opposite to the  $\Lambda$  direction of motion in order to be detected; if the proton goes forward, the pion goes backward and will not get boosted enough to be detected. Hence pion detection is most likely if the pion is moving forward already before the boost. (For this reason, in this analysis, this histogram is binned asymmetrically in  $\cos \theta_z$ , as the detector samples this quantity very asymmetrically.) The transverse directions  $x$  and  $y$  are much less sensitive to the acceptance and hence are flatter.

---

<sup>1</sup>This coordinate system in the  $\Lambda$  CMS is an example of the *helicity* frame. It may be contrasted with the *Gottfried-Jackson* (GJ) frame, in which the  $z$  direction is given by  $\hat{q}$ . The GJ frame is relevant for discussing the  $t$ -channel helicity density matrix, which is difficult to discuss in the context of having an undetected remnant  $X$  in the reaction  $\gamma - N \rightarrow \Lambda X$ . A full discussion of these frames (and others) is given in Reference [72].

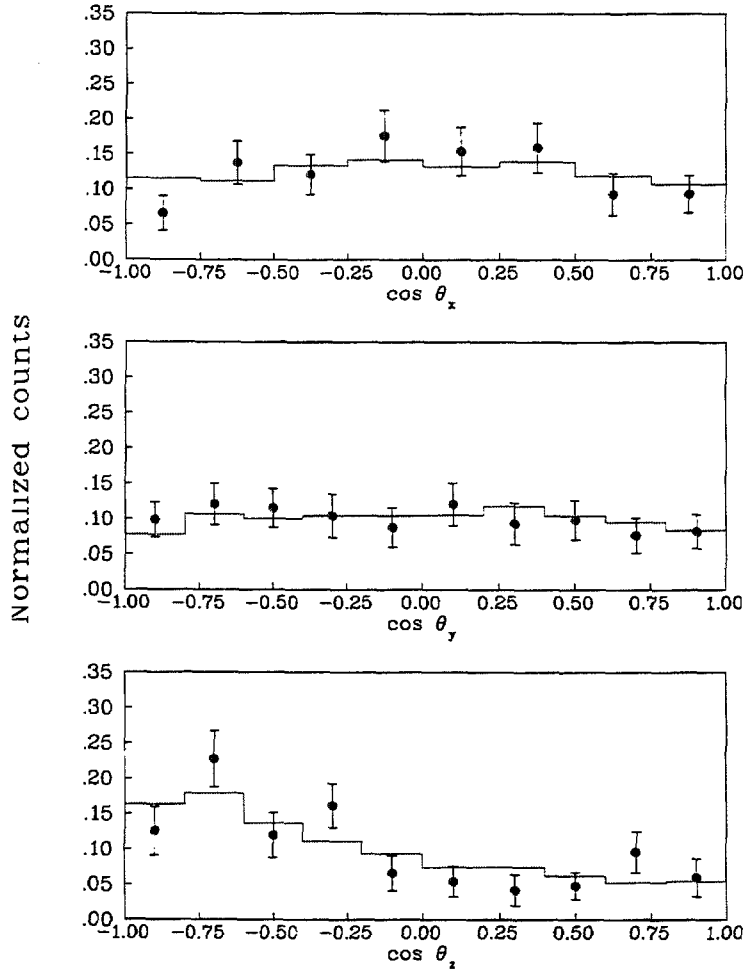


Figure 4.20: Raw angular distributions for  $\Lambda$  events for  $z < 0.5$ , with data (black circles) and Monte Carlo (red histogram). Top:  $\cos \theta_x$ ; middle:  $\cos \theta_y$ ; bottom:  $\cos \theta_z$ . The shapes differ radically due to differences in the acceptance.

#### 4.4.2 Acceptance Corrected Results.

The distributions were corrected in a fashion analogous to the distributions in  $\phi$ . A correction factor was constructed for each direction cosine:

$$C(\cos \theta_i) = N_{MC}; \quad (4.13)$$

$$\int_{-1}^1 C(\cos \theta_i) d(\cos \theta_i) = 1.$$

The data were then corrected with this factor  $C$ :

$$\frac{dN'(\cos \theta_i)}{d(\cos \theta_i)} = \frac{1}{C(\cos \theta_i)} \frac{dN_{data}(\cos \theta_i)}{d(\cos \theta_i)}. \quad (4.14)$$

where each sample is independently normalized to unity, since the absolute cross section for these production processes is not well described in the Monte Carlo. Then  $N'(\cos \theta_i)$  is normalized and fit to the function

$$\frac{1}{N'} \frac{dN'}{d(\cos \theta_i)} = 1 + \alpha P_i \cos \theta_i. \quad (4.15)$$

That is, extraction of the slope yields a value for  $P_i$ . An example is shown in Figure 4.21. Although the binning is not symmetric in  $\cos \theta_x$ , the result is insensitive to the bin choice; only the probability  $P_{\chi^2}$  is improved.

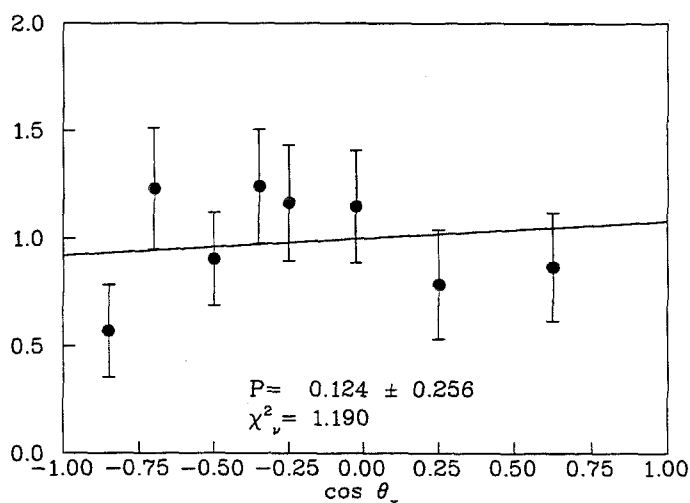


Figure 4.21: The histogram used to determine the final polarization  $P_x$ , as discussed in the text. The precision is representative of each polarization component.

The results for the three polarization directions were then sorted by kinematic bin and are tabulated in Tables 4.19, 4.20, and 4.21 with the associated confidence values.

Kinematic bin	1996		1997	
	$P_x$	$P_{\chi^2}$	$P_x$	$P_{\chi^2}$
$\langle p_T \rangle = 0.676 \text{ GeV}$	$0.195 \pm 0.289$	0.932	$0.529 \pm 0.276$	0.469
$\langle p_T \rangle = 0.311 \text{ GeV}$	$0.023 \pm 0.221$	0.179	$0.099 \pm 0.230$	0.172
$\langle Q^2 \rangle = 3.235 \text{ GeV}^2$	$-0.074 \pm 0.231$	0.143	$-0.211 \pm 0.293$	0.514
$\langle Q^2 \rangle = 1.431 \text{ GeV}^2$	$0.229 \pm 0.263$	0.766	$0.487 \pm 0.223$	0.354
$\langle z \rangle = 0.613$	$0.119 \pm 0.258$	0.433	$0.350 \pm 0.275$	0.652
$\langle z \rangle = 0.365$	$0.066 \pm 0.241$	0.246	$0.119 \pm 0.232$	0.306
$\langle x_F \rangle = 0.441$	$0.186 \pm 0.227$	0.324	$0.337 \pm 0.235$	0.201
$\langle x_F \rangle = 0.159$	$0.079 \pm 0.267$	0.245	$0.148 \pm 0.267$	0.530

Table 4.19: The extracted values for  $P_x$  for each year.

Kinematic bin	1996		1997	
	$P_y$	$P_{\chi^2}$	$P_y$	$P_{\chi^2}$
$\langle p_T \rangle = 0.676 \text{ GeV}$	$-0.247 \pm 0.258$	0.122	$-0.270 \pm 0.225$	0.023
$\langle p_T \rangle = 0.311 \text{ GeV}$	$0.009 \pm 0.210$	0.799	$-0.352 \pm 0.209$	0.308
$\langle Q^2 \rangle = 3.235 \text{ GeV}^2$	$-0.063 \pm 0.232$	0.651	$-0.193 \pm 0.265$	0.028
$\langle Q^2 \rangle = 1.431 \text{ GeV}^2$	$-0.126 \pm 0.230$	0.240	$-0.554 \pm 0.192$	0.440
$\langle z \rangle = 0.613$	$-0.300 \pm 0.248$	0.991	$-0.663 \pm 0.231$	0.622
$\langle z \rangle = 0.365$	$0.020 \pm 0.216$	0.513	$-0.229 \pm 0.206$	0.208
$\langle x_F \rangle = 0.441$	$-0.171 \pm 0.225$	0.898	$-0.628 \pm 0.198$	0.503
$\langle x_F \rangle = 0.159$	$-0.037 \pm 0.236$	0.645	$-0.219 \pm 0.240$	0.359

Table 4.20: The extracted values for  $P_y$  for each year.

In order to access fragmentation functions, the extracted polarizations must be scaled by the proper kinematic functions to determine the transfer coefficient for the photon's polarization, as restated in Equation 4.7.

Unlike the transverse polarization  $P_y$ , measurements of the other polarization components require polarized beam. Consequently, the spin transfer coefficients  $\Delta P_x$  and  $\Delta P_z$  can then be defined by combining the kinematic functions, the beam polarization and the extracted polarization:

$$\Delta P_x = -\frac{1}{4} \frac{1}{P_e} \frac{1}{\langle f_3(y) \rangle} P_x; \quad (4.16)$$

$$\Delta P_z = \frac{1}{P_e} \frac{1}{\langle D(y) \rangle} P_z.$$

Kinematic bin	1996		1997	
	$P_z$	$P_{\chi^2}$	$P_z$	$P_{\chi^2}$
$\langle p_T \rangle = 0.676$ GeV	$0.271 \pm 0.277$	0.390	$-0.209 \pm 0.263$	0.872
$\langle p_T \rangle = 0.311$ GeV	$0.243 \pm 0.213$	0.855	$0.211 \pm 0.195$	0.954
$\langle Q^2 \rangle = 3.235$ GeV <sup>2</sup>	$0.290 \pm 0.237$	0.789	$0.127 \pm 0.243$	0.832
$\langle Q^2 \rangle = 1.431$ GeV <sup>2</sup>	$0.195 \pm 0.240$	0.534	$0.042 \pm 0.204$	0.744
$\langle z \rangle = 0.613$	$0.015 \pm 0.256$	0.424	$0.217 \pm 0.255$	0.503
$\langle z \rangle = 0.365$	$0.392 \pm 0.220$	0.849	$0.022 \pm 0.192$	0.857
$\langle x_F \rangle = 0.441$	$0.176 \pm 0.234$	0.815	$0.097 \pm 0.216$	0.733
$\langle x_F \rangle = 0.159$	$0.286 \pm 0.239$	0.957	$0.070 \pm 0.217$	0.799

Table 4.21: The extracted values for  $P_z$  for each year.

### 4.4.3 Systematic Uncertainties.

As with the azimuthal measurements, the dominant systematic uncertainties result from the background and acceptance corrections. Each contribution will be considered in turn.

#### Background Correction.

While the background subtraction is important, the measured number of events in each bin is statistically corrected for it. Ideally, one would investigate the polarization of the background itself. The sidebands of the mass distribution do not provide enough events, unfortunately, to provide a good measure of the polarization. Instead, a conservative estimate was obtained by extracting the polarization with and without the background correction to look for sensitivity, as in Equation 4.9. This was done in all the kinematic bins, for each polarization state, to look at the importance of the background correction.

The results are shown in Table 4.22. The importance of correcting the background is shown for the spin transfer coefficients and for the transverse polarization.  $P_z$ , which was shown to have the most sensitivity to the acceptance by Figure 4.20, is also the most sensitive to the background. This is due to the variation of the background with the acceptance. These estimates are ultimately limited by the statistics of the data sample; the statistical uncertainty on each measurement is approximately that

Kinematics	$\delta\Delta P_x$	$\delta\Delta P_z$	$\delta P_y$
$\langle p_T \rangle = 0.676$ GeV	0.296	0.271	-0.026
$\langle p_T \rangle = 0.311$ GeV	-0.053	0.090	-0.020
$\langle Q^2 \rangle = 3.235$ GeV <sup>2</sup>	0.034	0.283	-0.093
$\langle Q^2 \rangle = 1.431$ GeV <sup>2</sup>	0.142	0.055	-0.107
$\langle z \rangle = 0.613$	0.089	-0.217	-0.117
$\langle z \rangle = 0.365$	0.017	0.323	-0.022
$\langle x_F \rangle = 0.441$	0.107	0.045	-0.090
$\langle x_F \rangle = 0.159$	0.000	0.223	-0.042

Table 4.22: The effect of the background correction on the extraction of each polarization state.

of the data themselves. Consequently, there are spurious effects, such as in  $P_z$ , where a large (small) value is seen in high  $z(x_F)$  and a small effect in high  $x_F$ , whereas it has been shown that the acceptance of these two physical quantities is positively correlated. Another way of stating this is that these differences are not statistically different from zero.

These results are not precise enough to determine uncertainties clearly. Thus, they are used only as a guideline to assign global values for the systematic uncertainties. Conservatively, an absolute background-related uncertainty of 20% was assigned to the spin transfers  $\Delta P_x$  and  $\Delta P_z$ , and a value of 10% is assigned for the contribution to the error on the transverse polarization  $P_y$ . The background apparently produces a false asymmetry in  $P_y$  since all the values are negative. To be exact, the error from this should be asymmetric to compensate for this; however, instead, a conservative symmetric error was assigned.

### Acceptance Correction.

An additional check is provided by the  $K_S$  sample, since symmetry demands that the spin-0 particle has no polarization. The polarization values are as well determined statistically as the  $\Lambda$  events and hence they may be used directly to estimate the systematic uncertainty; they are shown in Table 4.23. These values are all consistent with zero and do not indicate that there are additional poorly understood sources of



systematic uncertainty. Thus, they are consistent with understanding of the acceptance at the precision of the data and do not contribute an additional uncertainty.

Polarization	1996		1997	
	Value	$\chi^2_\nu$	Value	$\chi^2_\nu$
$\langle P_x \rangle$	$-0.046 \pm 0.141$	0.012	$-0.099 \pm 0.134$	0.867
$\langle P_y \rangle$	$-0.082 \pm 0.142$	0.516	$0.020 \pm 0.132$	0.535
$\langle P_z \rangle$	$-0.170 \pm 0.150$	0.715	$-0.048 \pm 0.140$	0.432

Table 4.23: Polarization of the  $K_S$ .

### Misidentification.

Using the results of Section 4.3.2, the contribution to the uncertainty from misidentification was estimated at 5% (absolute).

### Radiative Corrections.

Internal radiative corrections have not been calculated and thus are neglected in this analysis.

Monte Carlo events were analyzed before and after reconstruction in order to understand the external corrections, just as in Section 4.2.4. Figure 4.22 shows histograms in  $\delta(\cos \theta_i) \equiv \cos \theta_i^{rec} - \cos \theta_i^{gen}$  for the directions  $i = x, y, z$ .

These graphs indicate that while the transverse states are not affected very much by radiative corrections, the mean of the  $\delta(\cos \theta_z)$  is shifted to positive values by radiative corrections. No uncertainty is assigned for this correction, as this is small (1%) compared to the other systematic uncertainties.

### Spin Precession.

Because the magnetic field has a finite extent, the influence of the stray field in the region of the target cell on the spin precession can be estimated. The field strength in the region of the target cell is  $\sim 1$  mT [58].

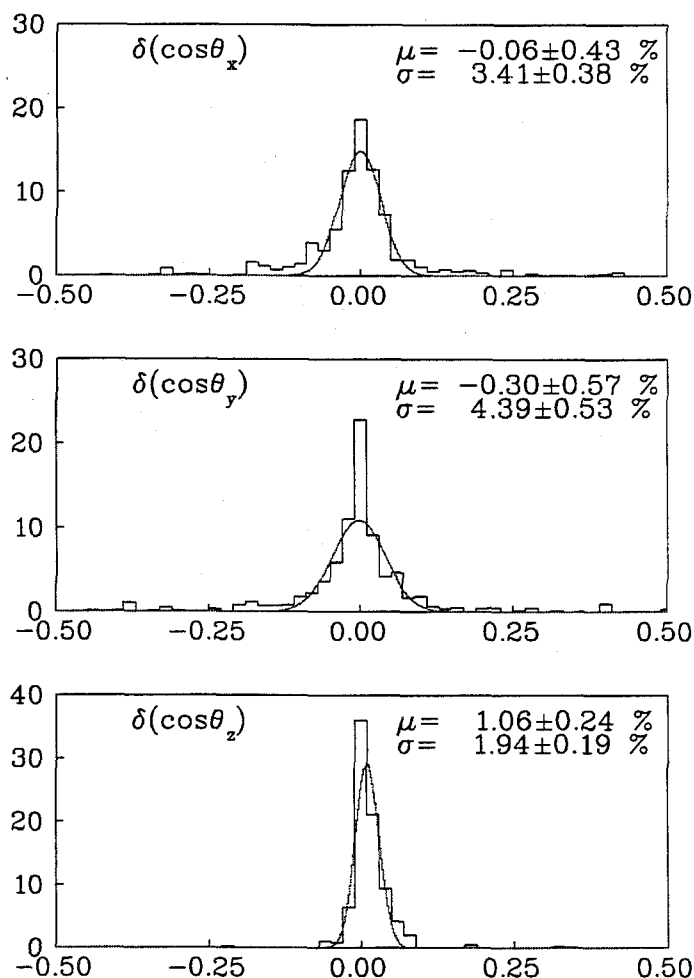


Figure 4.22: Effect of reconstruction on  $\Lambda$  angular distributions. The histograms represent the difference between generated and reconstructed Monte Carlo ( $e, e'\Lambda$ ) events. The graphs show the histograms corresponding, from top to bottom, to  $P_x$ ,  $P_y$ , and  $P_z$ .

This effect can be calculated by solving the elementary quantum mechanics problem of a spin-1/2 particle in a static magnetic field. The precession frequency is  $\Omega = B_z \mu_\Lambda / \hbar$ . Since the magnetic moment  $\mu_\Lambda$  for the  $\Lambda$  is  $0.613 \pm 0.004 \mu_N$ , where  $\mu_N$  is the Bohr magneton ( $\mu_N = e\hbar/2m_p = 3.15 \times 10^{-14}$  MeV/T), the frequency  $\Omega$  is 29 kHz, such that the relevant time constant is on the order of  $30 \mu\text{s}$ . Because the  $\Lambda$  are relativistic with  $\gamma \sim 6$ , they traverse the region of the field in nanoseconds before decaying. Hence this is a negligible contribution to the uncertainty.

### Dilution from $\Sigma$ Particles.

Reference [44] is an excellent guide for a treatment of dilution from  $\Sigma$  particles. In general, a  $\Lambda$  sample is composed of those produced directly by the interaction and the daughters of  $\Sigma$  particles. Following the assumptions in that reference, the authors conclude that dilution is  $\sim 20\text{-}30\%$  and that the interaction-induced polarization is increased somewhat.

Because no attempt is made to model the interaction and reproduce the polarization values exactly, the dilution of  $\Sigma$  particles is, to some extent, irrelevant. The values were not corrected for dilution since they represent the actual measurement extracted by this analysis.

### Other Contributions.

Other factors, discussed previously in Section 4.3.2, include the following:

- Cut selection.
- Kinematic factors.
- Monte Carlo precision.

All of these factors will be neglected, as before. Further, it should be noted that just as the hadron production is isotropic in the Monte Carlo generator, so is the  $\Lambda$  decay.

### Summary of Systematic Uncertainties.

The dominant background and acceptance corrections are listed in Table 4.24. The longitudinal polarization transfer is clearly the most difficult measurement to extract due to the skewed detector acceptance. These uncertainties are all significantly smaller than the statistical uncertainties in each kinematic bin.

Term	$\Delta P_x$	$\Delta P_z$	$P_y$
Background	0.20	0.20	0.10
Misidentification	0.05	0.05	0.05
Total	0.21	0.21	0.11

Table 4.24: Systematic uncertainties for polarization extractions.

#### 4.4.4 Polarization Results.

The results for the spin transfer coefficients are tabulated in Table 4.25 and shown in Figure 4.23 where the average beam polarization of  $+(-)0.55$  in 1996(1997) has been included. An analysis of these data using an asymmetry to construct the longitudinal spin transfer coefficient (thus using a technique independent of detector simulation) has extracted results which agree extremely well with this analysis [73].

Kinematics	$\Delta P_x$	$\Delta P_z$
$\langle p_T \rangle = 0.676 \text{ GeV}$	$0.290 \pm 0.315$	$0.664 \pm 0.531$
$\langle p_T \rangle = 0.311 \text{ GeV}$	$0.056 \pm 0.252$	$-0.011 \pm 0.400$
$\langle Q^2 \rangle = 3.235 \text{ GeV}^2$	$-0.056 \pm 0.287$	$0.241 \pm 0.472$
$\langle Q^2 \rangle = 1.431 \text{ GeV}^2$	$0.296 \pm 0.269$	$0.160 \pm 0.433$
$\langle z \rangle = 0.613$	$0.159 \pm 0.297$	$-0.282 \pm 0.503$
$\langle z \rangle = 0.365$	$0.047 \pm 0.264$	$0.437 \pm 0.403$
$\langle x_F \rangle = 0.441$	$0.105 \pm 0.258$	$0.080 \pm 0.442$
$\langle x_F \rangle = 0.159$	$0.055 \pm 0.298$	$0.253 \pm 0.447$

Table 4.25: Extracted spin transfer coefficients  $\Delta P_x$  and  $\Delta P_z$ .

The fact that  $\Delta P_z$  is consistent with zero indicates that the polarized fragmentation functions are very small, as discussed in detail in Reference [74]. The LEP experiments measured significant longitudinal polarization via the parity-violating  $q\bar{q}Z^0$  interaction; however, this process takes place via a different mechanism and so the results are not easily combined. The LEP experiments represent the process:

$$q \uparrow \rightarrow \Lambda \uparrow$$

whereas the DIS analogue is:

$$\gamma \uparrow + q \rightarrow q \uparrow \rightarrow \Lambda \uparrow$$

where the  $\uparrow$  denotes polarization. The small value for  $P_z$  does not clarify at which

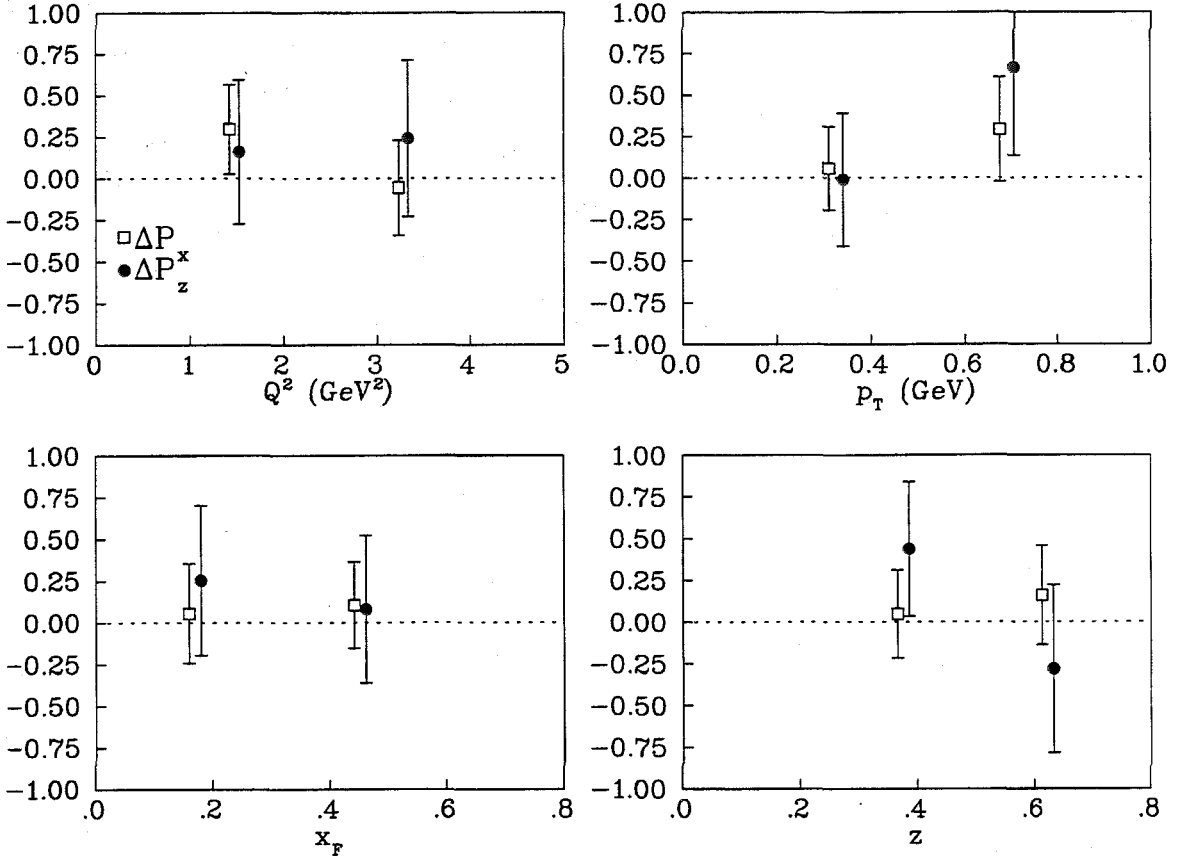


Figure 4.23: Extracted spin transfer coefficients.

point the helicity information is lost. The spin transfer to the unpolarized quark is apparently “inefficient” in that the hadronizing quark does not absorb a large fraction of the longitudinal polarization of the virtual photon. It is further unclear how the different kinematic regimes affect the comparison; the HERMES measurements are largely dominated by the valence  $u$  quarks, whereas the LEP measurements access the sea  $s$  quarks more readily. Assuming that the valence quarks dominate, the well-understood DF’s  $f_1$  for the  $u$  quark may be used to conclude that the polarized FF for  $u$  quarks fragmenting to  $\Lambda$  is small, given Equation 1.30:

$$P_z(x, z)N_\Lambda = P_e \frac{y(2-y)}{1+(1-y)^2} \frac{\sum_i e_i^2 f_1^i(x) G_1^i(z)}{\sum_i e_i^2 f_1^i(x)}. \quad (4.17)$$

Similarly, the observation that  $\Delta P_x$  is consistent with zero suggests that the higher twist fragmentation functions do not dominate the process either.

On the other hand, the transverse polarization  $P_y$ , which does not contain information about the beam helicity, is tabulated in Table 4.26. These values may be compared directly to hadron experiments, as in Figure 4.24. This figure indicates largely how difficult it will be to obtain comparable statistics to make meaningful comparisons to hadron data, although the current measurement suggests that this analysis could provide an interesting connection between electron scattering and hadroproduction. Furthermore, a suggestion of polarization at high  $x_F$  and high  $z$  is seen.

Kinematics	$P_y$
$\langle p_T \rangle = 0.676 \text{ GeV}$	$-0.260 \pm 0.170$
$\langle p_T \rangle = 0.311 \text{ GeV}$	$-0.172 \pm 0.148$
$\langle Q^2 \rangle = 3.235 \text{ GeV}^2$	$-0.119 \pm 0.175$
$\langle Q^2 \rangle = 1.431 \text{ GeV}^2$	$-0.378 \pm 0.147$
$\langle z \rangle = 0.613$	$-0.494 \pm 0.169$
$\langle z \rangle = 0.365$	$-0.110 \pm 0.149$
$\langle x_F \rangle = 0.441$	$-0.429 \pm 0.149$
$\langle x_F \rangle = 0.159$	$-0.126 \pm 0.168$

Table 4.26: The transverse polarization  $P_y$ .

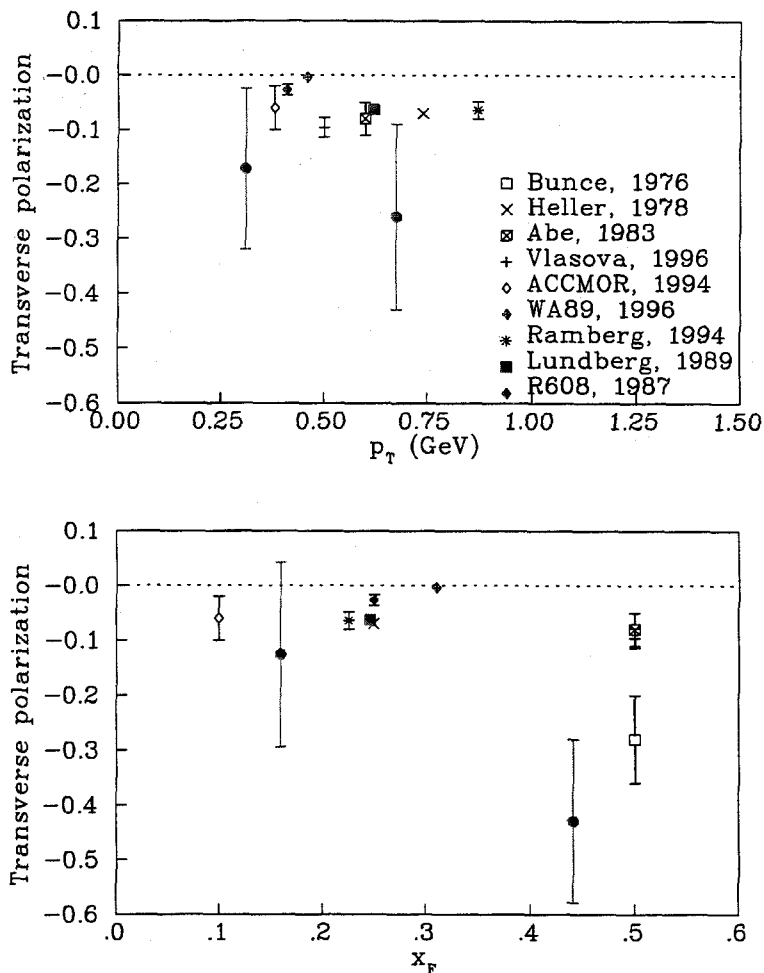


Figure 4.24:  $P_y$  for  $(e, e'\Lambda)$  and hadroproduced lambdas. The filled circles are HERMES data.

As a check of the acceptance, the  $\Lambda$  and  $K_S$  samples are compared in a large range of kinematics. Because the mean of the  $x_F$  distribution is higher for the  $K_S$ , the polarization is evaluated at slightly different values of  $x_F$ . The results are shown in Figure 4.25, in which the  $K_S$  results are consistent with zero across the range, whereas the  $\Lambda$  suggests an effect at high  $x_F$ .

In addition to comparisons with hadroproduction data, studies may be conducted with advance knowledge of the form of  $P_y$  in the language of fragmentation function physics. According to Equation 1.32,  $P_y$  may be expressed as:

$$P_y(x, z)N_\Lambda \sim \frac{M_\Lambda}{Q} \frac{\sum_i e_i^2 f_1^i(x) D_{1T}^{\perp(1)i}(z)}{\sum_i e_i^2 f_1^i(x)}, \quad (4.18)$$

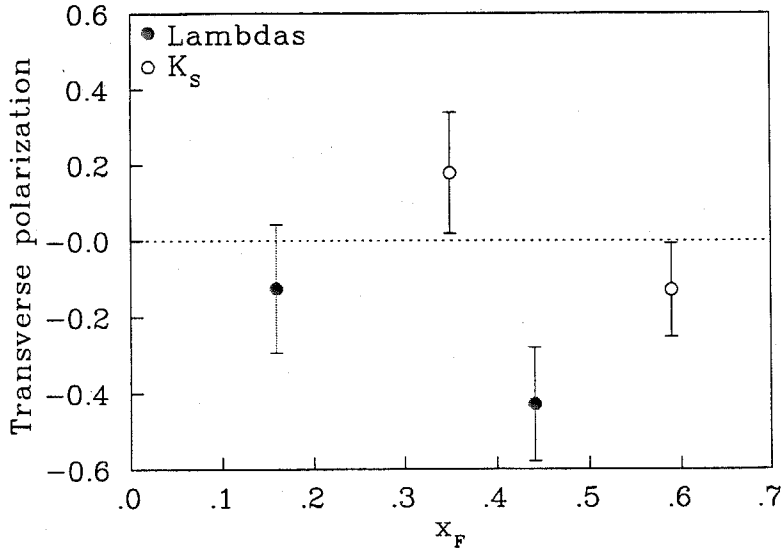


Figure 4.25:  $P_y$  of both  $\Lambda$  and  $K_S$  events.

where the missing proportionality constant is simply a kinematic factor. This suggests that the dependence should vary as  $1/Q$ , as is seen in Figure 4.26.

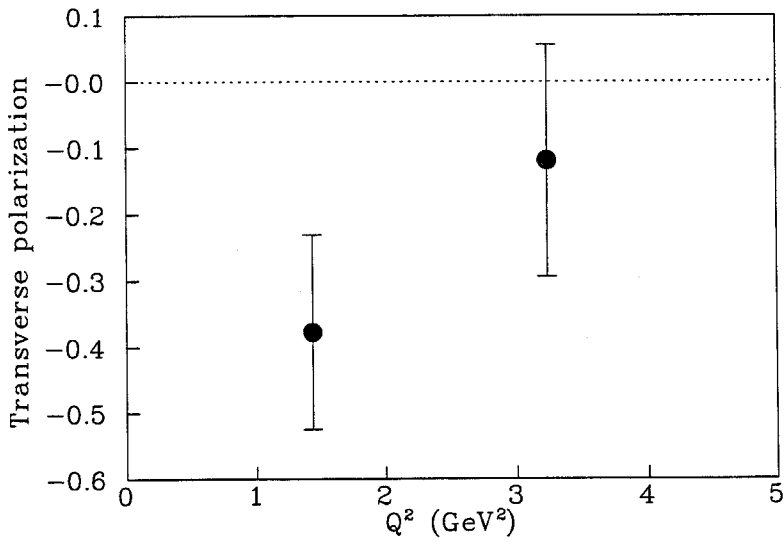


Figure 4.26: Dependence of  $P_y$  with  $Q^2$ .



## Chapter 5 Summary and Conclusions.

Azimuthal distributions were measured in electroproduction of charged pions with unpolarized light gaseous targets. Observed values of  $\langle \cos \phi \rangle$  agree well with previous measurements, although at low  $Q^2$  they do not vary as  $1/Q$ , indicating that simple kinematics are insufficient to explain the  $\langle \cos \phi \rangle$  behavior. The  $\langle \cos 2\phi \rangle$  moments are significantly larger and increase dramatically at low  $Q^2$ ; these two measurements jointly indicate the importance of higher-twist effects in describing azimuthal distributions. The  $\pi^-$  systematically show slightly higher values for  $\langle \cos 2\phi \rangle$  than the  $\pi^+$ , suggesting differences in the DF's or FF's.

Similar measurements were performed for the first time in electroproduction of  $\Lambda$  and  $K_S$ . Unlike pions, the strange particles show very small values for the azimuthal moments, indicating that the kinematic model for the valence quarks is insufficient to describe the hadronization dynamics of these particles.

In addition, this work presents the first search for spin transfer to  $\Lambda$  from a polarized beam. The absence of a clear signature for longitudinal polarization indicates that the polarized fragmentation function is small. Similarly, the transverse spin transfer  $\Delta P_x$  shows no signal, indicating that the higher twist interactions are not large, as expected.

Another new investigation was a search for transverse polarization in  $\Lambda$  production. These measurements suggest that the transverse fragmentation functions become significant at high  $x_F$  or high  $z$ , consistent with hadroproduction observations. This measurement offers additional access to determining the influence of the transverse momentum of the struck quark. Although imprecise, these measurements may be compared to hadroproduction data and a better understanding of final state interactions may be obtained.

These measurements indicate that a variety of interesting physics may be obtained via measurements of azimuthal distributions and that comparisons of pions and

strange particles access the momentum distributions of the valence and sea quarks in a novel fashion. Better background reduction will be achieved in the future with the improved particle identification capabilities implemented in the 1998-9 running cycle. With a polarized target, a complete description of fragmentation functions will become available. In particular, the strange particles offer a new avenue to examine the nucleon sea.

## Appendix A Formalism.

### A.1 The Coincidence Cross Section.

Equation 1.21 gives the azimuthal distribution of particles in a high-energy electron scattering process:

$$\frac{1}{N} \frac{dN}{d\phi} = 1 + Af_1(y)\cos\phi + Bf_2(y)\cos 2\phi + P_e C f_3(y)\sin\phi. \quad (\text{A.1})$$

This form for the distribution is not immediately obvious. Certainly the mathematics leading to this result is identical to that of lower energy ( $e, e'N$ ) experiments, as it results from the contraction of the lepton tensor  $L_{\mu\nu}$  and the hadron tensor  $W_{\mu\nu}$ . Thus, traditional nuclear physics may be used to understand the origin of this expression. Following Reference [75], this tensor analysis will be reviewed here in order to derive the azimuthal distribution. In this discussion, Cartesian coordinates will be denoted by  $\mu$  and  $\nu$ , while spherical coordinates are identified by  $\lambda$  and  $\lambda'$ .

#### A.1.1 The Lepton Tensor.

Initially, the general form for the tensor  $L_{\mu\nu}$  is naturally a  $4 \times 4$  Hermitian matrix; this is trivially reduced to a  $3 \times 3$  matrix by imposing current conservation. The set of nine remaining independent elements may be further reduced with the reflection symmetry  $L_{-\lambda, -\lambda'}^S = (-)^{\lambda-\lambda'} L_{\lambda, \lambda'}^S$ ; this is simply the statement that polarized photons have a preferred axis but no direction. This symmetry reduces the set of nine components to six independent terms.

This tensor is usually expressed in Cartesian coordinates in the laboratory frame, in which the  $x$ - $z$  plane is the electron scattering plane, with the  $z$  direction defined by the incident electron's momentum, and the  $y$  direction is perpendicular to the electron scattering plane. Furthermore, it may be understood by calculating the

photon density matrix  $\rho_{\mu\nu}$  and using the relation

$$L_{\mu\nu} = 2Q^2 \frac{1}{1-\epsilon} \rho_{\mu\nu}, \quad (\text{A.2})$$

where  $\epsilon$  is defined as

$$\epsilon = \left( 1 + 2 \frac{|\mathbf{q}|^2}{Q^2} \tan^2 \frac{\theta}{2} \right)^{-1}. \quad (\text{A.3})$$

$\epsilon$  is a measure of the transverse polarization of the virtual photon because it satisfies the equation  $L_{xx} = \frac{1+\epsilon}{1-\epsilon}$ , thus forming an analogy with the case for real photons propagating along the  $z$  direction with linear polarization of  $(1 + \epsilon)$  in  $x$ , relative to  $(1 - \epsilon)$  along the  $y$  direction. That is, with this definition,  $L_{\mu\nu}$  should reduce to the density matrix for linearly polarized real photons propagating along  $z$ , with strength  $(1 + \epsilon')$  in  $x$  relative to  $(1 - \epsilon')$  along  $y$ :

$$\begin{pmatrix} 1/2(1 + \epsilon') & 0 & 0 \\ 0 & 1/2(1 - \epsilon') & 0 \\ 0 & 0 & 0 \end{pmatrix}. \quad (\text{A.4})$$

With this definition, the lepton tensor element  $L_{zz}$  is given by

$$L_{zz} = -\frac{\omega^2}{Q^2} \frac{\epsilon}{1-\epsilon}, \quad (\text{A.5})$$

which diverges as  $Q^2 \rightarrow 0$ . Thus, it is regulated with the factor  $Q^2/|\mathbf{q}|^2$  by defining the term  $\epsilon_L$  as

$$\epsilon_L = \frac{Q^2}{|\mathbf{q}|^2} \epsilon, \quad (\text{A.6})$$

where the virtual photon four-momentum is written as  $q^\mu = (\omega, 0, 0, |\mathbf{q}|)$ .

The virtual photon's density matrix  $\rho_{\mu\nu}$  may now be written in the following way,

where the ordering in the matrix is  $x, y, z$ :

$$\begin{pmatrix} \frac{1}{2}(1 + \epsilon) & -\frac{i}{2}\sqrt{1 - \epsilon^2} & \frac{1}{\sqrt{2}}\sqrt{\epsilon_L(1 + \epsilon)} \\ \frac{i}{2}\sqrt{1 - \epsilon^2} & \frac{1}{2}(1 - \epsilon) & \frac{i}{\sqrt{2}}\sqrt{\epsilon_L(1 - \epsilon)} \\ \frac{1}{\sqrt{2}}\sqrt{\epsilon_L(1 + \epsilon)} & -\frac{i}{\sqrt{2}}\sqrt{\epsilon_L(1 - \epsilon)} & \epsilon_L \end{pmatrix}. \quad (\text{A.7})$$

This may be compared with the case of a real photon propagating along the  $z$ -axis with circular polarization. In this case,  $\rho_{\mu\nu}$  is given by:

$$\begin{pmatrix} 1/2 & i/2 & 0 \\ -i/2 & 1/2 & 0 \\ 0 & 0 & 0 \end{pmatrix}. \quad (\text{A.8})$$

It is thus evident that circular polarization is manifested in the anti-symmetric components of the photon, and thus the lepton, tensor.

Furthermore, the density matrix  $\rho_{\mu\nu}$  of Equation A.7 shows that virtual photon is in a pure polarization state given by:

$$(\epsilon_x, \epsilon_y, \epsilon_z) = \left( \frac{1}{\sqrt{2}}\sqrt{1 + \epsilon}, \mp \frac{i}{\sqrt{2}}\sqrt{1 - \epsilon}, \frac{|\mathbf{q}|}{\omega}\sqrt{\epsilon_L} \right), \quad (\text{A.9})$$

where the  $\mp$  sign refers to  $\pm$  helicity of the incident electron. Evidently, scattering with electrons yields photons with transverse linear and longitudinal components. If the electrons are polarized, then a circular component is introduced, with a different strength than the transverse linear component. Thus, a virtual photon has a longitudinal component and an elliptical one.

This result lies at the heart of electron scattering. By evaluating the photon tensor in this way, its contraction with the hadron tensor may be calculated to extract a cross section. A decomposition of the cross section for scattering with a virtual photon probe thus directly accesses the helicity structure of the target nucleon. It is also remarkable in that the density matrix for the spin-1/2 electron is directly proportional to that for the spin-1 photon, thus making simple geometric models

available<sup>1</sup>.

### A.1.2 The Hadron Tensor.

The hadron tensor  $W_{\mu\nu}$ , on the other hand, still has nine independent components, as the only demand is that it is Hermitian. In order to extract helicity distributions, two steps must take place. First, the tensors are transformed to spherical coordinates in order to extract helicity information. In the second step, the hadron tensor  $W$ , measured in the laboratory frame, is transformed back to its CM frame (where it is denoted by  $W'$ ). This requires a rotation by the angle  $\phi$  in order to make the electron scattering and hadron production planes coincide, and then a boost along the  $z$  direction. Since the rotation is only in  $x$  and  $y$  and thus does not affect the longitudinal components, the hadron tensor is transformed as follows, introducing a phase:

$$W_{\lambda\lambda'} = e^{i\phi(\lambda-\lambda')} W'_{\lambda\lambda'}. \quad (\text{A.10})$$

The contraction of the two tensors leads to the following coincidence cross section:

$$\frac{d\sigma}{d^3p_h d\Omega dE'} \sim L_{\mu\nu} W_{\mu\nu} \quad (\text{A.11})$$

$$\sim \rho_{\lambda\lambda'} F_{\lambda\lambda'} \quad (\text{A.12})$$

$$\sim \rho_{00} F_{00} + \rho_{11} F_{11} + \rho_{01} F_{01} + \rho_{1-1} F_{1-1} + h(\rho'_{01} F'_{01} + \rho'_{1-1} F'_{1-1})$$

$$= \rho^S F^S + h(\rho^A F^A)$$

where (1,-1) correspond to transverse directions and the symmetric (anti-symmetric) components of the tensors are given by superscripts S (A); the beam helicity  $h$  multiplies the anti-symmetric components. The tensor  $F_{\lambda\lambda'}$  is simply the hadron tensor  $W_{\mu\nu}$  transformed back into the hadron CM frame in a spherical basis. Thus, the

---

<sup>1</sup>Strictly speaking, the spin-one nature of the photon manifests itself in a density matrix which is decomposed into a set of Stokes matrices, or equivalently into rank-two spherical harmonics. However, such a decomposition is not necessary for understanding the reduction of the hadron tensor via geometric symmetries.

phases are contained in the components of  $F_{\lambda\lambda'}$ :

$$\begin{aligned}
 F_{00} &= f_{00} \\
 F_{11} &= f_{11} \\
 F_{01} &= f_{01} \cos \phi + \bar{f}_{01} \sin \phi \\
 F_{1-1} &= f_{1-1} \cos 2\phi + \bar{f}_{1-1} \sin 2\phi \\
 F'_{11} &= f'_{11} \\
 F'_{01} &= f'_{01} \sin \phi + \bar{f}'_{01} \cos \phi
 \end{aligned} \tag{A.13}$$

Traditionally, the response functions  $f_{\lambda\lambda'}$  are expressed in terms of nuclear currents. It is this interpretation that differs for the case of QCD phenomenology; nonetheless, the mathematical derivation is still valid.

The response functions  $f_{\lambda\lambda'}$  may be transformed back to the original hadron tensor  $W_{\mu\nu}$ :

$$\begin{aligned}
 f_{00} &= W_{00} \\
 f_{11} &= W_{xx} + W_{yy} \\
 f_{01} &= \sqrt{2}(W_{0x} + W_{x0}) \\
 f_{1-1} &= W_{yy} - W_{xx} \\
 f'_{11} &= -i(W_{xy} - W_{yx}) \\
 f'_{01} &= -i\sqrt{2}(W_{0x} - W_{x0}) \\
 \bar{f}_{01} &= -\sqrt{2}(W_{0y} + W_{y0}) \\
 \bar{f}_{1-1} &= W_{xy} + W_{yx} \\
 \bar{f}'_{01} &= -i\sqrt{2}(W_{0y} - W_{y0})
 \end{aligned} \tag{A.14}$$

The symmetries of  $W_{\mu\nu}$  may now be utilized in order to understand the coincidence cross section. The major consequences for an unpolarized target follow.

Remembering that the coordinate system is defined with the electron scattering plane as the  $x$ - $z$  plane, the symmetry of the unpolarized target may be exploited.

Since the  $y$ -axis is normal to this plane, components of  $W_{\mu\nu}$  with only one  $y$  index will vanish. Equivalently, all the “barred” structure functions  $\bar{f}_{01}$ ,  $\bar{f}_{1-1}$ , and  $\bar{f}'_{01}$  will disappear, as will  $f'_{11}$ .

If the incident electron is unpolarized, only the symmetric portion of the lepton tensor  $L_{\mu\nu}^S$  may contribute. Consequently, only the symmetric components,  $W_{\mu\nu}^S$ , will survive when the tensors are contracted. This affects only one of those terms that did not vanish by the previous argument: the structure function  $f'_{01}$ . Although it is antisymmetric in its Lorentz indices, it does not refer to the  $y$  coordinate. Thus, it is not required to disappear by the symmetry of the unpolarized target, but because the unpolarized beam forces  $L_{\mu\nu}$  to be symmetric. Thus, if the beam is polarized, this term will reappear. This is the “fifth structure function” of nuclear physics.

### A.1.3 Kinematic Factors.

Thus, under symmetry considerations, the form of the cross section must be the following:

$$\frac{d\sigma}{d^3p_h d\Omega dE'} \sim \rho_{00} f_{00} + \rho_{11} f_{11} + \rho_{01} f_{01} \cos \phi + \rho_{1-1} f_{1-1} \cos 2\phi + h(\rho'_{01} f'_{01} \sin \phi + \rho'_{1-1} F'_{1-1}). \quad (\text{A.15})$$

It remains only to show that the kinematic coefficients are equivalent. By using the relation  $\epsilon = 2(1-y)/(1+(1-y)^2)$ , and ignoring the kinematic factors that distinguish  $\epsilon_L$  from  $\epsilon$ , the expressions for the kinematic functions  $f_i(y)$  from Equation 1.22 may be reduced simply to the following:

$$\begin{aligned} f_1 &= \sqrt{\epsilon(1+\epsilon)/2}, \\ f_2 &= \epsilon/2, \\ f_3 &= \sqrt{\epsilon(1-\epsilon)/2}. \end{aligned} \quad (\text{A.16})$$

By referring to the photon polarization vector of Equation A.9, it is evident that the product  $\sqrt{\epsilon(1+\epsilon)}$  of  $f_1$  refers to  $x$ - $z$ , or  $LT$ , interference. Similarly, the product  $\sqrt{\epsilon(1-\epsilon)}$  of  $f_3$  describes  $y$ - $z$ , or  $LT'$ , interference. The kinematic factor of  $f_2$  scales



with  $\epsilon$ , indicating that it strictly describes transverse components and thus may be referred to as the  $TT$  term.

## A.2 Twist.

Following Reference [2], a definition of twist begins at Equation 1.4, in which the hadronic tensor  $W^{\mu\nu}$  was expanded in terms of currents  $J^\mu$  connecting intermediate states  $|X\rangle$  and the nucleon ground state  $|P\rangle$ . It is possible to rewrite this as the Fourier transform of a commutator:

$$\begin{aligned} 4\pi W^{\mu\nu} &= \sum_X \langle P|J^\mu|X\rangle \langle X|J^\nu|P\rangle (2\pi)^4 \delta(P+q-p_X) \\ &= \int d^4x e^{iq\cdot x} \langle P|[J^\mu(x), J^\nu(0)]|P\rangle. \end{aligned} \quad (\text{A.17})$$

In the deep inelastic ( $Q^2 \rightarrow \infty$ ) limit, this commutator is dominated by  $x^2 \sim 0$ . Thus, it can be expanded in  $x$  around  $x^2 = 0$  as a power series of operators  $\mathcal{O}$  with coefficients  $K_{\mathcal{O}}$ . This is known as the *Operator Product Expansion* (OPE) and is the formal realization of the separation of the scattering amplitude into short- and long-distance physics, as discussed in Section 1.1.4. It is assumed that the commutators are traceless and symmetric in the Lorentz indices (hereafter omitted):

$$[J(x), J(0)] \sim \sum_{\mathcal{O}} K_{\mathcal{O}}(x^2) x^{\mu_1} \dots x^{\mu_{n_{\mathcal{O}}}} \mathcal{O}_{\mu_1 \dots n_{\mathcal{O}}}(0). \quad (\text{A.18})$$

This can be substituted into Equation A.17:

$$4\pi W = \int d^4x e^{iq\cdot x} \sum_{\mathcal{O}} K_{\mathcal{O}}(x^2) x_1^{\mu} \dots x^{\mu_{n_{\mathcal{O}}}} \langle P|\mathcal{O}_{\mu_1 \dots n_{\mathcal{O}}}(0)|P\rangle, \quad (\text{A.19})$$

where the matrix elements are described in the following way, assuming a typical hadronic mass scale  $M$  and a coefficient  $f_{\mathcal{O}}$ :

$$\langle P|\mathcal{O}_{\mu_1 \dots n_{\mathcal{O}}}(0)|P\rangle = P_{\mu_1} \dots P_{\mu_{n_{\mathcal{O}}}} M^{d_{\mathcal{O}} - n_{\mathcal{O}} - 2} f_{\mathcal{O}} + \dots \quad (\text{A.20})$$

The “twist” of the operator  $\mathcal{O}$  is defined as  $t_{\mathcal{O}} \equiv d_{\mathcal{O}} - n_{\mathcal{O}}$ , where  $n_{\mathcal{O}}$  is the spin of the operator. The Fourier transform must now be performed by making the

substitution

$$x^\mu = -2iq^\mu \frac{\partial}{\partial q^2} \quad (\text{A.21})$$

to obtain

$$4\pi W \sim \sum_{\mathcal{O}} \left(\frac{M}{Q}\right)^{t_{\mathcal{O}}-2} \left(\frac{1}{x}\right)^{n_{\mathcal{O}}} f_{\mathcal{O}}. \quad (\text{A.22})$$

Thus the twist, which identifies the order at which  $M$  appears in the decomposition of the matrix element, is equivalent to the power at which  $Q$  appears in the hadronic tensor. The leading operators are of the lowest twist and have  $t_{\mathcal{O}} = 2$ .

In experimental physics, a slightly modified definition is used, where an effect showing a dependence of  $(1/Q^2)^p$  is said to have twist  $t = 2 + 2p$ , which is consistent with the formal definitions and can be used to decompose the matrix element.

### A.3 Notation.

The notation used to identify distribution and fragmentation functions follows that of Mulders [20] and is briefly summarized here.

- Lower case letters refer to distribution functions and upper case, to fragmentation functions. Only the unpolarized fragmentation function is referred to as  $D(z)$  to be consistent with the literature.
- The letter indicates the Lorentz structure of the operator:  $e$  refers to the operators  $1$  or  $i\gamma_5$ ;  $f$  is  $\gamma_\mu$ ;  $g$  is  $\gamma_\mu\gamma_5$ ; and  $h$  is the tensor term  $i\sigma^{\mu\nu}\gamma_5$ .
- The subscript  $1$  identifies a function that is twist-two (as described in Section A.2), while the subscript  $L$  or  $T$  refers to the target spin direction.
- Dynamics are included in terms with a tilde, such that the functions can be split into a “parton” term and an interaction term.
- The superscript  $\perp$  signals explicit presence of transverse momenta.
- The superscript  $(n)$  indicates the weighted moment of the relevant function, where distribution and fragmentation functions are given, respectively, by the following (using  $h_1$  as an example):

$$\begin{aligned}
 h_1^n(x) &= \int d^2\vec{p}_T \left( \frac{p_T^2}{2M^2} \right)^n h_1(x, \vec{p}_T) \\
 H_1^n(z) &= z^2 \int d^2\vec{k}_T \left( \frac{k_T^2}{2M_\Lambda^2} \right)^n H_1(z, -z\vec{k}_T)
 \end{aligned}
 \tag{A.23}$$

## A.4 Interpretation of Observable Asymmetries.

There are many observable azimuthal moments for various combinations of target and beam polarizations. In order to clarify the relations between these terms, Table A.1 identifies some of the leading-twist asymmetries  $\langle W \rangle$ , which are defined as integrated cross sections:

$$\langle W \rangle_{P_B P_T} = \int d\phi d^2 \mathbf{q}_T W(Q_T, \phi, \phi_S) \frac{d\sigma_{P_B P_T}}{dx dy dz d\phi d^2 \mathbf{q}_T}. \quad (\text{A.24})$$

In general  $W$  is also a function of the spin direction of the detected hadron, which is significant for the  $\Lambda$  polarization measurements; however, in this section, only those azimuthal distributions that have been widely considered theoretically and experimentally will be considered.  $P_B$  and  $P_T$  are unpolarized (U), or polarized either longitudinally (L) or transversely (T). The relevant  $DF$  and  $FF$  are identified, along with their behavior under time-reversal (given as  $+/-$ ).

$P_B$	$P_T$	$\langle W \rangle$	$DF$	$T_{DF}$	$FF$	$T_{FF}$
U	U	$\langle 1 \rangle$	$f_1$	+	$D_1$	+
U	U	$\langle \cos 2\phi \rangle$	$h_1^{\perp(1)}$	-	$H_1^{\perp(1)}$	-
L	U	$\langle \sin \phi \rangle$	$e$	+	$H_1^{\perp(1)}$	-
U	L	$\langle \sin 2\phi \rangle$	$h_{1L}^{\perp(1)}$	+	$H_1^{\perp(1)}$	-
U	T	$\langle \sin(\phi + \phi_S) \rangle$	$h_{1T}^{\perp(1)}$	+	$H_1^{\perp(1)}$	-

Table A.1: Single-spin leading-twist observables. The behavior under TR-transformations is given as well.

The first term of this table reflects the unpolarized cross section. The terms in  $\langle \cos 2\phi \rangle_{UU}$  and  $\langle \sin \phi \rangle_{LU}$  were investigated in this thesis. The leading-order term in  $\langle \sin 2\phi \rangle_{UL}$  and the sub-leading order term  $\langle \sin \phi \rangle_{UL}$  were investigated at HERMES recently as well [76], and are related to the asymmetry  $\langle \sin(\phi + \phi_S) \rangle$ , originally discussed by Collins [21]. All the leading-order  $\phi$  moments shown in Table A.1 contain the same TR-odd FF; the TR-even DF's appearing in the same moments must be chirally-odd in order to preserve the total symmetry of the matrix element.

The only sub-leading order term relevant to this work is the  $\langle \cos \phi \rangle_{UU}$  asymmetry,

which contains the sum of  $f^\perp D_1$  and  $f_1 \tilde{D}$ . In the absence of parton interactions, both the non-leading terms will reduce to their leading twist contributions; i.e.,  $f^\perp \rightarrow f_1$  and  $\tilde{D} \rightarrow D_1$ . Thus, the  $\langle \cos \phi \rangle_{UU}$  asymmetry, even at low  $Q^2$ , signals the importance of the dynamics in either the DF or FF (or both).

The formal definitions of the DF's and FF's presented thus far do not easily give any clear physical insight. Instead, as in the derivation of the form of the coincidence cross section, some insight may be gained by returning to more traditional nuclear physics. For instance, at first glance, the difference between  $\langle \cos 2\phi \rangle_{UU}$  and  $\langle \sin 2\phi \rangle_{UL}$  is simply the subscript  $L$  describing the longitudinally polarized target. This is equivalent to the statement that  $\langle \cos 2\phi \rangle_{UU}$  accesses the unpolarized portion of the transversity distribution  $h_1$ , while  $\langle \sin 2\phi \rangle_{UL}$  accesses a specific polarized component.

Together, these DF's may also be discussed in the language of many-body physics by discussing initial-state interactions (ISI). For instance, the difference between  $\langle \cos 2\phi \rangle_{UU}$  and  $\langle \sin 2\phi \rangle_{UL}$  may be seen as a spin-dependent term in the ISI. In fact, in this language, the kinematic effects discussed in Section 1.4 are a consequence of the ISI resulting from confinement.

Similarly, the FF's differ because they reflect final-state interactions (FSI) wherein the struck quark undergoes hadronization. Clearly, this process takes place in a strong field and hence fragmentation is essentially a many-body problem. This is reflected in the production of  $\Lambda$  polarization, discussed in Section 1.4. The spin-orbit effect is a classic example of FSI.

Factorization, then, is equivalent to separating the entire scattering process into ISI and FSI. Asymmetries in unpolarized experiments then are perhaps more intuitive if transverse momentum is included, since transverse effects result from confinement and represent familiar interactions from classical many-body nuclear physics. Similarly, spin-dependent effects may be interpreted in this language as well.

## Appendix B The Target Optical Monitor (TOM).

In 1995, the HERMES experiment measured spin-dependent structure functions with an internal  $^3\text{He}$  target. A novel device for studying the target *in situ*, the Target Optical Monitor (TOM), was constructed and its operation will be reviewed. It was then tested as a luminosity monitor for the polarized hydrogen target. The different electromagnetic environments in which it operated and the ensuing consequences will be discussed here.

### B.1 $^3\text{He}$ Optical Pumping and Polarimetry.

The technique of polarization of  $^3\text{He}$  via optical pumping is well-known [77] and will be briefly summarized. A radio-frequency (RF) discharge is used to produce the metastable  $2^3S_1$  atomic state, while the sample is held in a 30 G guiding field. Circularly polarized 1083 nm laser light is used to produce electron polarization in the metastable state via optically pumping the  $2^3P_0$  level; this polarization is transferred to the nuclei via the hyperfine coupling. A level diagram is shown in Figure B.1.

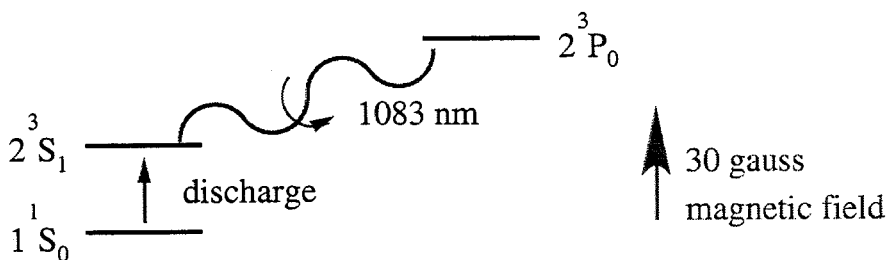
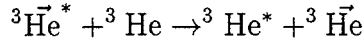


Figure B.1: Level diagram for optical pumping of  $^3\text{He}$ .

The atoms then undergo metastability exchange collisions where they retain their

nuclear polarization in the ground state. That is:



The polarization process takes place in a pumping cell external to the storage ring. In this pumping cell, the discharge also excites the  $3^1D_2$  level, where the hyperfine interaction transfers the nuclear polarization back to the electronic system. The resulting 667 nm photons from the decay to the  $2^1P_1$  state (see Figure B.2 for the levels) have circular polarization; this can be measured and related to the nuclear polarization [78].

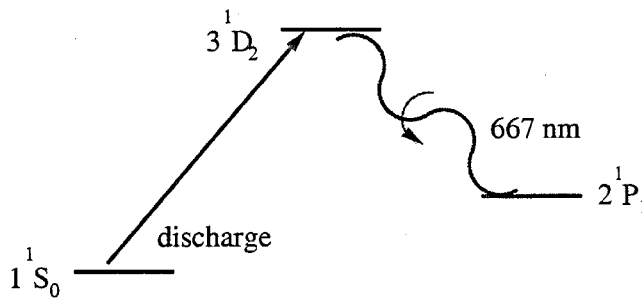


Figure B.2: Level diagram for optical polarimetry of  ${}^3\text{He}$ .

The device performing this analysis is the pumping cell polarimeter (PCP), where the circularly polarized photons pass through a rotating quarter-wave plate, a linear polarizer, and an interference filter centered at 667 nm, as is shown in Figure B.3. This path transforms circularly polarized light into linearly polarized light with intensity that varies in time as a sine wave.

The light then enters a photomultiplier tube. The signal is split and directed into both a DC amplifier and a lock-in amplifier, which measures the AC strength. The nuclear polarization  $P$  is simply given by

$$P = \alpha \frac{AC}{DC}. \quad (\text{B.1})$$

The proportionality constant  $\alpha$  is given by several factors, including the dependence of the nuclear polarization on the pressure in the pumping cell, the magnetic



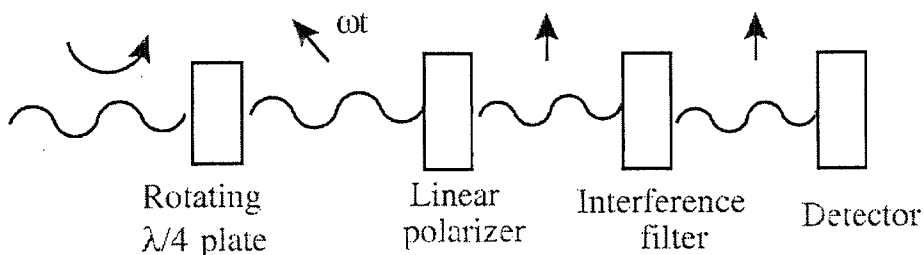


Figure B.3: The optics in the polarimeter. The action of each optical component on the incident light is shown; the intensity of the linearly polarized light varies as a sine wave.

field, and the observation angle. These factors are all determined off-line. The dominant calibration errors result from understanding the proportionality constant  $\alpha$ . In particular, knowledge of the dependence on the pumping cell pressure and the magnetic field contribute 2.0% each to the total error; this calibration was determined with NMR previously [79].

Because of this signal integration, the only uncertainty is systematic rather than statistical. Various contributions are discussed in detail elsewhere [58]; the total relative error on this measurement is 3.4%. The greatest measurement error results from determination of the DC component, as this contains an offset due to the light from the discharge; this level varies over time, contributing 1.4% to the error.

## B.2 The Principle of the TOM.

A schematic demonstrating the configuration at DESY is shown in Figure B.4. While the polarization is well determined in the PCP, the gas travels through a small conduit to reach the storage cell, where no traditional polarimetry can be conducted.

The TOM is a novel solution to the problem of *in situ* measurements of internal targets. It operates on a similar principle as the PCP, as discussed in Reference [80]. Instead of using a RF discharge to excite atomic states, the stored positron beam is used to excite these states via the Coulomb interaction.

The cross section for excitation of an atom of charge  $z$  by a relativistic electron

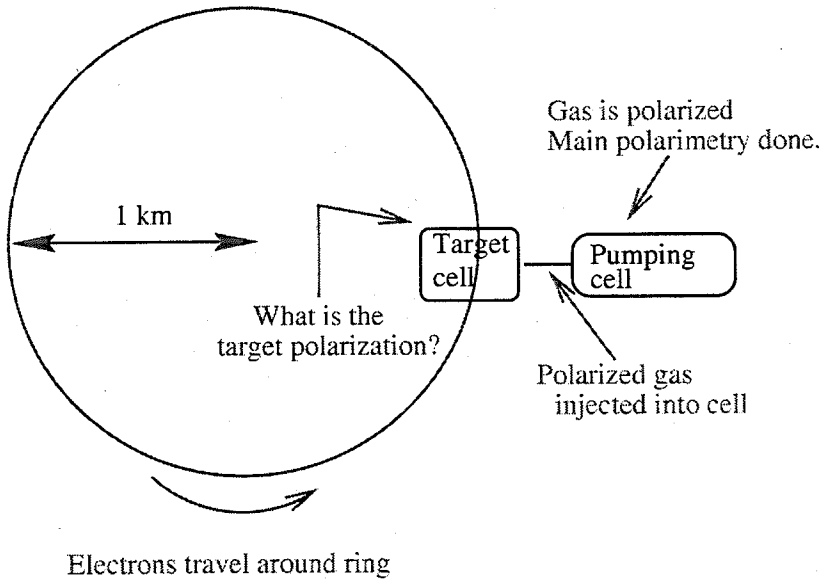


Figure B.4: Polarimetry with an internal target.

to an optically forbidden level  $n$  is given by the following [81]:

$$\sigma_n = \frac{8\pi a_0^2 R z^2}{m_e c^2} b_n. \quad (\text{B.2})$$

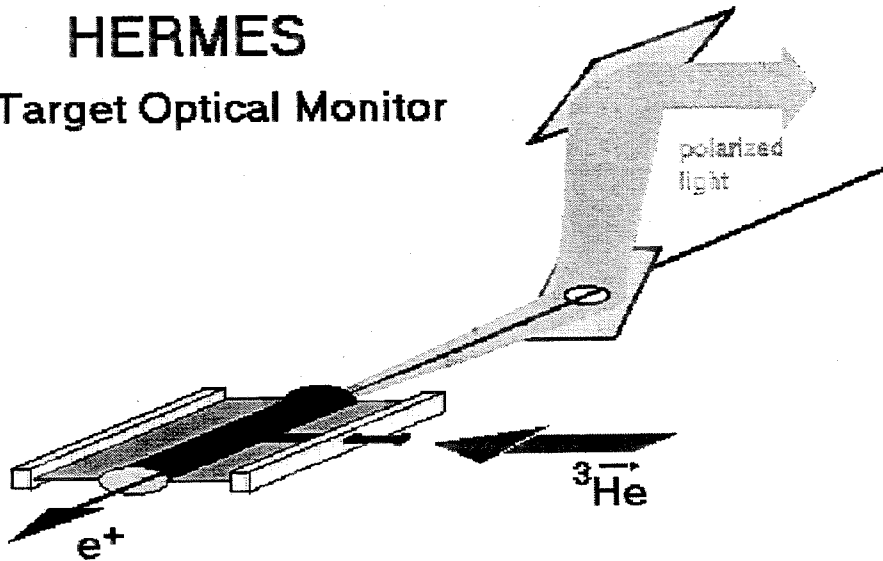
where  $a_0$  is the Bohr radius (0.53 Å),  $R$  is the Rydberg energy (13.6 eV), and  $b_n$  is an empirical constant. On the other hand, for an optically allowed transition to level  $n$ , the cross section is expressed as:

$$\sigma_n = \frac{8\pi a_0^2 R z^2}{m_e c^2} (M_n^2 [\ln(\gamma^2 \beta^2) - \beta^2] + C_n), \quad (\text{B.3})$$

where  $M_n^2$  is related to the oscillator strength  $f_n$  via  $M_n^2 = (R/E_n)f_n$  (for energy  $E_n$  of level  $n$ ), and  $C_n = M_n^2 [\ln c_n + \ln(2m_e c^2/R)] = M_n^2 [\ln c_n + 11.23]$ .

Once the atoms were excited, the backscattered photons from the decay were directed through a mirror assembly, out of the beamline, and into a detector. A schematic of the assembly is shown in Figure B.5, as well as the optical components comprising the TOM.

## HERMES Target Optical Monitor



## TOM Polarimeter Schematic

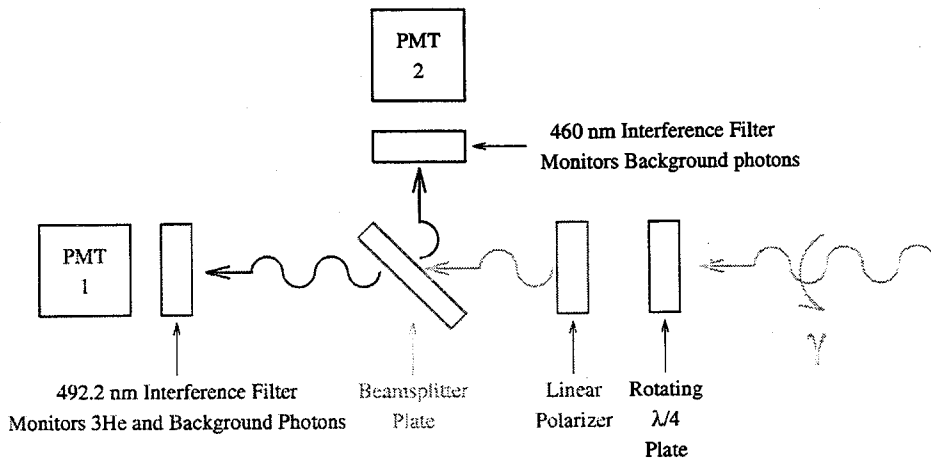


Figure B.5: The principle of the TOM. Top: A drawing of the target cell;  $^3\text{He}$  enters through a thin tube. The backscattered decay photons from the excitation by the beam leave the beamline through a mirror assembly to reach a detector. Bottom: The optical components of the TOM, discussed in more detail in the text.

The apparatus that directed the photons from the beamline to the detector has been described in detail previously [82] and here only the optical components will be discussed. Circularly polarized photons were directed through a rotating quarter wave plate, a linear polarizer, then through a beam-splitter to two phototubes: PMT1, with a 3 nm bandwidth interference filter centered at the central wavelength for the atomic line of choice, and PMT2, with a 10 nm filter at a nearby wavelength to sample the background. Each phototube thus recorded a sine wave with an amplitude proportional to the circular polarization of the incident photons; a rough schematic can be seen in Figure B.6.

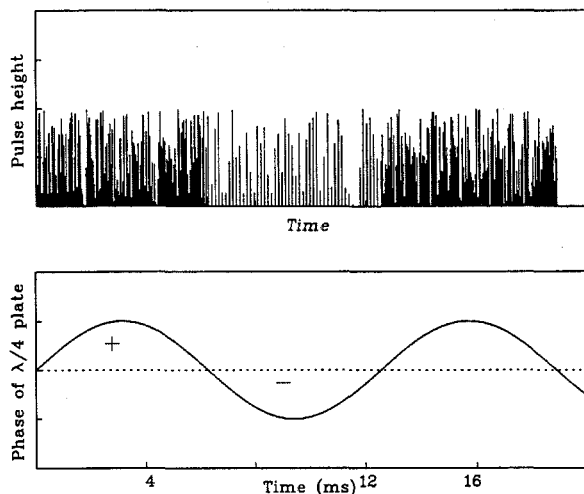


Figure B.6: A schematic representation of the signals. As the quarter-wave plate rotates, the intensity of the recorded light varies as well.

Due to the low rates, single photon counting techniques were used and an asymmetry is constructed:

$$A \equiv \frac{N_+ - N_-}{N_+ + N_-} = \left(\frac{2}{\pi}\right) \left(\frac{1}{1 + B/S}\right) P_\gamma. \quad (\text{B.4})$$

$N_{+(-)}$  refers to the number of counts in the positive (negative) lobe of the sine wave and  $P_\gamma$  is the measured circular polarization. The lobe of the sine wave was identified as follows: The circular mount for the quarter-wave plate had notches cut at 90 degree intervals around the circumference; one of the notches had a mirror inside

it in order to initialize the cycle. A small light source and detector were fixed on the same side of the mount, such that when the sensor received light, it initialized the coincidence circuitry. Then each quarter of the rotation was identified with another signal from the sensor. Thus, photoelectrons were counted for each quarter of the rotation and the appropriate sums and differences could be constructed.

$S/B$  is the signal-to-background ratio (typically 1:2), determined by measuring the rates in both PMT1 and PMT2 with the target empty. Most of the background was seen even with a closed shutter in front of the exit window and hence did not come from optical photons, such as synchrotron light, from inside the beam pipe. The  $S/B$  was also reduced by applying a timing veto, since the number of synchrotron photons in coincidence with the beam pulse swamped the signal by a factor of 100. Consequently, a 20 ns veto was applied, leaving 76 ns in which to detect the decay photons.

## B.3 The Helium Target.

### B.3.1 Spectroscopy.

The  $4^1D_2 - 2^1P_1$  transition (BR=75%) was used to analyze the  $^3\text{He}$  polarization; the level structure is shown in Figure B.7. Its 37 ns lifetime is well suited to the HERA beam structure, since the beam was pulsed in buckets 20 ps in length and incident at 10 MHz. Using the data of Reference [83], in which the energy dependence of the cross section for 0.05-6 keV electrons was shown to follow theoretical models fairly well, an estimate of  $2.7 \times 10^{-23} \text{ cm}^2$  was obtained for the cross section at HERA beam energies.

Because the helium target was operated in a weak magnetic field, the nuclear polarization was again transferred back to the electronic system via the hyperfine interaction. As a result, the decay photons of this excited state were circularly polarized. At the  $4D \rightarrow 2P$  transition, the relation between the circular polarization and the nuclear polarization at low pressures is well characterized by results of Pinard

and Van Der Linde [78].

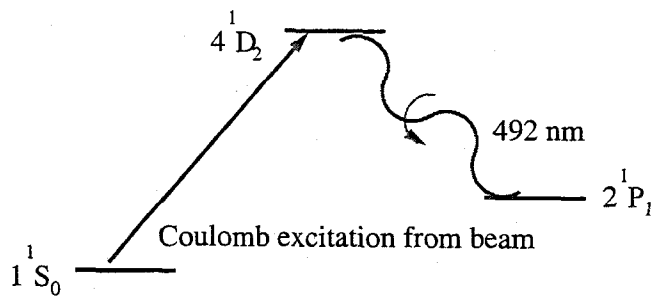


Figure B.7: The level diagram for TOM polarimetry.

The appropriate optics were selected for this measurement: In front of PMT1 lay a 492 nm (3 nm bandwidth) filter; and in front of PMT2, an interference filter centered at 460 nm (10 nm bandwidth). There is no  $^3\text{He}$  line at 460 nm and hence PMT2 was used to sample the background, which was assumed to have roughly the same intensity at that wavelength as at 492 nm.

### B.3.2 Results.

Initially, the rates for the helium target were unexpectedly high. While estimates for the cross section suggested that the expected rates should have been on the order of 80 Hz/mA at 30 mA, the observed rates were, in fact, 250 Hz/mA. This difference was ascribed to excitations taking place via the intermediate  $P$  state. This mechanism had been previously suggested in order to bring theoretical calculations and observed cross sections into agreement [84]. Furthermore, this mechanism explains the observation that the rate in the TOM varied with the current as  $I^2$ , rather than linearly as  $I$ .

Preliminary studies indicated that the measured asymmetry was  $\sim 50\%$  of its expected value, due probably to diffuse reflection of the photons off the cell walls. For this reason, the absolute nuclear polarization could not be computed directly from the asymmetry. On the other hand, the asymmetry could be used to extract a relative polarization measurement when compared to the PCP, providing a useful cross-check as well as additional information regarding possible polarization losses between the pumping cell and the storage cell.

The two phototubes' signals are plotted in Figure B.8. The target cell is filled with gas at  $t=0.5$  h and the 20 minute time structure of the spin flip for the target is clearly visible in PMT1, where the asymmetry clearly changes sign, whereas PMT2 sees no change. Both phototubes measured a non-zero asymmetry even with the target empty, indicating a background with circular polarization. This was perhaps due to synchrotron radiation being reflected downstream of the target, where it picked up a phase to become partially circularly polarized. Because of this large offset in the asymmetry, the magnitude of which varied as a function of beam conditions, the TOM was used as a relative monitor rather than as an absolute polarimeter.

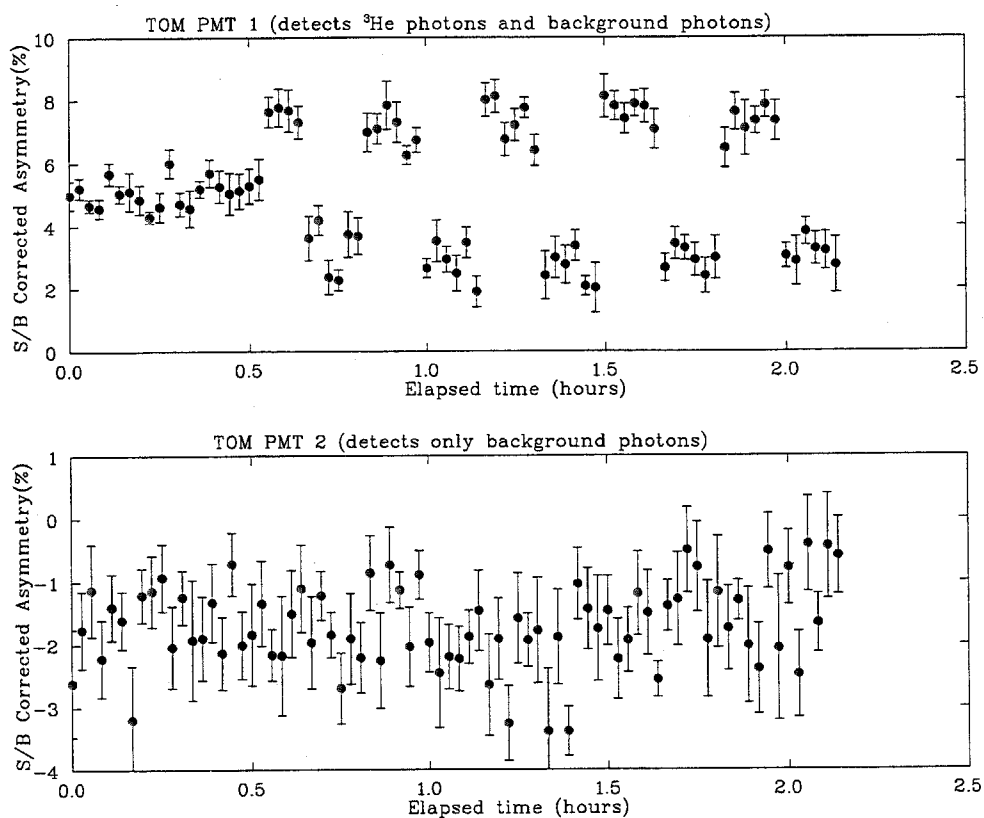


Figure B.8: A comparison of the signal seen in each of the two TOM phototubes. Top: PMT1, which sees the 492 nm  $^3\text{He}$  line and hence clearly sees the structure of the spin flips. Bottom: PMT2, which only sees background light at 460 nm.

In Figure B.9, the polarization measured with the TOM and the PCP are compared; the time structure of the spin flips is again clearly visible. The error bars shown on the TOM are purely statistical and can be reduced to  $\sim 2\%$  over the course of an 8-hour fill, though a systematic error of 6% remains, largely because of the imprecision of the S/B measurement.

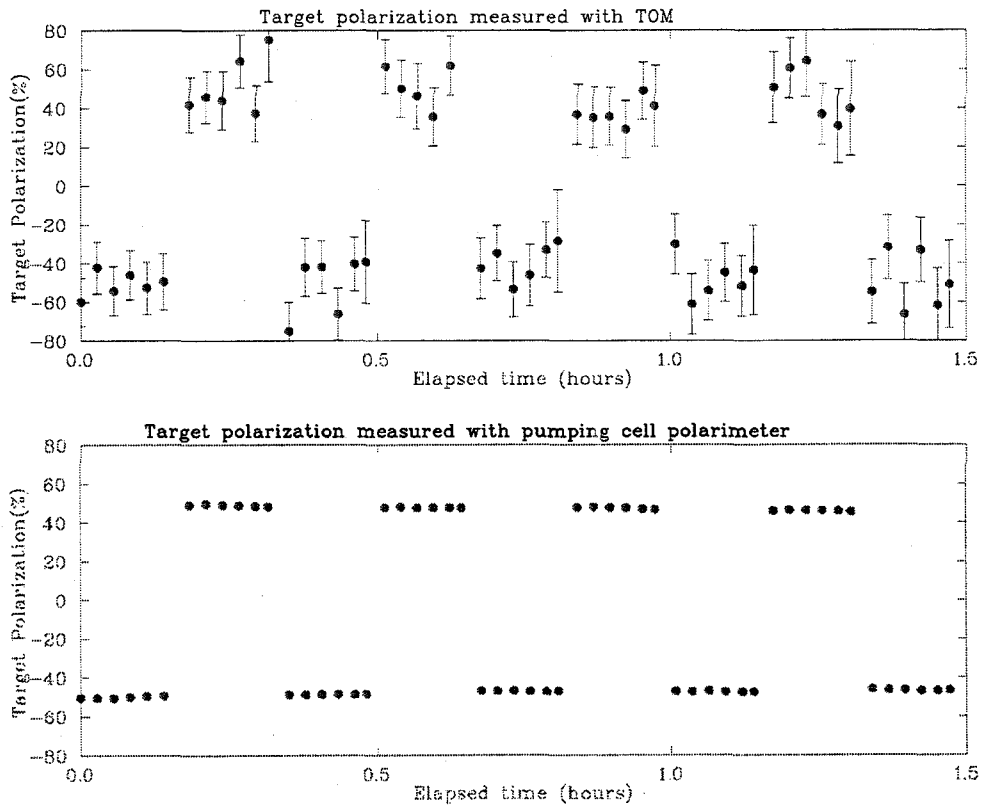


Figure B.9: A comparison of the polarization measured in the TOM versus the measurement in the PCP. The time structure of the helicity flip is clearly seen. The TOM measurement has been normalized to the PCP measurement.



### B.3.3 Search for Depolarization.

By comparing the TOM and the PCP, additional information could be gained regarding possible depolarization mechanisms inside the target. One possible source was the low temperature of the target. For a long elliptical target cell, the gas density varies as  $1/\sqrt{T}$  for temperature  $T$ , indicating that it would be favorable to keep the target cold. At low temperatures, however, there is a possibility that the gas atoms will be slowed down enough such that, when they interact with the surface, there is sufficient time for the spin to relax. Previous experiments on a similar target suggested that such effects would be negligible above 12 K [85]. This was confirmed in the range from 18-60 K, as shown in Figure B.10.

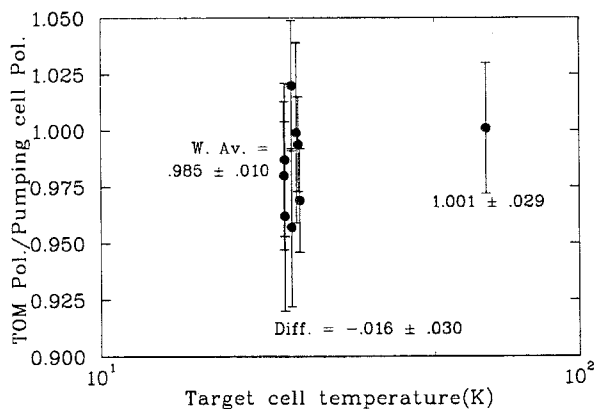


Figure B.10: The ratio of the TOM and PCP polarization measurements as a function of cell temperature. No evidence for depolarization at low temperatures is seen.

Another possible source of depolarization was the transient electromagnetic fields of the 10 MHz pulsed positron beam. The beam properties will be discussed further in Section B.5.1; however, it is sufficient to note that the magnetic fields may reach 60 mT. It is possible that this may disorient the spin vector of the helium nuclei. Since this transient field is directly proportional to the current, this effect may be investigated by studying the dependence of the polarization on the current. This study is shown in Figure B.11, where the relative change in the polarization in the target was measured to be less than 7%. Evidently, the transient magnetic fields did not depolarize the target.

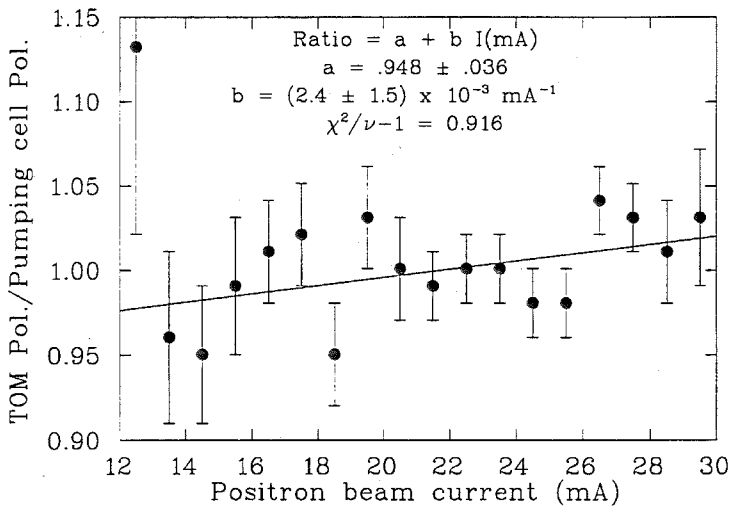


Figure B.11: The ratio of the TOM and PCP polarization measurements as a function of positron beam current. No evidence for depolarization by the beam is seen.

## B.4 The Hydrogen Target.

In 1996, the target gas was no longer  $^3\vec{\text{H}}\text{e}$  but  $^1\vec{\text{H}}$ . Originally, it was intended that the TOM be used as a monitor, using the Balmer  $4p \rightarrow 2s$  transition at 486.1 nm, which has a lifetime of 33 ns and a branching ratio of 28%. The cross section was expected to be much higher since that excitation was optically allowed, unlike the transition used for the  $^3\vec{\text{H}}\text{e}$  target.

The change in hardware provided new constraints for the TOM position and the device was moved accordingly to a position 1.8 m away from the beamline, such that the total optical path length was 2 m; this changed the background rates. An appropriate lens was installed in the TOM beam path to compensate for this change.

The HERMES polarized hydrogen target functioned as an atomic beam source (ABS) [86], wherein gaseous  $\text{H}_2$  was directed through a RF-dissociator to produce atomic hydrogen. The atomic gas was then directed into a sextupole magnetic focusing system, where the two higher hyperfine levels were focused and the lower two states were discarded, thus producing an electron-polarized source. Nuclear polarization was produced by using RF transition units to populate specific hyperfine states.

The atoms were then injected into the storage cell, which was inside a 3.5 T guiding field in which the electronic and nuclear magnetic moments were decoupled. The guiding field was produced by a superconducting solenoid.

There was a significant probability of recombination in the storage cell. The molecular fraction was measured by analyzing the gas exiting the storage cell via a sample tube. Unfortunately, the apparatus measuring the molecular fraction suffered the disadvantage of sampling gas that was not directly in the beam path and which traveled through an additional path along which it might undergo recombination. This measurement suggested that the molecular fraction was  $\sim 10\text{-}20\%$  and contributed a possible depolarization to the atomic sample [87].

Because the magnetic field was designed to decouple the atomic and nuclear polarizations, the TOM, which measured atomic polarization, could not be used to measure the nuclear polarization. It was thought that the TOM could be used as an additional determination of the molecular fraction if the second phototube could be used to monitor the population of  $\text{H}_2$  while the first phototube monitored the  $\text{H}_1$  population. The nuclear density of this target was only  $7 \times 10^{13}$  nucleons/cm<sup>2</sup>, compared to the  $10^{15}$  nucleons/cm<sup>2</sup> of the helium target. Originally, this was not anticipated to be a concern.

A primary question was the choice of an interference filter to select the  $\text{H}_2$  lines [88]. The  $3s \rightarrow 2p$  transition was chosen, as its wavelength of 450 nm was well suited to the characteristics of the phototube already in place in the TOM. An interference filter with 10 nm width was installed to avoid the nearby 434 nm atomic line.

It was soon discovered that the rates in PMT1, which was intended to measure atomic hydrogen, did not vary as expected; namely, they did not vary linearly with the density and current. The variations were much greater than those seen by the luminosity monitor, as seen in Figure B.12. As discussed in Section 2.3.4, the luminosity monitor detects Bhabha scattering. Like the TOM, its rate was proportional to the product of the current and the target electron density; this electron density was naturally assumed to be equivalent to the nucleon density.

The variations in PMT1 were not seen in PMT2, indicating that it was not a

problem with the electronics or of a systemic nature. Rather, the density seen by PMT1 appeared to vary much more greatly than that seen by the luminosity monitor.

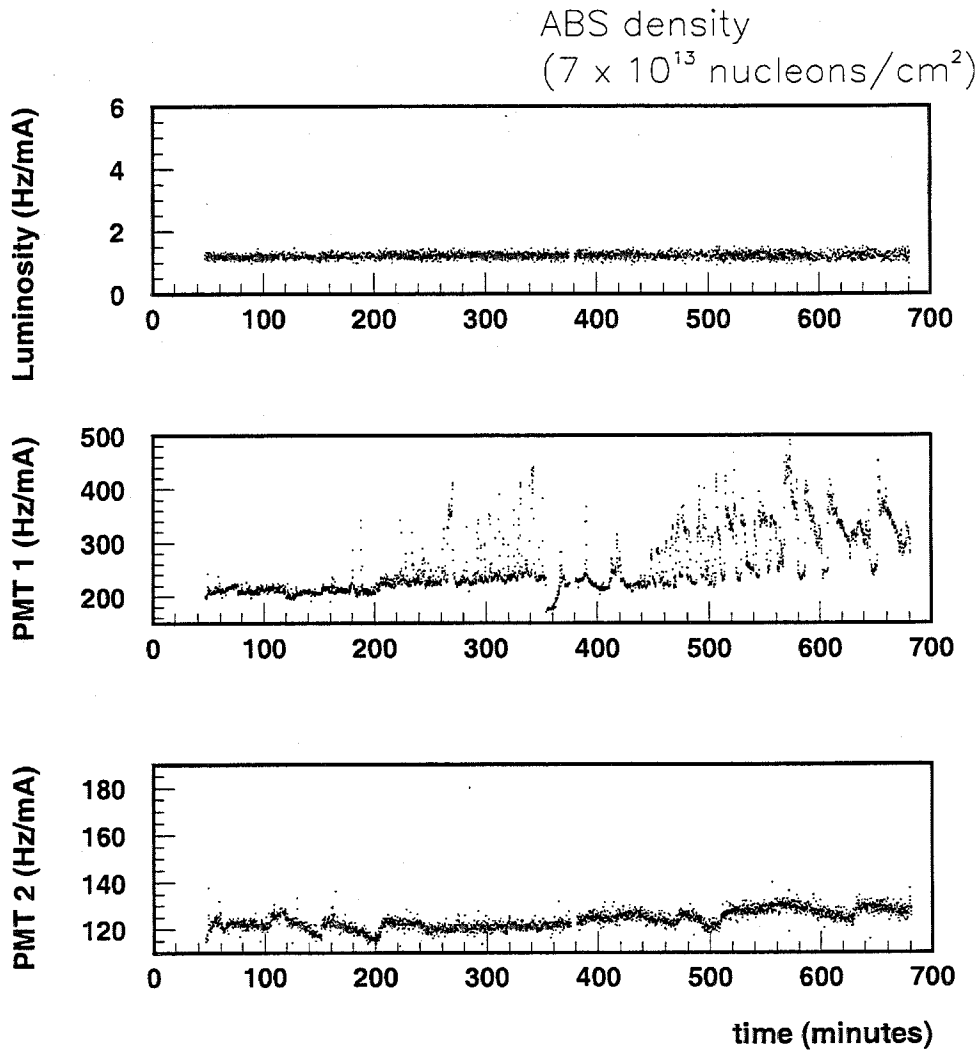


Figure B.12: TOM signal fluctuations with the ABS. The fluctuations in PMT1 were not seen in PMT2 nor in the luminosity monitor.

The background did not show the same fluctuations, as seen in Figure B.13. In these data, a shutter in front of the TOM was closed for ten minutes once every two hours to sample the background well. The background rates were lower by a factor of  $\sim 50$  relative to the helium results. This was attributed to the new position of the TOM; it experienced different conditions in the experimental hall, which was presumably bathed in photons. (A lead sheet surrounds the TOM, but hadronic background could simply induce showers and increase the background rates.) The background counted at a rate of  $\sim 75$  Hz/mA and varied only by 30%, unlike the signal, which varied by  $\sim 250\%$ .

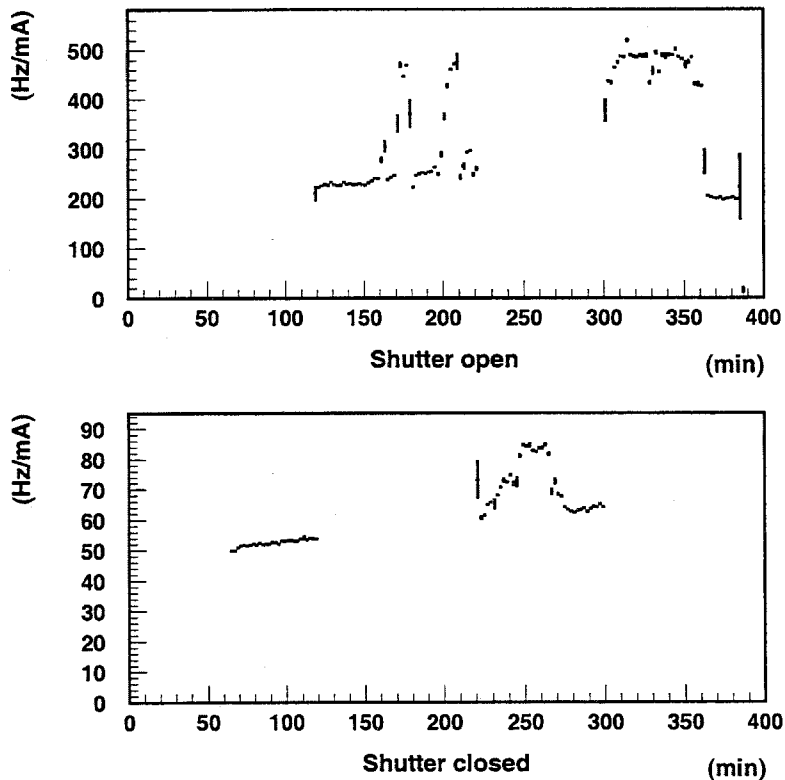


Figure B.13: The rates in PMT1 for shutter open (top) and closed (bottom). The shutter closed results show variations of  $\sim 30\%$ , unlike the shutter open rate, which varies by a factor of 2 or 3.

A very interesting series of observations and measurements followed, motivated largely by C. A. Miller [89]; later, the interpretation of the results was guided prin-

cipally by R. D. McKeown [90]. To both of these authors I am deeply indebted for an understanding of the dynamics of the hydrogen target; the TOM offered a unique opportunity to study the interesting system wherein a relativistic beam ionizes a gas in the presence of a strong magnetic field. Other interactions between the beam and the gas have been considered in Reference [91].

### B.4.1 Rate Dependence on the Magnetic Field.

When the ABS was on, the rates rose slightly as the holding field strength was increased, as seen in Figure B.14. The magnetic field strength was changed by increasing the current to the solenoid and it did not impact the electronics of the TOM at all. The luminosity monitor did not show the same rise, indicating a different density than that measured by the TOM phototube. The apparent difference in measured electron densities remained unclear.

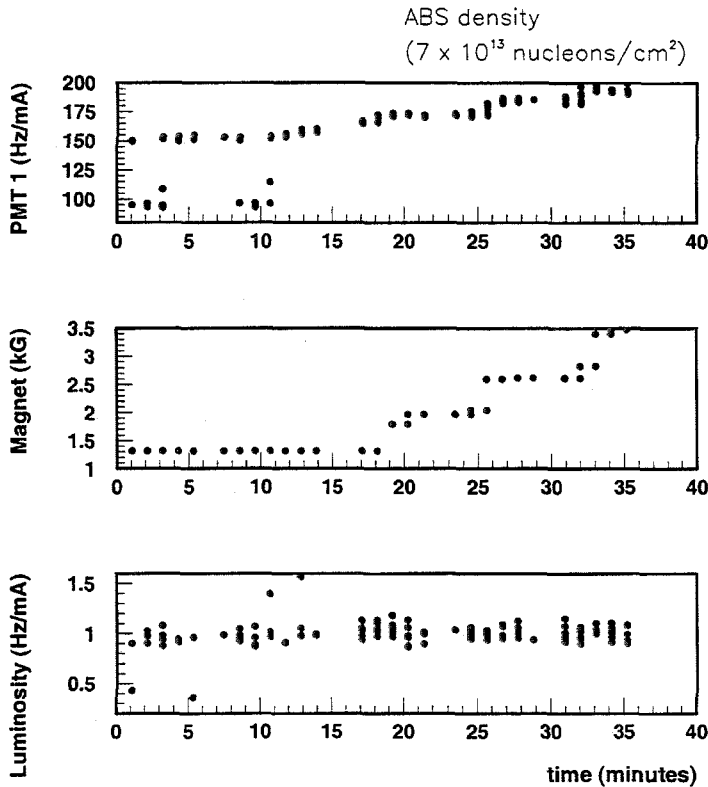


Figure B.14: The PMT1 variation as a function of magnetic field strength with the ABS on.

In order to examine this effect more closely, it was decided to fill the target cell with unpolarized hydrogen, as it could be injected at higher densities as high as  $10^{15}$  nucleons/cm<sup>2</sup>. Once again, the rates varied as a function of the magnetic field strength; in addition, hysteresis was observed when current was lowered again. These results are shown in Figure B.15. Furthermore, enough H<sub>2</sub> was present in the unpolarized gas that PMT2 can detect a signal. If the molecular fraction in the ABS was 15%, then the density of H<sub>2</sub> was only  $10^{13}$  nucleons/cm<sup>2</sup>; the unpolarized gas was operated at a density higher by a factor of 50.

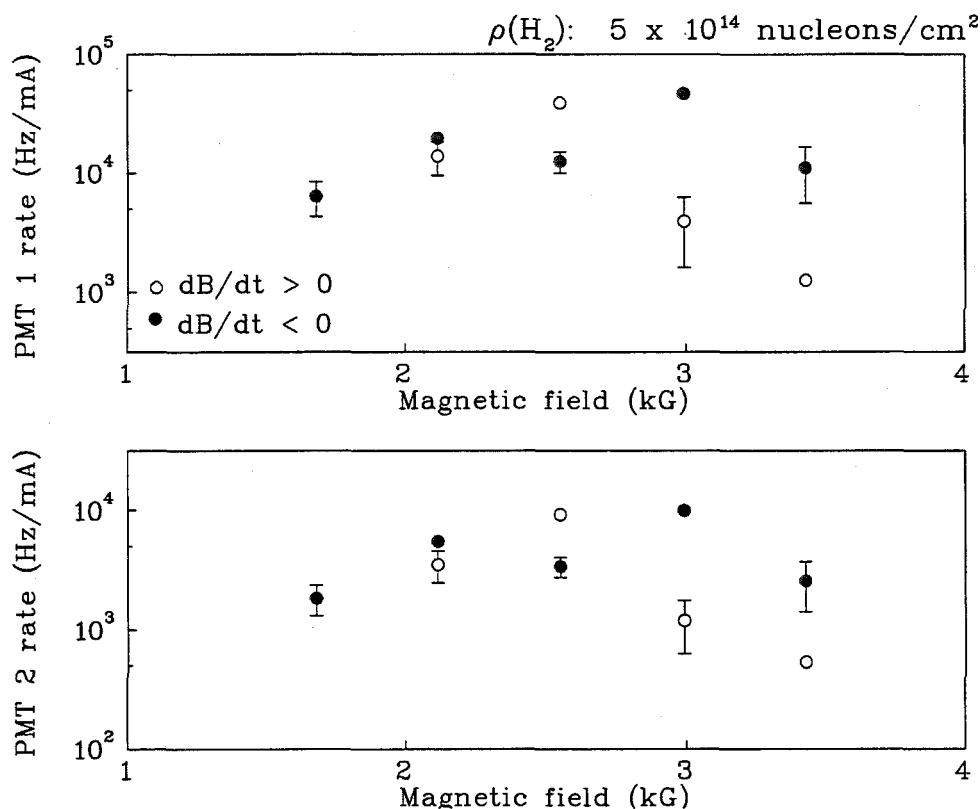


Figure B.15: Signal variation with magnetic field strength with H<sub>2</sub> gas. Unlike the ABS, there was sufficient H<sub>2</sub> in the unpolarized target that PMT2 can detect a signal. It sees the same hysteresis and magnetic field dependence as PMT1.

#### B.4.2 The “Amplifier” Effect.

The results of Section B.4.1 showed that there were insufficient electrons in the ABS output to excite the H<sub>2</sub> electrons at a rate that could be detected by PMT2. Fur-

thermore, the variation of the PMT1 signal with magnetic field indicated that the density of excited electrons varied with field strength.

In an interesting test, unpolarized helium was injected simultaneously with the ABS gas in order “amplify” the ABS signal by providing additional electrons. This was possible because the ABS output enters the target cell through a different valve than the unpolarized gases. Helium was chosen because no lines exist in the bandwidth of these interference filters, unlike the other available gases,  $H_2$  and  $D_2$ .

The interesting results are shown in Figure B.16. PMT1 did not see anything from the helium alone, whereas with the ABS on simultaneously, the rate was higher by an order of magnitude than that seen with the ABS alone (seen earlier in Figure B.12). Similarly, whereas PMT2 counted at 100 Hz/mA with just the ABS on, and 200 Hz/mA with only helium in the target cell, the result with the two gases flowing simultaneously was 800 Hz/mA rather than just the sum. In addition, the rates in both phototubes varied with magnetic field strength again. Non-linear phenomena were becoming increasingly evident in this system.

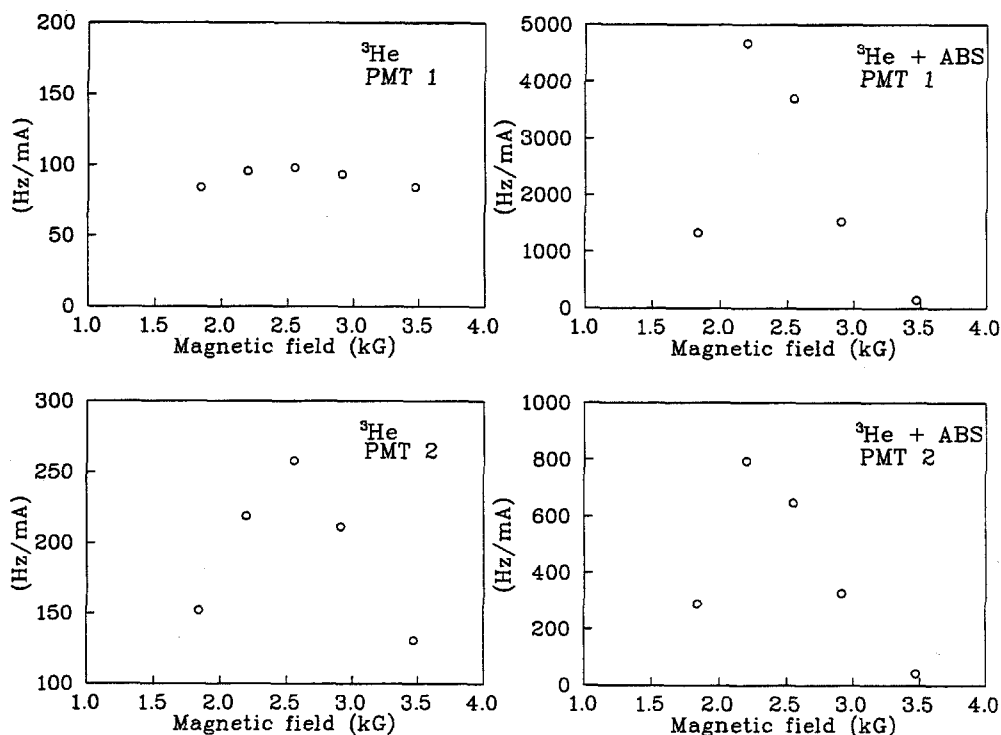


Figure B.16: The “amplifier” effect in a target filled with  $^3\text{He}$  and the ABS output.



### B.4.3 Dependence on the Density.

The results of Sections B.4.1 and B.4.2 suggested that the electron density varied tremendously in these tests. Since it was not possible to increase the density of the ABS alone, the next step was to vary the density of unpolarized  $H_2$ . This measurement was performed at 2.2 kG, the magnetic field strength at which the rates were highest in the studies of Figure B.15 and Figure B.16. The results are shown in Figure B.17, in which the rates increased non-linearly with the gas density.

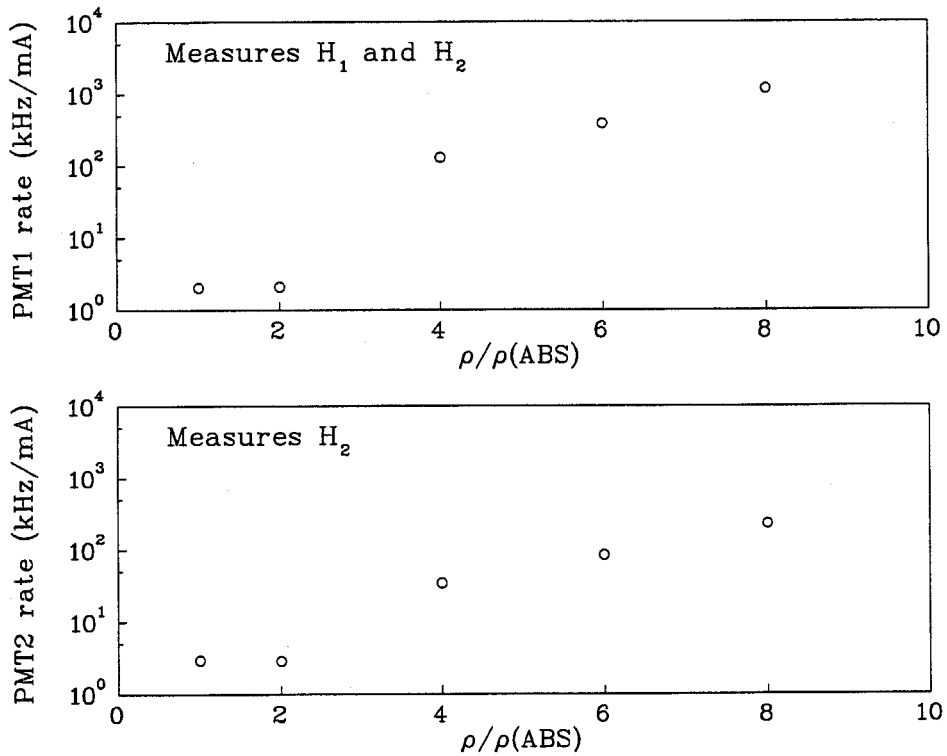


Figure B.17: Rates in both phototubes as a function of unpolarized gas density. All measurements were taken at 2.2 kG.

## B.5 Interpretation of the Hydrogen Results.

### B.5.1 Beam Properties.

The results shown in the previous section were not easy to interpret. The target gas apparently experienced interactions that varied non-linearly with magnetic field strength and target density. In order to explain these results, an understanding of the incident positron beam was necessary.

At a typical current of 30 mA, the 27.5 GeV positron beam has an associated magnetic field such that the field lines loop around the beam axis. At 0.01 cm, the approximate beam size, the magnetic field strength is  $\sim 60$  mT due to the 10 MHz time structure of the beam. Meanwhile, it also has an associated electric field, with lines extending radially from the beam axis. Since for a relativistic beam  $|E| \rightarrow c|B|$ , the electric field has a strength of  $\sim 2$  kV at a distance of 0.01 cm. Electrons trapped in this electric field will have then, on average, energies in the vicinity of several hundred electron-volts.

### B.5.2 Ionization.

Ionization may be described empirically by the following equation:

$$\begin{aligned} d\sigma/dE &= n\pi a_0^2 \frac{1}{\chi\epsilon} F(Z, \epsilon/\chi) & (B.5) \\ &= 1.63 \times 10^{-14} \frac{1}{\chi^2} q. \end{aligned}$$

where  $a_0$  is the Bohr radius;  $\chi$  is the ionization energy;  $\epsilon$  is the incident electron energy;  $n$  is the number of incident electrons; and  $Z$  is the charge on the ionized atom.  $q = (\chi/\epsilon)F(Z, \epsilon/\chi)$ , where  $F$  has been measured experimentally at low  $Z$  and calculations have been performed for infinite  $Z$ . Measurements are shown in Figure B.18 (taken from Reference [92]), where the results agree well with calculations and data shown in Reference [93].

For molecular hydrogen, data exist over a greater energy range, where it is seen

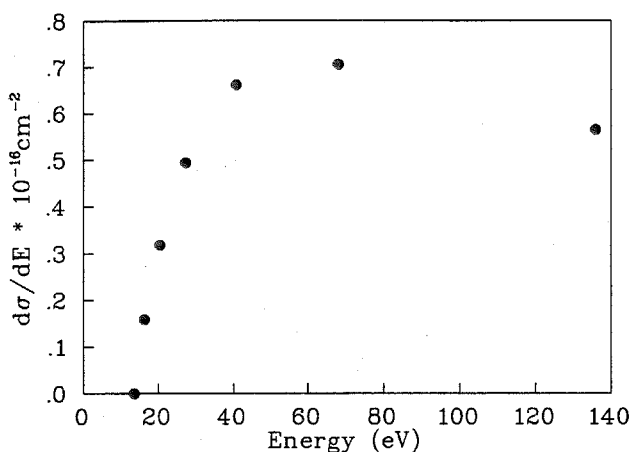


Figure B.18: Ionization cross section of atomic hydrogen. Taken from Reference [92].

in Figure B.19 that the peak ionization energy is still in the vicinity of 100 eV.

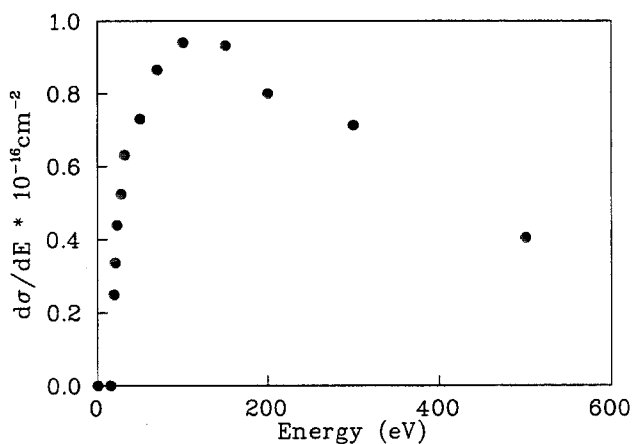


Figure B.19: Ionization cross section of molecular hydrogen. Taken from Reference [94].

An average cross section for ionization of hydrogen atoms may be estimated at  $0.5 \times 10^{-16} \text{ cm}^2$ . Combining this cross section, the ABS target density of  $7 \times 10^{13} / \text{cm}^2$ , and a 30 mA beam at 10 MHz, the ion production rate is  $7 \times 10^{12} / \text{s}$ ; this leads to  $7 \times 10^5$  ions produced per beam pulse. This process liberates electrons held in the electric field. Meanwhile, the ions inherit the kinematics of the parents and, at the cell temperature of 80 K, the kinetic energy of the ions is on the order of 7 meV.

Perhaps 10% of the electrons trapped in the field will have an energy of 70 eV,

where there is a peak in the ionization cross section. The associated momentum is then  $p_{\perp} = \sqrt{2mE} \sim 8 \text{ keV}$ . This is transverse to the beam direction because of the radial direction of the electric field lines.

### B.5.3 The Magnetic Mirror Effect.

The 0.35 T longitudinal holding field will force the electrons to orbit the beam axis. The cyclotron orbit period  $T_c$  is inversely proportional to the strength  $B$  of the magnetic field and is given by the following equation, for  $B$  in Tesla and  $T_c$  in seconds:

$$\begin{aligned} T_c &= \frac{2\pi}{e/mB} \\ &= 3 \times 10^{-11} / B. \end{aligned} \tag{B.6}$$

For  $B$  fields on the order of 1 T, the cyclotron orbit period approaches the beam bucket length of 20 ps. In this case, the electron orbits the beam axis during the entire duration of the transient electric field. Consequently, the electric field's attempt to push the electron radially toward the wall averages to zero over the electron's orbit around the beam axis.

This orbit takes place at the Larmor radius of  $p_{\perp}/(qB) = 0.016 \text{ cm}$ ; thus, the electron is placed at exactly the edge of the beam pulse<sup>1</sup>. The transverse velocity  $v_t$  is given by  $\beta_{\perp} = p_{\perp}/m = 0.016$ , giving a velocity of  $\sim 5 \times 10^8 \text{ cm/s}$ .

The non-linear variations of the TOM signal suggested that the electron density was augmented in an unexpected fashion. With the two orthogonal magnetic fields (one varying in time and a constant component), it is possible to have an environment in which the electrons are trapped if they satisfy the magnetic mirror criterion [62]:

$$v_l/v_t < \sqrt{B_{max}/B_{min} - 1}. \tag{B.7}$$

---

<sup>1</sup>The helium target was placed in a field lower by a factor of 100; for this reason, the cyclotron orbit period was correspondingly 100 times longer and hence the electron could execute only a fraction of a complete orbit before the beam pulse disappeared. Furthermore, such an electron would orbit at a distance of 2 cm instead and hence was not close enough to experience the higher field strength of the beam. Because its ionization cross section looks quite similar to that of hydrogen [93], in a different electromagnetic environment helium could also experience these effects.

This equation applies to longitudinal (transverse) velocities of  $v_l$  ( $v_t$ ) and maximum (minimum) values of the magnetic field of  $B_{max}$  ( $B_{min}$ ). The magnetic field produced by the superconducting solenoid varied by 2.5% at the center of the magnet, where the density profile was highest. Assuming that the electrons are trapped, this implies a longitudinal velocity of  $v_l = (\sqrt{0.025})(5 \times 10^8 \text{ cm/s}) = 8 \times 10^7 \text{ cm/s}$ . Therefore, it would take only  $20 \text{ cm}/(8 \times 10^7 \text{ cm/s}) = 0.25 \mu\text{s}$  to leave the target.

The 10 MHz beam returns only  $0.1 \mu\text{s}$  later, while the electron has only traveled  $(8 \times 10^7 \text{ cm/s})(10^{-7} \text{ s}) = 8 \text{ cm}$  in this time. The electric and magnetic fields return and perform the same exercise again, redirecting the longitudinal and transverse momenta, such that the electron's momentum vector is reoriented. Consequently the electron undergoes a random walk with step size  $d = 8 \text{ cm}$ . For a random walk with  $k = d_{total}/d_{step}$ , the average number of steps is  $k^2$ . Thus the random walk has  $(20 \text{ cm}/8 \text{ cm})^2 = 6.25$  steps, on average. As a result, the total path length traveled is  $d_{travel} = (6.25 \text{ steps})(10 \text{ cm/step})/\beta_{\perp} = 4 \times 10^3 \text{ cm}$ .

Because the magnetic field caused by the beam cannot be controlled experimentally in these measurements,  $v_l$  does not change. The holding field, in contrast, may be changed. At small fields, the electrons have larger orbits and may land on the cell surface. Because of the larger orbit, they absorb less energy from the electron beam and  $v_t$  decreases. It is then harder to satisfy Equation B.7.

On the other hand, with an increased holding field, the cyclotron radius decreases and forces the liberated electrons to be closer to the beam. At this point, the electrons are deeper in the potential well created by the beam and thus they are ionized with more energy; the result is that  $v_t$  increases as well. This is possible until fields are reached that are too high; at this point, the electron's orbit period approaches that of the beam pulse and hence it gains no energy from the transient field. Therefore, with high enough fields, the electron is actually less affected by the incident beam.

These conclusions together imply that an intermediate field strength exists such that the electron absorbs significant energy from the beam but not so much that it is thrown into the cell wall or dragged out of the cell longitudinally. This set of conditions appears to be fulfilled at 2.2 kG, according to the results shown in

Sections B.4.1 and B.4.2.

### B.5.4 The Density Dependence of the Chain Reaction.

The discussion of Section B.5.3 suggest that the rates should vary as a function of longitudinal magnetic field strength. On the other hand, the density dependence of the intensity was not yet explained by this analysis. The non-linear dependence of the signal on the density indicates that a chain reaction was triggered at densities between  $7 \times 10^{13} \text{ cm}^{-2}$  (the ABS density) and densities of  $10^{15} \text{ cm}^{-2}$  (unpolarized gas densities). The “flickering” of this signal should be understood in terms of simple gas kinetic theory.

The ABS gas density is  $7 \times 10^{13} \text{ nucleons/cm}^2$ ; in a target cell 40 cm long, the volumetric density  $\rho$  is  $(7 \times 10^{13} \text{ cm}^{-2})(40 \text{ cm})^{-1} \simeq 2 \times 10^{12} \text{ cm}^{-3}$ . In this gas, the mean free path  $\bar{d}$  will be given by  $\bar{d} \simeq 1/(\rho r_m^2)$  for molecules of size  $r_m$ . For diatomic hydrogen molecules,  $r_m$  will be roughly the same size as one molecule; that is,  $r_m \sim 1 \text{ \AA}$ , such that  $\bar{d} \simeq 5 \times 10^3 \text{ cm}$ .

Each freed electron will release more electrons; the average number of excess electrons is  $n_{excess} = \bar{d}/d_{travel}$ . At the ABS density,  $n_{excess} = 5 \times 10^3 \text{ cm}/4 \times 10^3 \text{ cm}$ , or  $n_{excess} = 1.2$  electrons, thus barely provoking a chain reaction.

In general, the chain reaction will take place if  $\bar{d} \geq d_{travel}$ , with  $d_{travel}$  defined by the beam properties and  $\bar{d}$  set by the target density. Therefore, the chain reaction will occur if the following condition is satisfied

$$\rho_c = \frac{1}{r_m^2 \bar{d}} \quad (\text{B.8})$$

for critical density  $\rho_c$ . Under the current configuration,  $\rho_c$  must be  $2.5 \times 10^{12}/\text{cm}^3$ , which is an areal density of only  $10^{14} \text{ cm}^{-2}$ . This agrees very well with the results of Figure B.17, which shows a threshold density of  $\rho_c = 4\rho_{ABS} \sim 3(7 \times 10^{13} \text{ cm}^{-2}) \simeq 2 \times 10^{14} \text{ cm}^{-2}$ .

## B.6 Summary and Conclusions.

The TOM was the first *in situ* monitor of a polarized internal gas target. By detecting the polarized photons of radiative decays, the TOM measured the atomic polarization of these targets as well as the luminosity.

In 1995, the TOM functioned well as a relative monitor of the nuclear polarization of the helium target. Synchrotron backgrounds were high and there was a polarized contribution to the background, thus making it impossible to use for absolute polarization measurements. It did, however, provide an excellent set of complementary measurements to the traditional polarimeter. In addition, it was possible to search for sources of depolarization.

In 1996, the target gas was hydrogen, rather than helium. The high guiding field needed for this target created a new environment in which a plasma was formed. This was evident by consideration of the dependence of the TOM luminosity on the magnetic field strength, as well as on the density. These observations were understood in terms of simple kinetic models. Because of the limited density of the ABS, the TOM could not be used to monitor the molecular hydrogen population. In addition, the instability of the signal made it difficult to use as an additional luminosity monitor.

The TOM did, however, shed light on the interesting electromagnetic environment created by the beam passing through a gas held in a high magnetic field. Evidently, this was a complicated system needing precise numerical modeling; however, the broad aspects of the results could be interpreted through straightforward physical models.

The use of the TOM for luminosity measurements in atomic hydrogen gas targets was not excluded by these observations. Presumably such a target will always require a strong holding field on the order of 2 kG. At another facility, however, the electron beam may differ considerably; namely, if it had a different time structure or peak beam current, the instabilities seen here could be reduced.

## Bibliography

- [1] F. Halzen and A.D. Martin. *Quarks and Leptons*. J. Wiley and Sons, 1984.
- [2] R. L. Jaffe, 1995. Lectures for the International School of Nucleon Structure, Erice.
- [3] J. Levelt and P.J. Mulders. *Phys. Rev. D*, 49:96, 1994.
- [4] T. Sloan, G. Smadja, and R. Voss. *Phys. Rep.*, 162:45, 1988.
- [5] K. Ackerstaff, *et al.* (HERMES Collaboration). *Phys. Lett. B*, 383:404, 1997.
- [6] K. Ackerstaff, *et al.* (HERMES Collaboration). *Phys. Rev. Lett*, 82:3025, 1999.
- [7] R. Jakob, P.J. Mulders, and J. Rodrigues. hep-ph/9707340.
- [8] R. K. Ellis, W. Furmaski, and R. Petronozio. *Nucl. Phys. B*, 212:29, 1983.
- [9] D. Boer, R. Jakob, and P.J. Mulders. *Nucl. Phys. B*, 504:345, 1997.
- [10] P.J. Mulders. In *Conference on Perspectives in Hadronic Physics*, Trieste, 1997. hep-ph/9707339.
- [11] S. Boffi. In *Lectures for the Second Winter Course of the Scuola su Interazioni Elettromagnetiche con gli Adroni ad Energi Intermedie*, Folgaria(Trento), 1991.
- [12] Robert N. Cahn. *Phys. Lett. B*, 78:269, 1978.
- [13] Howard Georgi and H. David Politzer. *Phys. Rev. Lett.*, 40:3, 1978.
- [14] R. D. Peccei and R. Rückl. *Nucl. Phys. B*, 162:125, 1980.
- [15] Junegone Chay, Stephen D. Ellis, and W. James Stirling. *Phys. Rev. D*, 45:46, 1992.



- [16] K.A. Oganessyan, *et al.* *Eur. Phys. J. C*, 5:681, 1998.
- [17] D. Boer and P.J. Mulders. hep-ph/9711485.
- [18] E.L. Berger. *Z. Phys. C*, 4:289, 1980.
- [19] A. Brandenburg, V.V. Khoze, and D. Müller. *Phys. Lett. B*, 347:413, 1995.
- [20] P.J. Mulders and R.D. Tangerman. *Nucl. Phys. B*, 461:197, 1996.
- [21] John Collins. *Nucl. Phys. B*, 396:161, 1993.
- [22] Aram Kotzinian. *Nucl. Phys. B*, 441:234, 1995.
- [23] R.D. Tangerman and P.J. Mulders. *Phys. Lett. B*, 352:129, 1995.
- [24] J. Levelt and P.J. Mulders. *Phys. Lett. B*, 338:357, 1994.
- [25] T. Gehrmann. hep-ph/9608469.
- [26] Liang Zuo-tang and B. Nolte-Pautz. *Z. Phys. C*, 57:527, 1993.
- [27] J.J. Aubert, *et al.* (EMC Collaboration). *Phys. Lett. B*, 130:118, 1983.
- [28] M. Arneodo, *et al.* (EMC Collaboration). *Z. Phys. C*, 34:277, 1987.
- [29] M.R. Adams, *et al.* (E665 Collaboration). *Phys. Rev. D*, 48:5057, 1993.
- [30] A. Mukherjee, *et al.* *Phys. Rev. Lett.*, 60:991, 1988.
- [31] A. Airepetian, *et al.* (HERMES Collaboration). In preparation.
- [32] Bo Anderson, Gösta Gustafson, and Gunnar Ingelman. *Phys. Lett. B*, 85:417, 1979.
- [33] Wei Lu and Bo-Qiang Ma. *Phys. Lett. B*, 357:419, 1995.
- [34] Mauro Anselmino, *et al.* *Phys. Rev. D*, 54:828, 1996.
- [35] R. L. Jaffe. *Phys. Rev. D*, 54:R6581, 1996.

- [36] M. Vlasova, *et al.* *JETP Lett.*, 64:258, 1996.
- [37] S. Barlag, *et al.* (ACCMOR Collaboration). *Phys. Lett. B*, 325:531, 1994.
- [38] E.A. Chudakov, *et al.* (WA89 Collaboration). *Nucl. Phys. B. (Proc. Suppl.)*, 50:223, 1996.
- [39] G. Bunce, *et al.* *Phys. Rev. Lett.*, 36:1113, 1976.
- [40] K. Heller. *Phys. Rev. Lett.*, 41:607, 1978.
- [41] F. Abe, *et al.* *Phys. Rev. Lett.*, 50:1102, 1983.
- [42] E.J. Ramberg, *et al.* *Phys. Lett. B*, page 403, 1994.
- [43] S. A. Gourlay, *et al.* *Phys. Rev. Lett.*, 56:2244, 1986.
- [44] B. Lundberg, *et al.* *Phys. Rev. D*, 40:3557, 1989.
- [45] Lee G. Pondrom. *Phys. Rep.*, 122:57, 1985.
- [46] A.M. Smith, *et al.* (R608 Collaboration). *Phys. Lett. B*, 185:209, 1987.
- [47] Julián Félix. *Modern Physics Letters A*, page 363, 1997.
- [48] K. Ackerstaff, *et al.* (OPAL Collaboration), hep-ex/9708027.
- [49] D. Buskulic, *et al.* (ALEPH Collaboration). *Phys. Lett. B*, 374:319, 1996.
- [50] M. Burkardt and R. L. Jaffe. *Phys. Rev. Lett.*, 70:2537, 1993.
- [51] D. de Florian, M. Stratmann, and W. Vogelsang. *Phys. Rev. D*, 57:1811, 1998.
- [52] V. Ravindran. *Nucl. Phys. B*, 490:272, 1997.
- [53] R. D. Field and R. P. Feynman. *Nucl. Phys. B*, 136:1, 1978.
- [54] Bruce Bray. *A Determination of the Neutron Spin Structure Function  $g_1^n$  with the 1995 HERMES Data*. PhD thesis, California Institute of Technology, 1997.

- [55] M. Düren. *The HERMES Experiment: From the Design to the First Results*. Habilitation thesis, Friedrich-Alexander-Universität Erlangen-Nürnberg, 1995. HERMES internal note 95-02.
- [56] W. Lorenzon. In Roy J. Holt and Michael A. Miller, editors, *Polarized Gas Targets and Polarized Beams Seventh International Workshop*, page 181, 1998.
- [57] A. Sokolov and I. Ternov. *Sov. Phys. Doklady*, 8:1203, 1964.
- [58] D. De Schepper, *et al.* *Nucl. Inst. and Meth.*, 419:16, 1998.
- [59] K. Ackerstaff, *et al.* (HERMES Collaboration). *Nucl. Inst. and Meth.*, 417:230, 1998.
- [60] Konrad Kleinknecht. *Detectors for particle radiation*. Cambridge University Press, 1986.
- [61] Donald H. Perkins. *Introduction to High Energy Physics*. Addison-Wesley Publishing Company, Inc., 1987.
- [62] J.D. Jackson. *Classical Electrodynamics*. J. Wiley and Sons, 1975.
- [63] W. Wander. *Reconstruction of High Energy Scattering Events in the HERMES experiment*. PhD thesis, Friedrich-Alexander-Universität Erlangen-Nürnberg, 1996. Translated by M. Aversch and R. Kaiser.
- [64] P. Chumney, *et al.*, September 1998. Internal Report to the HERMES Collaboration.
- [65] P. Geiger. *Measurement of Fragmentation Functions at HERMES*. PhD thesis, Ruprecht-Karls-Universität, Heidelberg, 1998.
- [66] Y.I. Azimov, *et al.* *Z. Phys. C*, 27:65, 1985.
- [67] R. Kaiser. *Measurement of the Spin Structure of the Neutron using Polarised Deep Inelastic Scattering*. PhD thesis, Simon Fraser University, 1997.

- [68] F. Menden. *Measurement of the Valence Quark Spin Distributions of the Nucleon Using Deep Inelastic Scattering at HERMES*. Diplomarbeit thesis, Simon Fraser University and University of Hamburg, 1997.
- [69] S. Bernreuther, December 1998. Private communication.
- [70] A. Brüll, July 1998. Private communication.
- [71] I. Akushevich, N. Shumeiko, and A. Soroko. hep-ph/9903325.
- [72] C. Bourrely, E. Leader, and J. Soffer. *Phys. Rep.*, 59:95, 1980.
- [73] G. Schnell. Private communication.
- [74] A. Airepetian, *et al.* (HERMES Collaboration). In preparation.
- [75] S. Boffi, C. Guisti, and F.D. Pacati. *Nucl. Phys. A*, 476:617, 1988.
- [76] Paul W. Carter. *The HERMES Experiment: I. Analyzing Powers in Pion Electroproduction; II. The Aerogel Radiator of the HERMES RICH*. PhD thesis, California Institute of Technology, 1999.
- [77] C. E. Jones. *A Measurement of the Spin-Dependent Asymmetry in Quasielastic Scattering of Polarized Electrons from Polarized  $^3\text{He}$* . PhD thesis, California Institute of Technology, 1992.
- [78] M. Pinard and J. Van Der Linde. *Can. J. Phys.*, 52:1615, 1974.
- [79] W. Lorenzon, T.R. Gentile, H. Gao, and R.D. McKeown. *Phys. Rev. A*, 47:468, 1993.
- [80] A. P. Dvoredsky. In Roy J. Holt and Michael A. Miller, editors, *Polarized Gas Targets and Polarized Beams Seventh International Workshop*, 1998.
- [81] Mitio Inokuti. *Rev. of Mod. Phys.*, 43:297, 1971.

- [82] M. L. Pitt, *et al.* In Hans Paetz gen. Shieck and Lutz Sydow, editors, *Sixth International Workshop on Polarized Beams and Polarized Targets*. World Scientific, London, 1996.
- [83] H. R. Moustafa-Moussa, *et al.* *Physica*, 40:517, 1959.
- [84] L.A. Vainstein and L.P. Presnyakov. *JETP*, 28:156, 1969.
- [85] W. Korsch, *et al.* *Nucl. Inst. and Meth. A*, 389:389, 1997.
- [86] J. Stewart. In Roy J. Holt and Michael A. Miller, editors, *Polarized Gas Targets and Polarized Beams Seventh International Workshop*, 1998.
- [87] B. Braun. In Roy J. Holt and Michael A. Miller, editors, *Polarized Gas Targets and Polarized Beams Seventh International Workshop*, 1998.
- [88] Ingvar Kopp, Rolf Lindgren, and Bo Rydh. *Table of Band Features of Diatomic Molecules in Wavelength Order*. Department of Physics, University of Stockholm, 1974.
- [89] C. A. Miller, March 1997. Private communication.
- [90] R. McKeown, May 1997. Private communication.
- [91] H. Kolster. In Roy J. Holt and Michael A. Miller, editors, *Polarized Gas Targets and Polarized Beams Seventh International Workshop*, 1998.
- [92] C. W. Allen. *Astrophysical Quantities*. University of London: The Athlone Press, 1963.
- [93] G. F. Drukarev. *Collisions of Electrons with Atoms and Molecules*. Plenum Press, New York and London, 1987.
- [94] S. J. Buckman and A. V. Phelps. *Tabulations of Collision Cross Sections and Calculated Transport and Reaction Coefficients for Electrons in H<sub>2</sub> and D<sub>2</sub>*. Number 27 in JILA Information Center. JILA, May 1985.